Large Eddy Simulation of Turbulent Combustion: A Novel Multivariate Probability Density Function Approach

Vom Fachbereich Maschinenbau
an der Technischen Universität Darmstadt
zur
Erlangung des Grades eines Doktor-Ingenieurs (Dr.-Ing.)
genehmigte

D i s s e r t a t i o n

vorgelegt von

M.Sc. Dávid Jesch

aus Nagykanizsa, Ungarn

Berichterstatter:	Prof. Dr.-Ing. Johannes Janicka
Mitberichterstatter:	Prof. Dr. rer. nat. Michael Schäfer
Tag der Einreichung:	26.01.2016
Tag der mündlichen Prüfung:	19.04.2016

Darmstadt 2016

D17

Acknowledgements

The research presented in this dissertation was carried out at the Institute of Energy and Power Plant Technology, at the Darmstadt University of Technology. I would like to express my sincerest gratitude to my advisor Prof. Dr.-Ing. Johannes Janicka for the opportunity to be part of his research group and for his support throughout the years. I have been motivated by the confidence he placed in me and his vast experience and knowledge contributed a lot to my professional development. I am also grateful to Prof. Dr. Francesca di Mare for our discussions and her insightful comments regarding our common work. Moreover, I would like to thank Prof. Dr. rer. nat. Michael Schäfer for his willingness and effort to report on my work.

This project has been funded by the Graduate School of Computational Engineering and their financial support is gratefully acknowledged.

I am indebted to my many colleagues who supported me and to whom I could always turn to with my questions. I cannot find words to express my gratitude to Guido Künne and Amer Avdić, who greatly contributed to this work with their vast amount of experience and from whom I have learnt a lot. I also have to mention and thank Alija Bevrnja who spent hours proofreading the manuscript and showed great skills in spotting mistakes.

Moving to a foreign country and working in a new environment would have been much harder without my first office mates who warmly welcomed me. Many thanks for that to Roozbeh Haghighi and Arash Hosseinzadeh. I have to admit that there were difficult moments during my last year and in those moments the cheerful and encouraging attitude of Henriette Garmatter, Arne Eggers, Martin Rißmann and Jens Hermann helped immensely. I will always be grateful to them!

There are many people without whom this work would have never been completed because it would have never been started in the first place. First and foremost I would like to thank my dear parents, Rózsa Jeschné Kocsis and András Jesch, and my brother, Áron Jesch, who have provided a loving atmosphere throughout my life and who have supported me during my long journey in every possible way they could ever since I was born. Without them, their values, and the rich and happy childhood they provided I would have never accomplished as much.

Then I would like to express my gratitude to my former teachers at my grammar school, especially to Dr. Pintér Ferenc, my teacher in mathematics. He gave me not only the solid fundamentals I could build upon but he also made learning a pleasure and pushed me to my limits. I am indebted to the faculty of Eötvös Loránd University where I completed my studies as a physicist. Without the core knowledge, the skills in mathematics and

physics, and the enthusiasm towards science I have acquired there, I would not be writing these lines now.

I owe my deepest gratitude to my former colleagues at the Department of Fluid Mechanics at the Budapest University of Technology and Economics, especially to Dr. Tamás Lajos, Dr. Gergely Kristóf, and Dr. János Vad, from whom I learnt the fundamentals of fluid mechanics. As a matter of fact I have learnt much more from them than pure science...

My gratitude is extended to Dr. Gábor Stépán, who not only gave great lectures, but also played a crucial part in my personal development. The two scholarships he helped me win truly changed my life and for this I cannot be grateful enough. One of those scholarships led my way to the University of Wisconsin-Madison where I spent one of the most memorable years of my life so far. Whatever adjective I would use here would be an understatement of how thankful I am to Prof. Jaal B. Ghandhi for accepting me and being my advisor.

It gives me great pleasure to mention my closest friends who unfortunately live thousands of kilometers away from me now, but without whom I would not have walked down the same path, and who were always there whenever I needed support, encouragement, or a helping hand. László Vörös, Ágnes Apostol, Zsolt Szigetvári, Attila Kiss and Miklós Varga and their enduring friendship are all parts of my achievements wherever we go in this life. A special thank you is due to my dear friend German Soto with whom I could only spend a couple of memorable and unforgettable months together in the same country, but he still took the time and effort to review my work. He literally has a few words in this work, and his positive attitude to life will always be exemplary for me!

Last but not least, I would like to share the credit of this work with my wife, Erika Pusztai. Her understanding, support, patience, and encouragement during the past years were invaluable. She gave me strength to finish my work and she showed a good example with her stamina and meticulous work she exhibited during her own PhD program.

Dávid Jesch

Darmstadt, January 2016

'We choose to go to the Moon in this decade and do the other things, not because they are easy, but because they are hard; because that goal will serve to organize and measure the best of our energies and skills, because that challenge is one that we are willing to accept, one we are unwilling to postpone...'

- John F. Kennedy -

Dedicated to my loving and supporting family.

Contents

Nomenclature **xi**

1 Introduction **1**
1.1 Energy and Environment . . . 1
1.2 Current Trends and Challenges in Combustion Technology . . . 3
1.3 Experiments and Simulations . . . 5
1.4 State of Research . . . 6
1.5 Objectives . . . 9
1.6 Thesis Outline . . . 9

2 Mathematical Description of Turbulent Flows **11**
2.1 Governing Equations . . . 11
2.1.1 General Form of Conservation Law . . . 12
2.1.2 Conservation of Mass . . . 13
2.1.3 Conservation of Momentum . . . 13
2.1.4 Species Transport . . . 13
2.1.5 Enthalpy Balance . . . 14
2.1.6 The Equation of State . . . 16
2.1.7 Summary of the Applied Equations . . . 16
2.2 Turbulence . . . 17
2.2.1 The Energy Cascade . . . 17
2.2.2 Numerical Treatment . . . 19
2.2.3 Large Eddy Simulation . . . 21
2.2.3.1 Filtering of Transport Equations . . . 21
2.2.3.2 Modeling of Subgrid-Scale Stresses and Fluxes . . . 23
2.2.3.3 Modeling of Subgrid-Scale Variances and Correlations . . . 25
2.3 Summary . . . 26

3 Fundamentals of Combustion **27**
3.1 Chemical Reaction Kinetics . . . 27
3.2 Flame Modes . . . 28
3.2.1 Non-Premixed Flames . . . 29
3.2.2 Premixed Flames . . . 31
3.2.2.1 The Progress Variable . . . 32
3.2.2.2 Laminar Flame Speed and Flame Thickness . . . 33
3.3 Chemistry Reduction Using the Flamelet Approach . . . 34
3.3.1 Flamelet Generated Manifolds . . . 35
3.3.2 Non-Adiabatic Tabulation . . . 36

3.3.3 Summary of Equations . . . 37

4 Flame-Turbulence Interaction 39
4.1 Scales and Diagrams of Turbulent Combustion . . . 39
4.2 Overview of Tools for Turbulent Combustion Modeling . . . 42
4.2.1 PDF Methods . . . 44
4.2.1.1 The Concept of PDF . . . 44
4.2.1.2 PDF Transport Equation . . . 46
4.2.1.3 Presumed PDF Approach . . . 46
4.3 Summary . . . 48

5 Novel Monte Carlo based Joint PDF Approach 49
5.1 Joint Discrete PDF Approach . . . 49
5.2 Creating a Joint PDF . . . 51
5.2.1 Multivariate Beta Distribution . . . 51
5.2.2 Morgenstern's System of Multivariate Distribution Functions . . . 52
5.2.3 Correlation Coefficient . . . 53
5.3 Setting Correlations with Simulated Annealing . . . 54
5.3.1 Generating Samples . . . 54
5.3.2 The Method of Simulated Annealing . . . 55
5.3.3 The Process . . . 58
5.4 Summary . . . 59

6 Numerical Implementations 61
6.1 General solution procedure . . . 62
6.1.1 Spatial discretization . . . 62
6.1.2 Finite Volume Discretization of Transport Equations . . . 63
6.1.3 Diffusive Fluxes . . . 65
6.1.4 Convective Fluxes . . . 67
6.1.5 Time Discretization . . . 68
6.1.6 Pressure Correction . . . 70
6.1.7 Initial and Boundary Conditions . . . 71
6.2 Simulated Annealing . . . 74
6.2.1 Stop conditions . . . 76
6.2.2 Initial Configuration . . . 78
6.2.3 Annealing Schedule . . . 79
6.3 Basic Test Configurations . . . 81
6.3.1 One-Dimensional Density Wave . . . 81
6.3.1.1 Description of Configuration . . . 82
6.3.1.2 Results . . . 83
6.3.2 One-Dimensional Premixed Flame . . . 87
6.3.2.1 Description of Configuration . . . 87
6.3.2.2 Results - Flame Structure . . . 87
6.3.2.3 Results - Flame Propagation . . . 88
6.3.3 One-Dimensional Stratified Premixed Flame . . . 92
6.3.3.1 Description of Configuration . . . 92

6.3.3.2 Results . . . 92
6.3.4 Summary . . . 94
6.4 Overall Solution Procedure . . . 95

7 Two-Dimensional Verification Cases 97
7.1 Two-Dimensional Isothermal Mixing Jet . . . 97
7.1.1 Description of Test Case . . . 97
7.1.2 Evaluation of Results . . . 98
7.2 Two-Dimensional Laminar Bunsen Flame . . . 100
7.2.1 Description of Test Case . . . 100
7.2.2 Evaluation of Results . . . 101
7.3 Two-Dimensional Unsteady Premixed Flame . . . 103
7.3.1 Description of Test Case . . . 103
7.3.2 Evaluation of Results . . . 104
7.4 Two-Dimensional Turbulent Planar Jet . . . 106
7.4.1 Description of Test Case . . . 107
7.4.2 Evaluation of Results . . . 107
7.5 Summary . . . 110

8 Applications 111
8.1 Sandia Flame D . . . 112
8.1.1 Description of Configuration . . . 112
8.1.2 Experimental Data . . . 113
8.1.3 Numerical Setup . . . 114
8.1.4 Results . . . 116
8.1.5 Summary . . . 119
8.2 Bluff-Body Stabilized Non-Premixed Flame . . . 120
8.2.1 Description of Configuration . . . 120
8.2.2 Experimental Data . . . 121
8.2.3 Numerical Setup . . . 122
8.2.4 Results . . . 123
8.2.5 Summary . . . 134

9 Summary and outlook 135

A Rhie and Chow momentum interpolation scheme 138

Bibliography 141

Curriculum Vitae 155

Nomenclature

Variables that are exlusivly used locally are not included in the nomenclature. Units that arise from a local context are denoted by the '$*$' symbol.

Upper case latin letters		**Unit**
A^a	Pre-exponential constant of the Arrhenius law	$*$
C_s	Smagorinsky coefficient	–
$\mathcal{C}$	Courant number	–
$\mathcal{D}$	Diffusion number	–
D_{th}	Thermal diffusion of the mixture	$\mathrm{m^2\,s^{-1}}$
D_α	Diffusion coefficient of the component α	$\mathrm{m^2\,s^{-1}}$
D_Φ	General diffusion coefficient of scalar Φ	$\mathrm{m^2\,s^{-1}}$
E	Error function	–
ΔE	Change in error function	–
E^a	Activation energy	$\mathrm{J\,mol^{-1}}$
$\mathscr{E}$	Efficiency function	–
$\mathscr{F}$	Thickening factor	–
$\mathcal{G}$	Spatial filtering operator	$\mathrm{m^{-3}}$
$\mathcal{J}$	Jacobi-Matrix	–
$\mathcal{J}^h$	Enthalpy flux	$\mathrm{Jm^{-2}s^{-1}}$
L_{ij}	Germano identity	$\mathrm{m^2\,s^{-2}}$
$\mathcal{L}$	Characteristic length scale	m
$\mathcal{M}$	Molar mass of the mixture	$\mathrm{kg\,kmol^{-1}}$
$\mathcal{M}_\alpha$	Molar mass of the species α	$\mathrm{kg\,kmol^{-1}}$
N_R	Number of reactions	–
N_s	Number of species	–
$\mathcal{O}$	In the order of	–
$P(\phi)$	Cumulative distribution function of variable ϕ	–
P	Probability	–

$\mathcal{P}(\phi)$	Probability density function of the variable ϕ	–
$\mathcal{P}_N^{(i)}$	Discrete probability density function of i variables represented with N samples	–
$\overline{P}$	Modified pressure within the LES	Pa
R_{ij}^{exp}	Expected correlation coefficient of variables i and j	–
R_{ij}	Correlation coefficient of variables i and j	–
$\mathcal{R}$	Perfect gas constant	$\mathrm{J\,kmol^{-1}K^{-1}}$
S	General surface	$\mathrm{m^2}$
S_{ij}	Rate of strain	$\mathrm{s^{-1}}$
T	Temperature	K
T_{SA}	Artificial temperature for simulated annealing	K
T_{SA}^0	Initial artificial temperature parameter	–
$\mathcal{U}$	Characteristic velocity	$\mathrm{m\,s^{-1}}$
U_c	Characteristic outflow velocity	m/s
V	General volume	$\mathrm{m^3}$
$V_{\alpha,i}$	Diffusion velocity of the component α into direction i	$\mathrm{m\,s^{-1}}$
Y_α	Mass fraction of the species α	–
$\mathcal{Y}$	Reaction progress variable	–
$\mathcal{Y}_{pv}$	Normalized reaction progress variable	–
$\mathcal{Z}$	Mixture fraction	–
$\mathcal{Z}_k$	Element mass fraction of the element k	–

Lower case latin letters **Unit**

c_p	Specific heat capacity of the mixture at constant pressure	$\mathrm{J\,kg^{-1}K^{-1}}$
$c_{p,\alpha}$	Specific heat capacity of the species α at constant pressure	$\mathrm{J\,kg^{-1}K^{-1}}$
$d_{A;B}$	Distance between point A and B	m
e	Specific internal energy of the mixture	$\mathrm{J\,kg^{-1}}$
e_t	Specific total internal energy of the mixture	$\mathrm{J\,kg^{-1}}$
g_i	Acceleration of gravity into direction i	$\mathrm{m\,s^{-2}}$
h	Specific enthalpy of the mixture	$\mathrm{J\,kg^{-1}}$
h_t	Specific total enthalpy of the mixture	$\mathrm{J\,kg^{-1}}$
h_α	Specific enthalpy of the species α	$\mathrm{J\,kg^{-1}}$
k_B	Boltzmann constant	$\mathrm{J\,K^{-1}}$
k_f, k_b	Rate coefficient of forward and backward reaction	$*$
l	General length	m
l_I	Integral length scale	m
l_m	Mixing length	m
m_α	Mass of the species α	kg

$\dot{m}$	Mass flow rate	kgs^{-1}
n_i	Surface normal vector component in direction i	–
n^a	Arrhenius law temperature exponent	–
p	Pressure	$\mathrm{kg\,s^{-2}m^{-1}}$
r_f, r_b	Reaction rate of the forward and backward reaction	$\mathrm{mol\ m^{-3}s^{-1}}$
s_a	Absolute flame speed	$\mathrm{m\,s^{-1}}$
s_l	Laminar flame speed	$\mathrm{m\,s^{-1}}$
$s_{l\Delta}$	Numerically computed laminar flame speed	$\mathrm{m\,s^{-1}}$
s_T	Turbulent flame speed	$\mathrm{m\,s^{-1}}$
t	Time	s
t_I	Integral time scale	s
u_i	Velocity (into direction i)	$\mathrm{m\,s^{-1}}$
v	Velocity (into direction y)	$\mathrm{m\,s^{-1}}$
x_F	Flame position	m
x_i or x, y, z	Cartesian coordinates	m

Upper case greek letters **Unit**

β^{ij}	Matrix of cofactors	–
Δ	Filter width	m
$\Delta h^{ref}_{\mathrm{f},\alpha}$	Enthalpy of formation of the species α at a reference temperature	$\mathrm{J\,kg^{-1}}$
Δ_t	Time step size	s
Δ_T	General time interval	s
Δ_x	Grid size (also Δ_y or Δ_z if direction is relevant)	m
Γ	Gamma function	–
Γ_Φ	General diffusion coefficient	$*$
$\mathit{\Phi}$	General scalar	$*$
Φ	General scalar variable per unit mass	$*$
Θ	Normalized temperature	–

Lower case greek letters **Unit**

δ_l	Laminar flame thickness	m
δ_r	Thickness of the flame reaction zone	m
δ_T	Thickness of the turbulent flame brush	m
δ_{ij}	Kronecker-symbol	–
ε	Dissipation of the turbulent kinetic energy	$\mathrm{m^2\,s^{-3}}$
η_K	Kolmogorov length scale	m

κ	Wave number (in the energy spectrum)	m^{-1}
λ	Thermal conductivity	$\mathrm{W\,m^{-1}\,K^{-1}}$
μ	Dynamic viscosity	$\mathrm{kg\,s^{-1}\,m^{-1}}$
μ_t	Turbulent dynamic viscosity	$\mathrm{kg\,s^{-1}\,m^{-1}}$
ν	Kinematic viscosity	$\mathrm{m^2\,s^{-1}}$
ν_t	Turbulent kinematic viscosity	$\mathrm{m^2\,s^{-1}}$
ν'_α	Stoichiometric coefficient of species α on the reactant side	–
ν''_α	Stoichiometric coefficient of species α on the product side	–
ξ_i	Local, cell oriented spatial coordinate	–
ρ	Density of the mixture	$\mathrm{kg\,m^{-3}}$
σ_{ij}	Components of total internal stress tensor	$\mathrm{kg\,s^{-2}\,m^{-1}}$
τ_{ij}	Components of the viscous stress tensor	$\mathrm{kg\,s^{-2}\,m^{-1}}$
τ	General time scale	s
τ_K	Kolmogorov time scale	s
ϕ	Equivalence ratio	–
χ	Scalar dissipation rate	$\mathrm{s^{-1}}$
χ_α	General species	–
$\dot{\omega}_\alpha$	Chemical source term of the component α	$\mathrm{kg\,m^{-3}\,s^{-1}}$
$\dot{\omega}_T$	Heat source	$\mathrm{J\,cm^{-3}\,s^{-1}}$
$\dot{\omega}_V$	General volumetric source term	$*$
$\dot{\omega}_S$	General surface source term	$*$

Indices

$\cdot'$	Temporal fluctuation
$\cdot''$	Spatial fluctuation
$\cdot_b$	State in the burnt gas
$\cdot_c$	Chemistry
$\cdot_D$	One node towards the downwind direction
$\cdot_F$	Fuel
$\cdot_f$	Forward reaction
$\cdot_l$	Lean flammability limit
$\cdot_{max}$	Maximum
$\cdot_{min}$	Minimum
$\cdot_{N,E,S,W,T,B}$	One node towards the north, east, south, west, top, bottom direction
$\cdot_{n,e,s,w,t,b}$	North, east, south, west, top, bottom face of a control volume
$\cdot_O$	Oxidizer
$\cdot_r$	Rich flammability limit
$\cdot^{ref}$	Reference conditions ($T = 298.15\,\mathrm{K}$, $p = 101\,325\,\mathrm{Pa}$)

$\cdot_{rms}$	Root mean square
$\cdot^{sgs}$	Subgrid-scale
$\cdot_{st}$	Stoichiometric conditions
$\cdot_T$	Turbulent
$\cdot_u$	State in the unburnt gas
$\cdot_U$ / $\cdot_{UU}$	One node / two nodes towards the upwind direction
$\cdot\big\vert_P$	Value at point P

Operators

$\bar{\cdot}$	Spatial filter (LES) or temporal average (RANS)
$\tilde{\cdot}$	Density weighted filtered/averaged value
$\hat{\cdot}$	Test filter (Germano)

Dimensionless numbers

Da	Damköhler number
Ka	Karlovitz number
Kn	Knudsen number
Le	Lewis number
Le_α	Lewis number of species α
Ma	Mach number
Pr	Prandtl number
Pr_t	Turbulent Prandtl number
Re	Reynolds number
Re_t	Turbulent Reynolds number
Sc	Schmidt number
Sc_α	Schmidt number of the species α
Sc_t	Turbulent Schmidt number

Abbreviations

ATF	Artificially thickened flame
CDS	Central difference scheme
CFD	Computational fluid dynamics
CDF	Cumulative distribution function
CSSA	Correlation set by simulated annealing
DNS	Direct numerical simulation

FASTEST	Flow Analysis by Solving Transport Equations Simulating Turbulence
FGM	Flamelet generated manifolds
FGM-1M	FGM method that uses only the first statistical moments of the control variables
FPI	Flame prolongation of intrinsic low-dimensional manifolds
FVM	Finite volume method
GPU	Graphical processing unit
GTCC	Gas turbine combined cycle
HCCI	Homogeneous charge compression ignition
HPC	High-performance computing
IEM	Interaction by exchange with the mean
IGCC	Integrated gasification combined cycle
ILDM	Intrinsic low-dimensional manifolds
LES	Large eddy simulation
LMSE	Linear mean-square estimation mixing model
LDSM	Low dimensional slow manifold
MC	Monte Carlo
MPI	Message passing interface
MULI	Multi-linear interpolation
PDF	Probability density function
RANS	Reynolds averaged Navier Stokes
RK	Runge-Kutta
SA	Simulated annealing
SIMPLE	Semi-implicit method for pressure-linked equations
TNF	International Workshop on Measurement and Computation of Turbulent Non-premixed Flames
TVD	Total variation diminishing
WOC	Without correlation

Chapter 1

Introduction

It would be hard to overestimate the pivotal role fire and combustion played in the history of humanity. Acquiring the capacity to manipulate fire thousands of years ago let our ancestors start the incredible journey that eventually led to our modern civilization. Fire contributed to the development of agriculture and to the fabrication of ever more sophisticated tools. It helped humans survive under harsh and unforgiving circumstances and allowed us to extend daylight hours artificially. Some researchers even argue that not only has it changed the living circumstances and the surroundings of our species but it has also changed our anatomy. According to these theories the proliferation of cooked food led to smaller guts and bigger brains [72]. No wonder that fire was considered as one of the four ancient elements, although it is essentially a reaction while the other three - earth, water, and air - are substances, which by itself shows that fire is special to humans. In 1720, the Dutch botanist Herman Boerhaave said with all reasons [155]:

'If you make a mistake in your exposition of the Nature of Fire, your error will spread to all the branches of physics, and this is because, in all natural productions, Fire... is always the chief agent.'

Later that century the importance of combustion grew even further when the fully developed version of the steam engine of James Watt and Matthew Boulton went into production. It made the conversion of thermal energy into kinetic energy, which can power machines, possible. The consequently emerging Industrial Revolution changed the world once and for all.

1.1 Energy and Environment

It is not an exaggeration to say that human history has been forged in fire. Not only has fire changed our society but it also has transformed our environment, our planet. Initially fire was a subset of natural history, now we live in an era in which one can argue that natural history, including climate, are becoming subsets of fire history [156]. In a combustion process chemically bound energy is transformed into heat while a reaction takes place between fuel and oxidizer. In a perfect reaction the commonly used hydrocarbons would turn into carbon dioxide and water, but in reality reactions in industrial systems are far from being perfect. This leads to the formation of various pollutants such as sul-

phur oxides, unburnt and partially burnt hydrocarbons, nitrogen oxides, carbon oxides, etc. None of their presence are desirable, but the group of the so-called greenhouse gases (GHG), including among others CO_2, CH_4, NO_x, are of particular importance. There is wide consensus in the scientific community that these gases are the main contributors to global warming [176]. We should be careful with using the term 'global warming' because it is somewhat misleading. One might find it hard not to see occasional extreme cold weather, blizzards, floods, storms, and heavy rainfalls contradictory to the concept of a warming planet. It is more appropriate to refer to the complex phenomenon as 'climate change'. Recent research has shown that the increased probability of extreme weather events can be explained with shifts from the polar jet stream's typical pattern. Due to the so-called Arctic amplification, warming is enhanced in high northern latitudes relative to the northern hemisphere. This leads to a decreasing temperature gradient between the Equator and the Arctic, which alters the characteristic flow patterns of the polar jet stream, thereby causing extreme weather events with an increasing frequency [62]. Therefore reducing CO_2 emissions is a challenge humanity must overcome. And it is a formidable one considering economic interests, society's increasing appetite for energy, and our reliance on fossil fuels.

Global primary energy consumption grew by 30% between 1989 and 2004 and by an additional 21% in the following decade [7]. According to the latest predictions, consumption will have grown by a further 33% by the year 2040. This is not surprising considering that there is plenty of room for further growth as the standard of living increases in developing countries: currently 17% of the global population still remains without electricity [10]. Meanwhile the share of fossil fuels in the total primary energy supply decreases only at a moderate rate: from 86.7% in 1973 to 81.4% in 2014 [9]. By 2040 estimations predict this share to shrink to 75% [10]. This single statistic shows that combustion of fossil fuels is going to remain the backbone of our energy production in the not-so-near future, which is particularly interesting in light of that many analysts in the 1970s warned about the depletion of fossil fuel reserves by the early 2000s. This has turned out not to be the case. As a matter of fact, due to new innovative technologies and changing economical circumstances, the total proved fossil fuel reserves kept on increasing: between 1994 and 2013 proved oil and natural gas reserves increased by 52% and 56%, respectively [7]. This means that at current consumption rates they will not be exhausted for another 52.5 and 54.1 years. Coal is even more abundant: current proved reserves are sufficient for 110 more years. The actual bottleneck of fossil fuel consumption is not the quantity of reserves but the production rate. Although crude oil production went up by 46% between 1973 and 2013, it can barely keep up with the consumption rate. During the same time period both natural gas and coal production increased almost threefold. The new reserves are increasingly hard to extract. Drilling at such remote locations as the Arctic Ocean, Greenland, or the Canadian wilderness is bound to inflict serious damage to the environment. Furthermore, the required disruptive technologies, such as hydraulic fracturing or the production from tar sands, often exacerbate the problem of greenhouse gas emissions. A significant amount of methane has been recently discovered to leak into the atmosphere at many natural gas production sites [29].

Despite all the aforementioned disheartening data, the year 2015 provided some reasons

for optimism. Global economic growth and energy-related emissions may be starting to decouple. For the first time in 40 years CO_2 emissions stayed flat while global economy grew by 3%[11]. Although it is premature to declare that we have reached peak emissions, the trend is definitely encouraging [87]. China has entered a less energy intensive phase of its development: each further unit of economic growth requires 85% less energy than in the previous 25 years. The Asian country intends to reach peak emissions by 2030 at latest. According to the agreement reached at the 2015 United Nations Climate Change Conference (COP21) in Paris, which is argued to be a groundbreaking one by many commentators, the USA is to reduce its GHG emissions by $26 - 28\%$ by 2025 compared to 2005 levels and the European Union pledges to cut GHG emissions by 40% by 2030 relative to 1990 levels [11].

The seemingly optimistic commitments are partly based on the continuing advancements in every sphere of renewable energy. In 2014 renewables accounted for half of the world's new power generation capacity [10]. Solar power is the fastest growing energy sector: its average growth rate has been 50% a year for 6 years. The cost of solar panels has fallen by 80% since 2005. Nevertheless, solar power still accounts for only less than one percent of the global energy supply [141]. Renewable energy has a long way to go and according to the latest predictions its share will have increased to only 25% by 2040 [10]. Even if we could completely phase out fossil fuel based power stations, combustion would still be needed for generating white heat demanded by modern industry. Consequently, combustion is here to stay for the foreseeable future and CO_2 emissions cannot be curbed without improving and further developing combustion systems, thereby increasing their efficiency.

1.2 Current Trends and Challenges in Combustion Technology

To meet the increasingly strict regulations regarding pollutant emissions, up until recently most methods have targeted the combustion products. However, post-combustion treatment is no longer sufficient and research and development efforts are moving towards the controlling of pollutant formation. The formation of NO_x is well-understood [189] and it points in the direction in which progress should be heading. Four sources of NO_x can be identified:

- Fuel bounded nitrogen: it is an issue in coal combustion but not in the case of hydrocarbons.
- Nitrous oxide (N_2O) mechanism: this is usually negligible.
- Thermal NO formation described by the Zeldovich mechanism [200]: the rate of formation grows exponentially with the temperature.
- Prompt NO: formation happens at the flame front in the presence of hydrocarbons.

The latter two processes provide most of the NO, consequently it is beneficial to move away from stoichiometric conditions, thereby avoiding the highest temperatures. This cannot be achieved in non-premixed combustion since diffusion flames inherently contain a stoichiometric zone. In lean premixed combustion the temperature and consequently the quantity of produced NO are lower. Furthermore, the oxidation of unburnt hydrocarbons and CO is enhanced by the presence of excess oxidizer. As a result, lean premixed combustion is increasingly preferred.

European Union legislation has set mandatory emission targets for new passenger cars according to which the amount of emitted CO_2 per kilometer has to be reduced by 40% until 2021 compared to 2007 levels [5]. State of the art research focuses on the development of homogeneous charge compression ignition (HCCI) engines. HCCI combines the favorable properties of conventional diesel and spark ignition engines. Its thermal efficiency is comparable to that of conventional compression ignition engines due to the high compression ratio, while the formation of nitric oxides is reduced by applying highly diluted charges [49].

The emission targets for jet engines are probably even more ambitious. The Flight Path 2050 vision developed by the Advisory Council for Aviation Research and Innovation in Europe [3] set goals such as reducing emissions of CO_2 by 75% and NO_x by 90% relative to aircraft that were new in 2000. Between 1968 and 2014 the average fuel burn of new aircraft fell 45%, but the progress was rather uneven. The annual reduction rate of 1.3% is merely an average as in the aviation industry changes happen in larger discrete steps when a new technology is introduced to the market [190]. The next step is hallmarked by the geared turbofan concept of Pratt & Whitney and CFM's Leap engine, which is the first commercial jet engine that uses ceramic matrix composites. CFM promises a 15% improvement in specific fuel consumption over the current CFM56 version [192], while Pratt & Whitney talks about 16% lower specific fuel consumption, 40% lower NO_x emissions, and a 16% reduction in CO_2 emissions compared to existing Airbus A320 engines, which will be replaced by the PW1100G turbofan on the A320neo version [191]. Both engines feature lean-burn technology [98; 111].

In 2013 transport accounted for 23% of global CO_2 emissions, but the sector of electricity and heat generation was a considerably larger contributor with its 42% share [8], hence curbing the emissions of power plants is of great importance. Carbon capture and storage technologies would make a great leap forward possible [1], but although these technologies are promising, at this point they are still under development [6]. Currently the state of the art is the gas turbine combined cycle (GTCC) technology. In GTCC, initially, the gas turbine generates electricity using natural gas. Then the heat of the exhaust gas emitted by the gas turbine is used to produce steam that drives the steam turbine to generate electricity. GTCC realizes an efficient plant because the heat emitted by the gas turbine, which is discarded in a conventional system, is recycled. In this way the thermal efficiency can be increased to even 63% compared to the 40% efficiency of standalone gas and steam turbines [76]. Compared to coal combustion power plants, natural gas turbine power plants are more efficient and emit significantly less CO_2. Furthermore, they are suitable for augmenting the non-controllable supply of renewable energy due to their flexibility and operational readiness.

Coal combustion is responsible for 46% of global CO_2 emissions [9] and its share in the global energy mix is 29%, which is projected to decrease especially in the developed world. Unfortunately the abundance of coal-fired power plants does not pair up with efficiency, which is only approximately 47%. The most promising technological developments aim at improving it by a further $10-20\%$ using the so-called integrated gasification combined cycle (IGCC). In IGCC coal is first gasified then once contaminants have been removed, it is fed into a gas turbine to generate electricity. Exhaust heat is utilized by a steam turbine similarly to GTCC [4].

Despite these new technologies, further innovation will be necessary to meet the emission targets that could give hope for a sustainable future. For example several difficulties have to be overcome regarding the aforementioned lean systems as their operation is rather challenging due to the low reaction rates, the possibility of extinction, and their sensitivity to mixing and instabilities [53]. Understanding and predicting the underlying physical and chemical phenomena is crucial for further progress. To this end researchers and engineers have two tools: experiments and numerical simulations.

1.3 Experiments and Simulations

When a new combustor is designed, the flow and species distribution fields have to be known to identify the sources of losses and pollutant formation. It is rather challenging to capture all the details because of the complex interaction between the turbulent flow field and the chemical reactions, which happens at very small time and length scales, thereby requiring high resolution to investigate.

State of the art experiments can provide valuable insight, but the applicability of modern measurement techniques has both economical and practical limits. The experimental stands have to be designed and built which is an expensive and time consuming procedure and also requires highly skilled operators. It is increasingly hard to meet in this manner the fast turnaround times required by today's industry. Furthermore, in order to carry out measurement campaigns, we have to modify and simplify the system of interest as most measurements rely on advanced laser-diagnostic techniques, which require the optical accessibility of the target domain. This accessibility cannot always be ensured. Numerical simulations do not have those kind of limitations, however, the algorithms have to be validated somehow, therefore their increasing reliability and accuracy do not render experimental observations superfluous. The ever improving measurements do provide invaluable information and are inherent parts of model development. The publicly available experimental database of the International Workshop on Measurement and Computation of Turbulent Nonpremixed Flames (TNF) [19], which have been used for validation purposes on countless occasions for many years, is a good example in this regard.

The development of computational fluid dynamics (CFD) codes are tightly connected to the performance of computer architectures. After the 1950s five decades of extraordinary exponential growth in performance made remarkable advancements is simulation capabilities possible. However, in the early 2000s the growth in single-processor performance

stalled. The energy consumption of a processor is proportional to its clock speed. Eventually that energy is transformed into heat, which has to be dissipated. We have reached a limit above which this dissipation is no longer feasible [64].

The demand for ever growing performance led to the emergence of multiple-processor parallel systems. These systems have their limitations as well. First, they have already reached a scale at which power consumption becomes both an economical and a technical issue. Second, performance does not scale linearly with the number of processors and new compelling paradigms are needed to efficiently exploit these parallel systems. Consequently high-performance computing (HPC) is on the cusp of a paradigm shift that will affect the future and development of state of the art CFD tools.

During the last decade the application of message passing (MPI) and thread (OpenMP) software models became mainstream. In the future, CFD codes may need to be developed to be capable of fully taking advantage of the potentials of the emerging massively parallel, heterogeneous HPC systems, which utilize hierarchical memory architectures, graphical processing units (GPU), and coprocessors [169]. Parallelization at such a complex level will require a higher degree of automation than what is common today.

It has to be kept in mind that performance is not the only bottleneck though. CFD workflows are often paced by geometry preprocessing and grid generation. Investing into the automation of these processes could bring huge benefits regarding turnaround times of industrial simulations.

Computers have made great strides in performance which have contributed immensely to the development of CFD tools. However, increasing performance by itself would not have amounted to much without the invention of ever more complex and accurate models to describe the physical processes.

1.4 State of Research

In spite of the thousands of years of common history of humanity and fire and the extraordinary progress made in the last couple of decades, accurately describing turbulent combustion processes still remains one of the great challenges in the discipline of engineering. It is a constantly evolving field the latest developments in which have been recently summarized in the review paper of Fiorina et al. [59]. The most frequently used state of the art models have been thoroughly compared in a joint publication of various research groups [58].

Reynolds Averaged Navier-Stokes (RANS) simulation of applied combustion systems were already carried out some 40 years ago. The drawback of RANS is that it only provides information about the mean flow field, but in the case of turbulent flames unsteady mixing effects play an important role. As the performance of computers increased, the application of Large Eddy Simulation (LES) to complex geometries became possible [163]. In LES only the smallest structures are modeled, the large scale dynamics are explicitly calculated, which makes it possible to account for unsteady effects and provides a higher resolution.

The concept of LES was originally introduced by Smagorinsky [170]. Later Germano came up with a dynamic procedure [67] that eliminated the geometry and flow condition dependent parameter, thereby making LES a more general modeling approach.

LES is an outstanding tool for describing turbulent flow fields, however, accommodating the description of chemical reactions in an LES framework is not straightforward [143]. A wide range of time scales are involved in chemical reaction kinetics, which leads to a stiff system of equations. Fortunately not all the reactions are equally important from a global point of view, which gives us an opportunity to reduce the reaction mechanisms [189]. The global process is dominated by the slower reactions, therefore the dimensionality of the problem can be lowered by eliminating the fast processes from the description. It can be done 'manually' by sorting out species in a quasi-steady state and reactions that are assumed to be in partial equilibrium [172; 189]; or for example by an eigenvalue analysis, called the method of intrinsic low-dimensional manifolds (ILDM), proposed by Maas and Pope [119]. The latter approach identifies an attractor subspace in the parameter space, which can be parametrized by only a few coordinates.

Short time scales are not the only difficulties as even the longest length scales of chemistry are generally below the resolution of a typical LES grid. The flame structure and the species distributions cannot be resolved, and the subgrid-scale flame-turbulence interactions need to be modeled. Various approaches exist, which work with different assumptions. The Artificially Thickened Flame (ATF) or Thickened Flame for LES (TFLES) models thicken the flame front until it can be resolved, meanwhile the flame speed is maintained [34; 42]. In the so-called geometrical approaches the premixed flame is treated as an interface that propagates with a prescribed velocity [147]. The G-equation formalism [92; 124] attaches the flame to a constant value of a level-set function, while the flame surface density (FSD) approach assumes that the source term is proportional to both the flame surface area and the propagation speed [26]. Within these methods not the chemistry itself rather its effect is modeled, therefore they cannot account for radicals and intermediate species, which are highly important when it comes to understanding pollutant formation. An efficient way to overcome this limitation is to separate the calculation of the detailed chemistry from that of the flow field instead of applying reduced mechanisms.

Williams [195; 196] postulated that the three-dimensional turbulent flame can be viewed as an ensemble of one-dimensional laminar flames, the so-called flamelets, that are embedded in a turbulent, non-reacting flow field. The flamelet solutions can be calculated in a preprocessing step using detailed chemistry, and the obtained thermochemical properties can be stored in a look-up table as functions of control variables. In this case transport equations only have to be solved for these control variables instead of for all the species mass fractions. The corresponding values can be looked up in the table. Peters [135; 136] used the mixture fraction to characterize non-premixed flames. Pitsch et al. [144] extended this description with unsteady flamelets to account for finite rate chemistry effects. To accommodate premixed flames and flamelets in a tabulated chemistry framework, the concept of reaction progress variable has been introduced leading to the Flamelet Generated Manifolds (FGM) [129] and the Flame Prolongation of ILDM (FPI) [70] methods. The choice of a progress variable is of crucial importance. The definition

may be facilitated by an automatic process [85], but most often it is a linear combination of certain species mass fractions. The FGM approach can be extended with further control variables, for example with the enthalpy to account for heat losses in non-adiabatic flames [94]. Furthermore, it can be coupled with ATF in a straightforward manner [108].

Several other ways of tabulation have been proposed based on the aforementioned concepts. Fiorina et al. [57] suggested a formalism based on a flame index to combine the application of non-premixed and premixed flamelet solutions in partially premixed regimes. Nguyen et al. [128] solved the flamelet equations in a two-dimensional parameter space and applied three scalar dissipation rates besides the mixture fraction and the progress variable, thereby including multi-dimensional diffusion effects in the chemistry table and eliminating the need for interpolations outside of the flammability or the extinction limits. The F-TACLES (Filtered Tabulated Chemistry for Large Eddy Simulation) model tabulates the unclosed terms by filtering one-dimensional laminar flames and storing the results as functions of the progress variable and the filter size [60].

The tabulated chemistry approaches decrease the number of equations to be solved and they make it possible to use detailed reaction mechanisms in an efficient manner. However, subgrid-scale fluctuations are not taken into account as these methods do not solve the problem of spatial resolution. That is defined by the filter size, usually the grid size, in an LES context. The subgrid-scale behavior of the control variables can be described in a statistical manner by the introduction of a probability density function (PDF).

Pope [148; 149] derived the PDF transport equation for the velocity-composition joint PDF, which contains the full information of the scalar statistics. On one hand, in this case the chemical source terms appear in a closed form, which is a major benefit. On the other hand, the mixing term has to be modeled [51; 88; 178; 186]. Unfortunately, the solution of the PDF transport equation is computationally expensive as costs increase exponentially with the number of variables. Several different stochastic Monte Carlo solution methods have been developed to overcome this obstacle, but they lead to the emergence of a statistical error that stems from the finite number of stochastic fields or particles. The most important ones are the Lagrangian [149] and the Eulerian [37] particle-based approaches as well as the Eulerian stochastic field method [17; 183]. Although they reduce the computational costs to a level at which they grow only linearly with the number of variables, these methods are still not suitable for industrial simulations.

It is more common to presume the shape of the PDFs [43] and characterize them with their statistical moments, which can be extracted from the transport equations and various models [18; 31; 140]. It is well-established to apply beta functions [160], although they are not suitable under all circumstances [106]. This approach can be easily coupled with the FGM method. The flamelet solutions can be pre-integrated and tabulated as functions of the considered statistical moments of the control variables [99]. On the downside this increases the dimensionality of the look-up table. Since assuming the shape of a multivariate joint PDF is rather difficult, the general assumption is that the control variables are statistically independent and correlations can be neglected [59]. Brandt el al. [30] proposed a discrete joint PDF approach that can, in theory, account for the covariances, however, in their work the correlations were not set in a rigorous, efficient

manner, besides the method still required a pre-integrated table. Nevertheless, the concept is rather promising and will be further developed in this work.

1.5 Objectives

The present work aims at increasing the accuracy with which we can take into account the subgrid-scale fluctuations, which play an important role in flame-turbulence interactions. We intend to relax the common assumption that the control variables are statistically independent. To this end a novel Monte Carlo based discrete joint PDF approach is developed, which is capable of accounting for the so far neglected covariances of the control variables in a coupled FGM-LES context.

The model is implemented in the academic code FASTEST (see Chapter 6) and shall be optimized to a point at which, contrary to present approaches [30; 93; 99], the pre-integration of the chemistry table becomes unnecessary and statistical moments can be taken into account on the fly during the simulation. This would decouple the presumed PDFs of the transported variables from the chemistry table, thereby opening flexible ways to carry out studies regarding the effects of various PDFs and look-up tables.

The objective of this work is not to investigate the effect of different turbulence models or the various shapes of PDFs, but to prove that the new modeling approach is feasible. Therefore at many points known simple submodels are applied and the focus is kept on the novelties and the critical aspects of the proposed method.

1.6 Thesis Outline

The next three chapters are devoted to the fundamentals of turbulent combustion modeling. First the governing equations of multicomponent fluid flows will be presented before we start discussing the theory and modeling of turbulence. LES will be elaborated on as this approach is applied in this work. In Chapter 4 the fundamentals of combustion are presented with a special emphasis on the FGM method. The second part of this chapter covers how flames interact with the eddies of a turbulent flow field and how, and under what assumptions, we can model this complex phenomenon. A brief overview of different approaches to describe the mean chemical source terms is followed by the more detailed description of the presumed PDF concept coupled with FGM. This serves as a starting point for the development of the Monte Carlo based approach, which is the main topic of this thesis.

Chapter 5 explains why it is difficult to presume the shape of the joint PDF of the control variables and evaluates some options that have proven to be inadequate before the new method is presented. Chapter 6 is about the numerical implementations. Once the discretization, pressure correction, and time-integration procedures in FASTEST are explained, the optimization and stability of the novel approach is discussed using some simple one-dimensional test cases. The verification and validation of the employed model

is demonstrated in Chapter 7 and 8, respectively. For validation purposes a turbulent flame being stabilized in the wake of a bluff-body and a piloted jet flame are simulated. Results are compared to both experimental data and to reference solutions calculated with a standard FGM method that uses only the mean values of the control variables to access the chemistry table (this method will be denoted as FGM-1M hereinafter referring to the first statistical moments being used). The last chapter summarizes the findings and provides an outlook on how this work might be and shall be continued in the future based on those findings.

Chapter 2

Mathematical Description of Turbulent Flows

In this chapter we present the basic set of equations and models that are necessary for describing turbulent flows and transport phenomena. The first section provides the discussion of the physics of fluid flows and the governing equations. In the second part of the chapter we elaborate on the modeling approaches to predicting the behavior of turbulent flows.

While we intend to give a full picture that makes it possible to put into context all the chosen models, a comprehensive overview of this broad field is beyond the scope of this work. Therefore we focus our attention on the methods that are relevant to the subsequent chapters.

2.1 Governing Equations

Fluids are built up of molecules and their properties are determined by these molecules and the interactions between them. When we investigate a fluid on a scale on which individual molecules can and have to be identified, we can realize that all the properties have highly non-uniform distributions. In gases the molecules are separated from each other by long distances compared to their dimensions but even in liquids the mass is concentrated in the nuclei of the atoms of the closely-packed molecules which yields a mass distribution far from uniform. At this level the motion, properties, and collisions of molecules shall be described, and statistical theories can relate the observed macroscopic properties to the collective properties of the individual molecules. (For more details the interested reader is referred to one of the well-known textbooks in this topic such as the ones of Cole [41] or Landau [110].)

However, this detailed description is both unnecessary and unfeasible when we deal with fluids of macroscopic scale such as flows in technical systems. Macroscopic in this context means that the ratio of the mean free path of molecules and the representative physical length scale of the system is much smaller than one. This ratio is also known as the Knudsen number: $Kn \ll 1$. In this case the *continuum hypothesis* is applied which states that the macroscopic behavior of the fluid is the same as if it was perfectly continuous in

its structure and the quantities such as the the pressure, mass, density, etc. are treated as being spread uniformly over the volume in question regardless of the underlying actual molecular structure [23].

Under the continuum hypothesis a set of coupled partial differential equations define the evolution of fluid flows. These equations will be described in the following sections using the common notations for Cartesian tensors and the Einstein summation convention (e.g. summation over a repeated suffix: $u_i u_i = \sum_{i=1}^{3} u_i u_i$). Following Hirsch [83], the description starts with that of the general form of a conservation law based on which the balance equations for all the conserved variables can be derived. These equations are then combined with the equation of state, expressing the dependencies of the variables among each other, and material laws to obtain a full description.

2.1.1 General Form of Conservation Law

Let us consider a flow related scalar quantity Φ and an arbitrary control volume V in the fluid flow bounded by an S closed surface. The general form of the conservation law for Φ can be written in the following form:

$$\frac{\partial}{\partial t}\int\limits_V \Phi \mathrm{d}V = -\oint\limits_S \overrightarrow{F}\cdot \mathrm{d}\overrightarrow{S} + \int\limits_V \dot{\omega}_V \mathrm{d}V + \oint\limits_S \overrightarrow{\dot{\omega}_S}\cdot \mathrm{d}\overrightarrow{S}. \tag{2.1}$$

The first term expresses the variation of Φ per unit time within the control volume. The second term is the *flux*, which is the amount of Φ that crosses S per unit of time. The final two terms account for the contributions of the sources of Φ split into volume and surface sources, respectively. Applying Gauss' theorem leads to the differential form of the conservation law:

$$\frac{\partial \Phi}{\partial t} + \frac{\partial F_i}{\partial x_i} = \dot{\omega}_V + \frac{\partial \dot{\omega}_{S,i}}{\partial x_i} \tag{2.2}$$

The flux term emerges as a sum of the F_C convective flux and the F_D diffusive flux. The convective flux represents the amount of Φ that is transported by the flow:

$$F_{C,i} = \Phi u_i, \tag{2.3}$$

where u_i is the velocity component in direction i. The diffusive flux is a result of thermal molecular agitation and can be present even when the fluid is at rest. The term can be approximated with Fick's law:

$$F_{D,i} = -\rho D_\Phi \frac{\partial \Phi}{\partial x_i}, \tag{2.4}$$

where D_Φ is a diffusion coefficient, ρ is the density, and Φ is the quantity Φ per unit mass.

Substituting the terms into equation (2.2) we obtain the differential form of the general transport equation:

$$\frac{\partial}{\partial t}(\rho\Phi) + \frac{\partial}{\partial x_i}(\rho u_i \Phi) = \frac{\partial}{\partial x_i}\left(\rho D_\Phi \frac{\partial \Phi}{\partial x_i}\right) + \dot{\omega}_V + \frac{\partial \dot{\omega}_{S,i}}{\partial x_i}. \tag{2.5}$$

By substituting the appropriate Φ variables into this form and by identifying the different parameters we can derive the conservation equations of mass, momentum, and energy as well as the species balance equation.

2.1.2 Conservation of Mass

The law of mass conservation, also known as the *continuity equation*, expresses that mass can neither disappear nor be created. In this case $\Phi = \rho$, external sources do not exist, neither does a diffusive flux for the mass transport, which leads to the differential form

$$\frac{\partial \rho}{\partial t} + \frac{\partial}{\partial x_i}\left(\rho u_i\right) = 0. \tag{2.6}$$

2.1.3 Conservation of Momentum

We can obtain the momentum conservation equation by substituting $\Phi = u_i$ into the general (2.5) formula. Similarly to the continuity equation, it is assumed that the diffusion of momentum is not possible. In this work gravity is the only volumetric force considered, therefore $\dot{\omega}_V = \rho g_i$. Assuming that the fluid is Newtonian, we can express the forces acting on the surface element with the total internal stress tensor

$$\sigma_{ij} = -p\delta_{ij} + \tau_{ij}, \tag{2.7}$$

where the first term is the isotropic pressure component and τ is the viscous stress tensor. Based on the Stoke's hypothesis, which is valid for a Newtonian fluid in local thermodynamic equilibrium, τ_{ij} can be expressed as

$$\tau_{ij} = \mu\left[\left(\frac{\partial u_i}{\partial x_j} + \frac{\partial u_j}{\partial x_i}\right) - \frac{2}{3}\frac{\partial u_k}{\partial x_k}\delta_{ij}\right]. \tag{2.8}$$

Knowing all these terms we end up with the final form of the momentum conservation equation also known as the Navier-Stokes equation:

$$\frac{\partial}{\partial t}\left(\rho u_i\right) + \frac{\partial}{\partial x_j}\left(\rho u_i u_j\right) = -\frac{\partial p}{\partial x_i} + \frac{\partial}{\partial x_j}\left[\mu\left(\frac{\partial u_i}{\partial x_j} + \frac{\partial u_j}{\partial x_i}\right) - \frac{2}{3}\mu\frac{\partial u_k}{\partial x_k}\delta_{ij}\right] + \rho g_i. \tag{2.9}$$

2.1.4 Species Transport

Reacting flows consist of multiple species, therefore besides the total mass conservation we have to ensure that the masses of individual species are also conserved. The composition of a mixture can be described with the mass fractions Y_k, which are defined for each species k as the mass of the given species relative to the total mass within the same volume:

$$Y_k = \lim_{V \to 0} \frac{m_k}{\sum_{\alpha=1}^{N_s} m_\alpha}, \tag{2.10}$$

where N_s is the total number of species.

Substituting $\Phi = Y_k$ into the general transport equation gives us the mass conservation equation for species k:

$$\frac{\partial}{\partial t}(\rho Y_k) + \frac{\partial}{\partial x_j}(\rho u_j Y_k) = \frac{\partial}{\partial x_j}\left(\rho D_k \frac{\partial Y_k}{\partial x_j}\right) + \dot{\omega}_k, \tag{2.11}$$

where D_k is the diffusion coefficient for species k. D_k can be expressed as a function of viscosity using the Schmidt number:

$$Sc_k = \frac{\mu}{\rho D_k}. \tag{2.12}$$

The different components in this work are assumed to have the same Schmidt number ($Sc_k = 0.7$) yielding a common diffusion coefficient to be consistent with the tabulation as we will see in Section 3.3.

The diffusion term can also be viewed as the introduction of a diffusion velocity V_k:

$$V_{k,j} Y_k = -D_k \frac{\partial Y_k}{\partial x_j}. \tag{2.13}$$

As stated in Section 2.1.1 this form uses Fick's law to approximate the diffusion velocity and we will stick to this formulation in this work, however, it has to be mentioned that other approaches do exist [147]. The other common approximation is that of Curtiss and Hirschfelder [45], which uses the X_k mole fraction of species k:

$$V_{k,j} X_k = -D_k \frac{\partial X_k}{\partial x_j}. \tag{2.14}$$

For the most general description and the complete system of equations the reader is referred to Williams [197].

If we add all the species conservation equations we have to get back the continuity equation since the mass of the considered fluid equals the sum of the masses of its species. This consideration yields three further conditions for consistency:

$$\sum_{k=1}^{N_s} Y_k = 1, \qquad \sum_{k=1}^{N_s} \dot{\omega}_k = 0, \qquad \sum_{k=1}^{N_s} V_{k,j} Y_k = 0. \tag{2.15}$$

2.1.5 Enthalpy Balance

Temperature plays an important role in combustion processes since chemical reactions are strongly dependent on it. In real industrial systems heat losses and flame-wall interactions are particularly interesting therefore we need a balance equation to describe energy transfer. In this work we will use the enthalpy state variable denoted with h. The enthalpy of the entire mixture can be expressed as the sum of the mass weighted species enthalpies:

$$h = \sum_{k=1}^{N_s} h_k Y_k, \tag{2.16}$$

where h_k is the enthalpy of species k,

$$h_k = \int_{T_{ref}}^{T} c_{p,k} \mathrm{d}T + \Delta h_{f,k}^{ref}. \tag{2.17}$$

$c_{p,k}$ is the specific heat capacity of the k species at constant pressure. The first term is the *sensible enthalpy*, which is temperature dependent, the second term is the *enthalpy of formation* at the T_{ref} reference temperature.

In order to obtain a balance equation we substitute $e_t = e + u_i u_i/2$ into the general conservation law, where e_t is the total energy written as the sum of the internal energy (e) and the kinetic energy per unit mass. Since we consider gravity as the only volumetric force and it acts on all components in equal measures its effect is canceled out from the equation. The diffusion term is written as a $\mathcal{J}_i^h$ enthalpy flux and as there are no external surface heat sources the surface sources are the results of the work done by the internal shear stresses. These considerations lead to the following equation:

$$\frac{\partial}{\partial t}(\rho e_t) + \frac{\partial}{\partial x_i}(\rho e_t u_i) = -\frac{\partial \mathcal{J}_i^h}{\partial x_i} + \frac{\partial}{\partial x_i}(-p u_i + \tau_{ij} u_j) + \dot{Q}, \tag{2.18}$$

where $\dot{Q}$ represents the effect of external sources or sinks such as, for example, radiation effects. In this work $\dot{Q} = 0$ as no external sources are applied.

Using this equation and the fact that the total enthalpy h_t equals on one hand $e_t + p/\rho$ and on the other hand $h + u_i u_i/2$, after some algebraic manipulations and subtracting the (2.9) momentum equation from the energy balance, we can obtain the following expression for h:

$$\frac{\partial}{\partial t}(\rho h) + \frac{\partial}{\partial x_i}(\rho h u_i) = \frac{Dp}{Dt} - \frac{\partial \mathcal{J}_i^h}{\partial x_i} + \tau_{ij}\frac{\partial u_j}{\partial x_i}. \tag{2.19}$$

The first and third terms on the right hand side account for the enthalpy change owing to pressure variations and viscous heating, respectively. In low Mach number flows these effects can be neglected [147].

The enthalpy flux stems from two sources: the heat conduction, which can be expressed according to *Fourier's law*, and the species diffusion described with Fick's law yielding

$$\mathcal{J}_i^h = -\lambda \frac{\partial T}{\partial x_i} - \sum_{k=1}^{N_s} \rho h_k D_k \frac{\partial Y_k}{\partial x_i}, \tag{2.20}$$

where λ is the thermal conductivity. Using the (2.16) and (2.17) formulas after some algebraic manipulations we obtain the following expression:

$$\mathcal{J}_i^h = -\frac{\lambda}{c_p}\frac{\partial h}{\partial x_i} + \rho \sum_{k=1}^{N_s} \left(D_k h_k \frac{\partial Y_k}{\partial x_i}(Le_k - 1) \right). \tag{2.21}$$

The second term on the right hand side represents the enthalpy flux emerging from the imbalance between the species diffusion and the thermal diffusion. The ratio of these is characterized by the *Lewis number*

$$Le_k = \frac{\lambda/c_p}{\rho D_k}. \tag{2.22}$$

The assumption that the diffusion coefficients are equal yields equal Lewis numbers, furthermore, in this work we use the unity Lewis number assumption [147], which means that the diffusion speed of heat and species are of comparable magnitude. This eliminates the second term on the right hand side of equation (2.21) and gives us the final form of the enthalpy balance equation:

$$\frac{\partial}{\partial t}(\rho h) + \frac{\partial}{\partial x_j}(\rho u_j h) = \frac{\partial}{\partial x_j}\left(\frac{\lambda}{c_p}\frac{\partial h}{\partial x_j}\right). \tag{2.23}$$

The coefficient in the diffusion term can be expressed in terms of the viscosity by introducing the dimensionless Prandtl number (Pr):

$$\frac{\lambda}{c_p} = \frac{\mu}{Pr}. \tag{2.24}$$

2.1.6 The Equation of State

We need a further equation that describes the relation among the state variables in order to close the system of equations. We will work with ideal gases exclusively, therefore the thermal equation of state provides this relation:

$$\rho = \frac{p}{T}\frac{\mathcal{M}}{\mathcal{R}}, \tag{2.25}$$

where $\mathcal{R}$ is the ideal gas constant and $\mathcal{M}$ denotes the mean molar mass of the mixture. Pressure variations can be induced either by mechanical compression, which is not considered in this work, or by large velocity variations. In low Mach number flows ($Ma < 0.3$) the emerging pressure fluctuations are small enough ($< 5\%$) to treat the flow as incompressible [15]. Considering that meanwhile the temperature variations can change the density by a factor of ten, it is justified to apply a constant reference pressure (p^{ref}) in the (2.25) state equation.

2.1.7 Summary of the Applied Equations

1. Conservation of mass
$$\frac{\partial \rho}{\partial t} + \frac{\partial}{\partial x_i}(\rho u_i) = 0 \tag{2.26}$$

2. Conservation of momentum
$$\frac{\partial}{\partial t}(\rho u_i) + \frac{\partial}{\partial x_j}(\rho u_i u_j) = -\frac{\partial p}{\partial x_i} + \frac{\partial}{\partial x_j}\left[\mu\left(\frac{\partial u_i}{\partial x_j} + \frac{\partial u_j}{\partial x_i}\right) - \frac{2}{3}\mu\frac{\partial u_k}{\partial x_k}\delta_{ij}\right] + \rho g_i \tag{2.27}$$

3. Species transport
$$\frac{\partial}{\partial t}(\rho Y_k) + \frac{\partial}{\partial x_j}(\rho u_j Y_k) = \frac{\partial}{\partial x_j}\left(\rho D_k \frac{\partial Y_k}{\partial x_j}\right) + \dot{\omega}_k \tag{2.28}$$

4. Enthalpy balance

$$\frac{\partial}{\partial t}(\rho h) + \frac{\partial}{\partial x_j}(\rho u_j h) = \frac{\partial}{\partial x_j}\left(\frac{\lambda}{c_p}\frac{\partial h}{\partial x_j}\right) \tag{2.29}$$

5. Thermal equation of state

$$\rho = \frac{p^{ref}}{T}\frac{\mathcal{M}}{\mathcal{R}} \tag{2.30}$$

2.2 Turbulence

The full numerical solution of the instantaneous balance equations described in Section 2.1.7 is limited to simplified cases in which the range of time and length scales is not too wide [185]. Unfortunately usually this is not the case when industrial systems are investigated. To understand where the wide range of scales comes from, let us introduce the dimensionless Reynolds number [158], which gives the ratio of the inertial forces to the viscous forces as

$$Re = \frac{\rho \mathcal{U}^2}{\mu \mathcal{U}/\mathcal{L}} = \frac{\mathcal{U}\mathcal{L}}{\nu}, \tag{2.31}$$

where $\mathcal{U}$ and $\mathcal{L}$ are the characteristic velocity and length scales of the flow, respectively. For low velocities, when the Reynolds number is not too large, the flows are controlled by the viscous forces, which are capable of sufficiently weakening the fluctuations of flow properties. Flows of this regime are called *laminar* and they exhibit a high degree of order.

At larger Reynolds numbers the laminar motion becomes unstable as the fluid's inertia overcomes the viscous stresses. Consequently the motion becomes rather chaotic with rapid velocity and pressure fluctuations as eddies of different size and frequency develop thereby introducing the aforementioned wide range of scales. This flow regime is described as *turbulent* and is characterized as unsteady, inherently three dimensional, and dissipative [194]. The randomly arranged differently sized vortex structures enhance the transfer of mass, momentum, and energy. This phenomenon is commonly known as turbulent diffusion and it can exceed the molecular diffusion by several orders of magnitude.

The transition between the laminar and the turbulent behavior happens at relatively low Reynolds numbers, therefore the flows in technical systems are often strongly turbulent. As a consequence, understanding and describing turbulent flows are paramount for simulating these configurations. In the following sections we intend to provide a brief overview of the topics in turbulence that are relevant to this work, but for a more comprehensive description the reader is referred to one of the many textbooks in this field [151; 181; 194].

2.2.1 The Energy Cascade

Let us have a closer look at the different scales mentioned in the previous section and try to quantify them following the analysis of Pope [151]. Richardson has introduced the

concept of the energy cascade [161]. Before elaborating on this approach we should clarify what we mean by energy in this context and how we can estimate it.

The energy contained in the turbulent structures is commonly referred to as the turbulent kinetic energy (k) and it is related to the turbulent velocity fluctuations. In order to estimate these fluctuations the u velocity has to be split into two parts:

- a time-averaged part
$$\overline{u} = \frac{1}{\Delta_T} \int_0^{\Delta_T} u(t)\mathrm{d}t, \tag{2.32}$$
where the Δ_T time interval needs to be sufficiently large,
- and a fluctuating part
$$u' = u - \overline{u}. \tag{2.33}$$

Using the fluctuating part we can express the turbulent kinetic energy:

$$k = \frac{1}{2}\overline{u_i' u_i'}. \tag{2.34}$$

In the energy cascade view turbulence is considered to be composed of eddies of different l sizes and corresponding characteristic $u(l)$ velocities along with $\tau(l) = l/u(l)$ time scales. Richardson's notion is that the large eddies are unstable and break up, transferring their energy to smaller eddies, which undergo a similar process. This cascade continues until the viscous forces become sufficiently large to dissipate the energy and no smaller vortices can be formed: the energy is released in the form of heat.

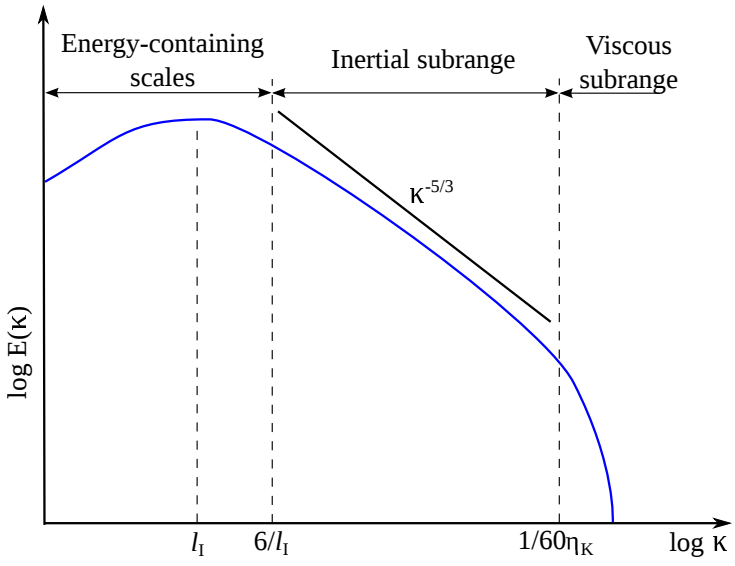

Figure 2.1: Schematic diagram of the turbulent kinetic energy spectrum as a function of the κ wavenumber describing the energy cascade of turbulent flows. The three subranges are depicted as well as the characteristic slope of $\kappa^{-5/3}$ in the inertial subrange [151].

This process is often illustrated with the energy spectrum given in Figure 2.1 in which the distribution of the turbulent kinetic energy is depicted as a function of the $\kappa = 2\pi/l$

wavenumber corresponding to a vortex of size l [151]. We can identify the three subranges the spectrum is commonly divided into and the characteristic length scales, which will be elaborated on in the following paragraphs.

The ε *rate of dissipation* is determined by the transfer of energy from the largest eddies. The l_I integral length scale can be considered as the characteristic length scale of these large eddies and it can be calculated based on two-point correlations in the fluctuating velocity field [151]. As these large scale fluctuations are caused by the largest eddies, the corresponding $u(l_I)$ characteristic velocity is proportional to the fluctuating component of the flow velocity, therefore it is proportional to the turbulent kinetic energy: $u(l_I) \approx \sqrt{k}$. Using these parameters an Re_t turbulent Reynolds number can be defined to characterize the turbulent flow field:

$$Re_t = \frac{u(l_I) l_I}{\nu}. \tag{2.35}$$

Then ε can be approximated as the ratio of the kinetic energy divided by the corresponding time scale:

$$\varepsilon = \frac{u(l_I)^2}{l_I / u(l_I)} = \frac{u(l_I)^3}{l_I}. \tag{2.36}$$

According to Kolmogorov's hypothesis the statistics of the small-scale motions have a universal form that is uniquely determined by ε and ν [104; 151]. Based on these two parameters the following length, velocity, and time scales can be defined, which are also known as the Kolmogorov scales:

$$\eta_K = \left(\frac{\nu^3}{\varepsilon}\right)^{1/4}, \qquad u_K = (\varepsilon\nu)^{1/4}, \qquad \tau_K = \left(\frac{\nu}{\varepsilon}\right)^{1/2}. \tag{2.37}$$

Having defined all these parameters now we can calculate the ratio of the integral length scale to the Kolmogorov length scale thus estimating the ratio of the sizes of the largest and smallest eddies:

$$\frac{l_I}{\eta_K} = \frac{u(l_I)^3/\varepsilon}{(\nu^3/\varepsilon)^{1/4}} = Re_t^{3/4}. \tag{2.38}$$

This result shows us that with an increasing turbulent Reynolds number the range of length scales that need to be captured increases rapidly. This will have important implications regarding the resolution requirements in simulations.

2.2.2 Numerical Treatment

In order to simulate a turbulent reacting flow the set of equations summarized in Section 2.1.7 has to be solved. Analytical solutions only exist for special and rather simplified cases, therefore the analytic approach is not a suitable one when it comes to real industrial systems. We need to apply numerical methods. The basis of these numerical techniques is the computational grid of cells on which the physical domain of interest is mapped. In this way the computational domain and the system of equations become spatially discretized (for details see Chapter 6) making the calculation of all the quantities of interest in the discrete control volumes at discrete points in time possible.

The discretized governing equations can account for all the turbulent structures only if the grid size does not exceed the sizes of the smallest eddies. If this requirement is fulfilled we talk about a **direct numerical simulation (DNS)**, which yields, apart from the numerical errors, the exact solution since no modeling is applied.

The dimensions of the smallest vortices are characterized by the Kolmogorov length scale as we saw in the previous section, therefore the number of grid points necessary for resolving all the turbulent structures will scale with $Re_t^{3/4}$ in every direction according to equation (2.38), consequently with $Re_t^{9/4}$ for a three-dimensional simulation. Computational costs rapidly become prohibitive as a system grows, therefore DNS at the current state of computer technology are only applicable to research purposes and simple geometries of limited spatial dimensions [146; 184]. For calculating complex realistic systems we somehow need to limit the range of scales to be considered. This can be done by either averaging the balance equations in time or by spatially filtering them. The first procedure is called **Reynolds Averaged Navier-Stokes (RANS)** modeling and the second one is referred to as **Large Eddy Simulation (LES)**.

In RANS each Φ quantity is split into a mean $\overline{\Phi}$ and a deviation from the mean Φ' according to equations (2.32) and (2.33). Using this concept we can average the instantaneous balance equations thereby significantly decreasing the demands on the spatial resolution compared to DNS as the averaged equations describe only the time-averaged quantities. However, this improvement comes at a price as unclosed and unknown correlations such as $\overline{\Phi' u'}$ appear. These terms have to be modeled. These models are sometimes optimized for specific circumstances, therefore a wide variety of them exist [151; 194], the detailed description of which are out of the scope and the focus of the current work.

One of the emerging unclosed correlations is particularly interesting, namely the one in the averaged continuity equation:

$$\frac{\partial \overline{\rho}}{\partial t} + \frac{\partial}{\partial x_i}\left(\overline{\rho u_i} + \overline{\rho' u_i'}\right) = 0. \tag{2.39}$$

It is favorable to avoid the modeling of the $\overline{\rho' u_i'}$ correlation, therefore a $\widetilde{\Phi}$ mass-weighted Favre average [54] is introduced as

$$\widetilde{\Phi} = \frac{\overline{\rho \Phi}}{\overline{\rho}}, \tag{2.40}$$

transforming the continuity equation into its Favre-averaged form:

$$\frac{\partial \widetilde{\rho}}{\partial t} + \frac{\partial}{\partial x_i}\widetilde{(\rho u_i)} = 0. \tag{2.41}$$

The same procedure can be applied to the other balance equations as well [185].

Most fluid dynamic simulations in an industrial environment are carried out with RANS since in many cases knowing the mean flow field is sufficient. The drawback of the approach is the large modeling part since the influence of all turbulent structures is only approximated (Figure 2.2). In turbulent flames strong unsteady mixing effects play an important role, therefore it is often insufficient to know only the statistical means. LES

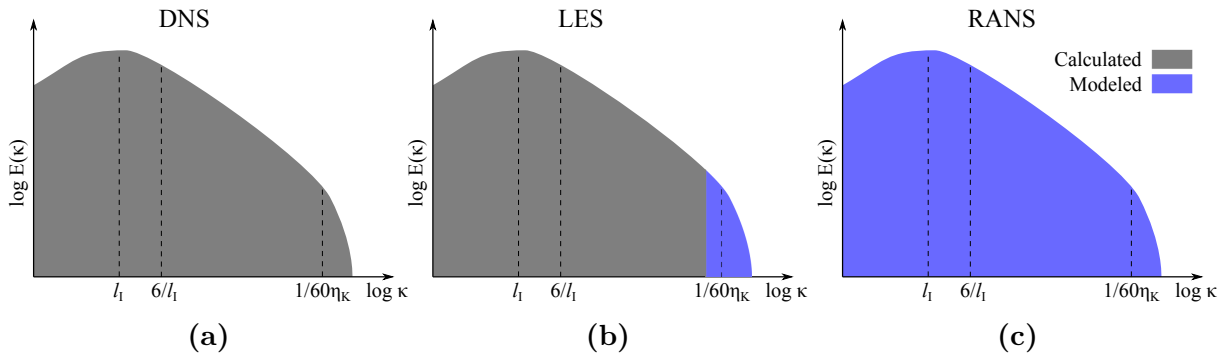

Figure 2.2: The fundamental difference among the three modeling approaches lies in which length scales are modeled and which are explicitely calculated. This is illustrated in this image using the turbulent kinetic energy spectrum [151]: blue color denotes the regime which is modeled while grey accounts for the regime of calculation.

aims to overcome this problem while keeping the computational costs at an affordable level.

In LES the largest structures of the flow, typically the ones that are larger than the grid spacing, are explicitly calculated while the effects of the smaller ones are modeled as it is illustrated in Figure 2.2. This is achieved by filtering the relevant quantities either in the spectral space or spatially in the physical space. This is often done implicitly since imposing a discrete grid on the domain by itself filters out the smaller structures [163].

Although flame-turbulence interaction occurring at the unresolved scales still has to be modeled, LES is considered as a great improvement compared to RANS in this context [185]. It is more appropriate to model only the smallest structures since those are independent of the geometry and therefore exhibit more universal properties. The large structures that are strongly affected by the actual geometry are explicitly calculated as well as the unsteady large scale mixing on which most of the global flame properties depend. LES is also a powerful tool when it comes to predicting instabilities since those depend on large scale coherent structures [124]. In a certain manner LES combines the positive aspects of DNS (capturing certain unsteady phenomena) and RANS (affordable computation time), therefore this method is used exclusively in this work and we discuss it in more details in the next section.

2.2.3 Large Eddy Simulation

2.2.3.1 Filtering of Transport Equations

In LES the small scales are filtered out by the application of a $\mathcal{G}$ low pass filter as

$$\overline{\Phi}(x_i) = \int \Phi(x')\mathcal{G}(x_i - x_i')dx_i', \tag{2.42}$$

with the following constraint for consistency:

$$\int_{-\infty}^{\infty} \mathcal{G}(x_i - x_i')dx_i' = 1. \tag{2.43}$$

Many different standard filters are known and the filtering procedures have been thoroughly investigated throughout the history of LES [163]. In this work we use a simple box filter that is imposed on the flow field implicitly by the numerical grid of Δ_i spacing in the i direction:

$$\mathcal{G}(x_i) = \begin{cases} \prod_{i=1}^{3} \frac{1}{\Delta_i} & : |x_i| \leq \frac{\Delta_i}{2} \\ 0 & : |x_i| > \frac{\Delta_i}{2} \end{cases} \tag{2.44}$$

For the same reasons as in the case of RANS, a density-weighted Favre filtering is applied in the same manner as it was defined in equation (2.40). Using this filtering technique all the Φ variables can be divided into a $\widetilde{\Phi}$ filtered and a Φ^{sgs} unresolved part, which corresponds to the subgrid-scale fluctuations.

$$\Phi = \widetilde{\Phi} + \Phi^{sgs}. \tag{2.45}$$

In order to derive the balance equations for the filtered quantities from the instantaneous ones described in Section 2.1.7, the filtering and differentiation operators need to be exchanged. This is theoretically valid only under restrictive assumptions, however, in most simulations the introduced errors are neglected since the approximation remains within the accuracy obtainable with a numerical scheme of second-order [68]. This leads us to the following set of filtered balance equations:

1. Conservation of mass
$$\frac{\partial \overline{\rho}}{\partial t} + \frac{\partial}{\partial x_i}\left(\overline{\rho}\widetilde{u}_i\right) = 0 \tag{2.46}$$

2. Conservation of momentum
$$\frac{\partial}{\partial t}\left(\overline{\rho}\widetilde{u}_i\right) + \frac{\partial}{\partial x_j}\left(\overline{\rho}\widetilde{u}_i\widetilde{u}_j\right) = -\frac{\partial \overline{p}}{\partial x_i} + \frac{\partial}{\partial x_j}\left[\overline{\tau}_{ij} - \overline{\rho}\left(\widetilde{u_i u_j} - \widetilde{u}_i\widetilde{u}_j\right)\right] + \overline{\rho}g_i \tag{2.47}$$

3. Species transport
$$\frac{\partial}{\partial t}(\overline{\rho}\widetilde{Y}_k) + \frac{\partial}{\partial x_j}(\overline{\rho}\widetilde{u}_j\widetilde{Y}_k) = \frac{\partial}{\partial x_j}\left[\frac{\overline{\mu}}{Sc_k}\frac{\partial \widetilde{Y}_k}{\partial x_j} - \overline{\rho}\left(\widetilde{u_j Y_k} - \widetilde{u}_j\widetilde{Y}_k\right)\right] + \overline{\dot{\omega}}_k \tag{2.48}$$

4. Enthalpy balance
$$\frac{\partial}{\partial t}(\overline{\rho}\widetilde{h}) + \frac{\partial}{\partial x_j}(\overline{\rho}\widetilde{u}_j\widetilde{h}) = \frac{\partial}{\partial x_j}\left[\frac{\overline{\mu}}{Pr}\frac{\partial \widetilde{h}}{\partial x_j} - \overline{\rho}\left(\widetilde{u_j h} - \widetilde{u}_j\widetilde{h}\right)\right] \tag{2.49}$$

In these equations unclosed correlations appear similarly to RANS. The subgrid components, expressed as $(\widetilde{u_i\Phi} - \widetilde{u}_i\widetilde{\Phi})$, need closure, which will be discussed in the next section.

2.2.3.2 Modeling of Subgrid-Scale Stresses and Fluxes

The objective is to model the subgrid components, which can no longer be computed due to having filtered out the information about the relevant scales, as functions of known values. The underlying assumption is that the influence of small-scale structures on the large-scale structures can be described with the large-scale features themselves. Several different approaches exist the detailed overview of which can be found in Sagaut's book [163]. Here we restrict ourselves to the presentation of the models applied in the current work.

These models belong to the family of *linear models* based on the eddy-viscosity approach the key assumption of which is that the small-scale turbulence affects the flow in the same way as the molecular viscosity. Therefore the subgrid components should be modeled by introducing a ν_t turbulent viscosity, which in combination with the ν molecular viscosity yields an effective viscosity. Applying this to the $\tau_{ij}^{sgs} = (\widetilde{u_i u_j} - \widetilde{u}_i\widetilde{u}_j)$ residual stress tensor would lead to

$$-\tau_{ij}^{sgs} = \nu_t \left(\frac{\partial \widetilde{u}_j}{\partial x_i} + \frac{\partial \widetilde{u}_i}{\partial x_j} \right) - \frac{2}{3}\nu_t \frac{\partial \widetilde{u}_k}{\partial x_k}\delta_{ij}, \tag{2.50}$$

however, in this case the trace of the stress tensor would be zero. In our work we use a pressure correction scheme discussed in Section 6.1.6 in the case of which this constraint may be lifted. The trace term of the stress tensor can be added to the pressure and the anisotropic part of τ^{sgs} can be expressed with ν_t:

$$\overline{P} = \overline{p} + \frac{1}{3}\overline{\rho}\tau_{kk}^{sgs}, \tag{2.51}$$

$$\tau_{ij}^{sgs} - \frac{1}{3}\tau_{kk}^{sgs}\delta_{ij} = -2\nu_t \left(\widetilde{S}_{ij} - \frac{1}{3}\widetilde{S}_{kk}\delta_{ij} \right), \tag{2.52}$$

where $\widetilde{S}$ is the filtered rate of strain

$$\widetilde{S}_{ij} = \frac{1}{2}\left(\frac{\partial \widetilde{u}_j}{\partial x_i} + \frac{\partial \widetilde{u}_i}{\partial x_j} \right). \tag{2.53}$$

This is the Boussinesq approximation.

The subgrid-scale components in the species and the enthalpy transport equations are closed with a gradient approach:

$$\widetilde{u_j Y_k} - \widetilde{u}_j\widetilde{Y}_k = -\frac{\nu_t}{Sc_t}\frac{\partial \widetilde{Y}_k}{\partial x_j}, \tag{2.54}$$

$$\widetilde{u_j h} - \widetilde{u}_j\widetilde{h} = -\frac{\nu_t}{Pr_t}\frac{\widetilde{h}}{\partial x_j}, \tag{2.55}$$

where Sc_t and Pr_t are the turbulent Schmidt and Prandtl number, respectively. As it was discussed in Section 2.1.4 and 2.1.5, in this work it is assumed that all components have the same Schmidt number ($Sc = 0.7$) and as all the Lewis numbers equal 1 which leads to $Pr = 0.7$. Furthermore, as it is common practice, the turbulent Schmidt and Prandtl numbers are assumed to equal their laminar counterparts: $Sc_t = Pr_t = 0.7$.

We have managed to express the unresolved subgrid-scale components with known quantities, however, we still have to establish a model for the introduced, and so far unknown, turbulent viscosity. The concept of the turbulent viscosity by itself highlights the advantage of LES over RANS. The analogy between the molecular and the turbulent diffusion implicitly implies that the turbulent diffusion is isotropic. We saw that the large-scale structures are geometry dependent, therefore this is not the case for RANS while it is a much better assumption when it comes to LES and its unresolved small-scale structures.

According to Prandtl's mixing length hypothesis [152] ν_t is proportional to a characteristic length scale, the so-called l_m mixing length, and the velocity gradient:

$$\nu_t \propto l_m^2 |\widetilde{S}|, \tag{2.56}$$

where

$$|\widetilde{S}| = \sqrt{2\widetilde{S}_{ij}\widetilde{S}_{ij}}. \tag{2.57}$$

The Smagorinsky model Smagorinsky [170] used the Δ filter size to define the characteristic length scale as

$$\nu_t = (C_s\Delta)^2 |\widetilde{S}_{ij}|, \tag{2.58}$$

where C_s is a model constant, which needs to be approximated. Depending on the case specific assumptions made, the suggested value of C_s varies between 0.065 and 0.2. The actual value strongly depends on the flow field. $C_s = 0.2$ is frequently used in the center of a channel while this value leads to the overestimation of ν_t near the walls causing excessive dissipation. For simple configurations this problem can be addressed by the introduction of the van Driest damping function [126], however, this is not a suitable solution for the description of complex geometries.

The Germano Procedure Germano introduced a dynamic procedure to overcome the problems caused by the inflexibility of the Smagorinsky model [67]. In this approach C_s is determined locally based on a similarity assumption, which uses a second larger filter: $\hat{\Delta} > \Delta$. With $\hat{\Delta}$ only a smaller part of the turbulent fluctuations remain resolved, consequently the contribution of the model will increase. The key idea is that if our model is consistent the C_s parameter should be the same in both cases.

First the numerical grid implicitly filters the flow field leading to the residual stress tensor

$$\tau_{ij}^{sgs} = \widetilde{u_i u_j} - \widetilde{u}_i\widetilde{u}_j. \tag{2.59}$$

In the next step we filter the resolved LES field explicitly with the larger filter. In this work we apply a box filter with a filtering molecule of 27 cells (the control volume in question and all the surrounding cells). This leads to

$$\widehat{\tau}_{ij} = \widehat{\widetilde{u_i u_j}} - \widehat{\widetilde{u}}_i\widehat{\widetilde{u}}_j. \tag{2.60}$$

The same filter is applied to equation (2.59):

$$\widehat{\tau_{ij}^{sgs}} = \widehat{\widetilde{u_i u_j}} - \widehat{\widetilde{u}_i\widetilde{u}_j}. \tag{2.61}$$

If we subtract this from equation (2.60), we obtain the amount of information lost due to the second filtering also known as the Leonard term

$$L_{ij} = \widehat{\tau}_{ij} - \widehat{\tau_{ij}^{sgs}} = \widehat{\widetilde{u}_i \widetilde{u}_j} - \widehat{\widetilde{u}}_i \widehat{\widetilde{u}}_j. \tag{2.62}$$

Assuming that the same modeling constant can be applied we can express both $\widehat{\tau}_{ij}$ and τ_{ij}^{sgs} using Smagorinsky's model described by the (2.58) formula and equation (2.52):

$$\tau_{ij}^{sgs} - \frac{1}{3}\tau_{kk}^{sgs}\delta_{ij} = -2C_s^2\Delta^2|\widetilde{S}_{ij}|\left(\widetilde{S}_{ij} - \frac{1}{3}\widetilde{S}_{kk}\delta_{ij}\right) = -2C_s^2 m_{ij}^{sgs} \tag{2.63}$$

$$\widehat{\tau}_{ij} - \frac{1}{3}\widehat{\tau}_{kk}\delta_{ij} = -2C_s^2\widehat{\Delta}^2|\widehat{\widetilde{S}}_{ij}|\left(\widehat{\widetilde{S}}_{ij} - \frac{1}{3}\widehat{\widetilde{S}}_{kk}\delta_{ij}\right) = -2C_s^2\widehat{m}_{ij}. \tag{2.64}$$

Substituting these expressions into equation (2.62) yields

$$L_{ij} - \frac{1}{3}L_{kk}\delta_{ij} = 2C_s^2 M_{ij}, \tag{2.65}$$

with the definition of $M_{ij} = \widehat{m_{ij}^{sgs}} - \widehat{m}_{ij}$. This represents five linearly independent equations for the determination of the C_s coefficient. It is not possible to satisfy all of them at the same time, therefore Lilly [116] proposed to minimize the mean square residual, which leads to the following relation:

$$C_s^2 = \frac{M_{ij}L_{ij} - \frac{1}{3}L_{kk}\delta_{ij}M_{ij}}{2M_{ij}M_{ij}} = \frac{M_{ij}L_{ij}}{2M_{ij}M_{ij}}. \tag{2.66}$$

This formulation can destabilize the simulation as the resulting C_s parameter might experience strong spatial and temporal fluctuations [61]. Hahn [77] and Olbricht [131] implemented a temporal relaxation procedure to ensure a smoother behavior:

$$C_s^2(t^{n+1}) = (1-w)C_s^2(t^n) + w\frac{M_{ij}L_{ij}}{2M_{ij}M_{ij}}, \tag{2.67}$$

where $w = 10^{-2}$ is a weighing factor. Furthermore, the procedure could yield negative values for the turbulent viscosity, which is rather unphysical and could introduce extra instabilities. Therefore the final constant is limited to $0 \leq C_s^2(t^{n+1}) \leq 1$.

2.2.3.3 Modeling of Subgrid-Scale Variances and Correlations

We can model the effects of the filtered out scales with the introduced turbulence models. However, to account for the turbulence-chemistry interaction, we will need to somehow approximate the subgrid variances and covariances of certain scalars. The most accurate results can be obtained by deriving transport equations for the variances [99] and less commonly for the covariances [30] of interest, but this is a very expensive solution.

Cook and Riley [43] developed a scale-similarity model that uses the self-similar behavior of turbulent properties at different length scales. They describe the subgrid-scale variance with the help of a larger test filter in an analogous manner to the Germano model

described in Section 2.2.3.2. For this model to work a scale-similarity constant has to be specified. Unfortunately this parameter is not universal and highly flow dependent thereby introducing large errors [188].

Branley and Jones [31] proposed a model that uses the resolved gradients to approximate the $\widetilde{\Phi''^2}$ subgrid-scale variance as

$$\widetilde{\Phi''^2} \approx C_\Phi \Delta^2 \left(\frac{\partial \widetilde{\Phi}}{\partial x_i} \frac{\partial \widetilde{\Phi}}{\partial x_i} \right). \tag{2.68}$$

In this simple and computationally cheap approach C_Φ is a constant with a value of $0.1 \leq C_\Phi \leq 0.2$. Pierce and Moin [140] proposed a dynamic formulation to evaluate the model constant. Balarac et al. [18] summarized all these different approaches and evaluated their deficiencies using the concept of optimal estimators. In light of their findings they proposed a new formulation based on a Taylor series expansion.

Although we acknowledge the shortcomings of the approach and that there is room for improvement in the future, in this work we use the gradient model of Branley and Jones with $C_\Phi = 0.15$ in accordance with the previous works of Hahn [77], Olbricht [131], and Ketelheun [93]. One of the benefits of this choice is that it can be extended to calculate the covariances in a straightforward manner [140]:

$$\widetilde{\Phi''\Psi''} \approx C_{\Phi\Psi} \Delta^2 \left(\frac{\partial \widetilde{\Phi}}{\partial x_i} \frac{\partial \widetilde{\Psi}}{\partial x_i} \right). \tag{2.69}$$

2.3 Summary

In this chapter we presented the brief overview of the fundamental equations and models used for describing turbulent flows of multiple species. We started with the governing equations and the assumptions made during their derivation then we elaborated on modeling turbulence. We addressed the issue of striking a balance between an affordable computational cost and a sufficiently fine spatial resolution, and highlighted the main properties, advantages, and shortcomings of the three big families of turbulence models: DNS, RANS, and LES. Our focus was on LES since in this work we use this approach exclusively. Besides presenting the filtered governing equations we payed special attention to how to model the emerging subgrid-scale fluxes and decided in favor of using the dynamic Germano approach. Subgrid-scale variances and covariances play a very important role in our model, therefore we investigated how to approximate them and chose to use the gradient approach of Branley and Jones.

There is one term left in the equations that has not been addressed so far: the $\widetilde{\dot{\omega}}_k$ filtered chemical source term. In order to be able to approach the formidable challenge of treating this term and appropriately describing the flame-turbulence interaction, first we need to overview the fundamentals of combustion. This is the topic of the next chapter.

Chapter 3

Fundamentals of Combustion

3.1 Chemical Reaction Kinetics

During combustion processes the potential energy of chemical connections is transformed into thermal energy. From a global point of view it means that fuel and oxidizer are converted into products while heat is being provided. This process can be presented as a single global reaction such as the one describing the reaction of methane and oxygen:

$$CH_4 + 2O_2 \rightarrow CO_2 + 2H_2O. \tag{3.1}$$

This simple description does not tell us anything about the temporal evolution or the intermediate steps of the reaction. In reality the CH_4 and O_2 molecules do not turn into the final products right away when they collide. Smaller molecules, radicals, even single atoms are formed as the larger molecules are broken up and these pieces then recombine to form new species. As hundreds of intermediate species do exist, we can only describe the global reaction in its completeness if we take into consideration all the underlying *elementary* reactions and we derive a balance equation for each and every species.

Let us consider N_s species denoted with χ_i and N_R elementary reactions with the stoichiometric coefficients $\nu'_{i,j}$ and $\nu''_{i,j}$ corresponding to species χ_i and reaction j. The entire set of elementary reactions can be summarized as

$$\sum_{i=1}^{N_s} \nu'_{i,j}\chi_i \rightleftharpoons \sum_{i=1}^{N_s} \nu''_{i,j}\chi_i \qquad\qquad j \in \{1, \ldots, N_R\}. \tag{3.2}$$

The arrows between the two sides of the equations indicate that some of these reactions are reversible and may evolve in both directions. Therefore an $r_{f,j}$ forward and an $r_{b,j}$ backward reaction rate should be defined for reaction j in order to be able to determine the $\dot{\omega}_i$ source term of χ_i. These reaction rates are the functions of the species concentrations:

$$r_{f,j} = k_{f,j} \prod_{i=1}^{N_s} \left(\frac{\rho Y_i}{\mathcal{M}_i}\right)^{\nu'_{i,j}} \qquad\qquad r_{b,j} = k_{b,j} \prod_{i=1}^{N_s} \left(\frac{\rho Y_i}{\mathcal{M}_i}\right)^{\nu''_{i,j}}. \tag{3.3}$$

The reaction rate coefficients $k_{f,j}$ and $k_{b,j}$ are usually approximated with the Arrhenius law:

$$k_{l,j} = A^a_{l,j} T^{n^a_{l,j}} \exp\left(-\frac{E^a_{l,j}}{\mathcal{R}T}\right) \qquad\qquad l \in \{f, b\}. \tag{3.4}$$

E^a is the activation energy, and the pre-exponent factor is decomposed into the A^a constant and its temperature dependent part expressed with the n^a exponent. The reaction rates can be calculated from the rate coefficients then we arrive to the expression of the $\dot{\omega}_i$ source term by summing up all the contributions of the individual elementary reactions:

$$\dot{\omega}_i = \mathcal{M}_i \sum_{j=1}^{N_R} \left(\nu''_{i,j} - \nu'_{i,j}\right) \left(r_{f,j} - r_{b,j}\right). \tag{3.5}$$

This leaves us with N_s equations for the source terms, the parameters of which should all be known. Therefore the knowledge of all the pre-exponential constants, temperature exponents, and activation energies is of paramount importance. Determining these coefficients is a research field on its own. The more species are considered, the more equations we have and the more parameters have to be defined. Detailed mechanisms including all the species can consist of thousands of reactions, however, not all of them are equally important. It is beneficial to simplify the mechanisms by eliminating the reactions that have minor effects on the overall process. To this end several techniques exist [189]. Most of them are based on the observation that the time scales of the different reactions span over several orders of magnitude, consequently the slower ones dominate the global process. We can lower the dimensionality of the composition space by identifying and eliminating the fast processes.

In this work the GRI3.0-mechanism [171] of methane-air combustion will be used unless it is stated otherwise. This mechanism consists of 53 species and 325 reactions and is commonly used in the combustion community.

Augmenting the mass, momentum, species, and enthalpy transport equations with the (3.5) set of source term equations and the respective reaction mechanism yields a complete system with the solution of which theoretically any given arbitrary flame can be described. However, for complex industrial applications this is rather unfeasible, therefore we need to further investigate combustion processes to establish reasonable assumptions and simplifications as well as practical models. This is the topic of the next sections.

3.2 Flame Modes

It is useful to distinguish and thoroughly investigate certain fundamental flame structures that can be used for the description of more complex configurations. Fuel and oxidizer need to mix in order for combustion to take place. Depending on whether they are completely mixed or separated before they reach the flame we can talk about premixed or non-premixed combustion respectively. The difference between the underlying mechanisms in the two cases has important implications regarding the flame structure, its dynamic behavior, and how the whole process can be treated from a modeling point of view on which we will elaborate in the remaining part of this section.

First let us quantify the fuel and oxidizer content of a given mixture. To this end the ϕ equivalence ratio is defined as the fuel-oxidizer ratio normalized with its value corresponding to the stoichiometric conditions under which both the methane and the oxygen

are completely consumed during the reaction:

$$\phi = \left(\frac{Y_F}{Y_O}\right) / \left(\frac{Y_F}{Y_O}\right)_{st}. \tag{3.6}$$

Depending on whether the fuel or the oxidizer is in excess compared to stoichiometric conditions ($\phi = 1$) one can talk about a rich ($\phi > 1$) or a lean ($\phi < 1$) mixture, respectively.

3.2.1 Non-Premixed Flames

In the case of non-premixed combustion the fuel and the oxidizer enter the chamber separately, then they mix and burn. The simplest example is a counterflow configuration in which fuel comes in from one side, oxidizer from the other, and the two streams flow in opposite directions thereby establishing a stagnation flow.

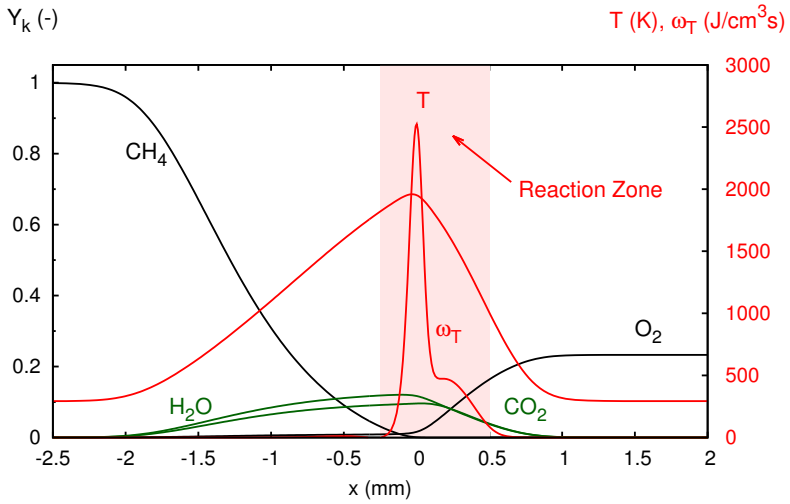

Figure 3.1: Structure of a one-dimensional non-premixed methane-air flame that burns in a counterflow configuration.

Chemical reactions can only proceed in a limited reaction zone where the components are mixed adequately. The emerging flame is usually close to where the mixture is stoichiometric. Heat is generated in the reaction zone and is transported away (see Figure 3.1). Mixing has to be fast enough to sustain the chemical reaction otherwise quenching can occur if the heat fluxes leaving the reaction zone become greater than the heat production. In a counterflow configuration this can be induced by increasing the velocities of the opposing jets.

The structure of a non-premixed flame depends on the ratio of the characteristic time scales of chemistry and diffusion. This ratio determines the thickness of the mixing zone and thereby that of the reaction zone, consequently a non-premixed flame does not have a characteristic thickness: it depends on the local flow conditions. Neither can non-premixed flames propagate. Their position is controlled by mixing which is why they

are often referred to as diffusion flames. Due to these properties it is safer to operate non-premixed systems compared to premixed ones.

To describe the mixing and thereby the entire flame structure controlled by it, the mixture fraction approach can be applied [197]. We made the following assumptions when we derived the transport equations in Section 2.1:

- there are no heat fluxes due to either concentration gradients (Dufour effect) or temperature gradients (Soret effect),
- there is no diffusion caused by either pressure gradients or external forces,
- radiation is negligible,
- the low Mach number assumption is valid: the pressure is constant,
- there is no viscous heating,
- the Lewis number equals 1 for all species: heat and mass diffusions are equal and there is no differential diffusion.

Under these assumptions (also known as the Shvab-Zeldovich formulation [168; 201]) the species and enthalpy transport equations have the same structure and they are no longer independent. The number of variables can be reduced by the introduction of the $\mathcal{Z}$ mixture fraction.

If we consider a single step chemical reaction between a fuel and an oxidizer, $\mathcal{Z}$ can be defined as an appropriate combination of fuel and oxidizer mass fractions that eliminates the source term from the combination of the species concentration equations [147; 185]. $\mathcal{Z}$ is normalized in a way that it equals 0 for pure oxidizer and 1 for pure fuel.

Bilger [25] proposed a more sophisticated definition, which is applicable to hydrocarbon-oxygen reactions. It is based on the Z_α element mass fractions of carbon, hydrogen, and oxygen:

$$\mathcal{Z} = \frac{2\left(\mathcal{Z}_C - \mathcal{Z}_{C,o}\right)/\mathcal{M}_C + \left(\mathcal{Z}_H - \mathcal{Z}_{H,o}\right)/\left(2\mathcal{M}_H\right) - \left(\mathcal{Z}_O - \mathcal{Z}_{O,o}\right)/\mathcal{M}_O}{2\left(\mathcal{Z}_{C,f} - \mathcal{Z}_{C,o}\right)/\mathcal{M}_C + \left(\mathcal{Z}_{H,f} - \mathcal{Z}_{H,o}\right)/\left(2\mathcal{M}_H\right) - \left(\mathcal{Z}_{O,f} - \mathcal{Z}_{O,o}\right)/\mathcal{M}_O}, \tag{3.7}$$

where $\mathcal{Z}_{\alpha,o}$ and $\mathcal{Z}_{\alpha,f}$ are the element mass fractions of element α in the oxidizer and the fuel, respectively.

The mixture fraction is a passive scalar obeying the following transport equation:

$$\frac{\partial}{\partial t}(\rho\mathcal{Z}) + \frac{\partial}{\partial x_j}(\rho u_j \mathcal{Z}) = \frac{\partial}{\partial x_j}\left(\frac{\mu}{Sc}\frac{\partial \mathcal{Z}}{\partial x_j}\right). \tag{3.8}$$

In this formulation the computation of diffusion flames can be decoupled into two problems [147]:

1. The mixing problem: the $\mathcal{Z}(x_i, t)$ field can be determined by solving the conservation equations of mass (2.26), momentum (2.27), and mixture fraction (3.8).

2. The flame structure problem: assuming that the structure of the non-premixed flame depends only on $\mathcal{Z}$ and t, the species conservation equations can be transformed into a coordinate-system attached to the iso-$\mathcal{Z}$ surfaces:

$$\rho \frac{\partial Y_k}{\partial t} = \frac{1}{2} \rho \chi \frac{\partial^2 Y_i}{\partial \mathcal{Z}^2} + \dot{\omega}_k, \tag{3.9}$$

where χ is the scalar dissipation rate, which controls mixing:

$$\chi = 2D \left(\frac{\partial \mathcal{Z}}{\partial x_i} \frac{\partial \mathcal{Z}}{\partial x_i} \right). \tag{3.10}$$

3.2.2 Premixed Flames

In a premixed flame the thin reaction zone separates perfectly mixed fresh and burnt gases in a mixture that is entirely within the flammability limits. Consequently there is a sharp temperature gradient in this zone: the temperature is approximately 5-7 times greater in the burnt gases [185] (see Figure 3.2). The emerging heat fluxes preheat the fresh gases, which eventually start to burn. As a result the flame propagates towards the fresh gases with an s_l flame speed that is in the order of $0.1 - 1\ m/s$ depending on the specific circumstances. This raises safety issues regarding premixed flame configurations as the flame can propagate towards the fuel supply. However, there are also benefits: premixed combustion yields higher efficiency and reduced emissions owing to the perfect mixing.

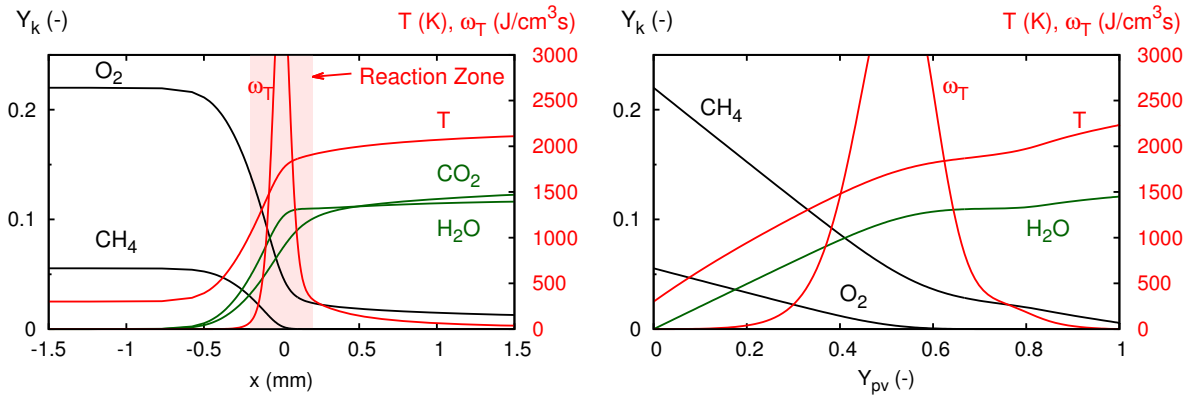

Figure 3.2: The diagram on the left shows the structure of a one-dimensional premixed methane-air flame. The mixture is stoichiometric. On the right this flame is parametrized by the progress variable, which is defined as the normalized CO_2 mass fraction.

3.2.2.1 The Progress Variable

The process is limited by the reaction rate, not by mixing. As a matter of fact in a perfectly mixed homogeneous mixture the mixture fraction is constant, therefore it is not sufficient for describing the flame structure contrary to non-premixed flames. To characterize a premixed flame, a $\mathcal{Y}_{pv}$ reaction progress variable is introduced such as $\mathcal{Y}_{pv} = 0$ in the fresh and $\mathcal{Y}_{pv} = 1$ in the fully burnt gases. The intention is to parametrize all the species mass fractions and thermochemical properties with this single variable. The progress variable should have the following properties to make this possible:

- it should be monotonic so that a unique relation between $\mathcal{Y}_{pv}$ and all the other scalars could exist,
- it should cover the whole flame,
- it should be well resolvable, which is important from a numerical point of view.

Several different progress variable definitions have been proposed, the common feature of which is that $\mathcal{Y}_{pv}$ is a normalized weighted combination of species mass fractions:

$$\mathcal{Y} = \sum_k b_k Y_k, \tag{3.11}$$

$$\mathcal{Y}_{pv} = \frac{\mathcal{Y} - \mathcal{Y}_{min}}{\mathcal{Y}_{max} - \mathcal{Y}_{min}}. \tag{3.12}$$

It is important to note that in the code the corresponding transport equation is solved for the non-normalized $\mathcal{Y}$ since $\mathcal{Y}_{min}$ and $\mathcal{Y}_{max}$ depend on the mixture fraction and the enthalpy which would lead to extra terms in the balance equation. In this work we use the CO_2 mass fraction weighted with its molar mass as the progress variable [95]:

$$\mathcal{Y} = \frac{Y_{CO_2}}{\mathcal{M}_{CO_2}}. \tag{3.13}$$

Fiorina showed that this definition does not provide a completely monotonic progress variable for all equivalence ratios [56]. The CO mass fraction can be added to the formulation to overcome this deficiency

$$\mathcal{Y} = Y_{CO_2} + Y_{CO}, \tag{3.14}$$

however, as Künne et al. [108] concluded, this leads to increased resolution requirements. The same applies to another commonly used definition that uses Y_{H_2O} and Y_{H_2} besides Y_{CO_2} [187]:

$$\mathcal{Y} = \frac{Y_{CO_2}}{\mathcal{M}_{CO_2}} + \frac{Y_{H_2O}}{\mathcal{M}_{H_2O}} + \frac{Y_{H_2}}{\mathcal{M}_{H_2}}. \tag{3.15}$$

Considering that the (3.13) formulation leads to only minor errors regarding the equilibrium density and temperature [94; 107] using the CO_2 mass fraction as a progress variable is a reasonable compromise between accuracy and affordable computational costs. The parametrization of a premixed flame with this definition is illustrated in Figure 3.2.

3.2.2.2 Laminar Flame Speed and Flame Thickness

The progress variable is sufficient for describing the structure of a premixed flame. In addition we can define two parameters that characterize the premixed combustion mode, namely the laminar flame thickness and the laminar flame speed.

The δ_l flame thickness is important from a numerical point of view since it gives information about how fine the resolution should be in the reaction zone. Different definitions exist [147], but the most appropriate one regarding the estimation of the resolution requirements is based on the evaluation of the temperature gradient

$$\delta_l = \frac{|T_b - T_u|}{max\left(|\frac{\partial T}{\partial x}|\right)}, \tag{3.16}$$

where T_u and T_b are the temperatures of the unburnt and burnt gases.

The s_l laminar flame speed is the velocity at which the laminar flame front would move in a stationary medium. In this work we will use three different definitions to check the consistency of our approach. Each definition is based on a different underlying process or quantity and their derivation can be found in [107].

1. The first approach follows the x_F flame position in time between two time instances (t and $t + \Delta t$) then subtracts the s_a absolute flame speed from the u_u velocity with which the unburnt mixture approaches the flame:

$$s_l^1 = u_u - s_a = u_u - \frac{x_F(t + \Delta t) - x_F(t)}{\Delta t}. \tag{3.17}$$

2. The flame speed can also be calculated by applying the continuity equation in a reference frame attached to the flame front:

$$s_l^2 = \frac{u_b - u_u}{\frac{\rho_u}{\rho_b} - 1}. \tag{3.18}$$

3. The third formulation is based on the fuel consumption calculated with the integration of the chemical source term:

$$s_l^3 = \frac{1}{\rho_u Y_{CO_2,b}} \int_{-\infty}^{\infty} \dot{\omega}_{CO_2} \mathrm{d}x. \tag{3.19}$$

3.3 Chemistry Reduction Using the Flamelet Approach

The application of detailed reaction mechanisms to the simulation of detailed technical systems in either a DNS or an LES context is not feasible owing to the wide range of time scales involved. The smallest time scales correspond to the fastest chemical reactions, therefore they can be eliminated from the calculation by using reduced reaction mechanisms. These reduced mechanisms can be obtained by assuming that certain reactions are in partial equilibrium or certain species are in a quasi-steady state [172; 189]. These assumptions and therefore the derived mechanisms are specific to the given conditions, which is a drawback. Besides, their application leads to a loss of information regarding the fine details of the combustion process.

Maas and Pope [119] suggested an eigenvalue analysis of the reaction mechanism to identify the slow reactions. The trajectories of the fast reactions in the composition space all collapse onto a low-dimensional manifold determined by these slow reactions and consequently the system can be described with fewer parameters. This so-called Intrinsic Low-Dimensional Manifolds (ILDM) method does not include diffusive processes and has difficulties in the low temperature regions.

Another approach is to separate the different timescales instead of merely eliminating the smaller ones. The several tabulated chemistry based methods serve this purpose: the detailed reaction kinetics are calculated in a preprocessing step and the results are stored in a look-up table as functions of a restricted number of control variables. Consequently the number of equations to solve decreases significantly as we only have to solve for the control variables and all the other properties can be retrieved from the table. This approach offers two major benefits while it circumvents the stiff coupling of the transport equations by separating the time scales of flow and chemistry. First, the computational costs remain reasonable. Second, the accuracy of the method is better than when reduced reaction mechanisms are used.

Williams [195; 196] represented the flame brush with an ensemble of laminar flames that are embedded in a turbulent, non-reacting flow field. He assumed that these embedded flames, referred to as flamelets, are thin compared to the Kolmogorov length scale, therefore even the smallest turbulent eddies are unable to disturb their inner structure.

Building on this concept Peters [135; 136] used the mixture fraction to determine the location of the flamelets and then transformed the species conservation equations into the mixture fraction space as it is described in Section 3.2.1. Since chemical time scales are assumed to be small compared to turbulent time scales, the steady flamelet equations are solved to establish a relationship between the mixture fraction and the Y_k variables:

$$\frac{1}{2}\rho\chi\frac{\partial^2 Y_i}{\partial \mathcal{Z}^2} + \dot{\omega}_k = 0 \tag{3.20}$$

The solutions are tabulated as functions of $\mathcal{Z}$ and χ. However, the flamelets obtained in this way do not cover the entire parameter space of interest due to the steady state assumption. In steady state high χ values lead to quenching while in reality flames can

survive dissipation rates even above the extinction limit if those conditions do not exist for too long. The missing values in the look-up table are gathered by either interpolation to the equilibrium condition or using unsteady flamelets as well [144] according to equation (3.9).

3.3.1 Flamelet Generated Manifolds

If we use the mixture fraction as the single control variable we cannot capture the slower development of the reactions since this description is equivalent to the assumption that what is mixed is burnt. This restriction in capabilities can be overcome by introducing the $\mathcal{Y}_{pv}$ progress variable described in Section 3.2.2.1.

This approach has been introduced independently by van Oijen and de Goey [129], and Gicquel et al. [70] and is named as Flamelet Generated Manifolds (FGM) and Flame Prolongation of ILDM (FPI), respectively. Both methods use one-dimensional, adiabatic, freely-propagating laminar premixed flames to generate a look-up table, which is then parametrized with $\mathcal{Z}$ and $\mathcal{Y}$.

In this work the flamelet equations are solved with the one-dimensional flamelet code CHEM1D [12] described in details by Somers [173]. For this calculation the diffusion coefficients of both the species and the enthalpy have to be known. Solving the multi-component diffusion equation [45] is usually avoided by using a relation expressing the temperature dependency of λ/c_p and μ/c_p [172]:

$$\frac{\lambda}{c_p} = 2.58 \cdot 10^{-4} \left(\frac{T}{298}\right)^{0.69}, \tag{3.21}$$

$$\frac{\mu}{c_p} = 1.67 \cdot 10^{-4} \left(\frac{T}{298}\right)^{0.51}. \tag{3.22}$$

We follow the previous assumption that the Lewis number equals one for all species, thereby neglecting the effects of preferential diffusion. For a simple fuel, such as the methane considered in this work, these effects are rather small [179]. Neglecting them considerably reduces the complexity of the procedure as in the case of prevalent preferential diffusion effects $\mathcal{Z}$ and h would not be constant within the flame front [130].

Similarly to the case of non-premixed flamelets, premixed flamelet solutions cannot be calculated for the entire ranges of the control variables: extrapolations are needed outside of the flammability limits. In this work we follow the extrapolation strategy of Ketelheun et al. [95].

- Mass fractions are approximated as linear functions of the mixture fraction:

$$Y_k = \begin{cases} Y_{k,l}\frac{\mathcal{Z}}{\mathcal{Z}_l} + Y_{k,O}\left(1 - \frac{\mathcal{Z}}{\mathcal{Z}_l}\right) & \text{if } \mathcal{Z} \leq \mathcal{Z}_l \\ Y_{k,r}\frac{\mathcal{Z}-1}{\mathcal{Z}_r-1} + Y_{k,F}\frac{\mathcal{Z}_r-\mathcal{Z}}{\mathcal{Z}_r-1} & \text{if } \mathcal{Z} \geq \mathcal{Z}_r, \end{cases} \tag{3.23}$$

  where the subscripts l, r, F and O denote the lean and rich flammability limits, and the fuel and oxidizer stream, respectively.

- The denisty is computed using the relation for a mixture of ideal gases:

$$\rho = \begin{cases} \frac{\rho_O \rho_l}{\rho_O \frac{\mathcal{Z}}{\mathcal{Z}_l} + \rho_l \left(1 - \frac{\mathcal{Z}}{\mathcal{Z}_l}\right)} & \text{if } \mathcal{Z} \leq \mathcal{Z}_l \\ \frac{\rho_O \rho_r}{\rho_r \frac{\mathcal{Z} - \mathcal{Z}_r}{1 - \mathcal{Z}_r} + \rho_F \frac{1 - \mathcal{Z}}{1 - \mathcal{Z}_r}} & \text{if } \mathcal{Z} \geq \mathcal{Z}_r. \end{cases} \tag{3.24}$$

It is interesting to note that Nguyen et al. [128] suggested a third way of tabulation. In their approach the detailed kinetics are calculated in a two-dimensional parameter space, which eliminates the need for extrapolation. However, the computational cost increases significantly.

3.3.2 Non-Adiabatic Tabulation

Following the described procedure we would end up with a look-up table with $\mathcal{Z}$ and $\mathcal{Y}_{pv}$ as control variables. Unfortunately it is not sufficient to account for heat losses. This is a major deficiency since for example in an internal combustion engine cold walls are the main causes of reduced efficiency, therefore the ability to describe heat losses is a crucial one from an engineering point of view.

Ketelheun [93; 94] introduced the enthalpy as an additional control variable, thereby making the look-up table three-dimensional. The table can be divided into three regimes depending on how the corresponding data is generated: the regime of adiabatic flamelets calculated at different enthalpy levels; the regime of burner stabilized flamelets with lowered enthalpy [130]; and the regime which contains extrapolated solutions. In this case two additional tables are needed. One for storing the h_{min} and h_{max} normalization parameters as they depend on the mixture fraction, and one for the $\mathcal{Y}_{max}$ and $\mathcal{Y}_{min}$ parameters that depend on both the mixture fraction and the normalized enthalpy. First h_{min} and h_{max} are extracted using $\mathcal{Z}$. Then the enthalpy is normalized and the result is used along with the mixture fraction to obtain $\mathcal{Y}_{max}$ and $\mathcal{Y}_{min}$. Once $\mathcal{Y}_{pv}$ is calculated we have all the three control variables in their appropriate form to access the three-dimensional look-up table [93].

In theory the number of control variables can be further increased by introducing newer and newer ones. This can be necessary for example when we intend to simulate a case with multiple fuel injections [79]. However, storing and accessing a multidimensional look-up table can be challenging regarding the memory not to mention the difficulties of multilinear interpolation.

In this work, if it is not explicitly stated otherwise, we use a three-dimensional table based on premixed flamelet solutions with the mixture fraction, reaction progress variable, and enthalpy as control variables. The table is based on the GRI3.0 mechanism [171] and the $Le = 1$ assumption is maintained. The table features 1001 data points in the mixture fraction, 101 in the progress variable, and 186 in the enthalpy directions.

It is worth mentioning that although it has been a well-established practice to generate look-up tables based on premixed flamelets and use them for the simulation of both

premixed and non-premixed flames, this approach has its limitations. Fiorina et al. [57] showed that when the mixture fraction is outside of the rich flammability limit in a non-premixed flame, diffusion of species through isomixture fraction surfaces becomes important. This cannot be captured with the application of premixed flamelet solutions and leads to errors. Nevertheless, we maintain the premixed flamelet approach in this work as these errors are of minor importance considering our main objectives and the chosen cases.

3.3.3 Summary of Equations

The look-up table contains all the necessary thermochemical data stored as a function of the control variables. Therefore we do not need to solve all the species transport equations anymore. In addition to the mass (2.46), the momentum (2.47), and the enthalpy (2.49) conservation equations, two transport equations are solved for the mixture fraction and the progress variable:

$$\frac{\partial}{\partial t}(\overline{\rho}\widetilde{\mathcal{Z}}) + \frac{\partial}{\partial x_j}(\overline{\rho}\widetilde{u}_j\widetilde{\mathcal{Z}}) = \frac{\partial}{\partial x_j}\left[\left(\frac{\overline{\mu}}{Sc} + \frac{\mu_t}{Sc_t}\right)\frac{\partial\widetilde{\mathcal{Z}}}{\partial x_j}\right], \tag{3.25}$$

$$\frac{\partial}{\partial t}(\overline{\rho}\widetilde{\mathcal{Y}}) + \frac{\partial}{\partial x_j}(\overline{\rho}\widetilde{u}_j\widetilde{\mathcal{Y}}) = \frac{\partial}{\partial x_j}\left[\left(\frac{\overline{\mu}}{Sc} + \frac{\mu_t}{Sc_t}\right)\frac{\partial\widetilde{\mathcal{Y}}}{\partial x_j}\right] + \overline{\dot{\omega}}_{\mathcal{Y}}. \tag{3.26}$$

It is important that in an LES context the filtered control variables are used for accessing the table, therefore the flame-turbulence interaction that happens at the unresolved subgrid-scales is not properly accounted for in this framework. Addressing this problem will be the topic of the next chapter.

Chapter 4

Flame-Turbulence Interaction

As we have seen in the previous chapters, due to the limited computational resources and the involved wide range of characteristic time and length scales, turbulent flows are usually described with filtered or time-averaged variables. As a consequence unclosed terms appear in the balance equations, which have to be closed either based on the known resolved variables (for example by applying a gradient approach) or by models. The calculation of the mean chemical source term is especially challenging because of the strong non-linearity of chemical reactions. In this chapter some of the most common turbulent combustion closure approaches will be presented. In order to be able to elaborate on the specific models first we have to answer some more fundamental questions in the next section such as: what happens with the flame front in a turbulent flow?; how can we characterize the interaction between the flame and the turbulent flow field?

4.1 Scales and Diagrams of Turbulent Combustion

Let us focus on premixed flames first. A laminar premixed flame can be characterized with its s_l laminar flame speed and its δ_l laminar flame thickness as we saw in Section 3.2.2.2. Furthermore, an even thinner reaction zone can be identified inside the flame with the thickness of $\delta_r \approx 0.1\delta_l$ [185]. This zone is defined as where heat is released. We can describe the flame-turbulence interaction based on how turbulence affects these representative parameters. The effect of turbulence is well-illustrated by the study of Meneveau and Poinsot [123] who simulated in two dimensions the interaction between a laminar premixed flame and a vortex pair.

In industrial applications it is preferred to have a turbulent flow field because turbulence increases the fuel consumption rate and hence the rate of heat release. The reason for this is that the flame front area increases compared to the laminar case owing to the presence of turbulent eddies as it is illustrated in Figure 4.1. Due to the wrinkled flame front we can identify a spatial region that contains the flame with a non-zero probability. This is the so-called turbulent flame brush, which defines the δ_T turbulent flame thickness according to Figure 4.1. An s_T turbulent flame speed can also be defined as the speed that is needed at the inlet of the control volume to keep the mean position of the turbulent flame stationary inside the control volume. This quantity can be measured. Bradley published a review of the large number of experiments with such an objective [28]. Damköhler [48]

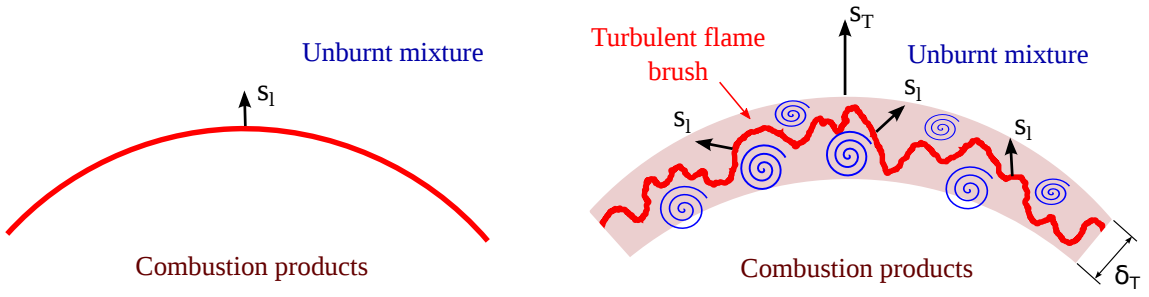

(a) Laminar flame **(b)** Turbulent flame

Figure 4.1: Schematic illustration of the propagation of a premixed (a) laminar and (b) turbulent flame. In the turbulent case the flame front is wrinkled thereby creating a flame brush with the width of δ_T.

proposed the following relation between the turbulent and laminar flame speeds and flame surface areas:

$$\frac{s_T}{s_l} = \frac{A_T}{A_l}, \tag{4.1}$$

where the A_T/A_l ratio of turbulent and laminar flame surface areas is the flame wrinkling factor. It has been found that for low levels of turbulence the flame speed increases proportionally to the u_{rms} root mean square velocity that also happens to be the $u(l_I)$ characteristic velocity corresponding to the largest eddies as it was discussed in Section 2.2.1. Further increasing the turbulence intensity, s_T levels off before the quenching limit is eventually reached [147].

The flame structure changes depending on the turbulence intensity and the sizes of the vortices. The most common way to characterize the different emerging structures is to classify the flames into different combustion regimes based on the relations among the characteristic time and length scales. These regimes are illustrated in a turbulent combustion diagram (Figure 4.2) originally proposed by Borghi [27] and later revised by Peters [137; 138].

The relevant time and length scales are the l_I integral length scale, the δ_l laminar flame thickness, the u_{rms} characteristic velocity fluctuation magnitude, and the s_l laminar flame speed. The different combustion regimes can be identified according to the u_{rms}/s_l and l_I/δ_l dimensionless ratios. Two additional dimensionless numbers can be introduced.

1. The Da Damköhler number is the ratio of the characteristic turbulent and chemical time scales:

$$Da = \frac{\tau_t}{\tau_c} = \frac{l_I/u_{rms}}{\delta_l/s_l}. \tag{4.2}$$

2. The Ka Karlovitz number compares the time scales of the smallest eddies to the chemical time scales. After some manipulation it can be also expressed as the ratio of the laminar flame thickness and the Kolmogorov length scale [185]:

$$Ka = \left(\frac{\delta_l}{\eta_K}\right)^2. \tag{4.3}$$

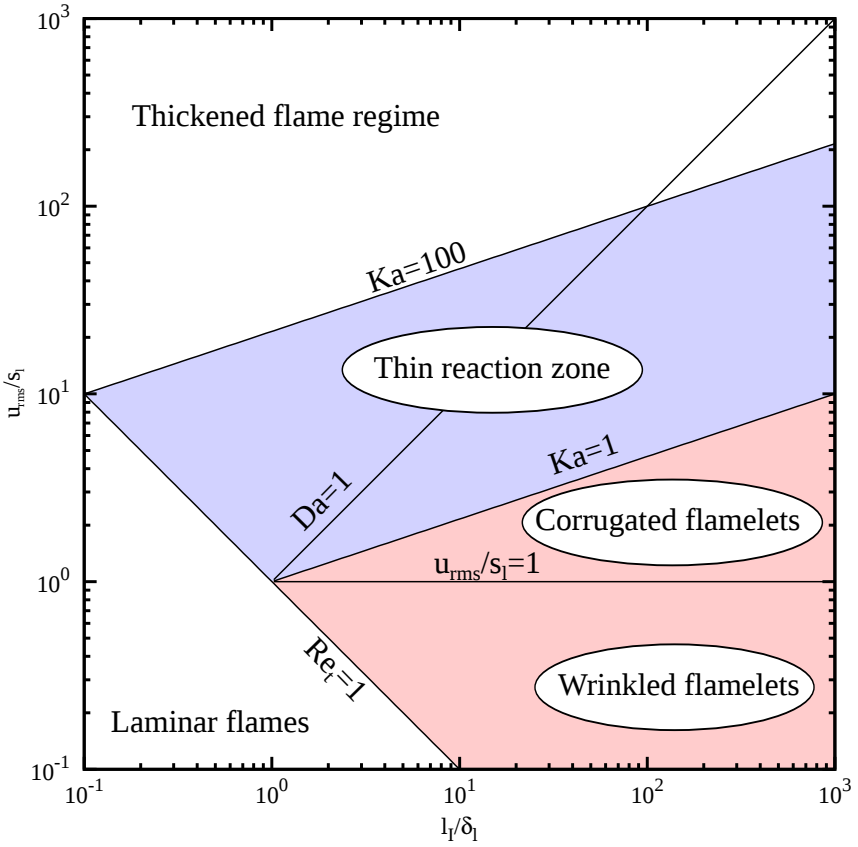

Figure 4.2: Combustion regimes

With these non-dimensional numbers we are equipped to describe the combustion regimes depicted in Figure 4.2 following Veynante and Vervisch [185].

- The bottom left corner consists of laminar flames for which the turbulent Reynolds number defined in equation (2.35) is less than one: $Re_t < 1$.
- The $Ka = 1$ line, commonly referred to as the *Klimov-Williams criterion*, separates two major regimes. For $Ka < 1$ the flame thickness is smaller than the smallest eddies, therefore those are able to wrinkle the flame but they cannot disturb its inner structure. On a micro-level the flame remains laminar, therefore this is called the *flamelet regime*, which can be further divided.
  - $u_{rms}/s_l < 1$: *wrinkled flamelets*. u'' is viewed as the rotation speed of eddies, therefore in this case turbulent structures are unable to wrinkle the flame as much that pockets can be created.
  - $u_{rms}/s_l > 1$: *corrugated flamelets*. The effect of larger structures leads to flame front interactions and the emergence of pockets.
- The $Ka > 1$ zone can be divided into two parts as well. The $1 < Ka \leq 100$ regime is commonly referred to as either the *thickened wrinkled flame regime* or the *thin reaction zone*. The latter naming is particularly telling. It refers to that although the smallest eddies are small enough ($\eta_K < \delta_l$) to affect the preheat zone of the

flame, they are still larger than the δ_r reaction zone thickness, consequently the thin reaction zone is not disturbed.

- $Ka > 100$: *thickened flame regime*. In this case the smallest eddies can enter the reaction zone which may lead to local extinction of the flame. The flame can no longer be considered as a closed interface and no laminar flame structure may be identified. Therefore this regime is also known as the regime of *broken reaction zone*.
- Instead of the $Ka = 100$ line Borghi [27] used the $Da = 1$ criterion. In his description this line represented the border of the flamelet regime as for $Da < 1$ the chemistry cannot keep up with the turbulent distortions.

It is important to keep in mind that these regimes serve as a rather qualitative description. They are the results of mere estimations based on the comparison of orders of magnitudes. Therefore the diagram should be used with great care. Künne [107] further elaborated on the consequences of assumptions made during the construction of the diagram.

The characterization of non-premixed combustion regimes is even more challenging owing to non-premixed flames not having intrinsic length and time scales as they cannot propagate. Nevertheless, three regimes can be identified with two limiting Da numbers [147; 185]. Below a Da_{ext} limit flame extinction occurs, while above a certain Da_{LFA} number the flame front may be viewed as a steady laminar flame element which is not affected by vortices. In between strong unsteady effects can be observed.

4.2 Overview of Tools for Turbulent Combustion Modeling

In Section 2.2.3.2 we have addressed the modeling of the unclosed terms in the filtered balance equations except for the $\overline{\dot{\omega}}_k$ mean source terms. The mean production and consumption rates have to be predicted using known quantities. To this end several special tools and modeling concepts have been developed. Here we intend to highlight the key ideas behind the various approaches in the LES framework, which will help with putting into context the new method proposed in the next chapter. For a comprehensive overview the interested reader is referred to one of the numerous textbooks [135; 147] or review papers [143; 185] devoted to this constantly evolving field of research.

The simplest and most direct approach to describe turbulent combustion is based on the Taylor-series expansion of the Arrhenius law, thereby expressing the mean reaction rate as a function of species mass fractions and temperature [147]. This approach can be useful for simple analyses in the low Damköhler number limit, however, in most situations is completely inadequate due to the strongly non-linear behavior of the reaction rate.

The **eddy-break-up (EBU) model** proposed by Spalding [174] focuses on the high Reynolds number and high Damköhler number limit in which the reaction is mainly controlled by mixing. Therefore the mean reaction rate can be expressed with a τ_t char-

acteristic turbulent mixing time and the temperature fluctuations:

$$\overline{\dot{\omega}}_\Theta = C_{EBU}\overline{\rho}\frac{\sqrt{\Theta''^2}}{\tau_t}, \tag{4.4}$$

where Θ is the normalized temperature. One of the obvious limitations of this model is that it does not include any effects of chemical kinetics. Besides, in LES the C_{EBU} model constant strongly depends on the particular flow conditions.

Generally speaking what we face is a problem of resolution. The typical thickness of a premixed flame is in the order of 0.1 mm, the reaction zone is one order of magnitude smaller. If a detailed reaction mechanism is considered, we end up with a resolution requirement of $\mathcal{O}(1\ \mu m)$. By keeping only the main species, the behavior of which is less stiff, the resolution requirement can be relaxed to $\mathcal{O}(100\ \mu m)$. This can be achieved by applying either reduced mechanisms or using a tabulated chemistry approach. In the latter case only the control variables are transported, which makes it possible to decrease the resolution to $\mathcal{O}(100\ \mu m)$. Nevertheless, this is still much smaller than the typical LES grid spacing of $\mathcal{O}(1\ mm)$.

Butler and O'Rourke [34] proposed to artificially thicken the flame with an appropriate coordinate transformation. This is the so-called **Artificially Thickened Flame (ATF) model**. According to premixed flame theory [197] the laminar flame speed and the flame thickness are proportional to the D_{th} thermal diffusivity and the reaction rate:

$$s_l \propto \sqrt{D_{th}\dot{\omega}} \qquad\qquad \delta_l \propto \sqrt{\frac{D_{th}}{\dot{\omega}}}. \tag{4.5}$$

If D_{th} is increased and $\dot{\omega}$ is decreased by the same $\mathscr{F}$ thickening factor, the flame thickness is multiplied by $\mathscr{F}$ while the flame speed is maintained:

$$s_l^{\mathscr{F}} \propto \sqrt{\mathscr{F}D_{th}\frac{\dot{\omega}}{\mathscr{F}}} = s_l \qquad\qquad \delta_l^{\mathscr{F}} \propto \sqrt{\mathscr{F}\frac{D_{th}}{\mathscr{F}\dot{\omega}}} = \mathscr{F}\delta_l. \tag{4.6}$$

As a result the flame becomes less sensitive to turbulent motions. An $\mathscr{E}$ efficiency function is introduced to account for the the lost subgrid-scale wrinkling and to establish a connection between the laminar and the turbulent flame speeds:

$$s_T = \mathscr{E}s_l. \tag{4.7}$$

To this end both the modified D_{th} and $\dot{\omega}$ are multiplied by $\mathscr{E}$. This leads to the following modified scalar transport equation [42]:

$$\frac{\partial}{\partial t}(\rho Y_k) + \frac{\partial}{\partial x_j}(\rho u_j Y_k) = \frac{\partial}{\partial x_j}\left(\rho\mathscr{F}\mathscr{E}D_k\frac{\partial Y_k}{\partial x_j}\right) + \frac{\mathscr{E}}{\mathscr{F}}\dot{\omega}_k. \tag{4.8}$$

Several different efficiency function formulations exist [35; 42]. Their effect as well as the ATF method generally has been thoroughly investigated by Künne [107; 108].

Other models work with an approach that is somewhat contrary to ATF: the flame thickness is set to zero instead of being increased, consequently these models are inherently

linked to a flamelet assumption. The flame front is described as a propagating interface between fuel and oxidizer or burnt and unburnt mixtures, therefore these types of models are commonly referred to as geometrical ones. Two concepts have to be mentioned in this model family: the G-equation and the flame surface density approach.

The **G-equation formalism** tracks the flame front using the G level set function. The flame front position is associated with a constant G_0 value. The G field can be resolved on the LES mesh since it does not need to follow the progress variable gradients. Eventually the so-called G-equation has to be solved [92]

$$\frac{\partial}{\partial t}\left(\overline{\rho}\widetilde{G}\right) + \frac{\partial}{\partial x_i}\left(\overline{\rho}\widetilde{u}_i\widetilde{G}\right) = \rho_0 \overline{s}_T |\nabla \overline{G}|, \tag{4.9}$$

in which the turbulent flame speed needs to be modeled. Although there is no universal model to describe this quantity, the G-equation technique is a popular one in the LES context [143].

The **flame surface density approach** assumes that the volumetric consumption rate of the unburned mixture can be expressed as the product of the flame surface and the propagation speed [26]. This makes the separation of the turbulent and chemical time scales possible. The subgrid flame density needs to be modeled. To this end transport equations [81], algebraic models [26], or similarity approaches [101] have been used. For further details see the work of Staufer [175].

The aforementioned models are able to properly capture the flame propagation and the main characteristics, however, when it comes to predicting radicals and intermediate species, the inner structure of the flame has to be investigated. This conclusion leads us to the statistical approaches to turbulent combustion modeling.

4.2.1 PDF Methods

4.2.1.1 The Concept of PDF

Let us consider a control volume filled with a stoichiometric mixture ($\overline{\mathcal{Z}}_0 = \mathcal{Z}_{st}$). In the FGM context described in Section 3.3 the dependent scalars are retrieved from the chemistry table using the $\overline{\mathcal{Z}}_0$ mean value. This single parameter though does not give us any information about the subgrid-distribution. Since in LES the smallest scales are not resolved, fluctuations do exist at this level. A cell filled with a perfectly mixed homogeneous mixture has the same mean mixture fraction as a cell in which the same amount of fuel and oxidizer are completely separated. In the former case the thermochemical properties should be that of the combustion products as opposed to the unmixed cell in which the properties retrieved from the table should be those of an unburnt mixture. We can see that the filtered dependent scalars do not equal the scalars corresponding to merely the filtered control variables,

$$\overline{\Phi(\mathcal{Z})} \neq \Phi(\overline{\mathcal{Z}}). \tag{4.10}$$

The relationship is non-linear and the subgrid-distribution has to be accounted for. This distribution can be described with a $\mathcal{P}(\mathcal{Z})$ probability density function (PDF), which

quantifies the probability of $\mathcal{Z}^* < \mathcal{Z} < \mathcal{Z}^* + \mathrm{d}\mathcal{Z}^*$ as $\mathcal{P}(\mathcal{Z}^*)\mathrm{d}\mathcal{Z}^*$. Consequently

$$\int_{\mathcal{Z}} \mathcal{P}(\mathcal{Z}^*)\mathrm{d}\mathcal{Z}^* = 1, \tag{4.11}$$

and the statistical moments can be easily calculated:

$$\overline{\mathcal{Z}} = \int_0^1 \mathcal{Z}^*\mathcal{P}(\mathcal{Z}^*)\mathrm{d}\mathcal{Z}^* \qquad \overline{\mathcal{Z}''^2} = \int_0^1 \left(\mathcal{Z}^* - \overline{\mathcal{Z}}\right)^2 \mathcal{P}(\mathcal{Z}^*)\mathrm{d}\mathcal{Z}^*. \tag{4.12}$$

In general, a PDF includes the entire scope of statistical moments and it can be reconstructed if all the statistical moments are available. If the joint subgrid-scale PDF $\mathcal{P}\left(y_1, y_2, \ldots, y_n\right)$ is known, which provides the complete statistical description of the physicochemical state in terms of the selected y_i normalized control variables, the mean value of an arbitrary $\Phi\left(y_1, y_2, \ldots, y_n\right)$ dependent scalar can be computed by a convolution over $\mathcal{P}$ as

$$\overline{\Phi\left(y_1, y_2, \ldots, y_n\right)} = \int_0^1 \ldots \int_0^1 \Phi\left(y_1, y_2, \ldots y_n\right) \mathcal{P}\left(y_1, y_2, \ldots, y_n\right) \mathrm{d}y_1 \ldots \mathrm{d}y_n. \tag{4.13}$$

Pope [150] has extended the PDF concept to LES by introducing the filtered distribution function (FDF). It is based on the fine-grained PDF of variable y_α at location $\boldsymbol{x}$ and time t:

$$\mathcal{P}_\alpha^{fg}(y_\alpha; \boldsymbol{x}, t) = \delta(y_\alpha - y_\alpha^*(\boldsymbol{x}, t)). \tag{4.14}$$

For the entire $\boldsymbol{y} = [y_1, y_2, \ldots, y_n]$ set of variables the joint PDF can be calculated as a product of the marginal ones:

$$\mathcal{P}^{fg}(\boldsymbol{y}; \boldsymbol{x}, t) = \prod_{\alpha=1}^{n} \delta(y_\alpha - y_\alpha^*(\boldsymbol{x}, t)). \tag{4.15}$$

The joint subgrid FDF can be obtained by applying the $\mathcal{G}$ LES filter defined in Section 2.2.3.1 to this fine-grained PDF as

$$\mathcal{P}(\boldsymbol{y}; \boldsymbol{x}, t) = \int_V \prod_{\alpha=1}^{n} \delta(y_\alpha - y_\alpha^*(\boldsymbol{x'}, t))\mathcal{G}(\boldsymbol{x} - \boldsymbol{x'})\mathrm{d}\boldsymbol{x'}. \tag{4.16}$$

A mass-weighted FDF can also be defined as $\overline{\rho}\widetilde{\mathcal{P}} = \rho\mathcal{P}$ and the Favre-averaged $\widetilde{\Phi}$ quantities can be calculated by a convolution over $\widetilde{\mathcal{P}}$. This work is carried out in an LES framework therefore there is no need to continuously emphasize the presence of the filter. We will use the expression 'PDF' to refer to the subgrid-scale, filtered distribution as well.

PDFs can be defined in any turbulent reacting flow field and they contain all the required information to describe these fields. The difficulty is to determine the PDF, which evolves in both space and time.

4.2.1.2 PDF Transport Equation

Pope derived a transport equation for the one-point, one-time velocity-composition joint PDF [148; 149] from which the equation for the composition PDF can be directly obtained by integrating over velocity [65; 82]. The major advantage of this approach is that the chemical source term appears in a closed form as it depends only on the local composition, which is described at any location by the one-point PDF. However, the mixing term has to be modeled. This term originates from the diffusion term of the transport equation and it involves spatial gradients. A spatial gradient cannot be evaluated based on only one point, additional length scale information is needed [80; 147]. Since a one-point PDF cannot provide it, we have to model this term. The most commonly used models are the *linear mean-square estimation* (LMSE) [51] and the *interaction by exchange with the mean* (IEM) methods [186]. Both approaches describe the relaxation of the PDF towards the mean value. Other approaches, such as the *Euclidean minimum spanning tree* (EMST) [178] and the modified *Curl mixing model* [88], have been found to be computationally more expensive.

The main drawback of the transported PDF methods stems from the high dimensionality of the joint PDF, which increases the computational costs exponentially with the number of variables. Stochastic Monte Carlo solution methods, in which virtual particles are transported in the solution domain, are frequently used to mitigate this problem. Several alternative Monte Carlo methods have been developed. The most important ones are the Lagrangian [149] and the Eulerian [37] particle-based approaches as well as the Eulerian stochastic field method [17; 183]. Although in these methods the computational costs rise only linearly with the dimensions of the PDF, the downside is that a statistical error emerges owing to the finite number of stochastic fields or particles.

4.2.1.3 Presumed PDF Approach

A PDF in theory can take any shape, however, some similarities can be identified regarding the PDFs that describe the control variable distributions in combustion processes. Hence it is viable to presume the shape of the PDF and parametrize this shape with the statistical moments. A PDF is known if all the statistical moments of the respective variable are known. In practice it is usually sufficient to use only the first and second moments to estimate the PDF. This is convenient as the means are known in an LES and the variances can be computed using one of the many approaches described in Section 2.2.3.3.

Let us consider now an FGM approach described in Section 3.3 with the commonly applied two general control variables: the $\mathcal{Z}$ mixture fraction and the $\mathcal{Y}_{pv}$ normalized reaction progress variable. As we saw, the FGM method in its original formulation does not account for the subgrid-scale variances. It uses only the mean control variables to retrieve the thermochemical properties from the look-up table (this approach is referred to as FGM-1M in this work). However, this method can be combined with the concept of presumed shape PDFs in a straightforward manner. In a given cell the joint distribution of the control variables are described with the $\mathcal{P}(\mathcal{Z}, \mathcal{Y}_{pv})$ PDF. The mean value of a Φ scalar in the given cell can be calculated as

$$\widetilde{\Phi} = \int_{\mathcal{Z}} \int_{\mathcal{Y}_{pv}} \Phi(\mathcal{Z}, \mathcal{Y}_{pv}) \mathcal{P}(\mathcal{Z}, \mathcal{Y}_{pv}) \mathrm{d}\mathcal{Z} \mathrm{d}\mathcal{Y}_{pv}. \tag{4.17}$$

where the $\Phi(\mathcal{Z}, \mathcal{Y}_{pv})$ values are retrieved from the look-up table.

It is very challenging to define a viable presumed shape for a multidimensional PDF, therefore the common assumption is that the variables are statistically independent. In this case the joint PDF can be expressed as the product of the marginal PDFs, which are parametrized with their means and variances:

$$\mathcal{P}(\mathcal{Z}, \mathcal{Y}_{pv}) \approx \mathcal{P}(\mathcal{Z}; \widetilde{\mathcal{Z}}, \widetilde{\mathcal{Z}''^2}) \mathcal{P}(\mathcal{Y}_{pv}; \widetilde{\mathcal{Y}_{pv}}, \widetilde{\mathcal{Y}''^2_{pv}}). \tag{4.18}$$

By substituting the marginal PDFs in the (4.17) integral, we can realize that the resulting $\widetilde{\Phi}$ is a function of the means and variances of the control variables. Consequently it can be stored in a four-dimensional chemistry table which is built in a preprocessing step by integrating the original two-dimensional table of the flamelet solutions according to (4.17). The remaining question is how to define the marginal PDFs.

It is well-established in the combustion community to use a beta function [160] as the PDF of the mixture fraction [43]:

$$\mathcal{P}(\mathcal{Z}; \widetilde{\mathcal{Z}}, \widetilde{\mathcal{Z}''^2}) = \frac{\Gamma(\alpha + \beta)}{\Gamma(\alpha)\Gamma(\beta)} \mathcal{Z}^{\alpha - 1} \left(1 - \mathcal{Z}\right)^{\beta - 1}, \tag{4.19}$$

where α and β are parameters that can be expressed with the statistical moments of $\mathcal{Z}$:

$$\alpha = \widetilde{\mathcal{Z}} \left(\frac{\widetilde{\mathcal{Z}}\left(1 - \widetilde{\mathcal{Z}}\right)}{\widetilde{\mathcal{Z}''^2}} - 1 \right) \qquad \beta = \frac{1 - \widetilde{\mathcal{Z}}}{\widetilde{\mathcal{Z}}} \left(\frac{\widetilde{\mathcal{Z}}\left(1 - \widetilde{\mathcal{Z}}\right)}{\widetilde{\mathcal{Z}''^2}} - 1 \right). \tag{4.20}$$

In order to improve the process of accessing the table, the mixture fraction variance is normalized by its theoretical maximum as

$$\widetilde{\mathcal{Z}''^2_N} = \frac{\widetilde{\mathcal{Z}''^2}}{\widetilde{\mathcal{Z}}\left(1 - \widetilde{\mathcal{Z}}\right)}. \tag{4.21}$$

This normalized variable is used as an additional control variable in the four-dimensional table.

While the beta function has been proved to be well-suited to represent the distribution of the mixture fraction, its use for the progress variable remains a subject of some controversy [32; 50; 164]. Kühne et al. [106] discussed the issues related to the use of both the beta function and, as a matter of fact, the also frequently used δ-function [77; 89] for the progress variable. Nevertheless, some applications [99] show that the beta function yields acceptable results, therefore it will be adopted throughout this work. Since our objective is to create a joint PDF without the statistical independence assumption, using a δ-function would not be appropriate in this context. On the other hand we do assume a δ-PDF for the enthalpy, which is the third control variable in our table as it was discussed in Section 3.3.2, in order to be able to focus on the joint PDF of the mixture fraction and the reaction progress variable in the remaining part of this work.

4.3 Summary

In this chapter we have investigated how the turbulent flow field interacts with the combustion process. First we identified the most important characteristic time and length scales, as well as further important non-dimensional numbers, and we presented the Borghi diagram of combustion regimes. Then we briefly described the most important modeling concepts regarding the unclosed mean source terms and highlighted their limitations. The PDF methods stood in the center of our interest since not only is a PDF the most accurate way of describing the statistical behavior of a variable, but also the concept of a subgrid PDF can be easily incorporated in the well-established FGM framework. Since solving a PDF transport equation is computationally expensive, the shapes of the PDFs are usually presumed, and the distributions are parametrized with their statistical moments obtained from transport equations and models. As it is challenging to handle multivariate PDFs in this manner, the common assumption is that the control variables are statistically independent, consequently it is sufficient to presume the univariate marginal PDFs. The entire process can be summarized in the following key steps for a simulation in which two control variables are considered:

- Preprocessing:
    1. Premixed flamelet solutions are generated with CHEM1D and the results are stored in a two-dimensional look-up table parametrized with the mixture fraction and the progress variable as control variables.
    2. The mixture fraction and the progress variable are assumed to be statistically independent and their subgrid-distributions are described with beta functions according to (4.19).
    3. The original two-dimensional table is pre-integrated following the (4.17) and (4.18) formulas using different statistical moment values to cover the entire parameter range. This yields a four-dimensional table parametrized with the means and variances of the control variables.
- Simulation:
    1. Transport equations are solved for the mean control variables.
    2. The variances of the control variables are calculated based on a gradient approach described in Section 2.2.3.3.
    3. Thermochemical properties are retrieved from the table using these means and variances.

In the next chapter we will investigate how valid the statistical independence assumption is and how we could properly take into account the so-far neglected correlations between the control variables. To this end a new method will be proposed based on a Monte Carlo sampling technique.

Chapter 5

Novel Monte Carlo based Joint PDF Approach

The commonly applied presumed PDF approach outlined in section 4.2.1.3 is based on the rather strong assumption that the control variables are statistically independent. However, results of experiments with turbulent flames indicate that this assumption is often a poor one [73; 75]. Gutheil and Bockhorn showed [74; 75] that turbulence-chemistry interaction in general, and particularly the covariance of the mixture fraction and the CO concentration, have a major effect on the mean chemical reaction rate [30], therefore neglecting the correlations could yield significant errors.

The other major limitation of the mentioned common approach lies in how the look-up table is constructed. Using two control variables, for example the mixture fraction and the progress variable, one ends up with a four-dimensional look-up table parametrized with the means and variances of these variables:

$$\widetilde{\Phi}(\widetilde{\mathcal{Z}}, \widetilde{\mathcal{Y}_{pv}}, \widetilde{\mathcal{Z}''^2}, \widetilde{\mathcal{Y}_{pv}''^2}) = \int\int \Phi(\mathcal{Z}, \mathcal{Y})\, \mathcal{P}(\mathcal{Z}; \widetilde{\mathcal{Z}}, \widetilde{\mathcal{Z}''^2}) \mathcal{P}(\mathcal{Y}_{pv}; \widetilde{\mathcal{Y}_{pv}}, \widetilde{\mathcal{Y}_{pv}''^2})\, \mathrm{d}\mathcal{Z}\, \mathrm{d}\mathcal{Y}_{pv}. \tag{5.1}$$

If we do not assume statistical independence, there are five parameters because the covariance of the two control variables have to be included as well. Generally speaking, if a joint PDF is created for N variables the resulting table will have $N(N+3)/2$ dimensions for the PDF being described by its statistical moments up to the second order: N means, N variances, and $N(N-1)/2$ covariances.

Tabulation for even three control variables would yield a nine-dimensional look-up table the storage of which would raise significant memory issues. Furthermore, the numerical integration in equation (5.1) and the multidimensional interpolation when retrieving data from the table would become difficult and computationally expensive. In this work we focus on developing a new approach to overcome these challenges.

5.1 Joint Discrete PDF Approach

The paper of Brandt, Polifke and Flohr [30] offers a starting point. They propose to approximate the joint probability density function $\mathcal{P}(y_1, y_2)$ with a corresponding discrete distribution represented by a sufficient number (N) of samples. For the sake of

simplicity let us consider a joint PDF of two variables in the following unless it is stated otherwise:

$$\mathcal{P}_N^{(2)}(y_1, y_2) = \frac{1}{N}\sum_{i=1}^{N}\delta(y_1 - y_1^{(i)})\delta(y_2 - y_2^{(i)}). \tag{5.2}$$

The discrete distribution is characterized by only its first and second moments which can be obtained from the transport equations. The authors calculate the mean of any variable of interest (source term, mass fractions, temperature, etc.) using the precalculated flamelet solutions and $\mathcal{P}_N^{(2)}$:

$$\begin{aligned}\overline{\Phi}_N &= \int_0^1\int_0^1 \Phi(y_1, y_2)\mathcal{P}_N^{(2)}(y_1, y_2)\mathrm{d}y_1\mathrm{d}y_2 \\ &= \frac{1}{N}\sum_{i=1}^{N}\int_0^1\int_0^1 \Phi(y_1, y_2)\delta(y_1 - y_1^{(i)})\delta(y_2 - y_2^{(i)})\mathrm{d}y_1\mathrm{d}y_2 \\ &= \frac{1}{N}\sum_{i=1}^{N}\Phi(y_1^{(i)}, y_2^{(i)})\end{aligned} \tag{5.3}$$

The key point is that the numerical integration has been replaced with simple ensemble averaging. The authors use this technique to build a look-up table from these mean values. Let us summarize the procedure:

1. Using a random number generator they draw samples from distributions with given means, variances, and covariances.
2. Prior to the CFD simulation they compute the mean values to be stored in the look-up table using the flamelet solutions and ensemble averaging.
3. During the simulation the statistical moments are extracted from the transport equations and are used to access the look-up table to obtain the mean quantities of interest.

Although the procedure addresses the problem of numerical integration, it still uses a look-up table that has the second moments of the control variables as additional parameters thereby increasing its dimensionality. We intend to tackle this latter issue by generating the samples on the fly at each step on a cell-by-cell basis. In this way for N control variables we would still need an only N-dimensional look-up table. The suggested steps are the following (remember that everything happens at the level of an individual control volume):

1. The statistical moments are retrieved from the transport equations.
2. A joint PDF is created based on these moments. $\rightarrow \mathcal{P}(y_1, y_2; \widetilde{y_1}, \widetilde{y_2}, \widetilde{y_1''^2}, \widetilde{y_2''^2}, \widetilde{y_1''y_2''})$
3. A set of samples is drawn from this distribution. $\rightarrow \mathcal{P}_N^{(2)}(y_1^{(i)}, y_2^{(i)})$
4. The look-up table is accessed by each sample and the $\Phi(y_1^{(i)}, y_2^{(i)})$ values are extracted.
5. The mean values are calculated by ensemble averaging. $\rightarrow \overline{\Phi}_N$

The next question is how to create an appropriate joint PDF based on the first and second moments. Instead of just elaborating on the proposed solution it is instructive to go through the thought process and the other techniques that were considered in the following section.

5.2 Creating a Joint PDF

The joint PDF $\mathcal{P}(y_1, y_2)$ has to satisfy certain expectations and mathematical conditions:

1. We work with normalized variables, such as the mixture fraction and the progress variable, therefore the variables should be bounded: $y_i \in [0, 1]$.

2. $p(y_1, y_2)$ is a probability density function, consequently its form cannot be chosen arbitrarily:

$$\mathcal{P}(y_1, y_2) \geq 0, \tag{5.4}$$

$$\int_0^1 \int_0^1 \mathcal{P}(y_1, y_2)\, \mathrm{d}y_1\, \mathrm{d}y_2 = 1 \tag{5.5}$$

3. As stated earlier, to describe the statistics of a single control variable turbulent combustion models frequently use a β-PDF owing to its flexibility. In a first step there is no apparent reason for giving up this well-established approach therefore it would be preferred if we could ensure that the marginal PDFs are beta distributions.

$$\int_0^1 \mathcal{P}(y_i, y_j)\mathrm{d}y_j = \frac{\Gamma(\alpha_i + \beta_i)}{\Gamma(\alpha_i)\Gamma(\beta_i)} y_i^{\alpha_i - 1}(1 - y_i)^{\beta_i - 1} \tag{5.6}$$

We can undertake the problem of finding an appropriate joint PDF in different ways. The next sections elaborate on the investigated approaches.

5.2.1 Multivariate Beta Distribution

The first idea that can naturally come into one's mind is to look for a multivariate extension of the beta distribution. Girimaji suggested a multivariate β-PDF to describe multivariate scalar mixing [71]. This proposed function is only appropriate if the variances of all variables are of the same order. Furthermore, the variables represent mass fractions and they must add up to unity. These constraints limit the applicability of such a PDF and make it inadequate for our general purposes.

Libby and Novick [115] came up with another generalized multivariate beta distribution

$$\mathcal{P}(y_1, y_2, \ldots, y_r) = \frac{\Gamma\left(\sum_{i=0}^{r} \alpha_i\right)}{\prod_{i=0}^{r} \Gamma\left(\alpha_i\right)} \frac{\prod_{i=0}^{r} \Gamma\left[\lambda_i^{\alpha_i} \left(\frac{y_i}{1-y_i}\right)^{\alpha_i - 1} \left(\frac{1}{1-y_i}\right)^2\right]}{\left[1 + \sum_{i=1}^{r} \lambda_i \left(\frac{y_i}{1-y_i}\right)\right]^{\sum_{i=0}^{r} \alpha_i}}, \tag{5.7}$$

the univariate marginal distributions of which are indeed beta distributions (more precisely scale parameter generalizations of the standard beta distributions):

$$\mathcal{P}(y_i) = \frac{\Gamma(\alpha_0 + \alpha_i)}{\Gamma(\alpha_0)\Gamma(\alpha_i)} \frac{\lambda^{\alpha_i} \left(\frac{y_i}{1-y_i}\right)^{\alpha_i - 1} \left(\frac{1}{1-y_i}\right)^2}{\left[1 + \lambda_i \left(\frac{y_i}{1-y_i}\right)\right]^{\alpha_0 + \alpha_i}}, \tag{5.8}$$

where λ_i is a scale parameter, which can be expressed with the parameters of the beta functions. Note, these marginal distributions are not independent: α_0 is a common parameter. We found that as a consequence the covariances of the variables are always non-negative when the shapes of the marginal distributions are close to that of the normal distribution. This does not fit our objective to find such a multivariate PDF that its statistical moments up to the second order can be set independently, which leads us to Morgenstern's functions.

5.2.2 Morgenstern's System of Multivariate Distribution Functions

Morgenstern proposed [109; 127] the following system of bivariate cumulative distribution functions (CDF):

$$P(y_1, y_2) = P_1(y_1)P_2(y_2)\left[1 + \lambda\left(1 - P_1(y_1)\right)\left(1 - P_2(y_2)\right)\right], \tag{5.9}$$

where $P_i(y_i)$ is the marginal CDF of the random variable y_i and $|\lambda| \leq 1$. The respective PDF is

$$\mathcal{P}(y_1, y_2) = \mathcal{P}_1(y_1)\mathcal{P}_2(y_2)\left[1 + \lambda\left(2P_1(y_1) - 1\right)\left(2P_2(y_2) - 1\right)\right]. \tag{5.10}$$

The joint PDF is expressed with its marginal distributions. Apart from the parameters of the marginal PDFs, the only coefficient is λ, which is directly related to the covariance of the random variables

$$\overline{y_1'' y_2''} = \frac{\lambda I_1 I_2}{\sqrt{y_1''^2 y_2''^2}}, \tag{5.11}$$

where I_i denotes the following integral:

$$I_i = \int_0^1 P_i(y_i)\left(1 - P_i(y_i)\right) \mathrm{d}y_i. \tag{5.12}$$

Knowing the covariance we can directly calculate λ. If it is computationally too expensive to evaluate the I_i integrals, they could be calculated in advance and tabulated as the functions of the parameters of the marginal PDFs. Note that the marginal distributions can be chosen independently and arbitrarily, which is one of the favorable properties of this formulation because it makes the procedure more general and flexible. No matter what kind of marginal PDFs are applied, as long as we can evaluate the I_i integrals the covariance still can be set by tuning λ. Furthermore, we can easily extend the (5.9)

definition to multiple variables as

$$P(y_1, y_2, \ldots, y_n) = \prod_{i=1}^{n} P_i(y_i) \left[1 + \sum_{i \neq j} \lambda_{ij} \left(1 - P_i(y_i)\right) \left(1 - P_j(y_j)\right)\right], \tag{5.13}$$

$$\mathcal{P}(y_1, y_2, \ldots, y_n) = \prod_{i=1}^{n} \mathcal{P}_i(y_i) \left[1 + \sum_{i \neq j} \lambda_{ij} \left(2P_i(y_i) - 1\right) \left(2P_j(y_j - 1)\right)\right], \tag{5.14}$$

where λ_{ij} can be expressed with the covariance of y_i and y_j similarly to the (5.11) formula.

Morgenstern's multivariate distribution functions seem to fit all our purposes. However, it was found that a very high number of samples would be needed to approximate the expected covariance with sufficient accuracy. We generated 2000 sets of samples for the same expected statistical moments then evaluated these sets to obtain their actual moments. We averaged these moments over the sets to see how much they varied over the sets. While the means and the variances were accurately represented even with only a hundred samples per set, this was not the case for the covariance. We observed that although the mean of these calculated covariances matched the expected value with sufficient accuracy, the standard deviation of the covariances could be up to 60% of their expected mean value. Even in the case of a thousand samples per set - which would slow down the computation considerably as the computational time is proportional to the number of samples - this ratio was close to 20% which is clearly unaccaptable since it would bring into question the very purpose of this approach, namely to set the covariance of the control variables.

Based on this finding it would seem to be advantageous if we could somehow set, instead of passively represent, the proper covariance while keeping the number of samples at a constant low value.

5.2.3 Correlation Coefficient

Baurle and Girimaji suggested the introduction of a C correlation coefficient to take into account temperature-composition correlations [24; 30]. Their key idea is to formulate the model using only the marginal PDFs instead of using an explicit joint PDF.

The assumption is that the state variables lie on or close to a Low-Dimensional Slow Manifold (LDSM). In this case the mean source term can be written as

$$\overline{\dot{\omega}(Y,T)} = \overline{f_Y(Y) f_T(T)}, \tag{5.15}$$

where f_Y and f_T are functions of only the composition and the temperature, respectively. Introducing the correlation coefficient we obtain the following form:

$$\overline{f_Y(Y) f_T(T)} = \overline{f_Y}(Y)\overline{f_T}(T) + \overline{f'_Y(Y) f'_T(T)} = \overline{f_Y}(Y)\overline{f_T}(T) + C\left(\overline{f''^2_Y}(Y)\overline{f''^2_T}(T)\right)^{1/2}. \tag{5.16}$$

When $C = 0$ this formulation relaxes to the ansatz of statistical independence. Otherwise, after having established a relationship between the temperature and the species mass

fractions using the LDSM assumption, the authors show that C can be expressed as a function of only the temperature [24]:

$$C = \frac{\overline{f_Y(T) f_T(T)} - \overline{f_Y}(T)\overline{f_T}(T)}{\left(\overline{f_Y''^2}(T)\overline{f_T''^2}(T)\right)^{1/2}} \tag{5.17}$$

The drawback of this approach is the restrictive assumption about chemical kinetics.

5.3 Setting Correlations with Simulated Annealing

We intend to preserve the feature of the correlation coefficient technique that only the marginal PDFs are used to create a representative set of samples with an expected covariance. Generally speaking the problem is of multivariate random number generation with given marginal distributions and a given correlation matrix.

Charmpis and Panteli summarized several reported approaches to this problem [36]. Numerous efficient techniques exist for sampling from multivariate normal distributions [38; 66], but the research on other multivariate distributions is more limited. Parrish presented a method suitable for a multivariate Pearson family of distributions [133], which is only applicable if the joint product moments of up to the fourth order are known. Vale and Maurelli's algorithm [182] works with non-normal distributions, but it also requires fourth-order moments. These approaches are unfeasible for our purposes since third- and fourth-order moments would need to be either modeled or calculated. Li and Hammond developed a method that is based on transforming a k-variate normal distribution into a k-variate distribution with given marginal distributions and a given correlation matrix [114]. Lurie and Goldberg modified this approach using a nonlinear optimization routine to minimize the error between the calculated and the expected correlation matrices [118]. However, these latter two procedures are computationally too intensive. Iman and Conover proposed to use the marginal distributions and a permutation algorithm to obtain a desired rank correlation matrix [86]. It has to be emphasized that this approach is only suitable for setting rank correlations while we have *Pearson* correlations extracted from our transport equations.

To overcome the limitations of the aforementioned approaches Charmpis and Panteli proposed to use the simulated annealing method, which is distribution-independent, to set the correlations of multiple sets of univariate random numbers [36]. Following and building on their work we also use simulated annealing to generate our samples with given statistical moments. The details of the procedure are discussed in the following sections.

5.3.1 Generating Samples

The first task is to generate univariate random samples from various distributions, the first and second moments of which are known. We assume the shapes of these distributions.

This problem is well-addressed in the literature. Several algorithms and routines are publicly available in books [66; 103; 154] as well as in software packages and libraries such as MATLAB, IMSL STAT/LIBRARY or NAG Library [36]. Ghosh and Vogt have summarized the most common approaches [69] out of which we mention here the three most popular ones:

1. Natural method

   In this case a population that obeys the distribution exists and we can sample from this population. Note that we do not need to know the exact formula of the distribution. For example think of surveys: we do not know the distribution of the answers in the entire population in advance, but we can still design a survey to sample from this distribution.

2. Rejective method

   Let $y \in [a; b]$ be a random variable with the PDF $\mathcal{P}(y)$. On the given interval $\mathcal{P}(y) \leq M$. In order to draw a sample from this distribution, we have to generate two uniform random variables y_0 and m on $[a; b]$ and $[0; M]$ respectively. If $m \leq \mathcal{P}(y_0)$ then y_0 is added to the set of samples, else it is rejected. This procedure is continued until we have enough samples. This method is called Lahiri's method [40].

   We successfully used this approach when we tested Morgenstern's functions (see section 5.2.2).

3. Inversive method

   This is probably the most straightforward approach, but its applicability is more restricted than that of the rejective method because we have to be able to invert the CDF $F(y)$ that characterizes the distribution we intend to draw samples from. If the CDF is invertible then we only have to generate a uniform random number r between 0 and 1 and add $y_i = F^{-1}(r)$ to our sample set.

In this work we use β-PDFs the CDF of which is invertible. We used the publicly available libraries of *J. Burkardt* (Florida State University) [33], `ranlib, rnglib, asa109` to draw our samples from a β-distribution using the inversive method. However, in the case of other PDFs one might want to turn towards the more general rejective method.

5.3.2 The Method of Simulated Annealing

We generate univariate samples $([y_1^i]_{i=1,\ldots,N}, [y_2^i]_{i=1,\ldots,N})$ in accordance with the calculated statistical moments and the assumed shapes of the one-dimensional marginal PDFs. Then these samples are organized into random pairs, as if they were 'coordinates', to create samples in the two-dimensional parameter space: $[y_1^i; y_2^i]_{i=1,\ldots,N}$. Our objective is to find such a π permutation of $1, \ldots, N$, that the correlation coefficient of the rearranged coordinates

$[y_1^i; y_2^{\pi(i)}]_{i=1,\ldots,N}$, calculated as

$$R_{12} = \frac{\sum_{i=1}^{N} \left(y_1^i - \overline{y}_1\right)\left(y_2^{\pi(i)} - \overline{y}_2\right)}{\sqrt{\sum_{i=1}^{N} \left(y_1^i - \overline{y}_1\right)^2 \sum_{i=1}^{N} \left(y_2^{\pi(i)} - \overline{y}_2\right)^2}}, \tag{5.18}$$

equals the expected value within a predefined margin of error. Note, this permutation does not affect the marginal distributions since only the indexing of the univariate samples is changed, not their values. This is a combinatorial optimization problem, which can be handled with simulated annealing.

In a general combinatorial optimization problem the aim is to find the minimum or the maximum of a function of multiple variables on a finite set of feasible solutions. (Since searching for the maximum can always be transformed into searching for the minimum, we consider the latter in the following discussion without loss of generality.) The function in question is the so-called objective function, which is created to measure the 'goodness' of a complex system.

The most well-known example of combinatorial optimization is the traveling salesman problem [96; 97]. A salesman has to visit N given cities. The cost of traveling between any two of these cities is known. One has to plan the route of the salesman in a way that minimizes the total costs.

As *Kirkpatrick* wrote in the paper introducing the concept of simulated annealing [97], there are two basic strategies for solving these kind of optimization problems:

- **Divide-and-conquer** - The problem is divided into subproblems, which can be managed easily, then the solutions have to be patched together.
- **Iterative improvement** - The procedure starts with a valid arrangement of the system. Then the algorithm rearranges it until the objective function is improved. The iteration continues as long as a stop condition is not fulfilled. Most often it means that no further improvement is possible, the objective function has reached its minimum.

Simulated annealing is an iterative process. We need to examine what the prerequisites of applying such a process are. The following three crucial components have to exist [96]:

1. A good representation of the system which is capable of accurately describing the many possible configurations.
2. An E scalar objective function that reduces the complexity of the system into a single representative number that has to be minimized.
3. A procedure for obtaining a new state from the initial one through local rearrangements. This will be called a 'step'. We want to be able to find the solution no matter what the initial configuration is. Therefore, the system has to be able to evolve from any possible state to any other possible state in a sufficient number of steps.

When we rearrange the system, E changes with ΔE. Therefore when defining E it should be kept in mind that it is beneficial if it is easier to calculate ΔE than E itself, because the former one has to be calculated in every step. If $\Delta E < 0$, the new state should be preserved and used as the initial state for the next step. However, if we simply always rejected the new state when $\Delta E \geq 0$, the solution could get stuck in a local minimum in spite of E improving in every step. Consequently this 'improvement-only' rule has to be revised: E should be occasionally allowed to increase in a controlled manner, which means that sometimes we should accept a worse state as a new one in order to leave the trap of a local minimum (Figure 5.1).

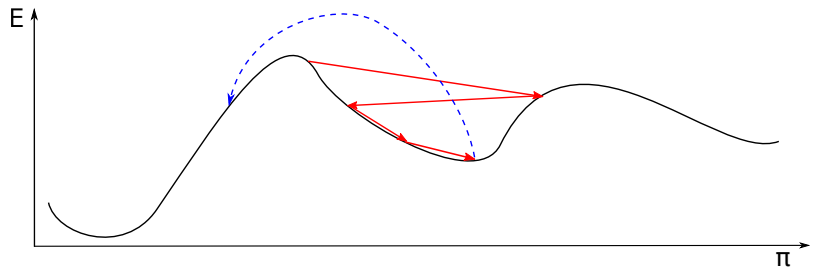

Figure 5.1: An iterative solution procedure that is only allowed to improve the error function (E) in every step (red arrows) can get stuck in a local minimum. In order to find the absolute minimum, E occasionally has to be allowed to increase temporarily (blue arrow), thereby the solution can leave the local potential valley.

Metropolis [125] proposed the following rules for evaluating a random rearrangement:

1. $\Delta E < 0 \rightarrow$ The new state is accepted.
2. $\Delta E \geq 0 \rightarrow$ The new state is accepted with the probability of

$$P(\Delta E) = \exp(-\Delta E / k_B T). \tag{5.19}$$

This procedure originates from statistical mechanics and was first used in thermodynamics [14; 154; 157] hence the Boltzmann-constant (k_B) and a T temperature appear in the original formulation. As a matter of fact the aforementioned rules in their presented form describe the thermal motion of atoms in thermal contact with a heat bath at temperature T [97]. The energy of a system in thermal equilibrium at temperature T is distributed among all different energy states. After enough steps the system evolves into a Boltzmann-distribution. It means, that even at low temperatures it is possible that the system is locally in a high energy state. The possibility depends on the actual temperature: as the temperature decreases the system freezes. This is where the name 'simulated annealing' comes from: when the low-temperature state of a material is determined experimentally, instead of simply cooling down the substance, one carries out an annealing procedure. First the substance is melted, then the temperature is lowered incrementally. This is how for example defect-free single crystals are grown. If the cooling happens too quickly, the crystal ends up having more defects because of having reached only locally optimal structures.

Through this practical analogy from the world of physics one can have a feeling for how Metropolis' rules can find the global minimum - or a sufficiently close local one - of the

objective function. We can also see how important a role the temperature plays. How we change the temperature controls the accessibility of the different states. From a numerical point of view this so-called *annealing schedule* has a major effect on the required number of iterations. We further elaborate on this parameter in section 6.2.3.

After this brief introduction let us investigate how we can adjust this method to our objectives.

5.3.3 The Process

The procedure consists of the following steps - remember, that everything happens at the level of individual cells:

1. Calculate the first and second moments of the control variables from the transport equations and the chosen models.
2. Generate univariate samples in accordance with the calculated statistical moments and the assumed shapes of the one-dimensional PDFs: $[y_1^i]_{i=1,\dots,N}, [y_2^i]_{i=1,\dots,N}$.
3. Let R_{12}^{exp} be the expected correlation coefficient.
4. Create points in the two-dimensional parameter space using the univariate samples: $(y_1^i; y_2^i)_{i=1,\dots,N}$ (Figure 5.2a).
5. Calculate the actual correlation coefficient according to the (5.18) formula: R_{12}.
6. Calculate the error: $E = |R_{12}^{exp} - R_{12}|$.
7. Pick two random points in the parameter space: $(y_1^j; y_2^j), (y_1^k; y_2^k)$ (Figure 5.2b).
8. Swap the y_2 coordinates of these points: $(y_1^j; y_2^j), (y_1^k; y_2^k) \rightarrow (y_1^j; y_2^k), (y_1^k; y_2^j)$ (Figure 5.2c).

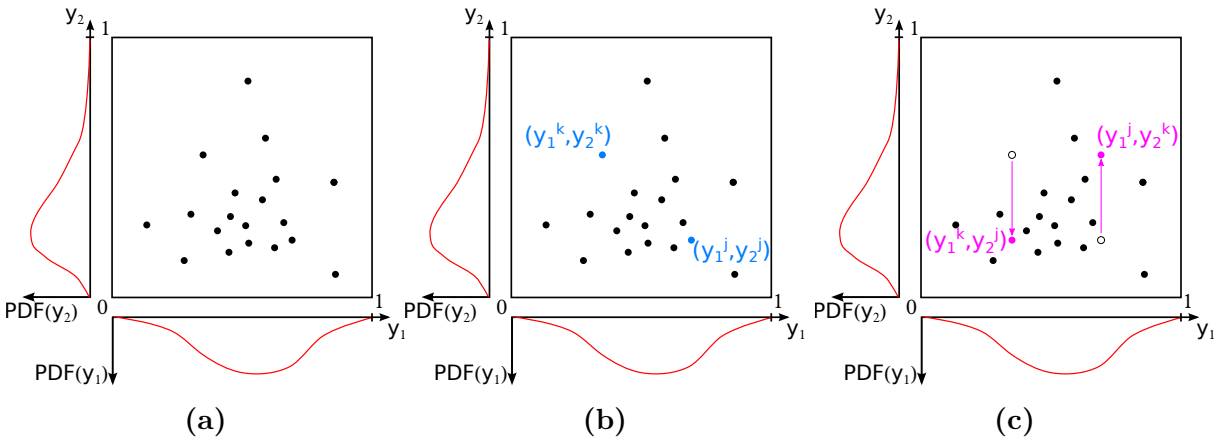

Figure 5.2: We use the univariate samples as coordinates to create random points in the two-dimensional parameter space with given marginal distributions (a). Then two random points are selected (b) and the y_2 coordinates of these points are swapped. Meanwhile the marginal PDFs remain unaffected.

9. Calculate the new correlation coefficient: R'_{12}. This calculation is cheap, because only two terms are affected in the (5.18) summation:

$$R'_{12} = R_{12} - \frac{1}{N\sqrt{\sigma_{y_1}\sigma_{y_2}}}(y_1^j - y_1^k)(y_2^j - y_2^k). \tag{5.20}$$

10. Calculate the new error: $E' = |R_{12}^{exp} - R'_{12}| \rightarrow \Delta E = E' - E$.

11. Evaluate the step:

    - If $\Delta E \leq 0$, then keep the new points.
    - If $\Delta E > 0$, then keep the new points with the probability of $P(\Delta E) = \exp(-\Delta E/T_{SA})$, where T_{SA} is the artificial temperature parameter.

    When the new points are accepted set $E = E'$ and $R_{12} = R'_{12}$.

12. Check the stop conditions and if necessary continue with the next iteration from step 7.

    The simplest stop conditions we can set are an upper limit for the error and a maximum number of iterations. However, as we will see in section 6.2 a more complex approach is required.

We can extend this procedure to m control variables in a straightforward manner. We can generate points in the m-dimensional parameter space just like we did with two variables: $[y_1^i; y_2^i; \ldots; y_m^i]_{i=1,\ldots,N}$. The expected R_{ij}^{exp} correlation coefficients can also be calculated. We start swapping the kth 'coordinates' once all the R_{ij} correlations are set, where $i, j < k$. The error function becomes a sum

$$E_k = \sum_{i=1}^{k-1} |R_{ik}^{exp} - R_{ik}|, \tag{5.21}$$

but this can be minimized by swapping random kth coordinates in the same way as the error function for only two control variables. Once the stop conditions have been fulfilled, we can proceed with the next control variable.

5.4 Summary

We devoted this chapter to giving an overview of how multivariate joint PDFs can be created based on their statistical moments and the assumed shapes of their marginal distributions. The difficulty lies in taking into consideration the covariances, which is necessary to relax the strong assumption regarding the statistical independence of the control variables. We propose to use the simulated annealing technique for this purpose, therefore in the following we refer to the procedure described in section 5.3.3 as the CSSA (**C**orrelation **S**et by **S**imulated **A**nnealing) method for the sake of brevity.

The CSSA approach has been shown to have several favorable properties:

1. The marginal distributions can be arbitrarily chosen as long as univariate samples can be drawn from them.
2. It can be extended to multiple control variables.
3. The look-up table does not have to be pre-integrated, the mean values are obtained by cheap ensemble averaging.
4. The look-up table has the same number of dimensions as the number of control variables, its dimensionality is independent of the order of statistical moments considered.

Further details regarding the stop conditions and the annealing schedule are yet to be clarified. We elaborate on these numerical aspects of CSSA in section 6.2 in the next chapter, which describes the applied numerical methods.

Chapter 6

Numerical Implementations

We cannot solve analytically the governing equations summarized in section 2.1, therefore numerical methods have to be applied in order to obtain the solutions for the given initial and boundary conditions with the desired precision. The numerical treatment of combustion processes is especially challenging because of the occurring steep gradients: density, viscosity, and temperature all change abruptly at the flame front. The implementation of the accordingly chosen numerical techniques and the general solution procedure are described in this chapter. All implementations are done within an LES framework using finite volume discretization.

In this work we used and further developed the academic CFD code FASTEST (Flow Analysis by Solving Transport Equations Simulating Turbulence). This program has a long history and has been used by many institutions for various purposes (acoustics, fluid-structure interaction, etc.). However, it has not always been capable of calculating reacting flows.

Originally FASTEST was developed as a RANS solver for constant density incompressible flows [52]. It uses finite volume method for discretization and the SIMPLE pressure correction scheme [134]. The variable arrangement is cell-centered on a non-staggered grid. In order to avoid undesired - and also unphysical - pressure oscillations a selective interpolation scheme for the mass fluxes proposed by Rhie and Chow [159; 199] has been implemented (a detailed description can be found in Appendix A). FASTEST was later extended at the Department of Energy and Power Plant Technology (TU Darmstadt) to become able to handle combustion processes. Maltsev [121] and Schneider [167] added the reactive flow capabilities within a RANS context, then Wegner [193] started the variable density implementations for LES. He observed stability problems and also showed that the implicit pressure correction scheme was not sufficiently effective for LES. These findings led to the PhD projects of Hahn [77] and Olbricht [131], who implemented the explicit Runge-Kutta time integration scheme with the pressure correction based projection method of Chorin [39] while preserving Majda's low Mach number formulation for variable density flows [120]. They have also developed a scheme that alters the treatment of the scalar transport equation to provide stability even if strong density variations are present. These approaches have been kept in the code to this date.

Through the subsequent years the extended capabilities of FASTEST were demonstrated for various different cases such as pure mixing in both simple and complex geometries [78]

or non-premixed flames using either the steady flamelet approach or the FGM method [132]. Künne implemented the ATF method with the objective of simulating premixed flames [107]. During the same years Ketelheun increased the number of applicable control variables within the FGM context via adding to the original set of conservation equations a new transport equation for the enthalpy [93; 94]. This made the program capable of treating heat losses.

These earlier developments have led to the starting point of the implementations conducted in this work. However, it needs to be pointed out that many ongoing parallel projects exist - such as the implementation of the Eulerian Monte Carlo stochastic field method by Avdić [17] - the developments of which have not yet been merged into the core code, therefore several, sometimes significantly different, versions of FASTEST exist.

In the next section the general solution procedure is reviewed. This part of the code has not been changed during this work but for the sake of completeness it is still worthwhile to highlight the applied methods. The following section elaborates on the numerical implementation of the simulated annealing technique which is one of the key components of this work.

6.1 General solution procedure

As stated earlier, FASTEST applies the finite volume method (FVM) [55; 83], which relies on the direct discretization of the integral form of the conservation equations. This distinguishes the FVM from the finite difference method as the integral form of a conservation equation is the most general one and it does not require the fluxes to be continuous. The solution starts with the spatial discretization of the computational domain: it is subdivided into small volumes, one control volume being associated with each mesh point. The different variables are stored in these mesh points discrete in time and space and the governing differential equations are approximated by appropriate interpolation methods. Then the integral conservation law is applied to each finite volume. The result of this procedure is a set of discretized equations which can be solved knowing the prescribed initial and boundary conditions.

6.1.1 Spatial discretization

In FASTEST the computational domain is discretized over a block-structured mesh comprising hexahedral cells. Applying multiple blocks makes it possible to cover even complex geometries and it also allows for straightforward parallelization using the Message Passing Interface standard (MPI). However, it has to be emphasized that FASTEST imposes certain requirements on the mesh. Hanging nodes are not supported, therefore O-grid structures have to be used for local refinement. Connectivity between the blocks is established by a layer of ghost cells. This ghost cell layer is of zero thickness in the direction normal to the boundary. All the grids used in this work were generated with ANSYS

ICEM CFD [2], which has inbuilt functions for elliptical smoothing in order to improve the orthogonality of the mesh.

6.1.2 Finite Volume Discretization of Transport Equations

The process of discretization and the applied interpolation methods are exemplified with the general transport equation of a scalar Φ described in Section 2.1.1 for all the governing equations being the special cases of this one:

$$\frac{\partial}{\partial t}\left(\rho\Phi\right) + \frac{\partial}{\partial x_i}\left(\rho u_i \Phi\right) = \frac{\partial}{\partial x_i}\left(\Gamma_\Phi \frac{\partial \Phi}{\partial x_i}\right) + \dot{\omega}_\Phi, \tag{6.1}$$

where $\Gamma_\Phi = \rho D_\Phi$ and $\dot{\omega}_\Phi$ is the source term of Φ that comprises both the volume and surface sources. Integrating (6.1) over a control volume yields

$$\int_V \frac{\partial}{\partial t}\left(\rho\Phi\right) \mathrm{d}V + \int_V \frac{\partial}{\partial x_i}\left(\rho u_i \Phi\right) \mathrm{d}V = \int_V \frac{\partial}{\partial x_i}\left(\Gamma_\Phi \frac{\partial \Phi}{\partial x_i}\right) \mathrm{d}V + \int_V \dot{\omega}_\Phi \mathrm{d}V. \tag{6.2}$$

The volume integrals ($\mathrm{d}V$) of the convective and diffusive fluxes can be transformed into surface integrals ($\mathrm{d}S$) by using the Gauss-Ostrogradsky theorem:

$$\int_V \frac{\partial}{\partial t}\left(\rho\Phi\right) \mathrm{d}V + \int_S \rho u_i \Phi n_i \mathrm{d}S = \int_S \left(\Gamma_\Phi \frac{\partial \Phi}{\partial x_i}\right) n_i \mathrm{d}S + \int_V \dot{\omega}_\Phi \mathrm{d}V, \tag{6.3}$$

where n_i denotes the component of the face normal vector in the i-direction. The surface integrals can be written as the sum of the integrals over the six surfaces of the hexahedron ($c = n, e, s, w, t, b$, where the notation refers to the *north, east, south, west, top, bottom* faces respectively as depicted in Figure 6.1).

$$\underbrace{\int_V \frac{\partial}{\partial t}\left(\rho\Phi\right) \mathrm{d}V}_{\mathcal{T}} + \sum_c \underbrace{\int_{S_c} \rho u_i \Phi n_i \mathrm{d}S_c}_{\mathcal{F}_c^C} = \sum_c \underbrace{\int_{S_c} \left(\Gamma_\Phi \frac{\partial \Phi}{\partial x_i}\right) n_i \mathrm{d}S_c}_{\mathcal{F}_c^D} + \underbrace{\int_V \dot{\omega}_\Phi \mathrm{d}V}_{\mathcal{Q}}. \tag{6.4}$$

Notice that no approximations have been made so far. Now each of the different terms in the above equation - the transient term ($\mathcal{T}$), the convective ($\mathcal{F}_c^C$) and diffusive ($\mathcal{F}_c^D$) fluxes through the face c, and the source term ($\mathcal{Q}$) - has to be rewritten in such an algebraic form that only uses the values stored in the discrete points of the mesh. Therefore we apply the midpoint rule to approximate the surface and volume integrals. We can evaluate the volume integrals directly since no information is needed from the neighboring cells and all the necessary variables are known at the cell center:

$$\mathcal{T} = \int_V \frac{\partial}{\partial t}\left(\rho\Phi\right) \mathrm{d}V \approx \frac{\partial}{\partial t}\left(\rho\Phi\right)\Big|_P \delta V, \tag{6.5}$$

$$\mathcal{Q} = \int_V \dot{\omega}_\Phi \mathrm{d}V \approx \dot{\omega}_\Phi\Big|_P \delta V. \tag{6.6}$$

However, the surface integrals are more difficult to approximate because both the variables and the gradients have to be known on the cell faces:

$$\mathcal{F}_c^C = \int_{S_c} \rho u_i \Phi n_i \mathrm{d}S_c \approx \left(\rho u_i \Phi n_i\right)\Big|_c \delta S_c, . \tag{6.7}$$

$$\mathcal{F}_c^D = \int_{S_c} \left(\Gamma_\Phi \frac{\partial \Phi}{\partial x_i}\right) n_i \mathrm{d}S_c \approx \left(\Gamma_\Phi \frac{\partial \Phi}{\partial x_i} n_i\right)\Big|_c \delta S_c. \tag{6.8}$$

These approximations require various interpolation methods utilizing the variables stored in adjacent cells, therefore the terms are evaluated in the local cell based coordinate system (ξ_i, ξ_2, ξ_3) illustrated in Figure 6.1a. Since the governing equations are written in the global coordinate system (x_1, x_2, x_3), a transformation is required between these two bases in order to be able to express the derivatives in the direction perpendicular to the given cell surface. We only need to transform the derivatives [55] because both coordinate systems are Cartesian:

$$\frac{\partial \Phi}{\partial x_i} = \frac{\beta^{ij}}{\mathcal{J}} \frac{\partial \Phi}{\partial \xi_j}, \tag{6.9}$$

where $\mathcal{J}$ is the Jacobian of the transformation

$$\mathcal{J} = \det\left(\frac{\partial x_i}{\partial \xi_j}\right), \tag{6.10}$$

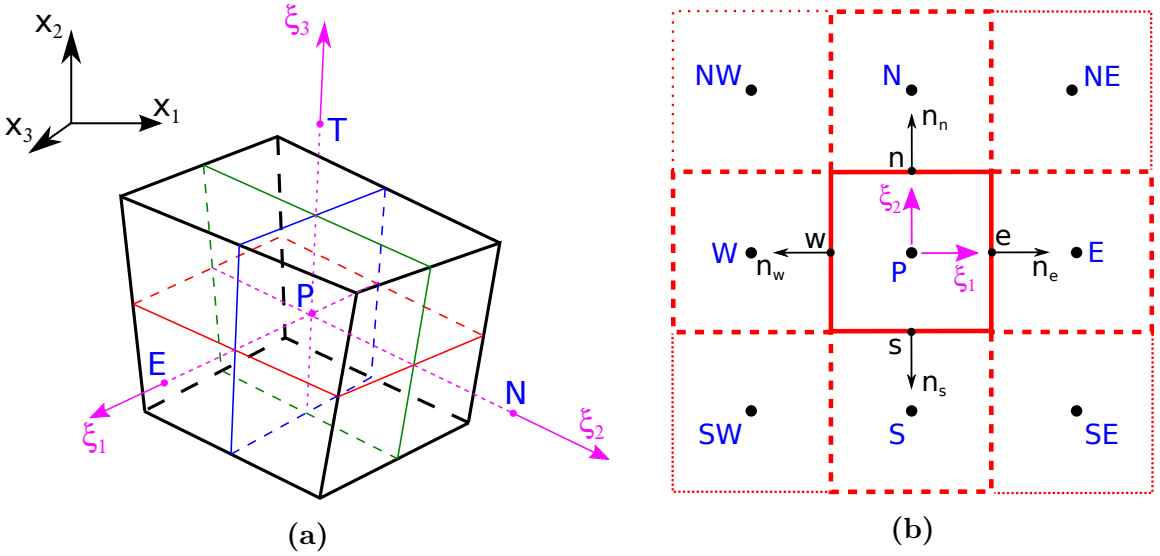

Figure 6.1: (a) A single control volume around a P cell center is shown to illustrates the local (ξ_1, ξ_2, ξ_3) and the global (x_1, x_2, x_3) coordinate systems. (b) The $\xi_3 = 0$ slice of this control volume and the neighboring cells are depicted. Capital letters denote the centers of the control volumes while lowercase refer to the control volume faces with the corresponding normal vectors n_i. The letters represent directions: n = north, s = south, e = east, w = west, t = top, b = bottom, The $\xi_1 = 0$ and the $\xi_2 = 0$ slices could be drawn similarly and the respective notations would follow the presented one.

and β^{ij} represents the cofactor of $\partial x_i/\partial \xi_j$. The entire β matrix of cofactors is

$$\beta = \begin{bmatrix} \frac{\partial x_2}{\partial \xi_2}\frac{\partial x_3}{\partial \xi_3} - \frac{\partial x_3}{\partial \xi_2}\frac{\partial x_2}{\partial \xi_3} & \frac{\partial x_3}{\partial \xi_1}\frac{\partial x_2}{\partial \xi_3} - \frac{\partial x_2}{\partial \xi_1}\frac{\partial x_3}{\partial \xi_3} & \frac{\partial x_2}{\partial \xi_1}\frac{\partial x_3}{\partial \xi_2} - \frac{\partial x_3}{\partial \xi_1}\frac{\partial x_2}{\partial \xi_2} \\ \frac{\partial x_3}{\partial \xi_2}\frac{\partial x_1}{\partial \xi_3} - \frac{\partial x_1}{\partial \xi_2}\frac{\partial x_3}{\partial \xi_3} & \frac{\partial x_1}{\partial \xi_1}\frac{\partial x_3}{\partial \xi_3} - \frac{\partial x_3}{\partial \xi_1}\frac{\partial x_1}{\partial \xi_3} & \frac{\partial x_3}{\partial \xi_1}\frac{\partial x_1}{\partial \xi_2} - \frac{\partial x_1}{\partial \xi_1}\frac{\partial x_3}{\partial \xi_2} \\ \frac{\partial x_1}{\partial \xi_2}\frac{\partial x_2}{\partial \xi_3} - \frac{\partial x_2}{\partial \xi_2}\frac{\partial x_1}{\partial \xi_3} & \frac{\partial x_2}{\partial \xi_1}\frac{\partial x_1}{\partial \xi_3} - \frac{\partial x_1}{\partial \xi_1}\frac{\partial x_2}{\partial \xi_3} & \frac{\partial x_1}{\partial \xi_1}\frac{\partial x_2}{\partial \xi_2} - \frac{\partial x_2}{\partial \xi_1}\frac{\partial x_1}{\partial \xi_2} \end{bmatrix}. \tag{6.11}$$

We describe the interpolation methods in the following subsections using the east face (e) of a cell as an example.

6.1.3 Diffusive Fluxes

A diffusive flux term (6.8) consists of two parts: the derivative of the transported scalar and the diffusion coefficient, both of which have to be evaluated on the cell face.

Computation of scalars The obvious first choice would be to apply the central difference scheme (CDS) to calculate the scalar quantities in the e cell face center. This would mean linear interpolation between the computational nodes P and E:

$$\Gamma_e = w_E \Gamma_E + w_P \Gamma_P, \tag{6.12}$$

where $w_E = d_{e,P}/d_{E,P}$, $w_P = d_{E,e}/d_{E,P}$, and $d_{A,B}$ denotes the distance between the points A and B ($x_{i,A}$ is the x_i coordinate of point A):

$$d_{A,B} = \sqrt{\sum_{i=1}^{3} (x_{i,A} - x_{i,B})^2}. \tag{6.13}$$

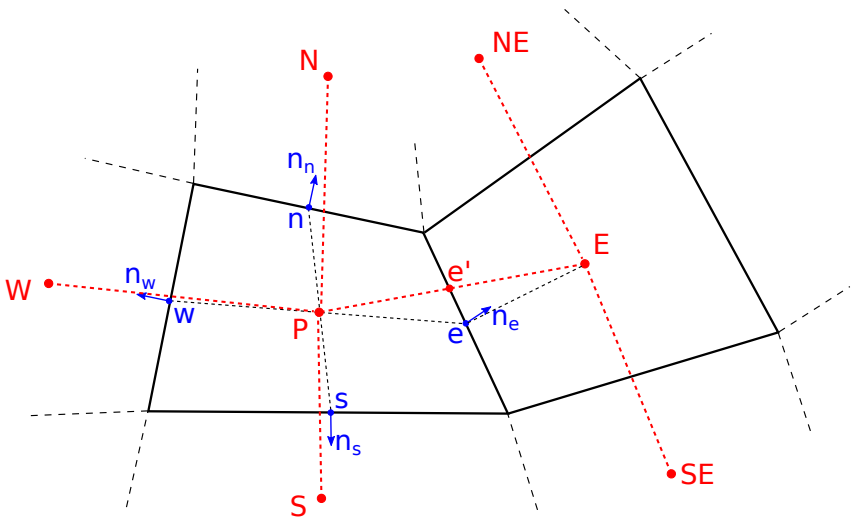

Figure 6.2: An arbitrary quadrilateral control volume is depicted with the cell centers of the neighboring control volumes. Since the e face center point is not located on the PE line connecting the center nodes, linear interpolation between P and E would not yield a second-order accurate approximation for variables in e.

This interpolation is second-order accurate for Cartesian grids, however, does not guarantee the second-order accuracy for a non-regular mesh as the face center point is usually not located on the line connecting the center nodes (Figure 6.2).

Furthermore, instabilities can occur when the gradient of the transported scalar is steep owing to the lack of numerical diffusion in CDS. In order to maintain second-order accuracy we apply the multi-linear interpolation scheme (MULI) of Lehnhäuser and Schäfer [113] which includes the adjacent nodes N, S, T and B apart from P and E:

$$\Gamma_e = w_E\Gamma_E + (1 - w_E)\Gamma_P + w_{NS}(\Gamma_N - \Gamma_S) + w_{TB}(\Gamma_T - \Gamma_B), \tag{6.14}$$

with the interpolation factors

$$\begin{aligned} w_E &= \frac{x_{i,P} - x_{i,e}}{\jmath_e}\psi_e^{1i}, \\ w_{NS} &= \frac{x_{i,P} - x_{i,e}}{\jmath_e}\psi_e^{2i}, \\ w_{TB} &= \frac{x_{i,P} - x_{i,e}}{\jmath_e}\psi_e^{3i}, \end{aligned} \tag{6.15}$$

where

$$\psi_e^{1i} = \epsilon_{ikl}\left[(x_{k,N} - x_{k,S})\,(x_{l,T} - x_{l,B})\right], \tag{6.16}$$
$$\psi_e^{2i} = \epsilon_{ikl}\left[(x_{k,T} - x_{k,B})\,(x_{l,E} - x_{l,P})\right], \tag{6.17}$$
$$\psi_e^{3i} = \epsilon_{ikl}\left[(x_{k,E} - x_{k,P})\,(x_{l,N} - x_{l,S})\right], \tag{6.18}$$
$$\jmath_e = (x_{i,E} - x_{i,P})\,\psi_e^{1i}. \tag{6.19}$$

This scheme is only slightly more computationally expensive than a classical CDS.

Computation of gradients The computation of the derivative is based on the coordinate transformation described by the (6.9) formula and uses the DABT interpolation scheme of Lehnhäuser [112] to ensure second-order accuracy:

$$\left(\frac{\partial\Phi}{\partial x_i}\right)_e = \frac{\Psi_{e,DABT}^{ji}}{\jmath_{e,DABT}}\Phi_{e,DABT}^{j}, \tag{6.20}$$

where

$$\begin{aligned} \Phi_{e,DABT}^{1} &= (\Phi_E - \Phi_P), \\ \Phi_{e,DABT}^{2} &= (\Phi_N - \Phi_S + \Phi_{NE} - \Phi_{SE}), \\ \Phi_{e,DABT}^{3} &= (\Phi_T - \Phi_B + \Phi_{TE} - \Phi_{BE}), \\ \Psi_{e,DABT}^{1i} &= \epsilon_{ikl}\left[(x_{k,N} - x_{k,S} + x_{k,NE} - x_{k,SE})(x_{l,T} - x_{l,B} + x_{l,TE} - x_{l,BE})\right], \\ \Psi_{e,DABT}^{2i} &= \epsilon_{ikl}\left[(x_{k,T} - x_{k,B} + x_{k,TE} - x_{k,BE})(x_{l,E} - x_{l,P})\right], \\ \Psi_{e,DABT}^{3i} &= \epsilon_{ikl}\left[(x_{k,E} - x_{k,P})(x_{l,N} - x_{l,S} + x_{l,NE} - x_{l,SE})\right], \\ \jmath_{e,DABT} &= (x_{i,E} - x_{i,P})\Psi_{e,DABT}^{1i}. \end{aligned} \tag{6.21}$$

6.1.4 Convective Fluxes

The (6.7) convective flux term does not contain any gradients, consequently it seems to be easier to treat it numerically than the diffusive term. However, maintaining second-order accuracy poses a challenge because the previously described MULI scheme, despite being more accurate than CDS, is still not sufficiently stable. Due to the lack of numerical diffusion, instabilities can occur as a consequence of steep scalar gradients. Therefore another approach is needed that is capable of handling such sharp changes without too much smoothening in order to not modify the flame physics significantly. For this purpose the total variation diminishing (TVD) scheme incorporating the CHARM-limiter suggested by Zhou [202] has been chosen. The value on the cell face is obtained from its downwind (index D) and upwind (U) nodes (Figure 6.3) according to

$$\Phi_e = \Phi_U + \frac{d_{e,U}}{d_{D,U}} B(r)(\Phi_U - \Phi_{UU}), \tag{6.22}$$

where $B(r)$ is the limiter function

$$B(r) = \begin{cases} \frac{r(3r+1)}{(r+1)^2} & : r > 0 \\ 0 & : r \leq 0. \end{cases} \tag{6.23}$$

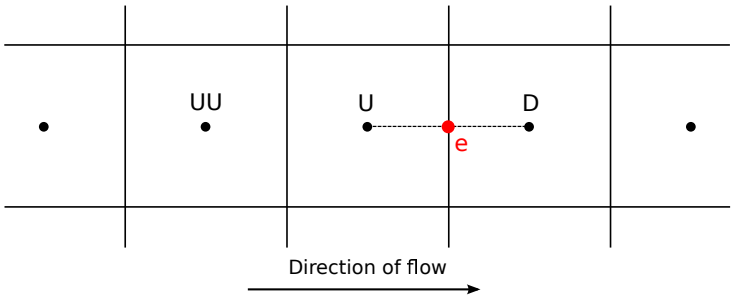

Figure 6.3: Notations for calculating the convective fluxes with a TVD scheme.

To keep the solution stable, the limiter function adjusts the interpolation according to the gradient ratio

$$r = \frac{d_{U,UU}}{d_{D,U}} \frac{\Phi_D - \Phi_U}{\Phi_U - \Phi_{UU}}. \tag{6.24}$$

If the gradient ratio is close to one, which means that the gradient of Φ is well resolved, the expression yields the linear upwind scheme of second-order. If the gradient is sharp ($r \to 0$ or $r \to \infty$), the solution converges non-linearly towards a pure upwind scheme of first order. This scheme is applied to obtain ρ_e and Φ_e in (6.7). u_i in point e requires further considerations.

Rhie and Chow interpolation Applying a central difference approximation for the mass flux computation can lead to the decoupling of the pressure and the velocity field

yielding a pressure distribution with unphysical oscillations that does not contribute to the pressure force in the momentum equation (which is physically correct) [165]. In order to avoid this phenomenon the Rhie and Chow [159; 199] interpolation scheme has been implemented for u_e. This scheme uses the MULI technique instead of linear interpolation for expressing the uncorrected u_e (see Appendix A for further details).

6.1.5 Time Discretization

Having discretized the different terms of Equation (6.4) in the previous sections we can represent the transport equation as an algebraic system of discrete variables:

$$\frac{\partial}{\partial t}\left(\rho\Phi\right)\Big|_P = \frac{1}{\delta V}\left(\sum_c \left(\mathcal{F}_c^D - \mathcal{F}_c^C\right) + \mathcal{Q}\right). \tag{6.25}$$

The next step is to choose an appropriate time integration method to approximate the transient term. However, before doing this, we should alter the transient term to increase the stability of the scheme [131]. Let us start with carrying out the partial integration:

$$\frac{\partial}{\partial t}\left(\rho\Phi\right) = \rho\frac{\partial\Phi}{\partial t} + \Phi\frac{\partial\rho}{\partial t}. \tag{6.26}$$

Expressing the last term using the continuity equation (2.6) leads to

$$\frac{\partial}{\partial t}\left(\rho\Phi\right) = \rho\frac{\partial\Phi}{\partial t} - \Phi\frac{\partial}{\partial x_i}\left(\rho u_i\right). \tag{6.27}$$

Once we have integrated this equation, the first term on the right hand side can be easily evaluated on the discrete grid:

$$\int_V \rho\frac{\partial\Phi}{\partial t}\mathrm{d}V \approx \left(\rho\frac{\partial\Phi}{\partial t}\right)\Big|_P \delta V_P. \tag{6.28}$$

We can split the second term on the right hand side of equation (6.27) into two parts when integrating it over the control volume. Φ can be expressed as the sum of an average value in the cell center (Φ_P) and a fluctuation around it (Φ'):

$$\int_V \Phi\frac{\partial}{\partial x_i}\left(\rho u_i\right)\mathrm{d}V = \int_V \left(\Phi_P + \Phi'\right)\frac{\partial}{\partial x_i}\left(\rho u_i\right)\mathrm{d}V = \Phi_P\int_V \frac{\partial}{\partial x_i}\left(\rho u_i\right)\mathrm{d}V + \int_V \Phi'\frac{\partial}{\partial x_i}\left(\rho u_i\right)\mathrm{d}V. \tag{6.29}$$

The fluctuation of the transported scalar and the momentum gradient are assumed to be uncorrelated. Consequently the second term on the right hand side disappears leaving only one term which we can approximate using the midpoint rule and the Gauss-Ostrogradsky theorem:

$$\Phi_P\int_V \left(\rho u_i n_i\right)\mathrm{d}S + \int_V \Phi'\frac{\partial}{\partial x_i}\left(\rho u_i\right)\mathrm{d}V = \Phi_P\sum_c \left(\rho u_i n_i\right)\Big|_c \delta S_c. \tag{6.30}$$

This expression bears resemblance to the (6.7) formula and the two can be grouped together into a generalized convective term:

$$\mathcal{F}_c^{C*} \approx \left(\rho u_i n_i\right)\Big|_c \delta S_c\left(\Phi_c - \Phi_P\right). \tag{6.31}$$

This formulation increases the stability of the numerical scheme by introducing additional diagonal elements in the solution matrix. This leads us to the final form of the spatially discretized transport equation to be integrated over time:

$$\left.\frac{\partial \Phi}{\partial t}\right|_P = \frac{1}{\rho_P \delta V_P}\left(\sum_c \left(\mathcal{F}_c^D - \mathcal{F}_c^{C*}\right) + \mathcal{Q}\right) = \mathcal{R}(\Phi). \tag{6.32}$$

$\mathcal{R}(\Phi)$ denotes all the spatially discretized terms on the right hand side, therefore it only contains discrete cell centered variables. In order to create an algebraic system to be solved, we have to choose an appropriate scheme to approximate the time derivative on the left hand side with an expression of discrete points of distance Δ_t in time.

In FASTEST a second-order three-stage Runge-Kutta (RK) scheme was implemented, which is an explicit scheme. The main advantage of applying an explicit scheme is that in this case the solution procedure is not iterative as opposed to implicit methods. In the context of turbulent combustion an iterative approach would mean that scalars that determine the fluid properties - such as the density or the viscosity - would have to be calculated multiple times during a single time step. Considering the challenges of obtaining these scalar values, this would make one time step computationally more expensive and would cause extra communication overhead in a parallel environment. The biggest drawback of using an explicit scheme is that it poses a limit on the maximum applicable time step. However, the simulation of transient combustion processes is usually limited by the small time scales and time increments anyway, therefore an explicit scheme is favored.

In a general RK scheme several intermediate values of the given variable ($\Phi^{RK,i}$) are calculated within a time step using the results of preceding stages:

$$\Phi^{RK,i} = \Phi^n + \Delta_t \sum_{j=1}^{s} \alpha_{ij} \mathcal{R}(\Phi^{RK,j}), \tag{6.33}$$

where Φ^n is the current time step. We obtain the final value at the next time step (Φ^{n+1}) as the linear combination of these intermediate results using the b_j weights:

$$\Phi^{n+1} = \Phi^n + \Delta_t \sum_{j=1}^{s} b_j \mathcal{R}(\Phi^{RK,j}). \tag{6.34}$$

The implemented three-stage second-order RK method is a low-storage scheme [198], which means that the number of stages that have to be stored is reduced. In this particular case only two arrays are needed: one for the current time step, and one more for the new stage that we can continuously overwrite because every new stage only depends on the previous one:

$$\begin{aligned} \Phi^{RK,1} &= \Phi^n + \frac{1}{3}\Delta_t \mathcal{R}(\Phi^n), \\ \Phi^{RK,2} &= \Phi^n + \frac{1}{2}\Delta_t \mathcal{R}(\Phi^{RK,1}), \\ \Phi^{n+1} &= \Phi^n + \Delta_t \mathcal{R}(\Phi^{RK,2}). \end{aligned} \tag{6.35}$$

This is a substantial benefit considering the memory requirements and the typical size of a grid applied in an LES.

Stability Knowing the discretized algebraic system we can evaluate the maximum possible time step using two important parameters, the Courant number [44] $\mathcal{C}$ and the diffusion number $\mathcal{D}$:

$$\mathcal{C} = \frac{u\Delta_t}{\Delta_x} \qquad\qquad \mathcal{D} = \frac{\Gamma\Delta_t}{\rho\Delta_x^2}, \tag{6.36}$$

where Δ_x is the grid size. In order to maintain stability (to avoid any unphysical behavior leading to divergence), these numbers must not exceed certain upper limits which depend on the applied time integration scheme [55; 83]. Künne derived the stability limits corresponding to the applied Runge-Kutta scheme [107]:

$$|\mathcal{C}| \leq 1.73 \qquad\qquad 0 \leq \mathcal{D} \leq 0.63. \tag{6.37}$$

6.1.6 Pressure Correction

We have obtained the discretized form of the system of governing equations in the previous sections. This should theoretically make it possible to calculate the time evolution of all the variables of interest. However, the system lacks an independent equation for the pressure. This poses some difficulties since the pressure gradient contributes to the momentum equations (note that only the gradient is of significance, the absolute pressure does not appear), therefore if we simply used the pressure from the previous step for the integration of the momentum equations, the obtained velocities would not satisfy the continuity equation.

In compressible flows the continuity equation can be used to calculate the density, then the pressure can be easily determined with the equation of state. This is not the case for incompressible flows for which the mass conservation is more of a kinematic constraint on the velocity field than a dynamic equation. We need to introduce a pressure correction term and to derive a pressure correction equation to be solved for this crucial variable [55].

The procedure implemented in FASTEST for this purpose is a so-called fractional step projection method using the low Mach number approximation introduced by Chorin [39].

In the first step we predict the momentum using the explicit RK stage and the variable values from the previous stage:

$$(\bar{\rho}\tilde{u}_j)^{*,RK,i} = (\bar{\rho}\tilde{u}_j)^n + \alpha_i\Delta_t\left(H^{RK,i-1} - \frac{\partial\bar{p}^{RK,i-1}}{\partial x_j}\right), \tag{6.38}$$

where the convective and diffusive terms are grouped together and denoted by H for the sake of brevity. Then a $(\bar{\rho}\tilde{u}_j)'$ momentum correction is introduced in order to satisfy the continuity equation:

$$(\bar{\rho}\tilde{u}_j)^{RK,i} = (\bar{\rho}\tilde{u}_j)^{*,RK,i} + (\bar{\rho}\tilde{u}_j)'. \tag{6.39}$$

The corresponding corrected pressure is defined as

$$\bar{p}^{RK,i} = \bar{p}^{RK,i-1} + \bar{p}'. \tag{6.40}$$

The governing equation for corrected momentum is

$$(\bar{\rho}\tilde{u}_j)^{RK,i} = (\bar{\rho}\tilde{u}_j)^n + \alpha_i \Delta_t \left(H^{RK,i-1} - \frac{\partial \bar{p}^{RK,i-1}}{\partial x_j} - \frac{\partial \bar{p}'}{\partial x_j} \right). \tag{6.41}$$

We can derive the relation between the momentum correction and the pressure correction by subtracting equation (6.38) from equation (6.41) and applying the (6.39) formula:

$$(\bar{\rho}\tilde{u}_j)' = -\alpha_i \Delta_t \frac{\partial \bar{p}'}{\partial x_j}. \tag{6.42}$$

Let us rewrite now the continuity equation using the (6.39) correction!

$$\frac{\partial \bar{\rho}}{\partial t} + \frac{\partial}{\partial x_j}(\bar{\rho}\tilde{u}_j)^{*,RK,i} + \frac{\partial}{\partial x_j}(\bar{\rho}\tilde{u}_j)' = 0, \tag{6.43}$$

from which we can directly obtain the final form of the Poisson-equation for the pressure correction by using equation (6.42):

$$\frac{\partial}{\partial x_j}\left(\frac{\partial \bar{p}'}{\partial x_j}\right) = \frac{1}{\alpha_i \Delta_t}\left(\frac{\partial \bar{\rho}}{\partial t} + \frac{\partial}{\partial x_j}(\bar{\rho}\tilde{u}_j)^{*,RK,i}\right). \tag{6.44}$$

This equation is discretized in accordance with the discretization techniques discussed in the previous sections, which leads to the following relation between the pressure correction and the mass defect within a single control volume:

$$\sum_c \left(\frac{\partial \bar{p}'}{\partial x_j} n_i\right)\Big|_c \delta S_c = \frac{1}{\alpha_i \Delta_t} \underbrace{\left(\left.\frac{\partial \bar{\rho}}{\partial t}\right|_P \delta V + \sum_c \left(\left((\bar{\rho}\tilde{u}_j)^{*,RK,i} n_j\right)\Big|_c \delta S_c\right)\right)}_{\epsilon_{\dot{m}}}, \tag{6.45}$$

where $\epsilon_{\dot{m}}$ is the mass defect. Considering all control volumes we can build an algebraic system $\mathbf{A}\mathbf{p}' = \mathbf{b}$ for the pressure correction which is solved in FASTEST with the iterative strongly implicit procedure of Stone [177]. An incomplete lower and upper triangular matrix decomposition (ILU) is applied, which takes advantage of $\mathbf{A}$ having non-zero elements only on the diagonals corresponding to the neighboring cells. The solver performs a given number of inner iterations to obtain the pressure correction. This pressure correction is then used to calculate the momentum correction according to Eq. (6.42). Finally we calculate the mass defect to check whether the continuity equation is fulfilled. If $\epsilon_{\dot{m}}$ is lower than a certain proportion of the mass flux incoming into the computational domain, then convergence is obtained. Otherwise the iteration procedure continues with the next loop of inner iterations.

6.1.7 Initial and Boundary Conditions

The problem definition is not complete without prescribing initial and boundary conditions, which are required for obtaining a unique solution. Regarding the flow field, initial conditions are of minor importance as a steady state solution is independent of them by

definition and a transient problem also becomes independent after a sufficient amount of physical time. Consequently the only requirement is that the initial conditions should allow the numerical scheme to converge. The case of reacting flows is slightly different because the mixture usually needs to be ignited 'manually' in order to stabilize the flame. To achieve this goal, in this work we set the scalar field in a predefined region to its chemical equilibrium value.

We need to provide the boundary conditions at inlets, outlets, and walls:

1. **Inlet**

   At inlets values are directly set, in other words the *Dirichlet* boundary condition is applied. For the temperatures and the species mass fractions constant values are provided but one needs to pay attention to setting the inlet velocities. Ideally an appropriate portion of the upstream geometry should be included to ensure that the incoming flow field is already developed. In LES the time required by the simulation is a major concern. Therefore those parts of the geometry that are not targeted by the given simulation (for example the pipe leading to the intake port of a cylinder in an internal combustion engine) are usually omitted. In order to still achieve physically correct results despite this kind of simplification, we have to model the effects of these omitted parts. One way to do this is to prescribe known velocity profiles and, if necessary, to add spatially and temporally correlated velocity fluctuations to create an artificial turbulent inflow. In this work we use the turbulent inflow generator developed by Klein [100], which requires the turbulent length and time scales as input parameters.

2. **Outlet**

   At the outlet boundaries *von Neumann* boundary conditions are set: in the boundary normal direction the gradients of the variables of interest are set to zero. This implies that the value of each unknown variable in the center of the CV located at the domain boundary is equal to its value on the face that is part of the actual boundary. We apply this treatment to all the variables in this work except for the velocity component normal to the boundary which needs special attention once again.

   It has been observed that setting the aforementioned velocity gradient to zero introduces instabilities in the form of pressure fluctuations. We can avoid these instabilities by computing the velocity normal component with the convection equation [162]

   $$\frac{\partial u_n}{\partial t} + U_c \frac{\partial u_n}{\partial n} = 0, \tag{6.46}$$

   where U_c is a characteristic convection velocity which must be provided. Usually a uniform bulk velocity is sufficient but in certain cases setting a profile can be helpful (for example a Gaussian profile was needed for jet flows).

   However, simply calculating the outlet normal velocity is not enough because it would not ensure mass conservation. For this end within an incompressible context the velocity has to be scaled by the mass fluxes. The preliminary mass flux exiting

the domain is

$$\dot{m}^*_{out} = \int_S \rho u^*_n \mathrm{d}S_{outlet}. \tag{6.47}$$

$\dot{m}^*_{out}$ does not equal the exact mass flux, which can be calculated by taking into account the inlet boundary condition and the density change in the domain due to chemical reactions:

$$\dot{m}_{out} = \int_S \rho u_n \mathrm{d}S_{inlet} - \int_V \frac{\partial \rho}{\partial t} \mathrm{d}V_{domain}. \tag{6.48}$$

In light of these mass fluxes the appropriate normal velocity component can be obtained with the following simple scaling:

$$u_n = u^*_n \frac{\dot{m}_{out}}{\dot{m}^*_{out}}. \tag{6.49}$$

It has to be pointed out that the correction is usually small, in the order of $1 \pm \mathcal{O}(10^{-4})$ [107].

3. **Wall**

   On walls von Neumann boundary conditions are applied to species mass fractions while the temperature value is usually directly set. For kinematic reasons the velocity component normal to the wall is set to zero and the tangential component is set to the desired wall velocity.

4. **Symmetry**

   It is not uncommon that the computational domain is not bordered by walls but remains open. In these cases usually a symmetry boundary condition is prescribed. This means that the gradients of all scalars are set to zero in the boundary normal direction except for the normal velocity component which still has to obey the kinematic conditions, therefore it equals zero in this case, too.

   It has to be emphasized that different boundary conditions can be set for different variables. For example an adiabatic wall can be realized by setting a wall condition for the velocity but a symmetry condition for the temperature.

6.2 Simulated Annealing

The general procedure of applying the technique of simulated annealing (hereinafter: SA) to setting the statistical moments of the sample set has already been outlined in section 5.3.3. However, the details of the implementation regarding the numerics have not been described yet. In this section we investigate these finer details to make the calculation as quick and effective as possible. This is crucial since a sample set has to be generated for each individual cell, therefore a slow SA algorithm would make the application of the CSSA approach unfeasible when it comes to realistic configurations.

In order to identify the bottlenecks and the key parameters, let us have a look at a specific example. Let us generate a set of 100 samples with the following parameters: $\widetilde{y_1} = 0.15$, $\widetilde{y_2} = 0.5$, $\widetilde{{y_1}''^2} = 0.01$, $\widetilde{{y_2}''^2} = 0.1$, and the expected correlation coefficient is $R_{12}^{exp} = 0.3$ in the first, and $R_{12}^{exp} = 0.6$ in the second case. Hereinafter when we use the term 'correlation' we refer to the correlation coefficient unless it is explicitly stated otherwise.

In both cases the calculation starts from the initial configuration depicted in figure 6.4a. Here the univariate samples are randomly organized into pairs to define points in the two-dimensional parameter space, consequently the correlation of the two random variables is close to 0. The SA algorithm is applied to set the correlation to either 0.3 or 0.6. The final sample sets are plotted in Figure 6.4b and 6.4c respectively.

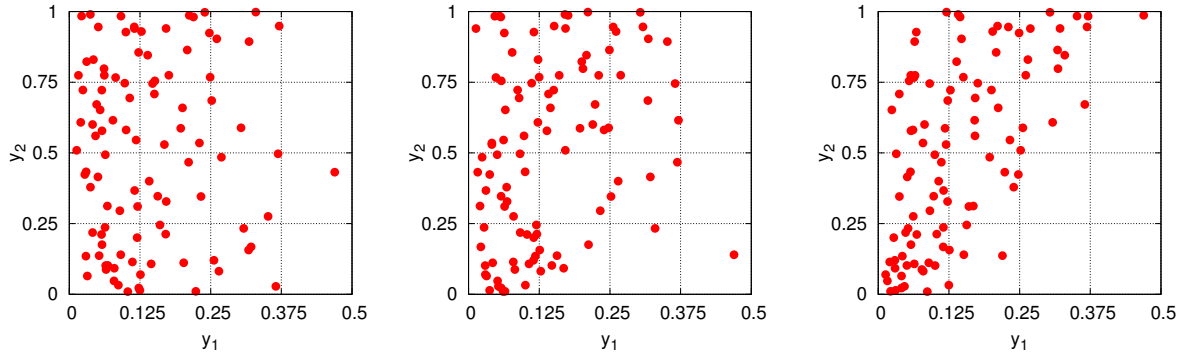

(a) $R_{12} \approx 0$ **(b)** $R_{12} \approx 0.3$ **(c)** $R_{12} \approx 0.6$

Figure 6.4: Sets of 100 samples with the following parameters: $\widetilde{y_1} = 0.15$, $\widetilde{y_2} = 0.5$, $\widetilde{{y_1}''^2} = 0.01$, $\widetilde{{y_2}''^2} = 0.1$. (a) is the initial random set with 0 correlation; (b) is the final set with the correlation of 0.3 and (c) is the final set with the correlation set to 0.6.

The algorithm could reach the desired correlations but there is a significant difference between the two cases: the number of steps required. Both the error of the correlation and the artificial temperature are plotted as functions of the steps taken in Figure 6.5. While the algorithm concluded after 296 steps when the expected correlation was 0.3, it took 13052 steps to set the correlation to 0.6.

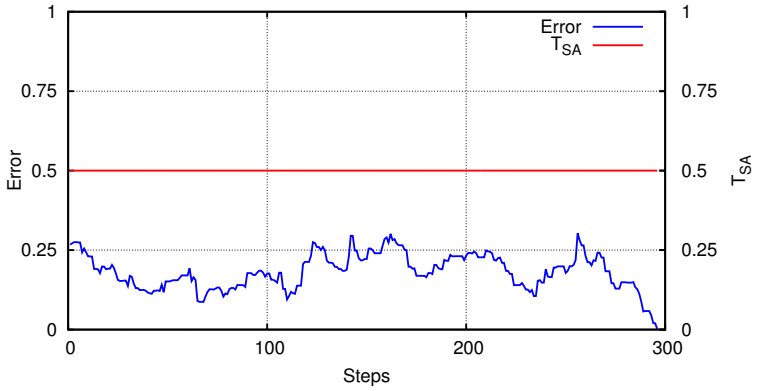

(a) $R_{12}^{exp} = 0.3$

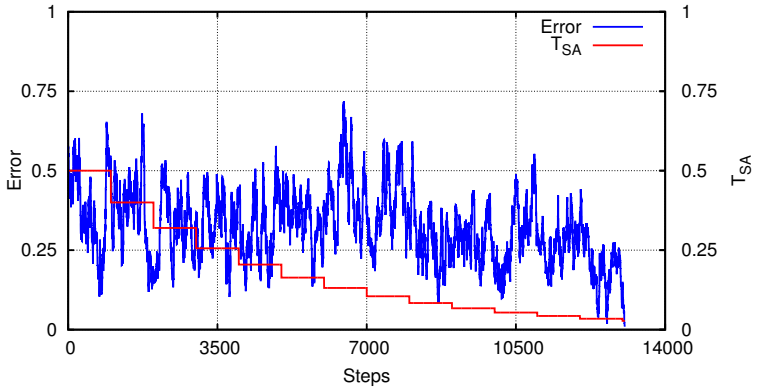

(b) $R_{12}^{exp} = 0.6$

Figure 6.5: Error and artificial temperature as a function of steps taken during simulated annealing. $\widetilde{y_1} = 0.15$, $\widetilde{y_2} = 0.5$, $\widetilde{y_1''^2} = 0.01$, $\widetilde{y_2''^2} = 0.1$, (a) $R_{12}^{exp} = 0.3$; (b) $R_{12}^{exp} = 0.6$.

This single example properly illustrates the need for optimization. Apparently - in accordance with intuition - it is quicker to set correlations that are closer to 0 since it means that the final configuration is closer to the initial random one, therefore fewer swaps are needed to reach it. The question arises: should we be worried about such high correlation values as 0.6? Do these values occur during the simulations of real systems? To answer these questions, let us have a look at the correlation between the mixture fraction and the reaction progress variable in the bluff-body case described in detail in Section 8.2. The correlation values are depicted in Figure 6.6.

It is obvious that the absolute value of the correlation is higher than 0.6 (even than 0.9) in most parts of the domain of interest. Therefore optimizing for setting the correlation to high absolute values ($|R_{12}^{exp}| > 0.6$) is indeed necessary. It is also worth noting, that the correlation changes significantly in the exact same zones where the source term is the largest: where the chemical reaction takes place. This is not surprising considering the structure of a non-premixed flame. If we approach the flame front from the fuel-rich-side, the mixture fraction decreases due to mixing while the reaction progress variable increases due to the ongoing chemical reaction at the flame front; the correlation between them is negative. After we leave the flame front towards the oxidizer-rich-side both

the mixture fraction and the reaction progress variable decrease which yields a positive correlation.

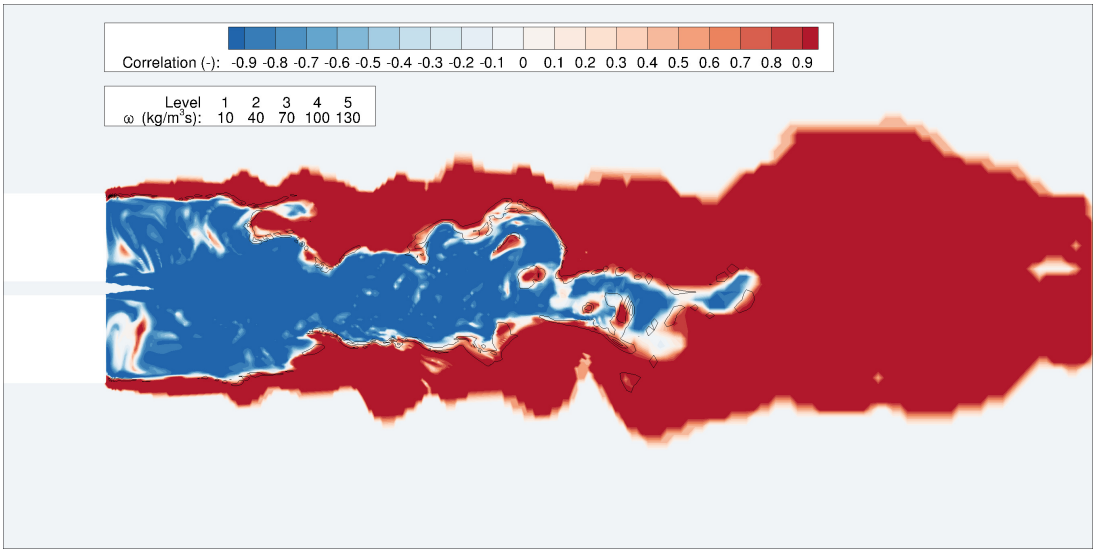

Figure 6.6: Two-dimensional cut of the bluff-body case (detailed description in Section 8.2). The colors represent the correlation between the mixture fraction and the reaction progress variable, while the isolines depict the source term of the reaction progress variable.

These brief considerations leave us with three key points to address in this section regarding optimization:

1. **Stop conditions** - What if the expected correlation cannot be set within a reasonable number of steps? When should the calculation stop?
2. **Initial configuration** - Is there a way to set different initial configurations for different expected correlations?
3. **Annealing schedule** - How should the artificial temperature be set and how should it be changed during the calculation?

6.2.1 Stop conditions

First we have to make sure that the algorithm eventually concludes and that it does not enter an infinite loop even if the expected correlation cannot be set. We could set a fixed upper bound for the number of possible iterations, but this would not be an efficient solution since it would not take into consideration whether the iteration was heading in the right direction when it was stopped or it got stuck thousands of steps earlier. In our implementation (Algorithm 1) we adopted the solution of Charmpis and Panteli [36], which works with two nested loops and five parameters. In the pseudocode we introduced the following notation: $\boldsymbol{y_2}$ shall denote the ordered set of univariate samples $[y_2^{\pi(i)}]_{i=1,\dots,N}$, where π is a permutation of the indices $1, \dots, N$.

The key element of this implementation is that the algorithm stops after α outer iterations in which the solution has not been improved and the algorithm is 'frozen', which means

that the ratio of accepted swaps is below γ. Based on the recommendations of Charmpis and Panteli [36] after some tuning we set $\gamma = 0.02$, $\alpha = 10$, $\beta = 5$ and $\delta = 0.8$. T_0 is worth further examination which takes place in Section 6.2.3.

Algorithm 1 Simulated Annealing

procedure INITIALIZATION
  $\boldsymbol{y}_2^{best} = \boldsymbol{y}_2$
  $T_{SA} = T_{SA}^0$
  $i_{out} = 0$
  E_{tol} is set ▷ The accuracy with which we would like to match R_{12}^{exp}
end procedure
procedure ITERATION
  while $i_{out} \leq \alpha$ **do** ▷ Outer Loop
    for $i_{in} = 1, \beta \cdot N$ **do** ▷ Inner Loop
      Compute $\boldsymbol{y}_2^{new}$ by swapping 2 elements of $\boldsymbol{y}_2$
      Calculate the new error: $E^{new} = |R_{12}^{new} - R_{12}^{exp}|$
      Calculate the change of error: $\Delta E = E^{new} - E$
      if $\Delta E \leq 0$ **then**
        $\boldsymbol{y}_2 = \boldsymbol{y}_2^{new}$ and $E = E^{new}$
      else
        $\boldsymbol{y}_2 = \boldsymbol{y}_2^{new}$ and $E = E^{new}$ with probability $P(\Delta E) = \exp(-\Delta E / T_{SA})$
      end if
      if $E < E_{tol}$ **then**
        $\boldsymbol{y}_2^{best} = \boldsymbol{y}_2$ and exit calculation
      end if
    end for
    if percentage of accepted moves in for-loop $< \gamma$ **then** $i_{out} = i_{out} + 1$
    if $E(\boldsymbol{y}_2) < E(\boldsymbol{y}_2^{best})$ **then**
      $\boldsymbol{y}_2^{best} = \boldsymbol{y}_2$ and $i_{out} = 0$
    end if
    $T_{SA} = \delta \cdot T_{SA}$
  end while
end procedure
$\boldsymbol{y}_2^{best}$ is the optimum rearrangement

6.2.2 Initial Configuration

We have already shown that starting the SA algorithm from a random sample set, for which $R_{12} \approx 0$, is not practical when R_{12}^{exp} is of a high absolute value ($|R_{12}^{exp}| > 0.5$) because reaching this value needs many coordinate swaps (see Section 6.2). The number of necessary steps could be reduced if we set the initial sample set in a way that its correlation is closer to R_{12}^{exp}.

Let us consider the univariate random variables $[y_1^i]_{i=1,\dots,N}$ and $[y_2^i]_{i=1,\dots,N}$. The theoretical maximum and minimum correlation between these variables can be realized by sorting y_1^i in ascending order ($\hat{y}_1^i \leq \hat{y}_1^j$ when $i < j$) and y_2^i in either ascending or descending order before we create the points $[\hat{y}_1^i; \hat{y}_2^i]_{i=1,\dots,N}$ in the parameter space yielding the theoretical maximum (R_{12}^{max}) and theoretical minimum (R_{12}^{min}) correlation respectively for the given set of random variables.

This means that after any steps of the SA process the actual R_{12} will be in the $[R_{12}^{min}; R_{12}^{max}]$ interval. When R_{12}^{exp} is outside of this interval, for example $R_{12}^{max} < R_{12}^{exp} \leq 1$, running the SA algorithm becomes unnecessary: we can immediately use the sorted samples as the closest possible approximation of R_{12}^{exp}. Following this logic let us use the following initial sample sets:

- $|R_{12}^{exp}| < 0.5$: use the initial random sample
- $R_{12}^{exp} < -0.5$: use the sorted samples corresponding to R_{12}^{min}
- $R_{12}^{exp} > 0.5$: use the sorted samples corresponding to R_{12}^{max}

These choices ensure that even if $|R_{12}^{exp}|$ is large the initial set has a correlation that is closer to R_{12}^{exp} than it would be if we simply used the initial random sample set as a starting point.

We can carry out the sorting efficiently using the *heapsort* algorithm [154] thereby only slightly increasing the computational cost while there is much more to gain: in Figure 6.7 we can observe the exact same process as in Figure 6.5b except for this time we sorted the initial sample depicted in Figure 6.4a before starting the SA algorithm. The number of necessary steps has decreased with orders of magnitude.

However, having run the same calculation multiple times we observed that sometimes the algorithm concluded without having set R_{12} to R_{12}^{exp}. Figure 6.8 illustrates one of these cases. We can see that in certain steps the error increased significantly which tells us that we were too permissive when we evaluated the steps that temporarily led to more disadvantageous sets. In order to overcome this issue and to let the system 'cool down', using the annealing analogy introduced in Section 5.3.2, we need to investigate the effect of the artificial temperature, which controls the probability of accepting the steps yielding these jumps in the error.

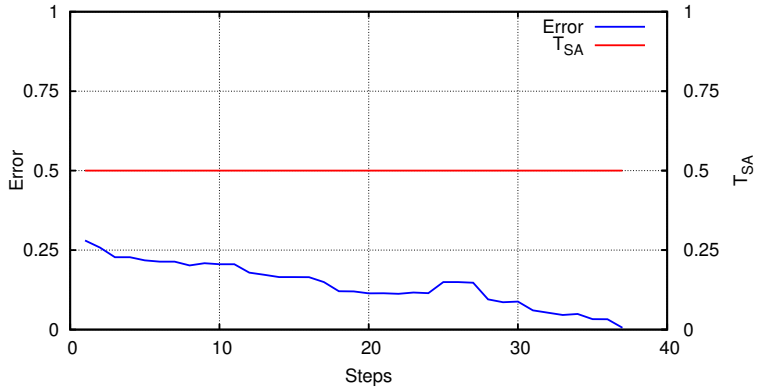

Figure 6.7: Error and artificial temperature as a function of steps taken during SA. $\widetilde{y_1} = 0.15$, $\widetilde{y_2} = 0.5$, $\widetilde{y_1''^2} = 0.01$, $\widetilde{y_2''^2} = 0.1$, R_{12}^{exp} is 0.6, the initial random samples were sorted before the SA algorithm started.

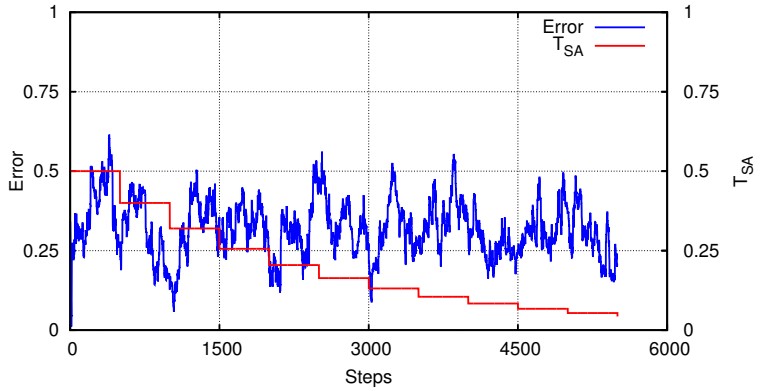

Figure 6.8: Error and artificial temperature as a function of steps taken during an unsuccessful run of SA. $\widetilde{y_1} = 0.15$, $\widetilde{y_2} = 0.5$, $\widetilde{y_1''^2} = 0.01$, $\widetilde{y_2''^2} = 0.1$, R_{12}^{exp} is 0.6, the initial random samples were sorted before the SA algorithm started.

6.2.3 Annealing Schedule

We have to set two parameters in order to define the annealing schedule: the T_{SA}^0 initial artificial temperature and the δ cooling parameter. The cooling parameter controls how the temperature is reduced between two outer iterations described in Algorithm 1. We chose to use $\delta = 0.8$ as it was discussed in Section 6.2.1.

When swapping the coordinates of two points in the parameter space increases the error function with ΔE, the artificial temperature controls the probability of accepting this new configuration: $P(\Delta E) = \exp(-\Delta E/T_{SA})$. The smaller T_{SA} is, the more unlikely it is that we accept the new configuration. Consequently a lower initial temperature would allow for smaller increases in the error function. On one hand it could lower the number of necessary steps, on the other hand it could increase the chance of the solution getting stuck in a local minimum and not matching the expected correlation value in the end. We carried out a parameter study to strike a balance and find an optimal T_{SA}^0.

We used an actual simulation of the bluff-body case described in details in Section 8.2 to

extract a representative ensemble of control variables with their first and second statistical moments. Then we tried to generate for each case a sample set representing the corresponding joint PDF while using different T_{SA}^0 values. The same calculation was repeated a thousand times without changing any parameters. The average number of necessary iteration steps in the SA algorithm (n_{it}) and the η percentage of successful iterations (meaning that the expected correlation has been reached) are shown in Figure 6.9a as functions of T_{SA}^0 and the N number of samples.

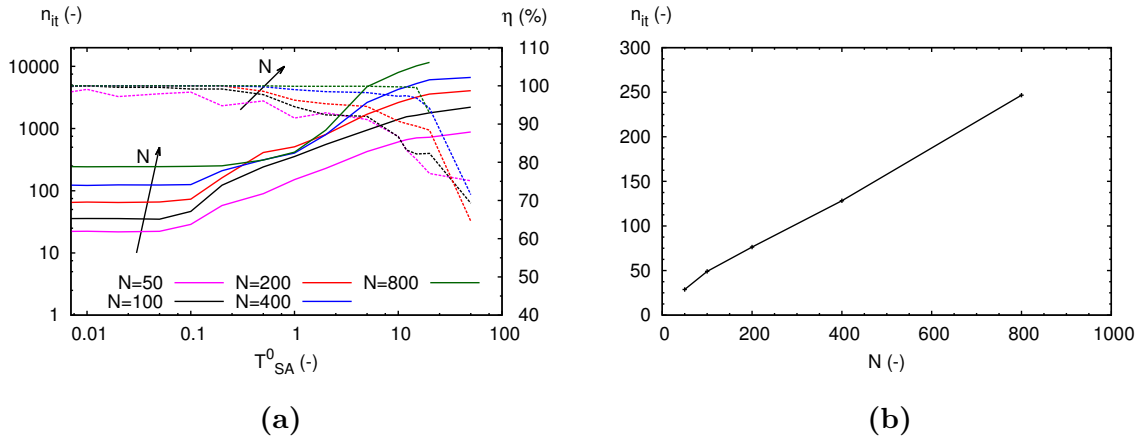

Figure 6.9: (a) The average number of iteration steps (n_{it} - solid line) and the percentage of successful iterations (η - dashed line), meaning that the expected covariance could be set, as a function of the T_{SA}^0 parameter. (b) The average number of iteration steps as a function of the N number of samples for $T_{SA}^0 = 0.1$.

The critical T_{SA}^0 above which the number of necessary iterations increases rapidly while the rate of successful iterations decreases was found to be relatively independent of N. Based on these results T_{SA}^0 was chosen to be 0.1 in this work. It is also noteworthy that $N = 50$ was insufficient for setting the correlations properly every time even at low T_{SA}^0 values, therefore $N = 100$ seems to be an appropriate choice for further calculations. Striking a balance between accuracy and computational costs by choosing N is important as according to Figure 6.9b the latter increases linearly with the number of samples.

These optimization considerations have sped up the algorithm considerably. The average number of necessary iteration steps has been lowered by two orders of magnitude to 10-50 depending on the actual moments. This major reduction is of two orders of magnitude which obviously cannot be improved significantly by further adjustments considering the already very low value of n_{it}.

6.3 Basic Test Configurations

In the preceding sections we have investigated the SA algorithm with respect to the numerics: the key parameters have been identified and optimized. In this chapter we start testing the entire CSSA method. We will especially scrutinize the treatment of the density as it often introduces instabilities through the continuity equation. Therefore we need to investigate variable-density flows. The following three basic one-dimensional configurations have been selected:

- one-dimensional density wave,
- one-dimensional premxied flame,
- one-dimensional stratified premixed flame.

The results obtained with the CSSA model are compared to reference solutions, which provides insights regarding the appropriate treatment of the density. Based on the conclusions we will manage to arrive to the final form of the CSSA model, which will be validated and applied to more complex configurations in the following chapters.

6.3.1 One-Dimensional Density Wave

Our intention is to evaluate the control variables one-by-one therefore first we focus on the mixture fraction. The first case is of pure mixing, consequently the progress variable is constant throughout the process. A strong density variation is created in a form of a density wave which propagates through the one-dimensional domain with a constant velocity.

We apply different boundary conditions to investigate the interaction between the mixture fraction and the enthalpy. In the first case the entire system is adiabatic, the temperature is constant, while in the second case we establish three zones: an adiabatic, a preheating, and a cooling one. This is a standard configuration when it comes to testing a new numerical scheme. It has been used multiple times in previous works related to FASTEST [17; 107; 131; 193], however, contrary to some of them we do not neglect the diffusion term.

In this case the correlation of the control variables cannot be set during the calculation since the progress variable is constant. Our objective is to evaluate the table access of the CSSA method and to estimate the effect of the stochastic contribution which emerges from having a finite number of random samples representing the joint PDF in each cell. We generate the reference solutions with the simple FGM-1M approach because the implementation of that method in FASTEST has been thoroughly investigated and validated in previous studies.

6.3.1.1 Description of Configuration

FASTEST applies a finite volume method, therefore our one-dimensional calculation is actually a quasi-one-dimensional one using $384 \times 1 \times 1$ control volumes in the x, y, z directions respectively. The domain has a length of 100 mm in physical space and it is homogeneously filled with a methane-air mixture. The initial temperature of this mixture is T_0, the density is ρ_0 and the mixture fraction is $\mathcal{Z}_0 = 0.05$. We chose to use a non-zero mixture fraction in order to move away from the edge of the chemistry table where the temperature is fixed for $\mathcal{Z} = 0$ and errors are more prevalent [107].

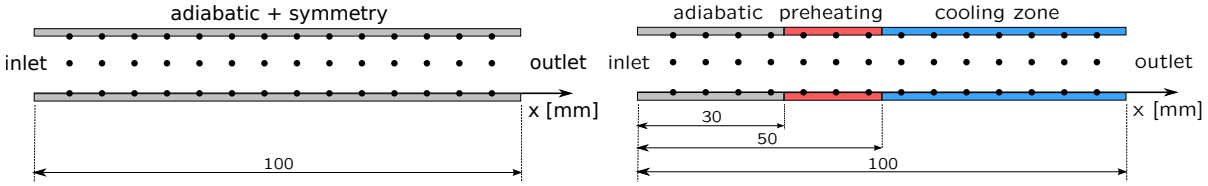

(a) Adiabatic boundary conditions (*D1*) **(b)** Non-adiabatic boundary conditions (*D2*)

Figure 6.10: Configuration of the one-dimensional density wave case. In the x direction not all the 384 computational nodes are depicted. (a) Adiabatic case, the temperature is kept at T_0. (b) The domain is split into three zones: an adiabatic zone, a preheating zone with T_h temperature, and a cooling zone with a temperature of T_c. In both cases, symmetry boundary condition is applied to the velocity.

	$\#cells$ (-)	L (mm)	Δx (mm)	u (m/s)	$\mathcal{Z}_0, \mathcal{Z}_i$ (-)	T_0, T_i (K)	T_h, T_c (K)
D1	384	100	0.26	2	0.05, 0.1	330, 330	-
D2	384	100	0.26	2	0.05, 0.1	330, 330	500, 300

Table 6.1: Parameters of the simulated cases

At $t = 0\ s$ we introduce a more dense mixture of air and methane into the domain through the inlet with T_i temperature, ρ_i density, and $\mathcal{Z}_i = 0.1$ mixture fraction at a velocity of u_i. (The parameters are summarized in Table 6.1) A sharp edge between the two mixtures could lead to numerical instabilities therefore the following smoother profile is applied:

$$\mathcal{Z} = 0.05 + 2.5 \cdot 10^{-2} \left[1 - \tanh\left(\frac{t_{0.5} - t}{T_S}\right)\right], \tag{6.50}$$

where $t_{0.5}$ denotes the time required to increase $\mathcal{Z}$ with half of $\mathcal{Z}_1 - \mathcal{Z}_0$, T_S controls the shape of the slope ($T_S = 0.001$ is set and for $T_S = 0$ the sharp edge would be retained) and t is the current time. At the outlet zero-gradient boundary conditions are applied. We also have to set the boundary conditions at the walls. Two cases are set up in both of which we apply symmetry boundary condition to the velocity. However, in the first one (*D1*) we work with adiabatic conditions, while in the second one we split the domain into three zones according to Figure 6.10b: an adiabatic zone, a preheating zone with T_h temperature, and a cooling zone with T_c temperature. We apply 4000 time steps of $\Delta t = 10^{-5}\ s$ in all simulations.

6.3.1.2 Results

The results of *D1* calculated with the CSSA method compared to the reference solution obtained with FGM-1M are summarized in Figure 6.11. We can make two observations:

- The propagation of the density wave is captured properly. The results of the two methods show only minor differences in the densities and mixture fractions.
- Instabilities do appear. We can see that not only the curves representing ρ become 'hairy' due to fluctuations, but also the velocity shows unphysical behavior. Instead of being constant as it is supposed to be, non-physical jumps occur. This is unacceptable, therefore the phenomenon needs further investigation.

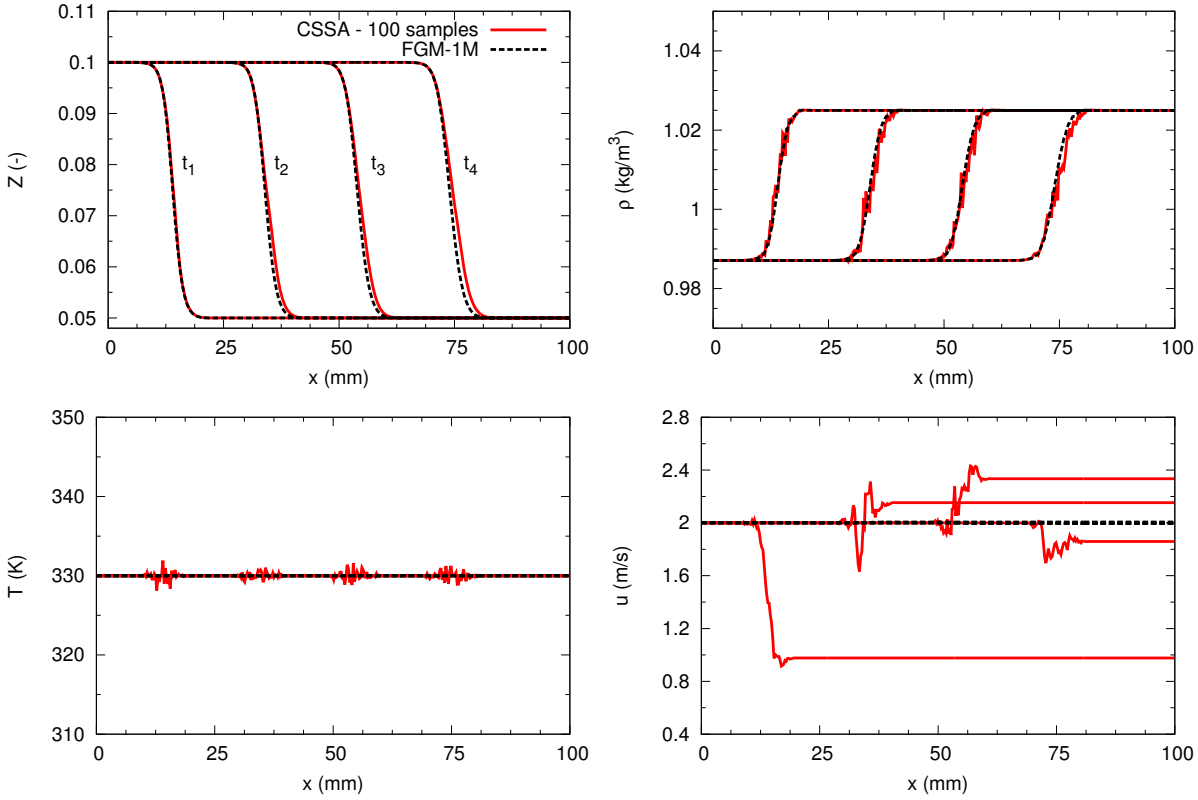

Figure 6.11: Results of the adiabatic simulation of the one-dimensional density wave at four different time instances ($t_1 = 10\ ms, t_2 = 20\ ms, t_3 = 30\ ms, t_4 = 40\ ms$): spatial distribution of the mixture fraction ($\mathcal{Z}$), the density (ρ), the temperature (T) and the velocity (u) obtained with either the FGM-1M method (black dotted line) or the CSSA method (red line).

First we have to admit that if we look at it closely even the FGM-1M solution shows negligible jumps in the velocity. The reasons are twofold. First, looking up and interpolating the thermochemical properties from the chemistry table necessarily introduces some uncertainties. Second, the integration of the scalar transport equations, which are written in a non-conservative form for the sake of stability, leads to a slight mass leakage. This is a known phenomenon and its magnitude is acceptable. However, the fluctuations corresponding to the CSSA solution are major ones. If we increase the number

of samples to 200 and 5000 we can see that the fluctuations gradually decrease and the solution converges to the FGM-1M solution (Figure 6.12). This indicates that the error is a stochastic one originating from not having a sufficient number of samples to represent the density. The density strongly depends on $\mathcal{Z}$ and the solution is very sensitive to it since the time and spatial derivatives of the density appear in the continuity equation. We generate separate sample sets for each individual cell, therefore the errors in neighboring cells are independent of each other and this could lead to incorrect gradient values as it is illustrated in Figure 6.13.

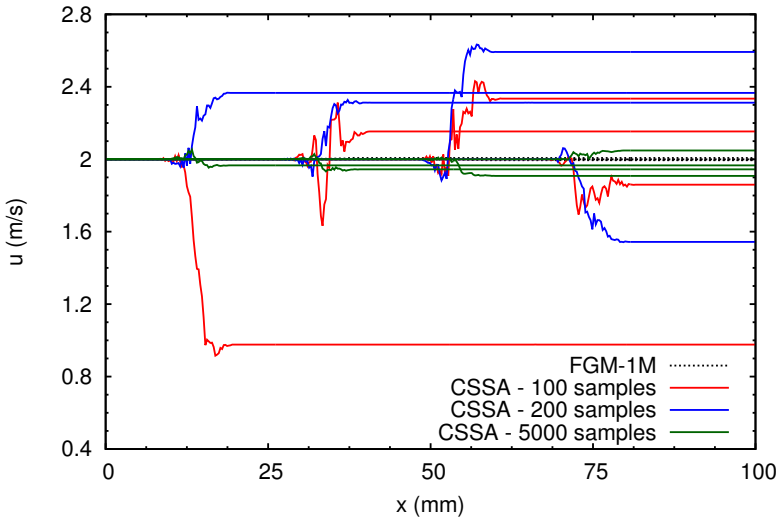

Figure 6.12: The spatial distribution of the velocity at four different time instances during the adiabatic simulation of the one-dimensional density wave. The four curves correspond to the the FGM-1M solution (black), the CSSA solution with 100 (red), 200 (blue) and 5000 (green) samples.

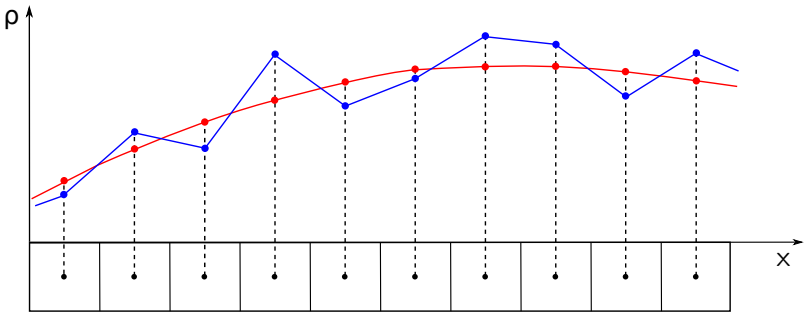

Figure 6.13: Samples are generated independently in every cell therefore the errors in representing the mean density are also independent. This leads to major errors in the gradient. The red curve depicts a smooth density profile calculated with the FGM-1M method while the blue curve illustrates what could happen when the errors in neighboring cells become independent of each other. The diagram serves illustration purposes and uses exaggerated deviations.

This is an important difference compared to the stochastic field method [17] where although errors of statistical nature do occur, for each field the neighboring cells are interconnected and the fields are smooth on their own in this sense. In that case only temporal fluctuations appear, which also exist in the CSSA context. Avdić [17] investigated several methods in an effort to reduce these fluctuations:

- smoothing the time derivative of the density [153],
- dynamic smoothing of the temporal change of the density using B-splines [102],
- Hodrick-Prescott filter for the density [84].

These methods cannot be applied in the CSSA context because fluctuations occur not only with respect to time but also to space. Smoothing the fluctuations of both nature would be computationally unfeasible.

As a consequence we overcome the problem by retaining the corresponding density from the chemistry table using only the respective mean control variables instead of the samples and the ensemble averaging, thereby connecting the densities in neighboring cells and consequently smoothing the derivatives. Results obtained with this modified procedure are depicted in Figure 6.14.

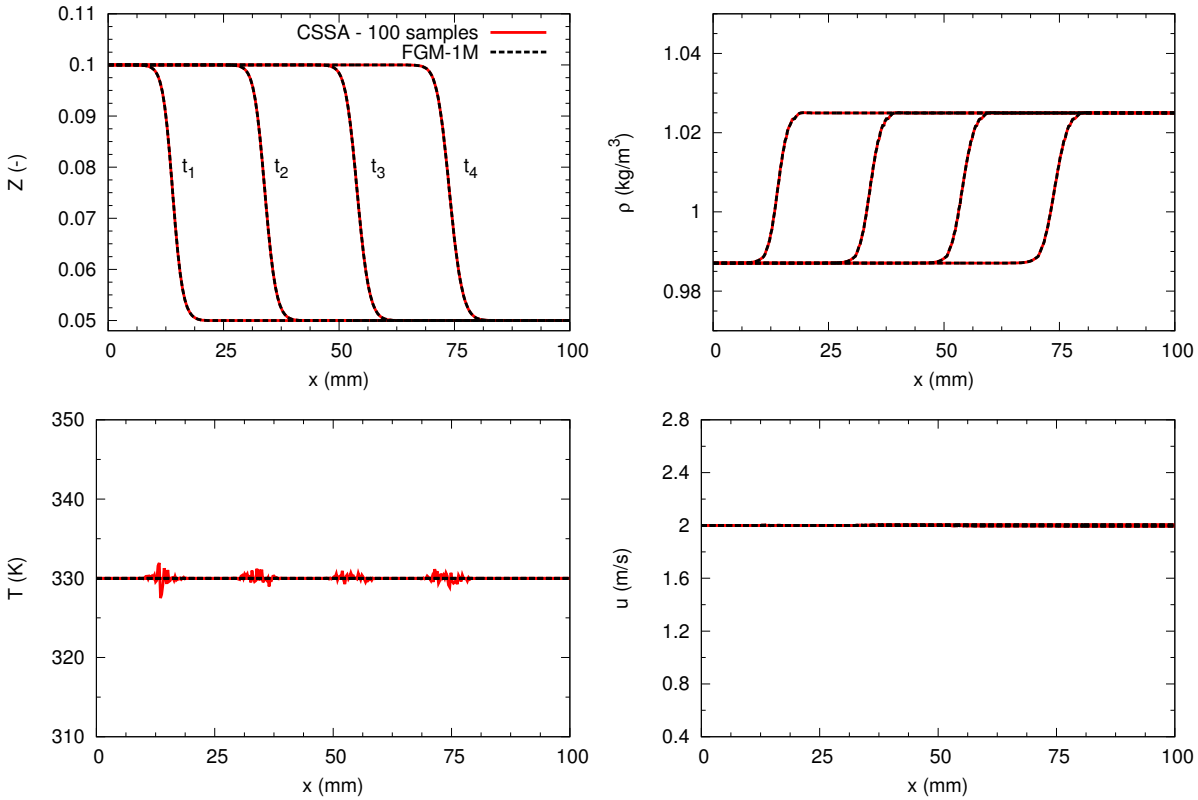

Figure 6.14: Results of the adiabatic simulation of the one-dimensional density wave at four different time instances ($t_1 = 10\ ms, t_2 = 20\ ms, t_3 = 30\ ms, t_4 = 40\ ms$): spatial distribution of the mixture fraction ($\mathcal{Z}$), the density (ρ), the temperature (T) and the velocity (u) obtained with either the FGM-1M method (black dotted line) or the CSSA method with the updated density treatment that only uses the mean values of the control variables when accessing the table (red line).

The CSSA and the FGM-1M results are in very good agreement indicating that we have correctly implemented the procedure regarding the mixture fraction. In the remaining part of this work we stick to the density treatment described in this section.

Figure 6.15 shows the results for the *D2* configuration. The profiles obtained with the FGM-1M and the CSSA method coincide confirming that the interaction of the mixture

fraction and the enthalpy with the momentum equation is implemented correctly as well as the process of accessing the chemistry table with the generated samples.

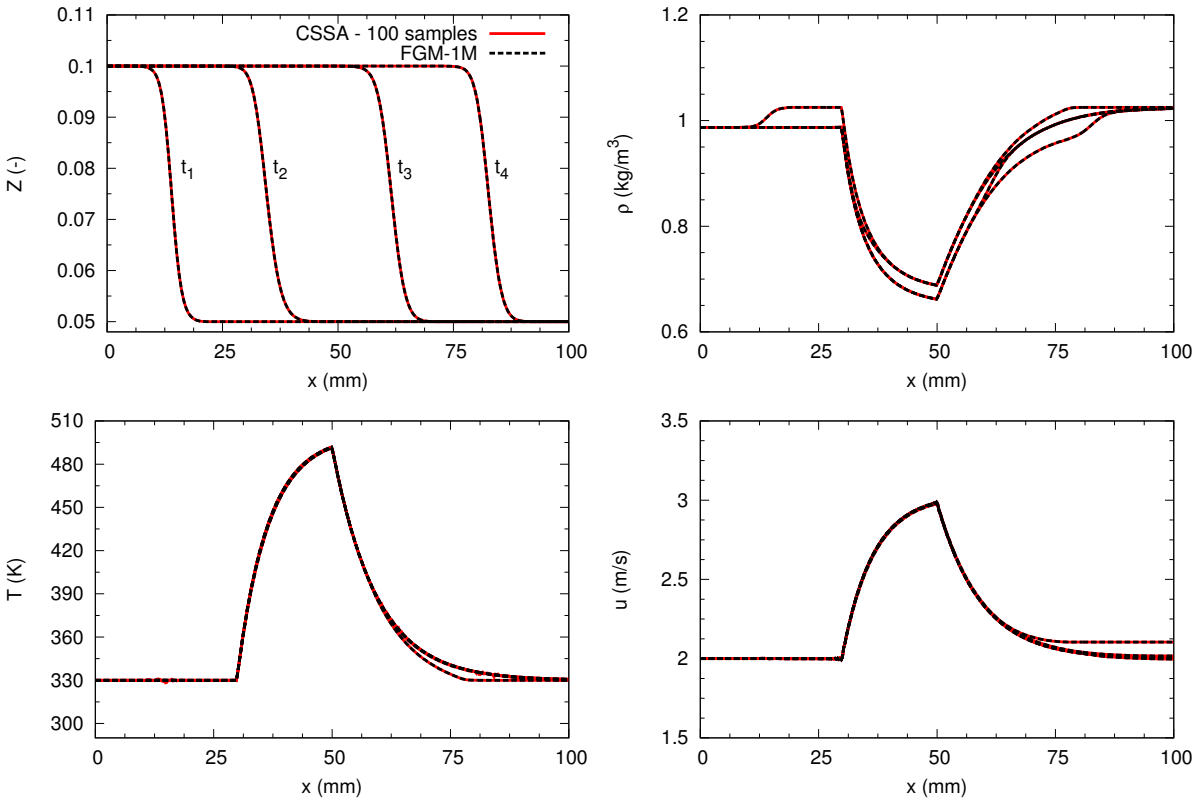

Figure 6.15: Results of the non-adiabatic simulation of the one-dimensional density wave at four different time instances ($t_1 = 10\ ms, t_2 = 20\ ms, t_3 = 30\ ms, t_4 = 40\ ms$): spatial distribution of the mixture fraction ($\mathcal{Z}$), the density (ρ), the temperature (T) and the velocity (u) obtained with either the FGM-1M method (black dotted line) or the CSSA method (red line).

6.3.2 One-Dimensional Premixed Flame

The focus of our attention now shifts from the mixture fraction to the progress variable: our next test case is a one-dimensional laminar premixed flame. A stoichiometric mixture of methane and air is ignited and the flame propagates through the domain. This means that the mixture fraction remains constant throughout the process while the progress variable changes as the mixture reaches a burnt state from the initial unburnt one. The complexity of the test case is greater than that of the density wave as our model has to accurately describe the flame structure and the propagation. Matching the laminar flame speed is of crucial importance for correctly predicting the flame position when describing more sophisticated combustion systems. This has major implications on the quality of results.

The result of a detailed chemistry calculation with CHEM1D will be used as a reference solution and we will also compare the CSSA solutions to the respective FGM-1M results. On coarser grids the results will also be compared to those obtained with the ATF method with a thickening factor of 4. With this test case we expect to verify that the treatment of the progress variable and the table access are correctly implemented in the CSSA context. We will also look for arising instabilities in connection with the flame propagation.

6.3.2.1 Description of Configuration

The physical length of our quasi-one-dimensional domain is constant: $L = 19.2\ mm$. The number of applied cells varies between 32 and 256 in order to provide insight about the grid dependence of the solution. The finest grid has a spacing of $\Delta_x = 0.075\ mm$ while the coarsest one is of $\Delta_x = 0.6\ mm$. At the inlet the stoichiometric mixture of methane and air enters the computational domain at the temperature of 300 K with a speed of either $u_i = 50\ cm/s$ or $u_i = 15\ cm/s$. These two values are chosen in a manner that lets us evaluate whether the calculated laminar flame speed depends on the boundary conditions. The laminar flame speed of the stoichiometric mixture under these conditions is 28.32 cm/s thus in the first case the flame will propagate towards the outlet as opposed to the second case when it will propagate against the flow. We apply symmetry boundary conditions to the sides of the domain.

6.3.2.2 Results - Flame Structure

We carried out simulations on grids of four different resolutions: $\Delta_x = 0.075, 0.15, 0.3$ and $0.6\ mm$ respectively. Figure 6.16 summarizes the results illustrating the temperature (T) and density (ρ) fields as well as the source term ($\dot{\omega}_{CO_2}$) and mass fraction of CO_2 (Y_{CO_2}). The inlet speed was $u_i = 50\ cm/s$.

Coarse grids with spacing above $0.15\ mm$ show significant deviations from the reference solution as the flame structure becomes not sufficiently resolved. However, on all grids the respective results obtained with the CSSA and the FGM-1M approach are almost identical. This should not come as a surprise considering that this is a laminar test case

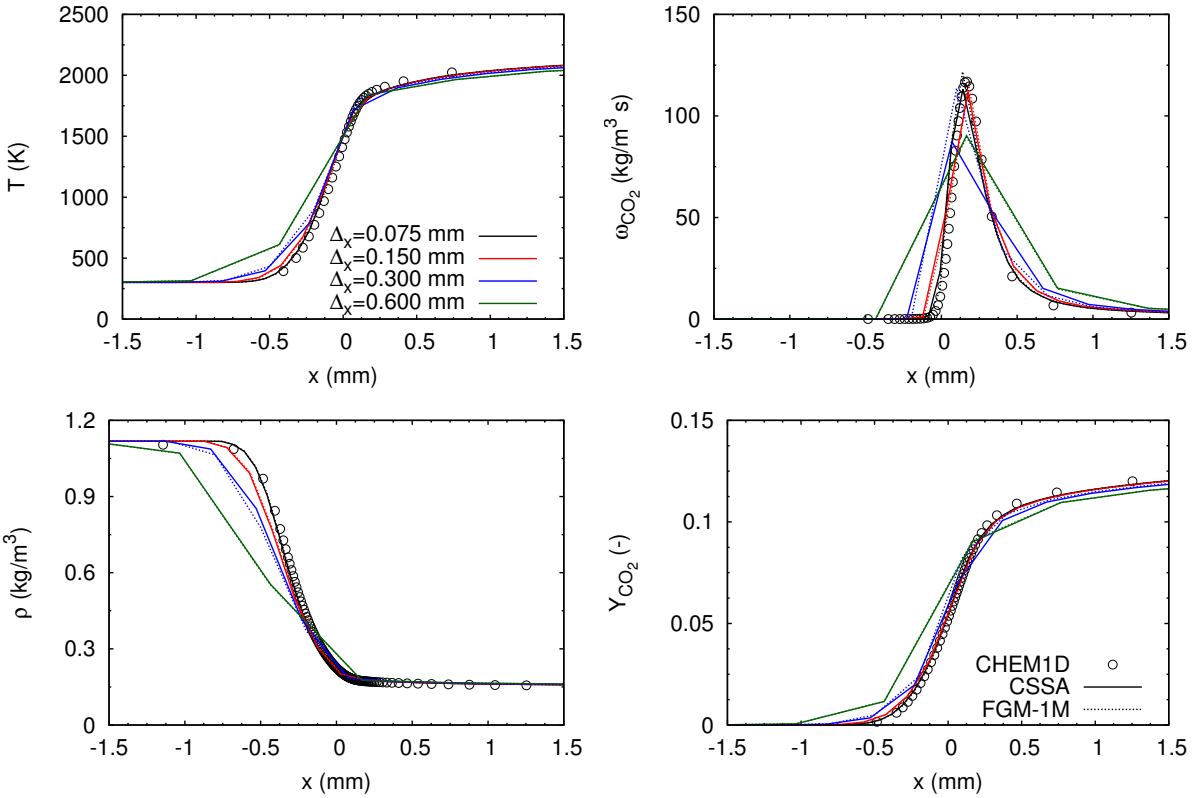

Figure 6.16: The flame structure represented by the temperature (T), the density (ρ), the CO_2 source term ($\dot{\omega}_{CO_2}$) and the CO_2 mass fraction (Y_{CO_2}) profiles obtained by 2 different techniques: the FGM-1M method (dashed line) and the CSSA method (continuous line). The reference solution (circles) was calculated with CHEM1D.

consequently the subgrid-scale fluctuations are negligible, especially on the fine grids. The results suggest that the table access is correctly implemented, but we need further test cases to look into the correlation of the mixture fraction and the progress variable. We also need to have a closer look at the propagation of the flame, which could reveal instabilities or temporal inaccuracies.

6.3.2.3 Results - Flame Propagation

In a detailed study Künne [107] showed that if the flame structure is not sufficiently resolved, numerical uncertainties start to dominate the flame propagation. This is an important finding since the flame structure becomes poorly predicted already at $\Delta_x \approx 0.17\ mm$. As a consequence the calculated flame speed is independent of neither the grid spacing nor the inlet speed. Furthermore, we can expect that the numerics specific to the CSSA method, such as the number of samples per cell, also have an effect on the calculated numerical flame speed, which will be denoted by $s_{l\Delta}$ while s_L refers to the correct laminar flame speed.

As we discussed in Section 3.2.2 $s_{l\Delta}$ can be and will be calculated in three different ways using the (3.17), (3.18) and (3.19) formulas. Figure 6.17 shows the results obtained on

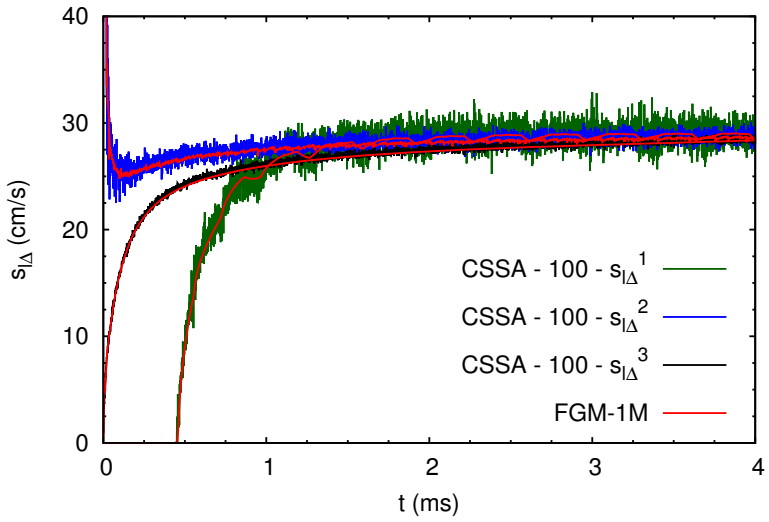

Figure 6.17: Numerical flame speeds calculated on a fine grid ($\Delta_x = 0.075\ mm$) using three different formulas: $s^1_{l\Delta}$ (3.17) - green; $s^2_{l\Delta}$ (3.18) - blue; and $s^3_{l\Delta}$ (3.19) - black. The red lines depict the respective numerical flame speeds of the reference solution obtained with the FGM-1M method.

a grid of $\Delta_x = 0.075\ mm$ with the inlet speed of $u_i = 50\ cm/s$. We can immediately notice that although the mean flame speeds are in accordance with the respective FGM-1M results, the calculated numerical flame speeds fluctuate, the level of which depends on the chosen flame speed definition. These fluctuations come from the stochastic errors introduced by the sampling technique, consequently we expect them to decrease when the number of samples is increased. This can be observed in Figure 6.18 where the calculated numerical flame speeds corresponding to a 100 and a 1000 samples per cell are depicted.

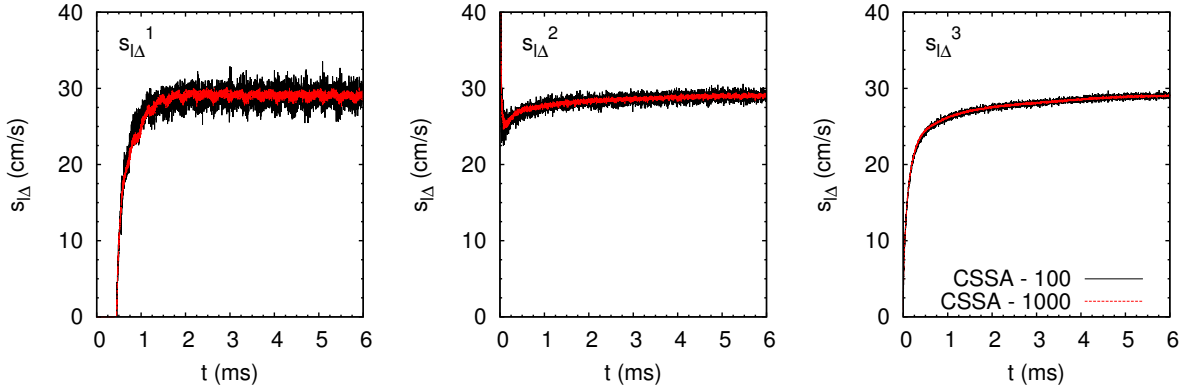

Figure 6.18: The effect of the number of generated samples on the fluctuation of the numerical flame speeds. Numerical flame speeds are calculated on a fine grid ($\Delta_x = 0.075\ mm$) using three different formulas ($s^1_{l\Delta}$ (3.17), $s^2_{l\Delta}$ (3.18), $s^3_{l\Delta}$ (3.19)), and different number of samples: 100 - black; 1000 - red.

The fluctuations have also been evaluated in a qualitative manner: we calculated the statistics of the numerical flame speeds once the initial transient phase has been passed. The standard deviations as a percentage of the corresponding means are plotted in Figure 6.19 as a function of the number of generated samples. The decreasing trend is obvious

and we can also note that the standard deviation is proportional to $N^{-1/2}$ in agreement with our expectations based on well-known statistical relations.

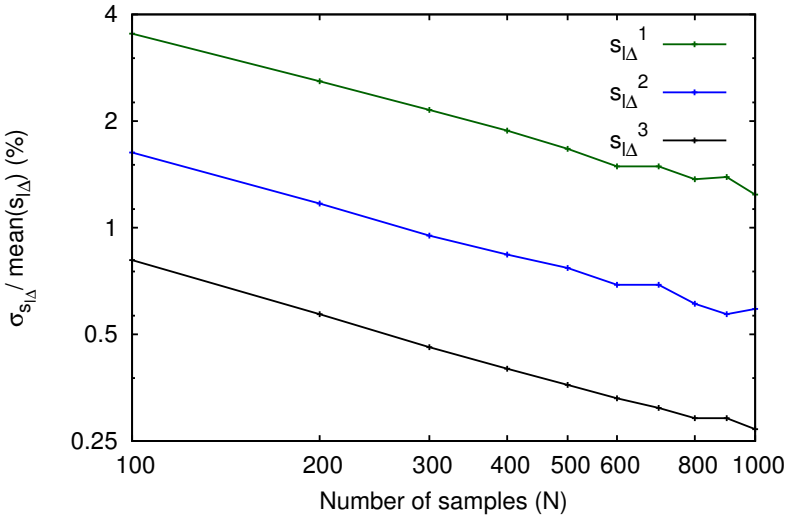

Figure 6.19: The fluctuations of the calculated numerical flame speeds depend on the number of applied samples. The standard deviation of $s_{l\Delta}$ is proportional to $N^{-1/2}$.

It is important to emphasize that despite of these fluctuations the flame position is accurately predicted (Figure 6.20) on the fine grids, but this breaks down on the coarser grids.

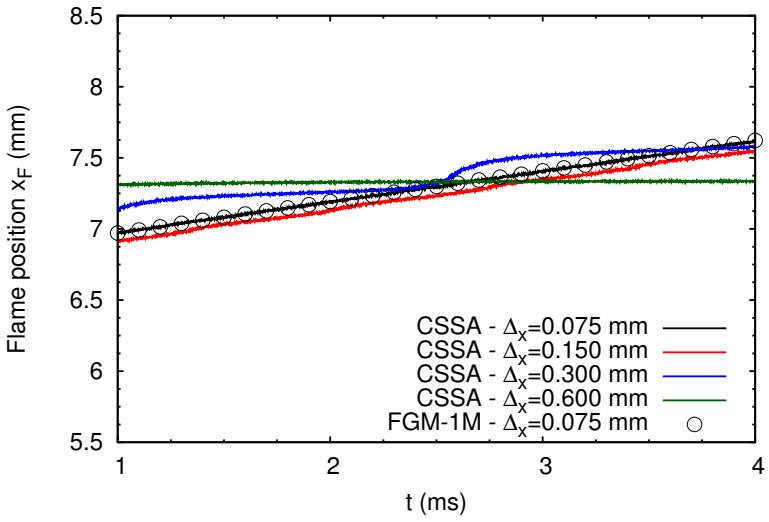

Figure 6.20: Flame position as a function of time calculated with the CSSA method on grids of different spacings. The reference solution was calculated with the FGM-1M method (circles).

In Figure 6.21 the flame speed is shown as a function of the grid spacing for two different inlet velocities. We can see that the CSSA and the FGM-1M solutions are consistent on the fine grids and they are very close to the CHEM1D reference solution for both boundary conditions. However, deviations do occur once the resolution is not sufficient and the flame structure is poorly predicted as we highlighted in the previous sections.

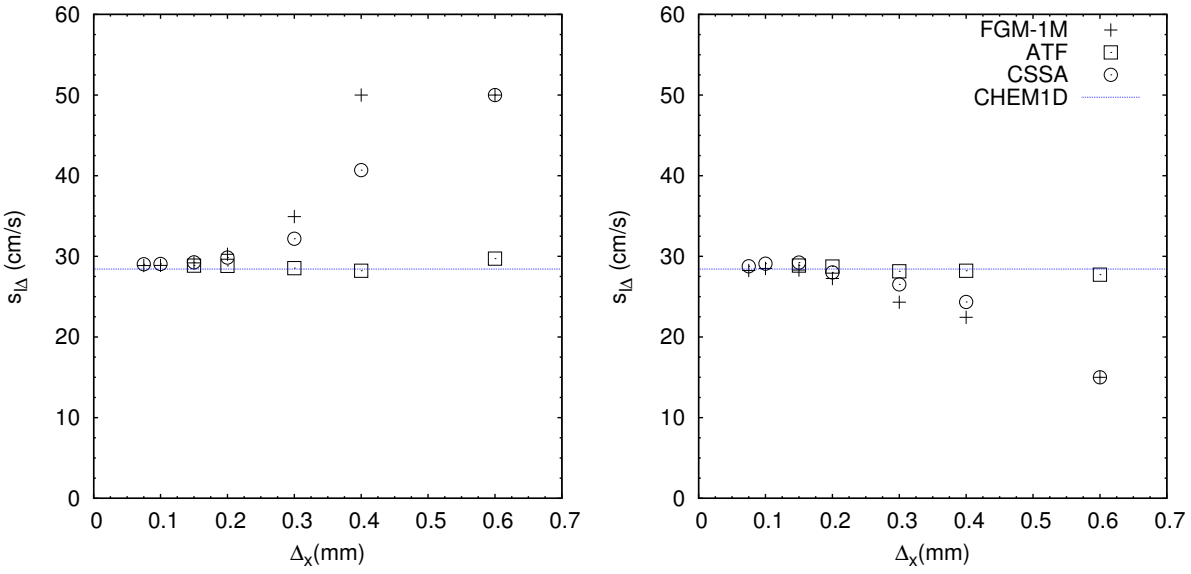

(a) $u_i = 50\ cm/s$ **(b)** $u_i = 15\ cm/s$

Figure 6.21: Grid dependence of the numerical flame speed $s_{l\Delta}$. The reference solution calculated with CHEM1D is depicted with the blue line. The FGM-1M, CSSA and ATF simulations are represented by symbols. The thickening factor applied for the ATF method was 4.

On the coarse grids the CSSA method gives wrong results but it is interesting to note that those predictions are closer to the reference solution than the FGM-1M results. However, the CSSA method cannot match the ATF approach in this regard. This is in accordance with our expectations: taking into consideration the subgrid-scale fluctuations does not solve the problem of resolving the flame structure, therefore we shall not expect correct flame speeds on coarse grids but the more detailed description should enable us to make less inaccurate predictions than with the FGM-1M method.

We can conclude that the CSSA method is able to properly describe a one-dimensional premixed flame as long as the grid is sufficiently fine ($\Delta_x < 0.2\ mm$). This resolution requirement is comparable to that of the FGM-1M method. On coarser grids the CSSA gives better, but still incorrect, results than FGM-1M. Owing to the stochastic nature of the procedure, the numerical flame speed does fluctuate during the solution but we are still able to capture its mean value and thereby the flame position even with only 100 samples per cell. On coarser grids the flame is no longer resolved which causes the chemical source term profile to deviate from the reference solution leading to incorrect numerical flame speeds and flame positions. This is in accordance with our expectations. In light of these inferences we can state that the treatment of the progress variable and the table access are correctly implemented. Now we are ready to have a closer look at the interaction between the mixture fraction and the progress variable.

6.3.3 One-Dimensional Stratified Premixed Flame

We have already shown that the table access and the treatment of the mixture fraction and the progress variable are correctly implemented in the CSSA context. We have managed to match the reference solutions obtained with either the verified FGM-1M method or using detailed chemistry and CHEM1D. However, we have not encountered yet zones in which both control variables change at the same time. Since our main objective is to improve how joint PDFs are approximated, a simple test case is needed to investigate what happens when $\mathcal{Z}$ and $\mathcal{Y}$ experience gradients simultaneously. We will use a one-dimensional stratified methane/air flame for this purpose following the work of Da Cruz et al. [142]. Künne also investigated this configuration in details [107] to evaluate the effect of the thickening factor and the efficiency function in the ATF context.

6.3.3.1 Description of Configuration

This time the quasi-one-dimensional domain is 80 mm long. The finest grid is obtained by dividing this domain into 1024 uniform cells which yields a spacing of $\Delta_x = 0.078\ mm$. We have also used coarser grids with 512 and 256 cells. A mixture fraction profile is set according to a hyperbolic tangent function:

$$\mathcal{Z}(x) = \mathcal{Z}_i + 0.5 \cdot (\mathcal{Z}_{st} - \mathcal{Z}_i) \cdot (\tanh(B \cdot (x - x_f)) + 1)\,, \tag{6.51}$$

where $\mathcal{Z}_i = 0.02$ is the mixture fraction at the inlet, $\mathcal{Z}_{st}$ is the stoichiometric mixture fraction, B is a parameter that sets the steepness of the profile, and $x_f = 0.02$ is the location where the profile is centered: $\mathcal{Z}(x_f) = (\mathcal{Z}_i + \mathcal{Z}_{st})/2$. The $\mathcal{Z}$ profile is kept constant until the flame reaches its predefined proximity. This is necessary for creating well-defined initial conditions. The inlet velocity is 20 cm/s and the inlet temperature is 310 K. We chose the later value to move away from the 'edge' of the chemistry table, where errors are more prevalent. To the sides of the domain symmetry conditions are applied and a convective outlet condition is set for the outflow.

6.3.3.2 Results

Since the inlet speed is lower than the laminar flame speed under these conditions, the initially stoichiometric flame propagates towards the inlet at the beginning. As soon as the flame starts to interact with the mixture fraction gradient, the flame speed changes. The equivalence ratio drops which leads to a decreased chemical source term and consequently to a significantly lower flame speed which eventually causes the flame to propagate downstream. The temporal evolution of the flame can be observed in Figure 6.22.

While we would like to compare the different methods it is not appropriate to directly compare the instantaneous snapshots of the propagating flames because even minor differences in the temporal evolution might lead to seemingly major discrepancies. The reason for it is twofold. Firstly, as we have shown in the previous section, the stochastic nature of the CSSA method causes fluctuations in the flame speed and consequently in the flame

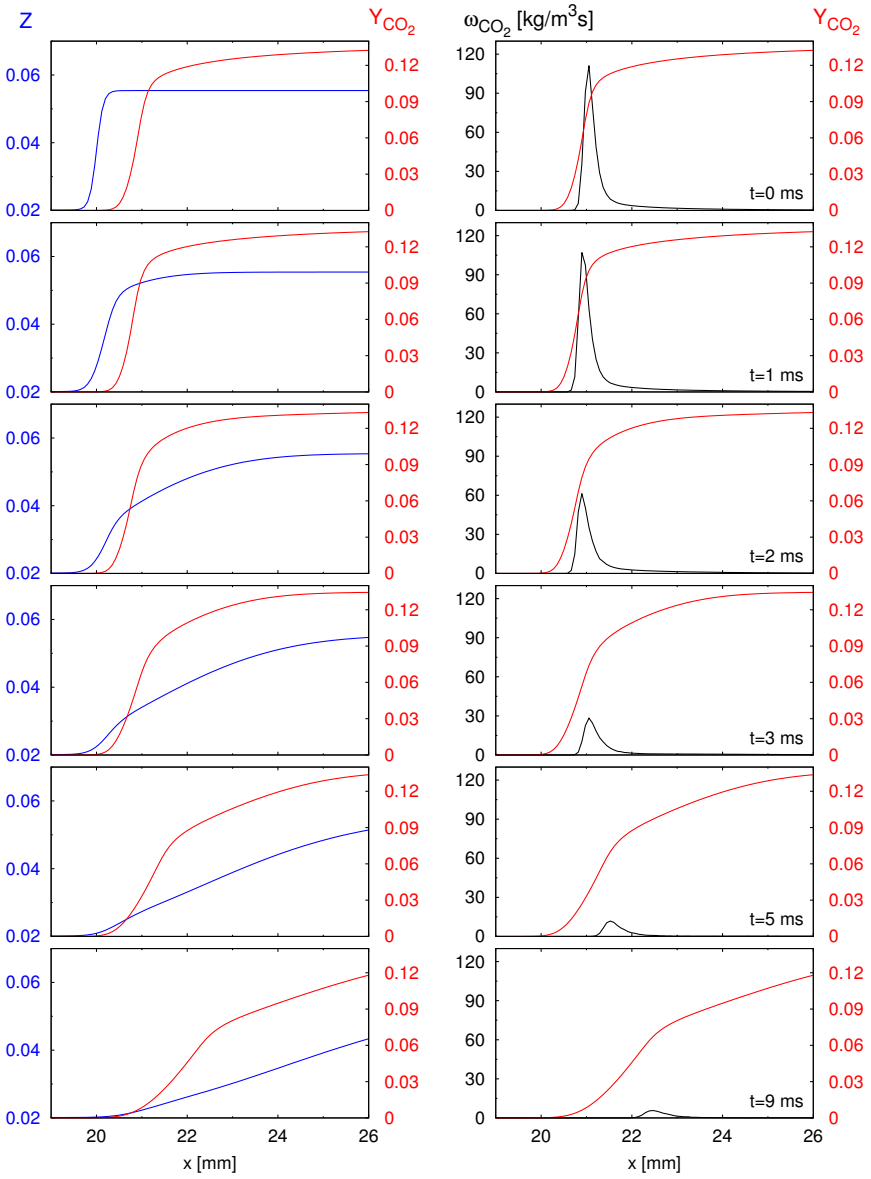

Figure 6.22: Temporal evolution of a one-dimensional stratified premixed flame calculated with the CSSA method.

position. Secondly, the $\tilde{Z}$ profile is kept constant until the flame reaches it, which can happen at slightly different times as a consequence of the aforementioned fluctuations. This might shift the initial time of interaction between the gradient and the flame but not necessarily changes the flame structure itself. Therefore it is better to compare the numerical flame speeds as functions of the equivalence ratio (ϕ).

The evaluation of the flame speed is not straightforward in a stratified case. The (3.18) and (3.19) formulas require well-defined burnt and unburnt states which are hard to provide in this case as they are functions of the mixture fraction. Equation (3.17) on the other hand requires the flame position, which is also difficult to extract as due to the stratification the flame structure changes continuously. Building on Da Cruz's work [84] Künne used

(3.19) and defined the burnt and unburnt states based on the equivalence ratio at the point of maximum heat release [107]. In this study we maintain this approach.

Künne has also showed that the FGM-1M solution differs from that of the homogeneous flame calculations and depends on the selected method of calculating the flame speed. However, this is not a concern for us as our objective is to verify that in a well-resolved case the CSSA method can match the FGM-1M results. This is indeed the case as we can observe in Figure 6.23a which depicts the results obtained on a grid of 1024 cells (grid spacing is $\Delta_x = 0.078\ mm$).

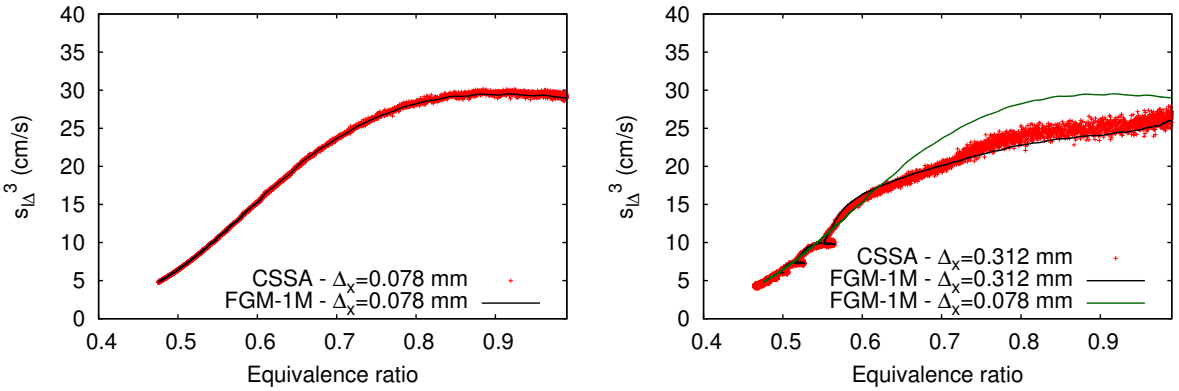

(a) 1024 cells, $\Delta_x = 0.078\ mm$ **(b)** 256 cells, $\Delta_x = 0.312\ mm$

Figure 6.23: Numerical flame speeds as functions of the equivalence ratio. Symbols represent the results obtained with the CSSA method and the lines depict those of the FGM-1M method.

If we take a coarser grid (256 cells, $\Delta_x = 0.312\ mm$) the solutions deteriorate from the reference solution (Figure 6.23b). This is not surprising considering that the CSSA method does not address the problem that the thin premixed flame is not resolved on such a coarse grid. Improvements can only be expected in connection with diffusion flames where the unresolved subgrid-scale fluctuations are more significant. This will be investigated in the subsequent two- and three-dimensional cases in the later chapters.

6.3.4 Summary

As a conclusion we can state that the one-dimensional test cases have verified that the treatment of the control variables and the table access are correctly implemented in the CSSA context. We have also addressed the introduced stochastic errors and discussed the important issue of how to handle the density. We applied 100 samples per cell and we still managed to match the reference solutions. Therefore hereinafter, if it is not explicitly stated otherwise, we will generate 100 samples per cell in this work. In light of these results it is time to summarize the overall solution procedure before we move on to looking at more complex cases.

6.4 Overall Solution Procedure

Künne [107] has provided a comprehensive overview of the overall solution procedure that has been implemented in FASTEST. Here we mainly focus on the parts that have been modified in order to accommodate the SA algorithm to make sure that the concept of the discrete sample generation and the mechanism of accessing the look-up table are properly understandable. The overall procedure consists of two main parts. The first one is the initialization during which the primary variables must be either provided by the user or read from a restart file. An existing mixing simulation can be ignited at this point by setting the species mass fractions to their equilibrium value.

The second part is the time step itself. First the chosen turbulence model - in our case the Germano model (Section 2.2.3.2)) - is used to calculate the turbulent viscosity and the turbulent diffusion according to the (2.54) formula using Sc_t. Then the Runge-Kutta stages start with the transport of the mixture fraction (3.25), the progress variable (3.26) and the enthalpy (2.49) followed by the preliminary computation of the momentum (2.47). This leads to the phase of accessing the table, which uses the non-adiabatic approach described and implemented by Ketelheun [93].

- As we have concluded in Section 6.3.1.2, the density needs to be treated separately. The mean mixture fraction ($\widetilde{\mathcal{Z}}$), progress variable ($\widetilde{\mathcal{Y}}$) and enthalpy ($\widetilde{h}$) are used to extract the density from the look-up table, which will be substituted in the equations as a filtered density ($\overline{\rho}$) in the following Runge-Kutta stage.
- To calculate the viscosity and the chemical source term (optionally the species mass fractions for post-processing purposes), the discrete joint PDF approach is used, which has been discussed in details in Section 5.1:
    1. The variances and covariances of the control variables are calculated with the gradient approach following the (2.68) and (2.69) formulas.
    2. Univariate samples are generated according to these statistical moments and the assumed shapes of the one-dimensional PDFs.
    3. The SA algorithm is used to set the correlation between the univariate sample sets, thereby creating points in the multidimensional parameter space following the procedure discussed in Section 5.3.3.
    4. The look-up table is accessed by each sample, thereby retrieving a set of viscosity and source term values.
    5. The mean viscosity and source term are calculated based on the retrieved sets using simple ensemble averaging.

With these new values the diffusion coefficients get updated and the temporal change of the density can be calculated. The latter one is required for the pressure correction procedure Section 6.1.6 elaborated on: the corrected pressure and momentum are calculated in an iterative manner until the convergence criterion regarding the mass defect is fulfilled. After that the next Runge-Kutta stage follows.

Chapter 7

Two-Dimensional Verification Cases

In this chapter simple two-dimensional cases are investigated with the intention of verifying and evaluating the CSSA method. Results are compared to appropriate benchmark data obtained with the extensively validated FGM-1M method. Our selection consists of reacting and non-reacting, steady and unsteady as well as laminar and turbulent configurations in order to assess the performance of the CSSA model under various circumstances. Each case focuses on a different phenomenon (such as mixing, flame structure, near-wall heat loss, flame-flow interaction in unsteady reacting flows) and they are presented in an increasing order of complexity.

7.1 Two-Dimensional Isothermal Mixing Jet

In this first case we test the ability of the CSSA model to capture pure mixing. For this purpose a two-dimensional isothermal jet is considered in which a lean premixed methane-air mixture mixes with pure air.

7.1.1 Description of Test Case

The computational domain is depicted in Figure 7.1a: it consists of two flow streams separated by a 15 mm-high no-slip wall at the inlet. The dimension of the domain is 80 $mm \times 20$ mm and it is discretized using two uniform meshes with different grid spacings to evaluate the grid dependency of the solution. The coarser grid has a grid spacing of $\Delta_x = 0.5$ mm, while the finer one is of $\Delta_x = 0.25$ mm. On the left side of the wall the methane-air mixture with the mixture fraction of 0.05 enters the domain at a bulk velocity of $u_f = 25$ m/s. On the other side of the wall there is a stream of pure air. Its velocity is set to $u_a = 7.5$ m/s for $x < 15$ mm and this velocity is increased to 15 m/s at $x = 20$ mm according to an exponential profile. This is necessary for ensuring that the jet is narrow enough and the mixing process takes place inside the domain without reaching the sides, where symmetry boundary condition is applied. It also facilitates a smoother outflow at the outlet with convective outflow boundary condition. Temporally and spatially correlated artificial velocity fluctuations [100] are imposed on the inlets to enhance mixing. The applied time step was $2 \cdot 10^{-6}$ s, simulations ran until $t = 0.3$ s, which was sufficient for obtaining properly averaged results.

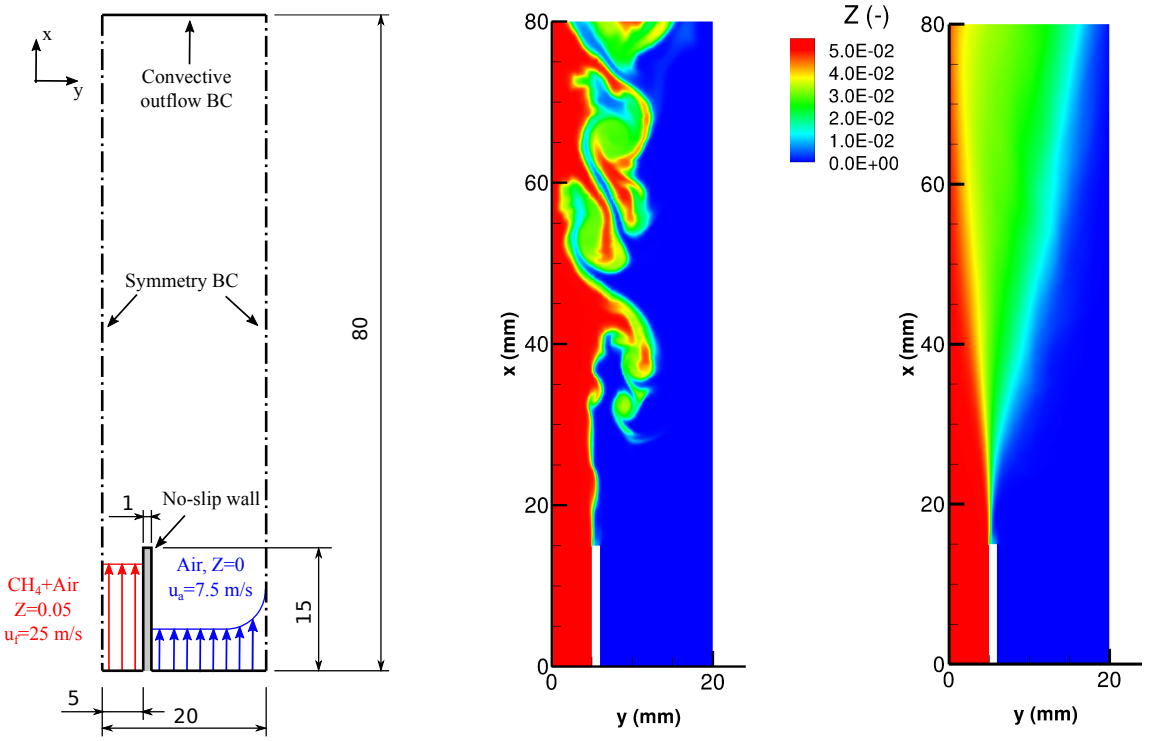

(a) Geometry **(b)** Mixture fraction **(c)** Mean mixture fraction

Figure 7.1: (a) Geometry of the computational domain (lengths are given in millimeters). Instantaneous (b) and time-averaged (c) mixture fraction fields calculated with the CSSA method.

7.1.2 Evaluation of Results

In Figure 7.1 one can observe a snapshot of an instantaneous mixture fraction field along with the time-averaged results. The former one shows the effect of the shear layer between the two streams: it leads to the development of a vortex street. In Figure 7.2 one of the first developing vortices is depicted, which emerged $4 \cdot 10^{-6}$ s after we had initialized the mixture fraction in the entire domain as a function of the x coordinate in the same way as at the inlet. We can use this structure to compare the instantaneous mixture fraction profiles obtained with the CSSA and the FGM-1M methods. According to Figure 7.2 there is a slight difference between the results corresponding to the different meshes (symbols are used to denote the FGM-1M result on the finer mesh, which is used as a reference solution), but the CSSA and FGM-1M profiles are perfectly aligned in both cases. We can make the same observation when we look at either the axial or the radial velocity profiles in Figure 7.3 or the mean and the root mean square of the mixture fraction in Figure 7.4. Based on these observations we can conclude that the CSSA method is capable of accurately reproducing pure mixing.

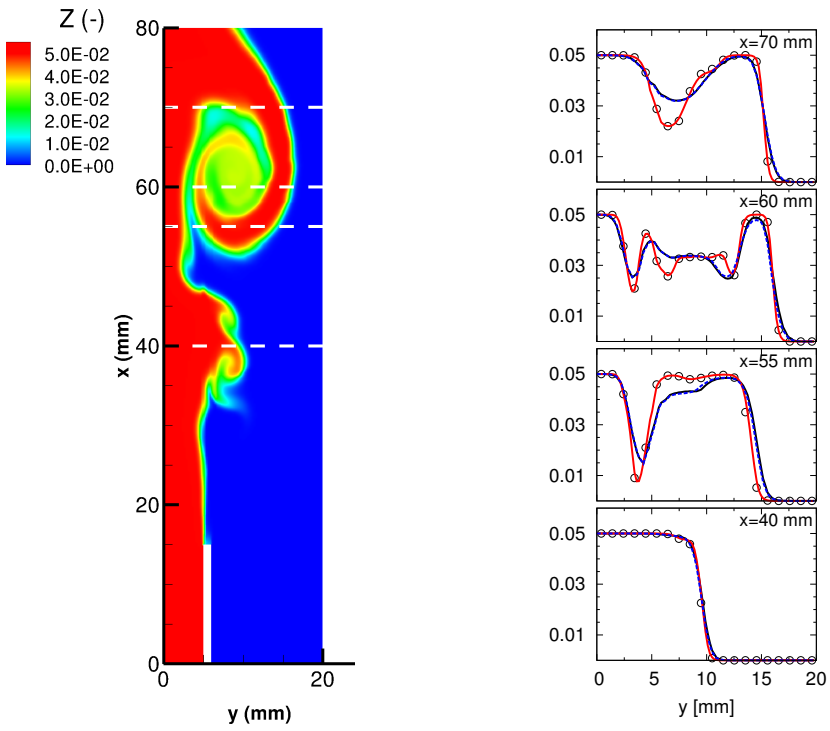

Figure 7.2: Comparison of the instantaneous mixture fraction fields calculated with the FGM-1M and the CSSA method. 2 meshes of different spacings were used: FGM-1M, $\Delta_x = 0.25\ mm$ - symbols; CSSA, $\Delta_x = 0.25\ mm$ - red line; FGM-1M, $\Delta_x = 0.5\ mm$ - black line; CSSA, $\Delta_x = 0.5\ mm$ - blue line

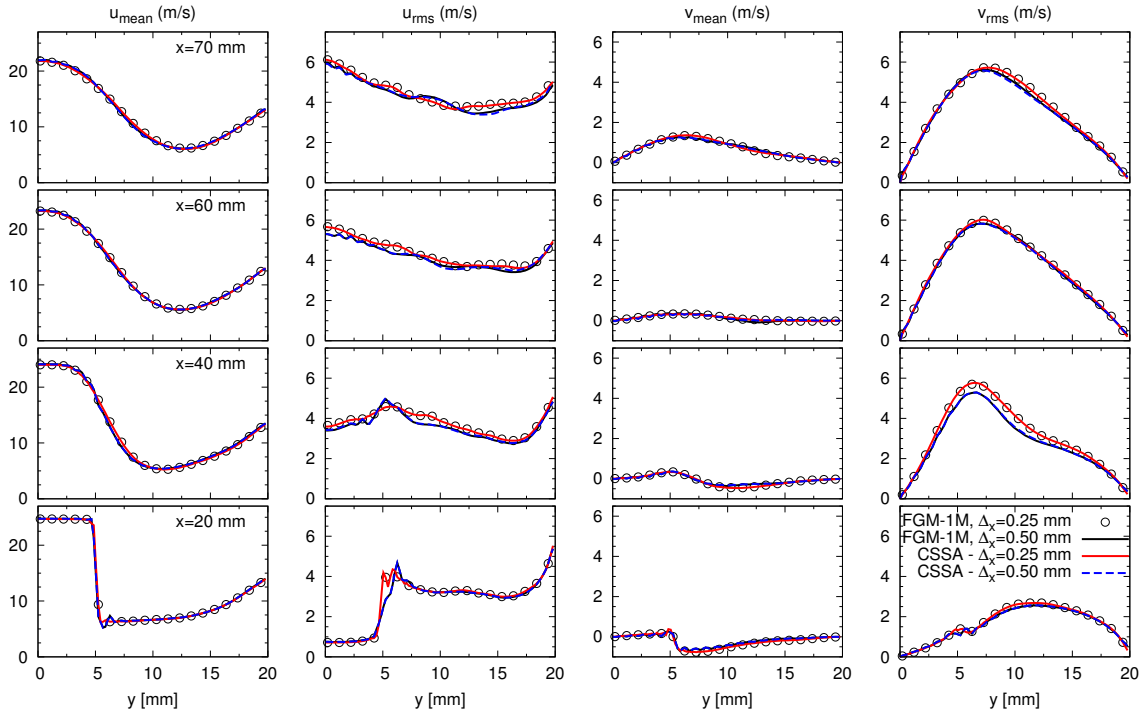

Figure 7.3: Mean and fluctuating velocity profiles at different axial positions.

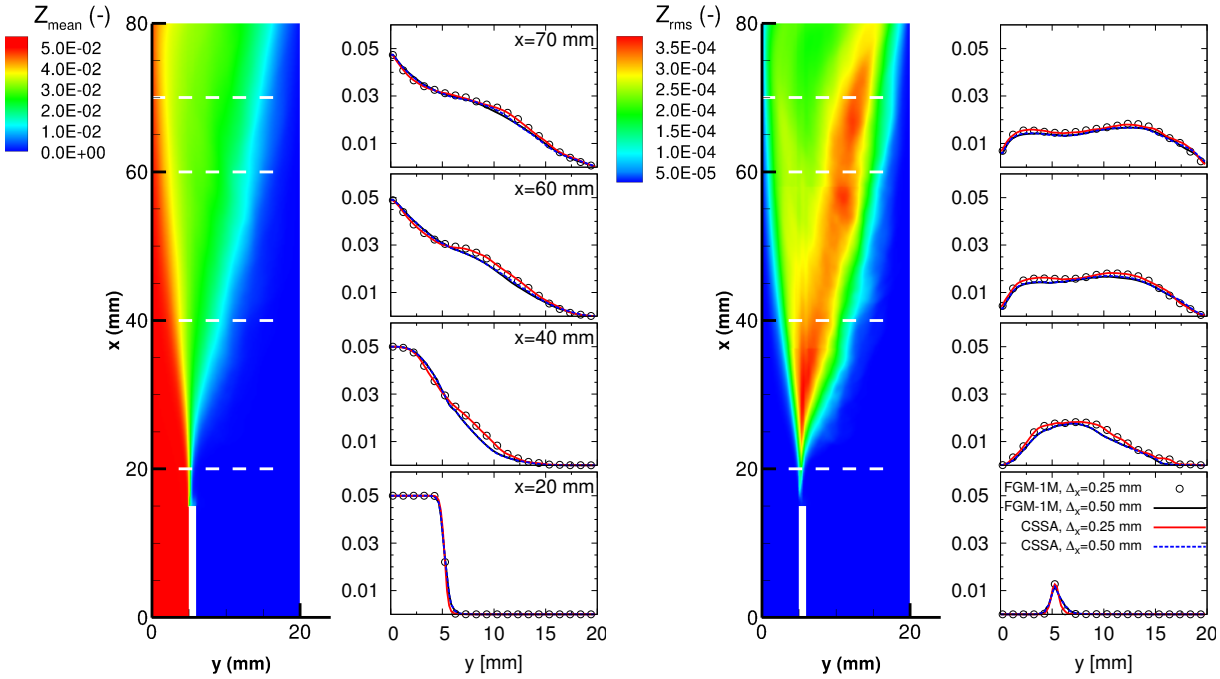

Figure 7.4: Mixture fraction field calculated with the CSSA method and corresponding profiles at different axial positions: mean values (left), root mean square (right).

7.2 Two-Dimensional Laminar Bunsen Flame

After having investigated the treatment of the mixture fraction through the case of pure mixing, we should turn our attention towards the progress variable and how the flame structure can be captured. As a first step the mixture fraction is kept constant and the influence of the flame-turbulence interaction is mitigated as much as possible by setting up a laminar premixed case, namely a Bunsen flame. The other objective of this test case is to evaluate how the CSSA model can account for the near-wall heat losses. Therefore two variants of the same configuration will be considered: one with adiabatic and one with non-adiabatic wall boundary conditions.

7.2.1 Description of Test Case

The dimensions of the computational domain and the applied boundary conditions are illustrated in Figure 7.5a. At the inlet a lean methane-air mixture with $\mathcal{Z} = 0.045$ enters the domain. The inlet velocity has the following prescribed profile:

$$u(y) = -4\frac{U_0}{d^2}\left(y + \frac{d}{2}\right)^2 + 4\frac{U_0}{d}\left(y + \frac{d}{2}\right), \tag{7.1}$$

where d denotes the width of the slot and $U_0 = 1.1\ m/s$ is the maximum velocity. The gray surfaces represent the walls in Figure 7.5. As we can observe, the flame stabilizes as a

Bunsen flame above the backward-facing step behind the inlet. Two cases are investigated. In the first case adiabatic wall boundary conditions are prescribed, which means that a wall boundary condition is applied to the velocity and a symmetry boundary condition to the temperature at the walls. This will make the flame stabilize directly at the wall (Figure 7.5b). In the second case the boundary conditions at the walls are changed to non-adiabatic ones: the wall boundary condition is kept regarding the velocity, but a Dirichlet boundary condition is imposed on the temperature ($T = 300\ K$). As a consequence the flame can stabilize only above the cold wall as a lifted-flame. Symmetry boundary condition is applied to the centerline in both cases. The domain is discretized using a uniform mesh which consists of 26000 cells and has a grid spacing of $\Delta_x = 0.05\ mm$. Coarser meshes have also been investigated and the presented one has been proven to provide a grid-independent solution. The applied time step is $1 \cdot 10^{-6}\ s$.

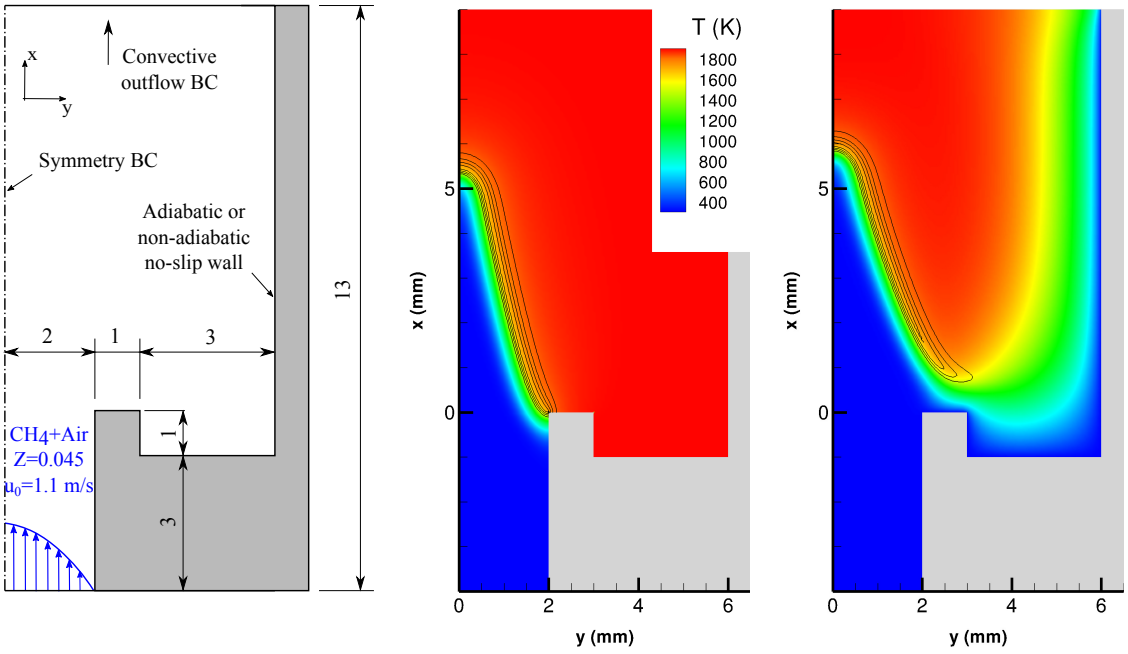

(a) Geometry **(b)** Adiabatic **(c)** Non-adiabatic

Figure 7.5: (a) The geometry of the computational domain used for the laminar Bunsen flame simulation (lengths are given in millimeters). In the other two images the contours of the temperature calculated with the CSSA method as well as the isolines of the time-averaged progress variable source term are shown with adiabatic (b) and non-adiabatic (c) wall boundary conditions.

7.2.2 Evaluation of Results

In Figure 7.6 profiles of the mean velocities, CO_2 mass fraction, and temperature are compared. The root mean squares of these quantities are not interesting now since it is a laminar case, therefore all of them are negligible. We can clearly observe the difference between the adiabatic (black) and the non-adiabatic (red) results. The agreement between

the respective FGM-1M (symbols) and CSSA results (lines) is very good: the heat loss is well predicted by the CSSA method as well as the flame structure. We can identify only one minor difference: the CSSA method predicts a slightly lower flame tip position as we can infer from the temperature profiles.

Based on these findings we can conclude that CSSA is able to match the reference solutions under the given circumstances: both the flame structure and the heat losses are well predicted, which means that the treatment of the enthalpy variable has been correctly implemented. It should also be pointed out that no stability issues have been observed confirming once again that the solution proposed in section 6.3.2.3 to treat the density is an appropriate one.

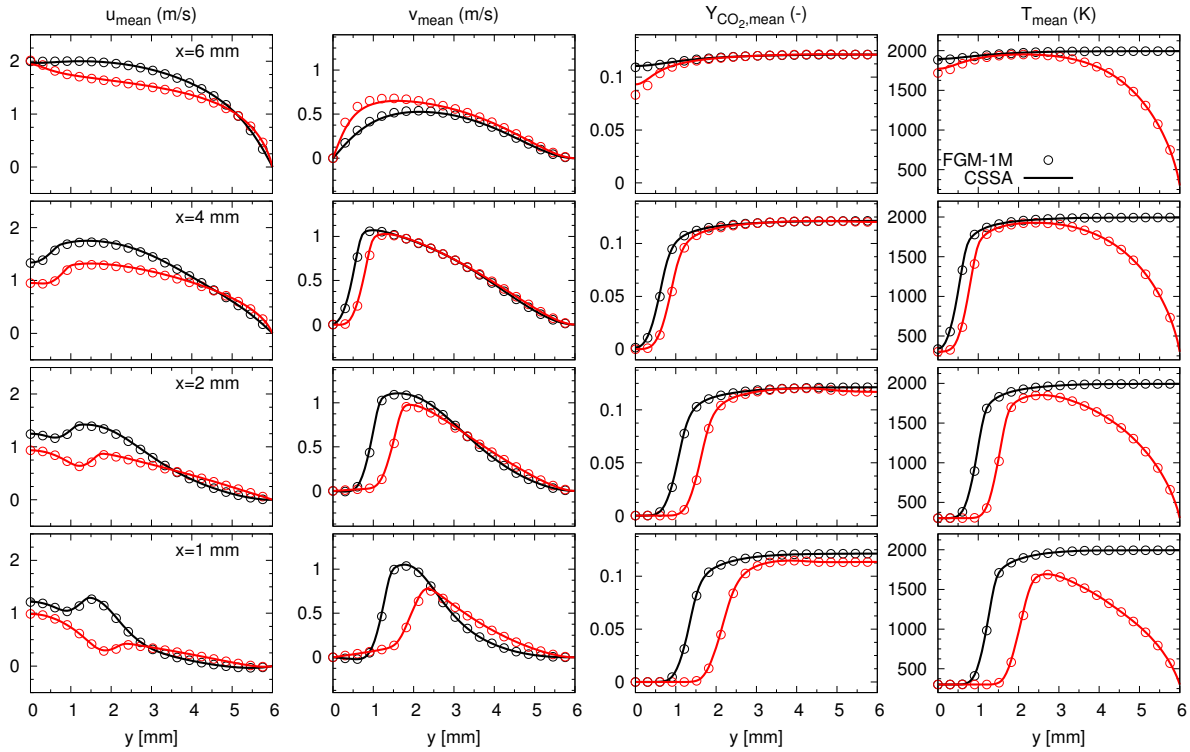

Figure 7.6: Profiles of the mean axial (u) and radial (v) velocities, the CO_2 mass fraction (Y_{CO_2}), and the temperature (T) in the Bunsen flame. CSSA results are depicted with lines, while the FGM-1M solutions are denoted with symbols. Color black refers to the non-adiabatic wall boundary conditions and color red is used for the adiabatic case.

7.3 Two-Dimensional Unsteady Premixed Flame

So far we have investigated the mixture fraction in a pure mixing case and the progress variable in a laminar premixed case. Now we turn our attention to a configuration in which the flame-turbulence interaction is significant. In this section a two-dimensional unsteady reacting case is considered in which the incoming turbulent premixed methane-air mixture is ignited by a jet of hot burnt gases.

7.3.1 Description of Test Case

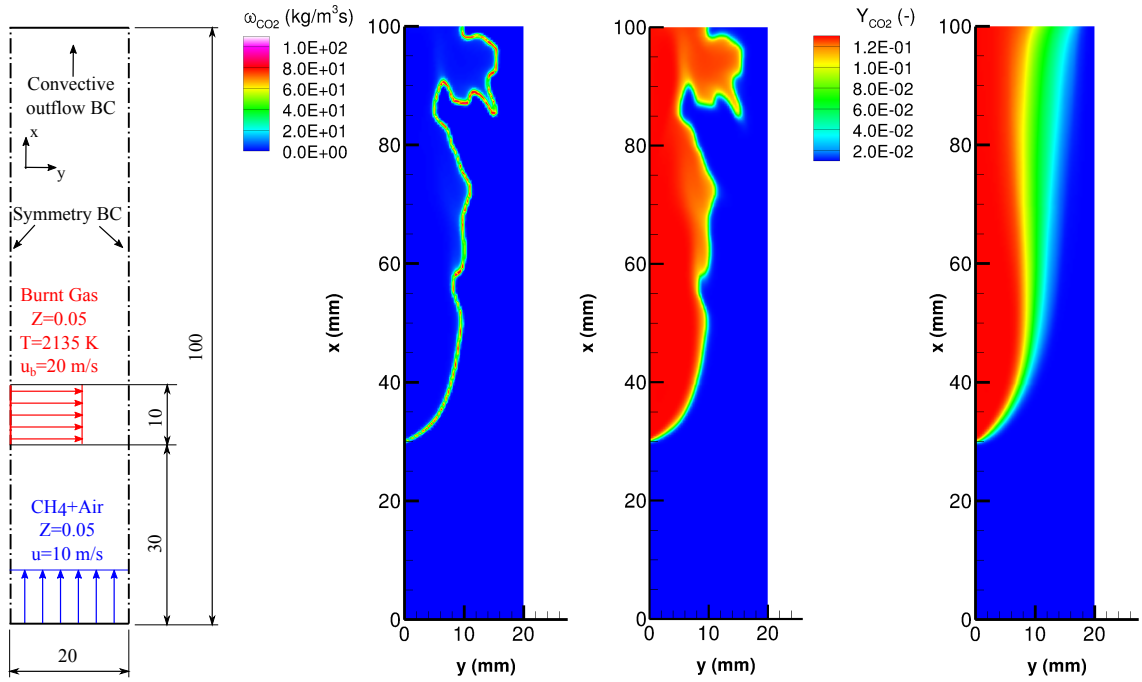

(a) Geometry **(b)** CO_2 source **(c)** Y_{CO_2} **(d)** Mean Y_{CO_2}

Figure 7.7: (a) The geometry and the boundary conditions of the unsteady flame configuration. Contours of the CO_2 source term (b) and the CO_2 mass fraction (c) at a given moment. The wrinkled flame front can be clearly observed. (d) Mean value of the CO_2 mass fraction.

The computational domain of 20 mm × 100 mm is depicted in Figure 7.7a. Symmetry boundary condition is applied at both the left and the right side of the domain while convective outflow condition is chosen at the outlet. The domain has two inlets. The first one is at $x = 0$ mm where a lean methane-air mixture of $\mathcal{Z} = 0.05$ enters with the bulk velocity of $u = 10$ m/s. In order to enhance the flame-turbulence interaction, artificially generated turbulent fluctuations are superimposed on the inflow. A second inlet is located on the left side of the domain between $x = 30$ and 40 mm. Here the incoming flow has a velocity of $u_b = 20$ m/s and it consists of burnt gases at the temperature of 2135 K. The interaction between the burnt gases and the methane-air mixture stabilizes the unsteady

flame. The imposed turbulent field makes the developing flame front wrinkled as we can observe in Figure 7.7c, which illustrates the CO_2 mass fraction at a given moment.

We utilize two grids with different spacings. The finer grid comprises 50000 control volumes and has a spacing of $\Delta_x = 0.2\ mm$. This grid provides us with a reference solution. The coarser grid has only 12500 control volumes as a result of a spacing of $\Delta_x = 0.4\ mm$. The applied time step is $2 \cdot 10^{-7}\ s$. Similarly to the previous cases, the CSSA results are compared to those of the FGM-1M method.

7.3.2 Evaluation of Results

In Figure 7.8 and 7.9 profiles of the mean and root mean square velocities and control variables calculated with different methods are compared, respectively. The FGM-1M solution on the finer grid is considered as a reference and is denoted with circles.

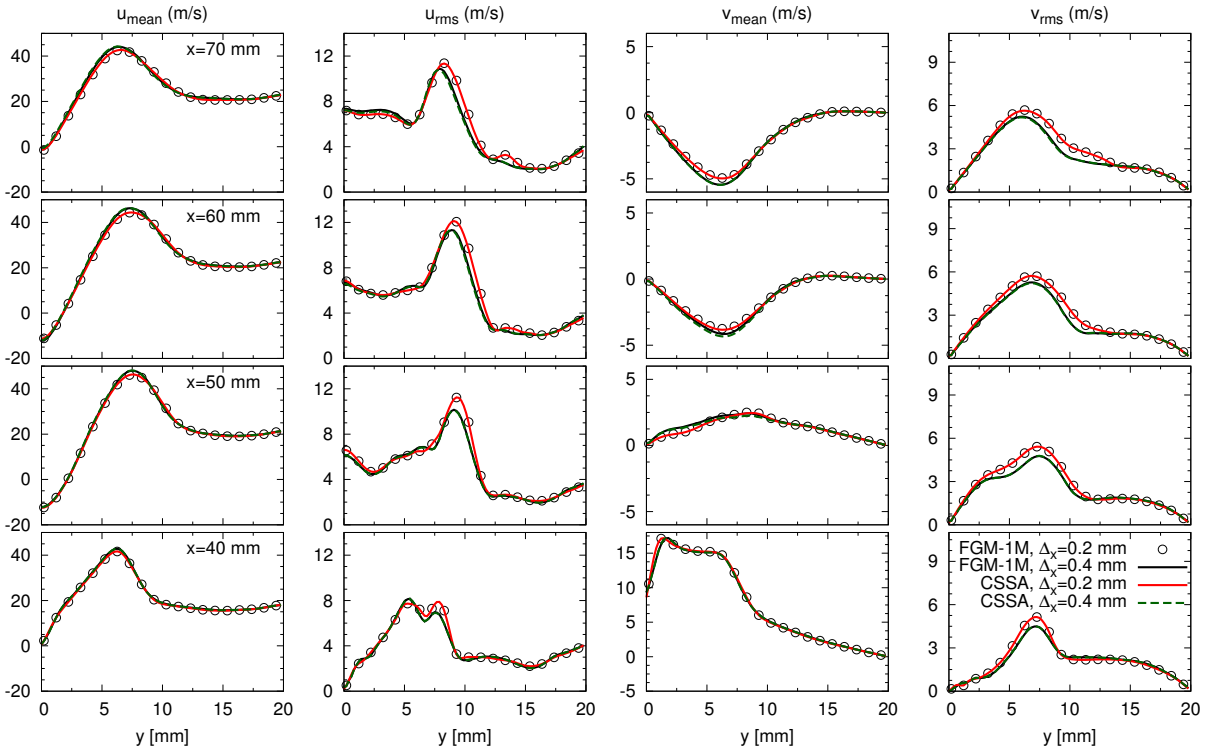

Figure 7.8: Axial u and radial v velocity profiles, both the mean and the root mean square values, at different x axial positions. The reference solution is calculated with the FGM-1M method on a fine grid and is denoted with circles. The lines represent the following solutions: fine grid, CSSA method - red; coarse grid, CSSA - green; coarse grid, FGM-1M - black.

The axial velocity increases significantly in the zone where the incoming flow interacts with the jet of burnt gases: the methane-air mixture ignites and due to the thermal expansion the velocity increases. We can also observe that the axial velocity becomes negative at higher x values close to the left boundary of the computational domain indicating that a recirculation zone comes to existence above the second inlet.

The temperature fluctuations are high in a wide interval. This shows that the flame brush is thick as it is expected considering the wrinkling effect of the turbulent inflow. The flame brush can be clearly observed in Figure 7.7d.

We can conclude that the CSSA and the FGM-1M methods provide identical results. The results on the coarser grid show some discrepancies when they are compared to those of the finer one, but even on this grid there is no discernible difference between the performance of the two methods. CSSA is able to reproduce the well-resolved reference solution in this configuration.

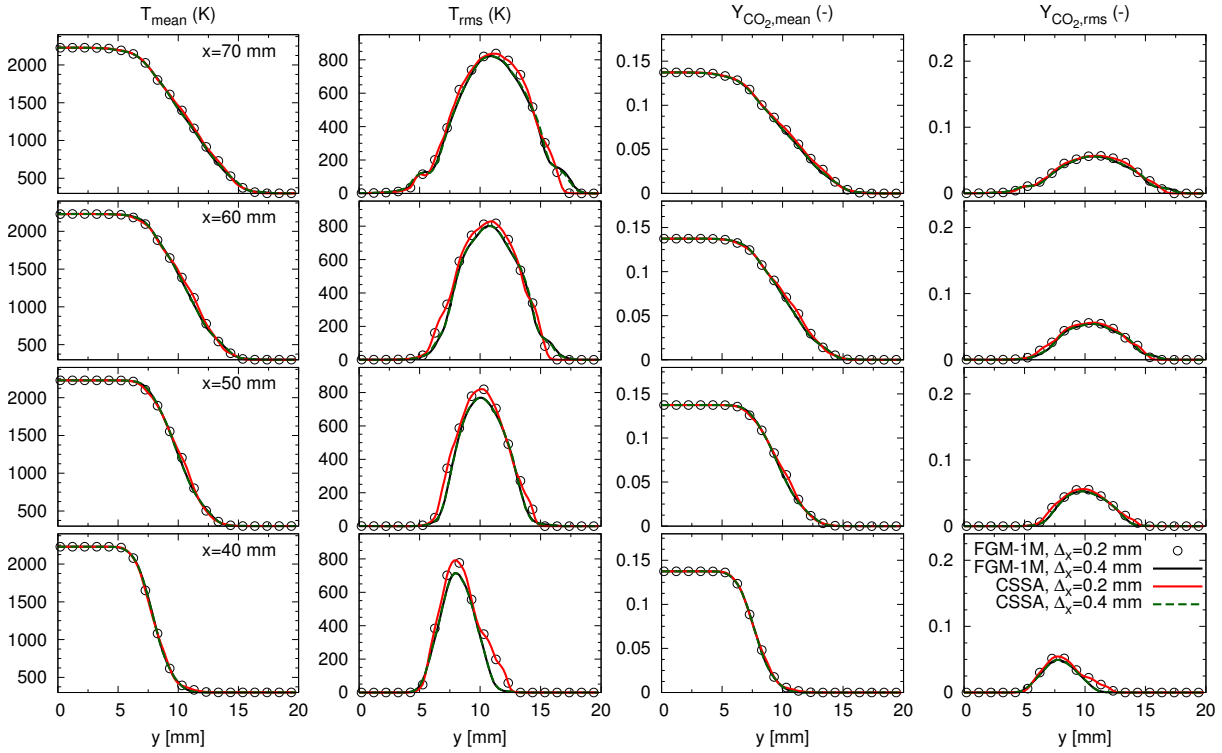

Figure 7.9: Profiles of the temperature (T) and the CO_2 mass fraction (Y_{CO_2}) at different axial positions: fine grid, FGM-1M - circles; fine grid, CSSA method - red line; coarse grid, CSSA - green line; coarse grid, FGM-1M - black line.

7.4 Two-Dimensional Turbulent Planar Jet

After having investigated the mixture fraction and the progress variable separately, we now evaluate a final two-dimensional test configuration in which both control variables change and the flame-turbulence interaction is also significant: a turbulent planar jet based on a similar configuration described by Liu et al. [117].

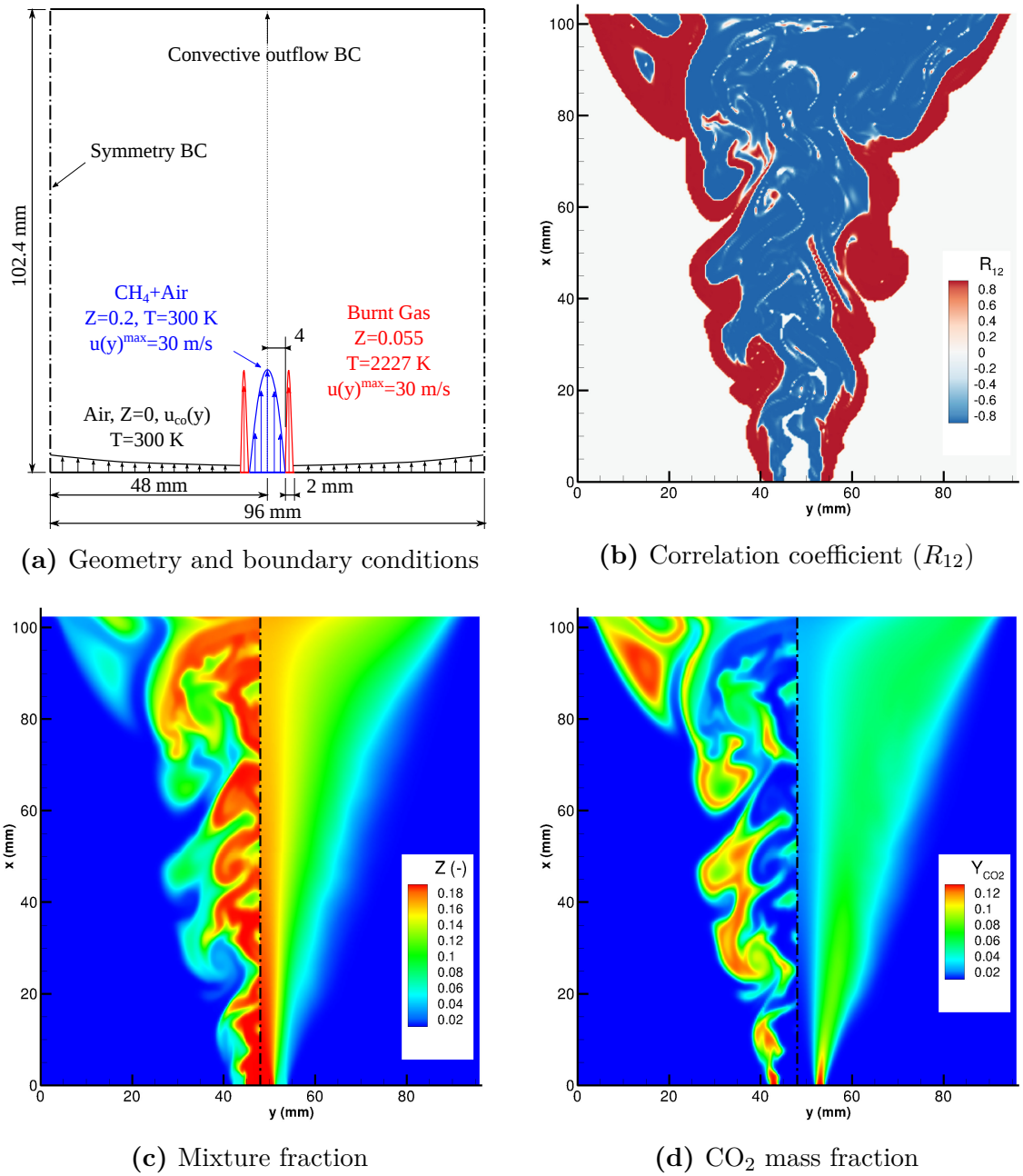

(a) Geometry and boundary conditions

(b) Correlation coefficient (R_{12})

(c) Mixture fraction

(d) CO_2 mass fraction

Figure 7.10: Illustration of the computational domain (a), the correlation coefficient (R_{12}) (b), an instantaneous and the mean mixture fraction field ($\mathcal{Z}$) (c), and an instantaneous and the mean CO_2 mass fraction field (Y_{CO_2}) (d) for the two-dimensional planar jet. In the split images of (c) and (d) the snapshots of the instantaneous values are on the left while mean values are presented on the right side.

7.4.1 Description of Test Case

The two-dimensional computational domain is 96 $mm \times 102.4$ mm. Symmetry boundary condition is applied to both the left and right sides and convective outflow condition to the outlet. In order to facilitate the smooth outflow of the flow structures, an exponential profile is set up for the U_c characteristic convection velocity introduced in equation (6.46):

$$U_c(y) = u_{max} \exp\left(-B\frac{(y - y_{center})^2}{d^2}\right), \tag{7.2}$$

where y_{center} is the respective coordinate of the centerline, d is the width of the domain, $u_{max} = 30$ m/s is the maximum velocity, and $B = 2.5$ is a parameter.

The inlet ($x = 0$ mm) is divided into 3 zones according to Figure 7.10a. The main jet's width is $d_j = 8$ mm. The incoming methane-air mixture is fuel rich: it has a mixture fraction of 0.2 and a temperature of 300 K. The predefined velocity profile is parabolic with a maximum value of 30 m/s:

$$u_{co}(y) = u_{co} + u_0\left(1 - \left(\frac{y - y_{center}}{d_i/2}\right)^2\right), \tag{7.3}$$

where $u_{co} = 1$ m/s is the velocity of the co-flow and $u_0 = 29$ m/s. In order to enhance flame-turbulence interaction, artificially generated turbulent fluctuations are superimposed on this velocity field.

The main jet is surrounded by a pair of outer slots with the width of $d_p = 2$ mm. These inlets are for hot ($T = 2227$ K) burnt gases of a stoichiometric methane-air mixture and they serve as a heat source ensuring ignition and stabilization. The inflow at these slots also have parabolic velocity profiles similarly to the main jet: the maximum velocity is 30 m/s and the minimum at the outer edges of the slots is 1 m/s.

The axial velocity of the pure air co-flow ($T = 300$ K, $\mathcal{Z} = 0$) follows an exponential profile that helps with keeping the flame within the boundaries. The maximum velocity at $y = 0$ and 96 mm is approximately 3 m/s:

$$u(y) = u_{co} \exp\left(C\left(|y - y_{center}| - d_j/2\right)\right), \tag{7.4}$$

where $C = 24$ is an appropriately chosen numerical parameter. The radial velocity (v) is set to 0 at the entire inlet.

The domain is discretized with a uniform grid with the spacing of $\Delta_x = 0.2$ mm, which has been proven to provide a grid independent solution. This yields 245760 control volumes. The time step is $2 \cdot 10^{-6}$ s.

7.4.2 Evaluation of Results

The configuration has been simulated with three different methods. The first two are the FGM-1M method, which provides our reference solution, and the CSSA method as it was

the case in the previous sections. However, we would also like to evaluate the effect of taking into account the correlations, therefore we have also used the CSSA method but with the SA algorithm being turned off. It means that we still generate the samples but only the means and variances are taken into account and we use the random pairs in the parameter space without adjusting the covariance. This modified procedure will be referred to as CSSA-WOC (WithOut Correlation).

Although this case involves strong turbulence-flame interaction and both the mixture fraction and the progress variable vary, we still do not expect significant differences between the results obtained with the various approaches. The reason is that this free jet is a simple case from the point of view of unresolved variances: no quenching, local extinction or flame-wall interaction are present, the subgrid-scale fluctuations are not expected to have a major effect. The results confirm these expectations: except for a few minor differences, they are almost identical for the three methods. In Figure 7.11 the axial and radial velocity profiles are shown while in Figure 7.12 we can observe the means and variances of the control variables. The results are in very good agreement. At higher axial positions we can detect slight differences regarding $Y_{CO_2,mean}$. The same is true for the mean temperature values in Figure 7.13. This shows that taking into consideration the correlations can indeed change the results, however, these changes are minor ones in this particular case.

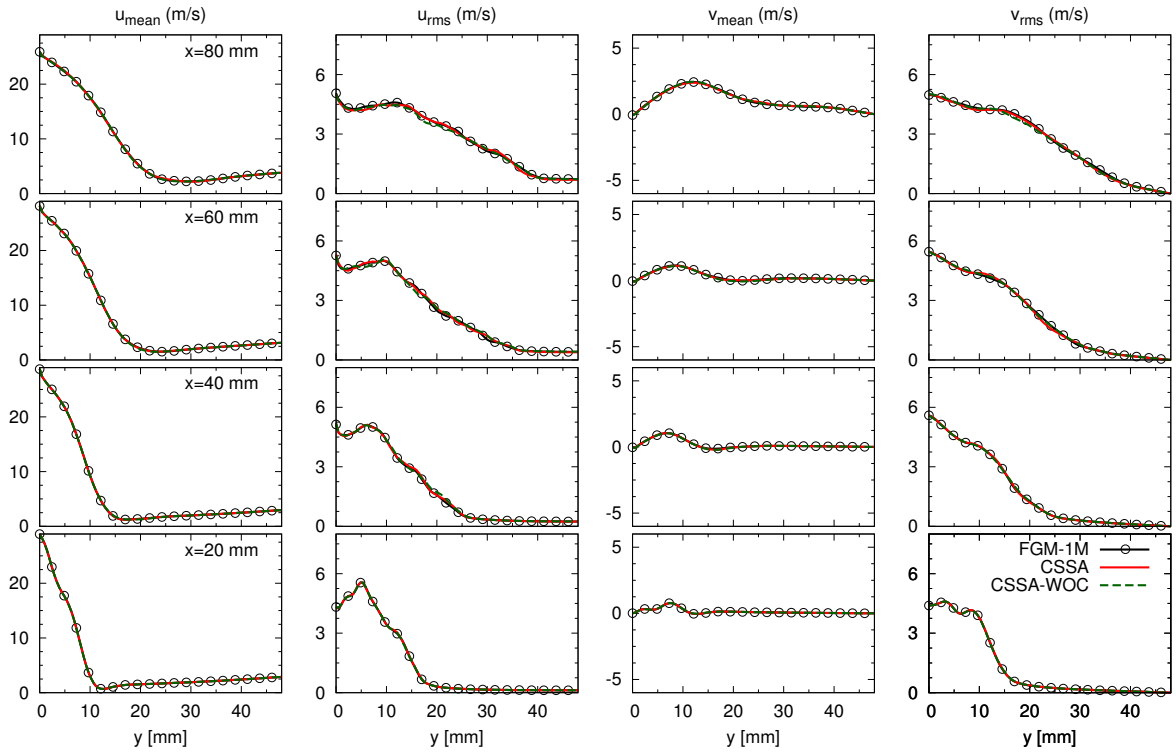

Figure 7.11: Axial u and radial v velocity profiles at different axial positions calculated with three different methods: FGM-1M (black line + symbol), CSSA (red solid line), CSSA without the correlations (green dashed line),

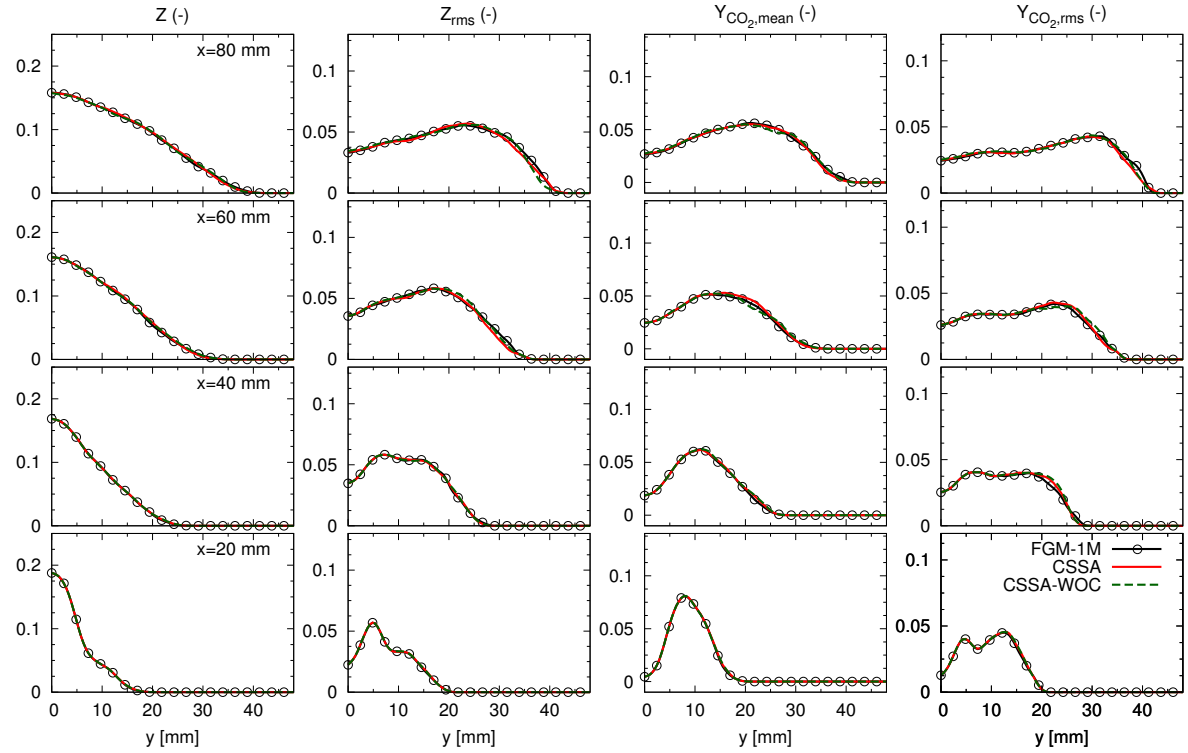

Figure 7.12: Profiles of the mixture fraction ($\mathcal{Z}$) and the CO_2 mass fraction (Y_{CO_2}) at different axial positions.

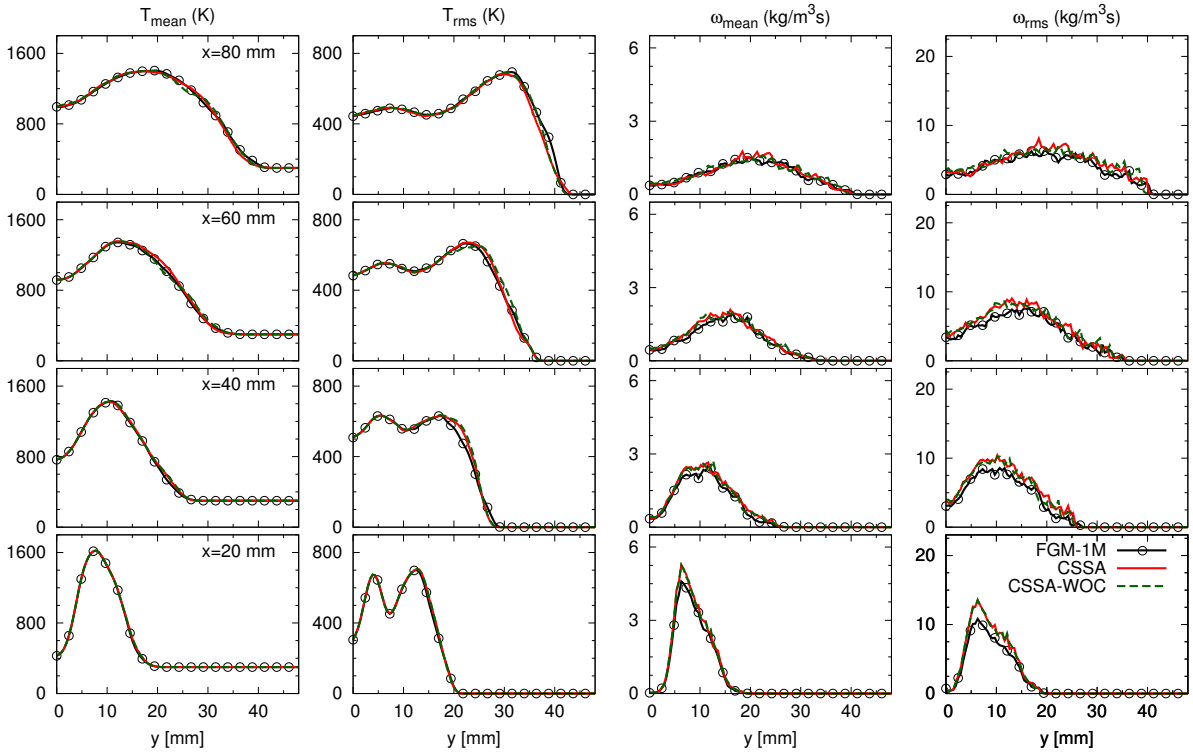

Figure 7.13: Profiles of the temperature (T) and the CO_2 source term ($\dot{\omega}$) at different axial positions.

At lower axial positions CSSA - both with and without having set the correlation - predicts higher mean CO_2 source term values (Figure 7.13). This can be explained with the sharp distribution of the source term which covers only a few cells close to the inlets coupled with the fact that the chemical source term is a strongly non-linear function of the control variables.

Based on these results we can draw the conclusion that for this non-premixed case the CSSA method can reproduce the reference solutions obtained with the FGM-1M method. This shows us that the SA algorithm and the sample generation have been correctly implemented and the whole procedure is capable of handling complex cases with changing mixture fraction and progress variable in the presence of intensive flame-turbulence interaction.

7.5 Summary

We presented four different two-dimensional cases in this chapter the calculations of which were carried out with the intention of verifying the CSSA method. Each case focused on either a different control variable or on a specific phenomenon in order that we could assess various aspects of the model and that the tests could have identified the nature of any shortcomings.

1. **Isothermal Mixing Jet** - a non-reacting case with pure mixing.
2. **Bunsen Flame** - a laminar premixed flame with constant mixture fraction in the domain. Two variants were evaluated: an adiabatic and a non-adiabatic one in which the heat losses at the walls had to be accounted for. This tested the implementation of the enthalpy variable.
3. **Unsteady Premixed Flame** - constant mixture fraction but intensive flame-turbulence interaction. The flame was stabilized in a turbulent flow field which led to a wide flame brush and the wrinkling of the flame front.
4. **Planar Jet** - a complex case in which all control variables evolved and owing to the turbulent fluctuations imposed on the inflow, the flame-turbulence interaction was significant.

The CSSA results were compared to reference solutions calculated with the FGM-1M method on fine grids. The results were in very good agreement, only minor differences have been observed in the case of the planar jet. In this particular configuration we investigated the effect of accounting for the correlations by comparing the CSSA results to the results of simulations during which the simulated annealing procedure was turned off thereby only the variances were considered. We found only minor differences indicating that taking into consideration the correlation can alter the results, although in this particular case the changes were of little importance. Overall we can conclude that the CSSA method has been verified and it is capable of properly describing turbulent combustion processes. In the next chapters we will proceed with applying the model to three-dimensional cases and comparing the results with experimental data.

Chapter 8

Applications

In this chapter we use the CSSA method to simulate well-known three-dimensional configurations, which have been thoroughly investigated for many years. Our objective is to validate the new method by comparing the simulation results to the existing experimental data.

In terms of complexity these standard test cases do not reach the level of real industrial systems, but this is a compromise we have to make in order to be able to gain sufficiently detailed experimental results. These measurements mostly rely on advanced laser diagnostic techniques which require the domain of interest to be optically accessible which is not the case for most industrial systems. Furthermore, if all the fine details and auxiliary parts of such a system were included in the computational domain, the computational costs would increase significantly. Simulating all the zones which are non-relevant from a combustion point of view would make parameter studies unfeasible due to increased calculation times.

Although simpler in geometry, the chosen test cases do reproduce important physical processes that are relevant to the industrial applications. All the considered setups are open and combustion takes place under ambient conditions ($p = 1\ bar$ and $T_a = 300\ K$). In all the cases the chosen fuel is methane which reacts with air. The methane-air mixture has the advantages of being both relevant to gas turbines along with having a reaction path that is well understood. Additionally, the skeletal mechanisms for the numerical work of this mixture are well-established. In the simulations the GRI3.0 mechanism [171] is used to describe reaction kinetics as it was the case in the previous sections.

Owing to the simple and easily accessible domains of interest we can focus our investigations on the underlying fundamental processes. The experiments yield fine details which provide valuable insight regarding the emerging flame structure and flame-turbulence interaction. This makes the thorough validation of novel modeling approaches possible. Validation data exists for both isothermal and reacting cases therefore the flow field and the combustion process can be studied separately. We focus our attention on the reacting cases since the CSSA model's novelty lies in the treatment of the control variables. The effects of grid spacing, boundary and initial conditions, time steps, etc. have been extensively studied in previous works for the discussed configurations and the settings of our simulations have been chosen accordingly.

Although we do not address here the problem of comparing mass weighted LES results

to unweighted experimental data, we should point out that it is still an open issue and one should exercise great care. Künne elaborated on this topic [107] pointing out that the applied $Le = 1$ assumption yields a constant mixture fraction through the flame while in reality due to preferential diffusion a slight drop can be observed at the flame front. This effect is exacerbated by that in experiments species concentrations are measured not element mass fractions as required by the mixture fraction definition. Consequently the simulations can overpredict the mixture fraction, however, considering all the other uncertainties this discrepancy should be a minor one.

The chapter consists of two sections, which discuss the Sandia Flame D and the Sydney Bluff-Body case, respectively.

8.1 Sandia Flame D

Flame D is a piloted methane-air jet flame stabilized on a burner developed by the University of Sydney [122]. It is one of the standard cases included in the Sandia flame series, which comprises multiscalar measurement data. Due to the detailed experimental results, Flame D is one of the most frequently used test cases when it comes to validating new models [16]. The most recent results can be found in the Proceedings of the International Workshop on Measurement and Computation of Turbulent Nonpremixed Flames (TNF) [19].

For a detailed description of the configuration and the measurements the reader is referred to the openly accessible documentation provided by TNF [21]. Here we restrict ourselves to highlighting the most important features of this test case.

8.1.1 Description of Configuration

The two-dimensional cross-section of the inlet zone of the axially symmetric configuration is depicted in the schematic diagram of Figure 8.1. The inlet of the domain consists of three parts: the main jet, the pilot, and the coflow.

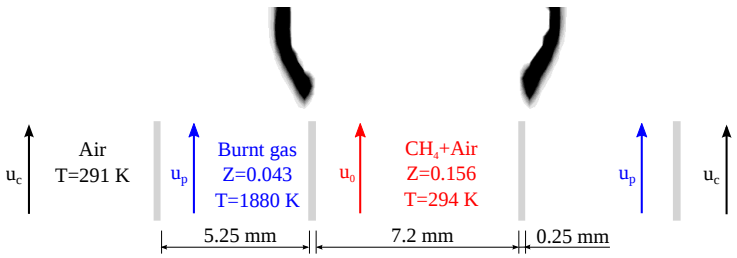

Figure 8.1: Schematic diagram of the inlet zone with the important parameters. The inlet zone consists of three parts: the main jet, the pilot, and the coflow. The mean CO_2 is also depicted in the diagram showing that the chemical reaction happens between the main jet and the pilot.

The inner diameter of the central nozzle is $d = 7.2\ mm$. The bulk velocity of the main jet is $u_0 = 49.6\ m/s$ and the mixture is made of 75% air and 25% methane by volume which means a mixture fraction of $\mathcal{Z}_0 = 0.156$. The temperature of the mixture is 294 K. The pilot annulus has an inner diameter of $d_{pi} = 7.7\ mm$ (the wall thickness is 0.25 mm) and an outer diameter of $d_{po} = 18.2\ mm$. The bulk velocity of the incoming hot burnt gases is $u_p = 11.4\ m/s$, their temperature is $T_p = 1880\ K$. Tang et al. [180] pointed out that the model predictions tend to be very sensitive to the uncertainty of the pilot boundary conditions, which can be measured with only limited accuracy.

The pilot flame is oxidizer-rich ($\mathcal{Z}_p = 0.043$) and the hot burnt gases not only play the role of stabilizing the flame but also provide oxidizer for the fuel-rich main jet. Consequently the flame starts burning directly at the inlet between the pilot and the main jet. Since the main jet is partially premixed, the flame length is reduced and the flame is more robust than it would be if it was a pure methane flame. As a result the flame can be operated at a reasonably high Reynolds number ($Re = 22400$) without significant local extinction [20]. Owing to the high enough mixing rates, the flame burns as a diffusion flame. Experiments suggest that there is no significant premixed reaction in the fuel-rich mixture.

The outer diameter of the burner is $d_{po} = 18.9\ mm$ (the wall thickness is 0.35 mm) and it is surrounded by a coflow of pure air. The velocity and the temperature of this coflow are $u_c = 0.9\ m/s$ and $T_c = 291\ K$.

8.1.2 Experimental Data

The velocity measurements were carried out at the Technical University of Darmstadt using two component laser-Doppler anemometry (LDA) [166]. Sandia National Laboratories provided the temperature and species mass fractions data, including N_2, O_2, H_2O, H_2, CH_4, CO, CO_2, OH, and NO, measured by Barlow et al. [20–22] and Frank et al. [63].

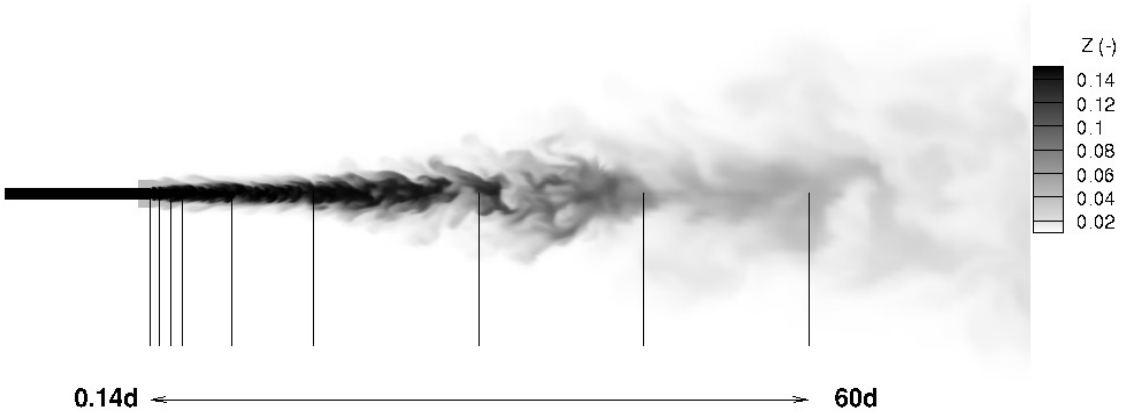

Figure 8.2: Axial positions of the profile measurement planes. At $x/d = 0.14$ only the velocity components are measured, the mixture fraction, the species mass fractions, and the temperature are not.

The temperatures were obtained with Rayleigh scattering except for close to the burner ($x/d \leq 3$) where they were determined using the ideal gas law and the total density inferred from the species mass fraction data. Most species mass fractions were measured with Raman scattering, but laser induced fluorescence (LIF) was used for the species OH, NO, and CO. Radial profiles of scalar measurements are available at different axial positions depicted in Figure 8.2. The data set includes Reynolds- and Favre-averaged mass fractions and root mean square fluctuations.

8.1.3 Numerical Setup

The block-structured hexahedral grid used for this simulation consists of 437 blocks and 3.3 million control volumes the smallest of which are approximately 0.125 mm in the radial and 0.25 mm in the axial direction. This choice is in accordance with the findings of Aschmoneit [16] who compared grids of different spacings. An O-grid structure made it possible to combine the fine resolution in the flame zone with a reduced number of cells near the outflow (Figure 8.3b). The dimensions of the rotationally symmetric computational domain are scaled with the d diameter of the inner nozzle and are illustrated in Figure 8.3a.

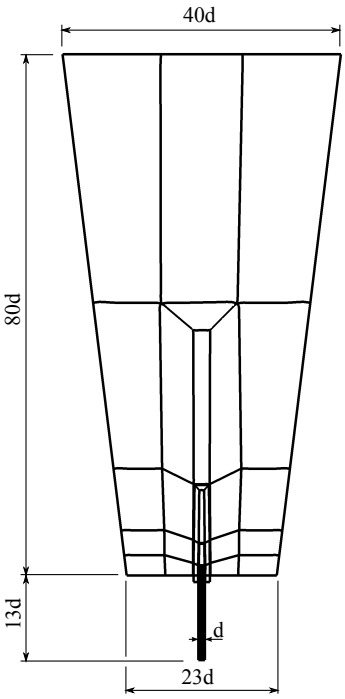

(a) Block structure and dimensions

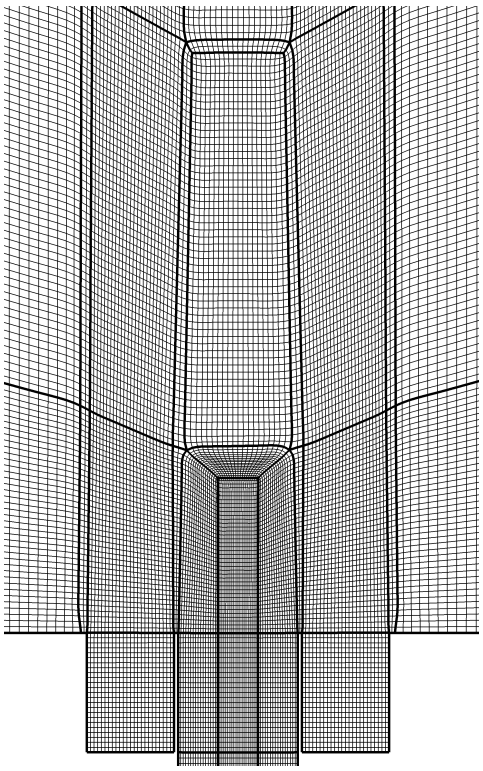

(b) O-grids are applied

Figure 8.3: The dimensions of the computational domain are provided in the units of the diameter of the main nozzle (d). The grid consists of 437 blocks and 3.3 million cells. An O-grid structure was applied to ensure the sufficient resolution of the flame zone. The grid was provided by Flavia Miranda (TU Darmstadt).

The domain has a height of $80d$ and its width is linearly increasing axially from $23d$ to $40d$. Additionally $13d$ of the upstream region of the main nozzle is simulated to allow the turbulent velocity profiles to develop in the pipe. The inlet of the pilot is positioned at $x = -1d$.

In the experiment the pilot is not a simple coflow jet, but a premixed flame ejected through a large number of small holes. This shows that setting the boundary conditions appropriately is not straightforward since there are inherent simplifications in the simulation. Vreman et al. [187] set the inflow boundary conditions using the measurement data obtained at low axial positions at the nozzle exit or just above. We take a somewhat similar approach but following Aschmoneit [16] instead of taking the measured profiles directly as inlet boundary conditions we set the inlet velocities for the inner nozzle and the pilot respectively to obtain such a flow field at $x = 1\ mm$ that closely matches the experimental velocity results. After having carried out a parameter study we settled for the bulk velocities of $u_0 = 51.9\ m/s$ and $u_p = 13.0\ m/s$ on which we imposed artificially generated turbulent fluctuations [100]. Outside of the pilot tube the axial velocity is set to $u_{co} = 0.9\ m/s$. The bulk radial velocity is 0 at all inlets. These inlet conditions yielded the velocity profiles in Figure 8.4. We will further elaborate on the visible discrepancies in the next section. At the outlet ($x = 80d$) convective ouflow boundary condition is applied.

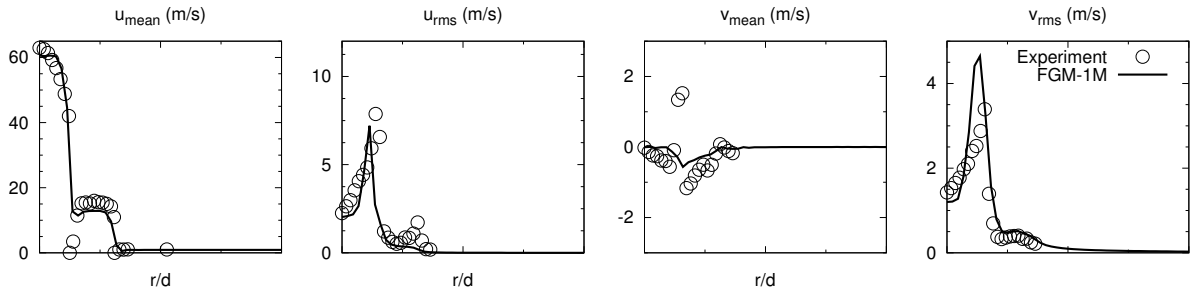

Figure 8.4: Measured (symbols) and calculated (solid line) velocity profiles at $x = 1\ mm$ just above the nozzle exit.

The mixture in the main jet consists of 25% methane and 75% air. In the postprocessing the mixture fraction is set that $\mathcal{Z} = 1$ corresponds to this mixture while $\mathcal{Z} = 0$ refers to pure air. We used the same chemistry table as in the previous cases. The flamelet solutions were calculated with the GRI3.0 mechanism [171] and equal diffusivities for all species were assumed ($Le = 1$). The table features 1001 data points in the mixture fraction, 101 in the progress variable, and 186 in the enthalpy directions.

8.1.4 Results

The velocity, mixture fraction, and progress variable profiles are illustrated in Figure 8.5 and 8.6.

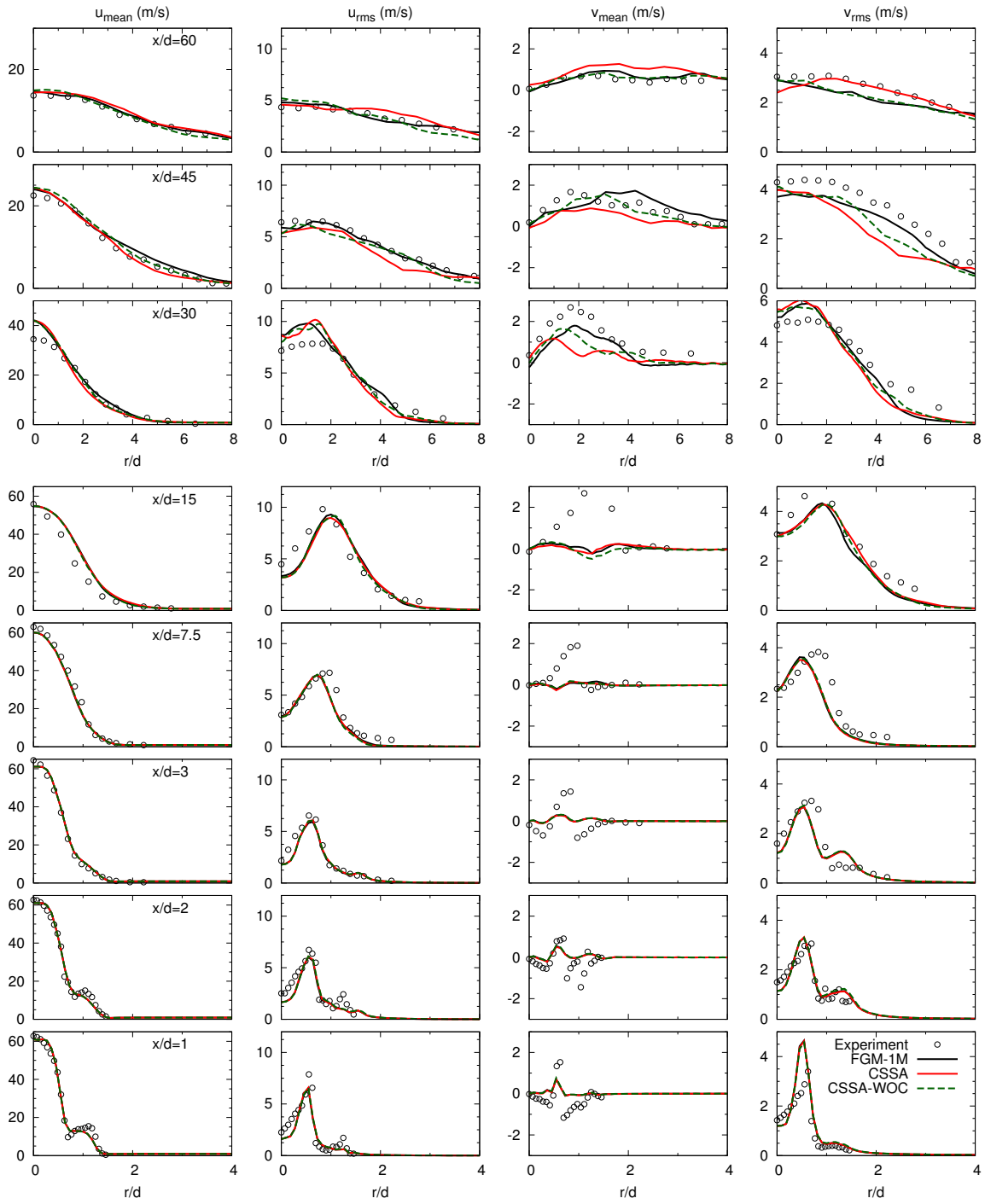

Figure 8.5: Axial u and radial v velocity profiles at different axial positions calculated with three different methods and compared to experimental results (symbols): FGM-1M (black solid line), CSSA (red solid line), CSSA without the correlations (green dashed line).

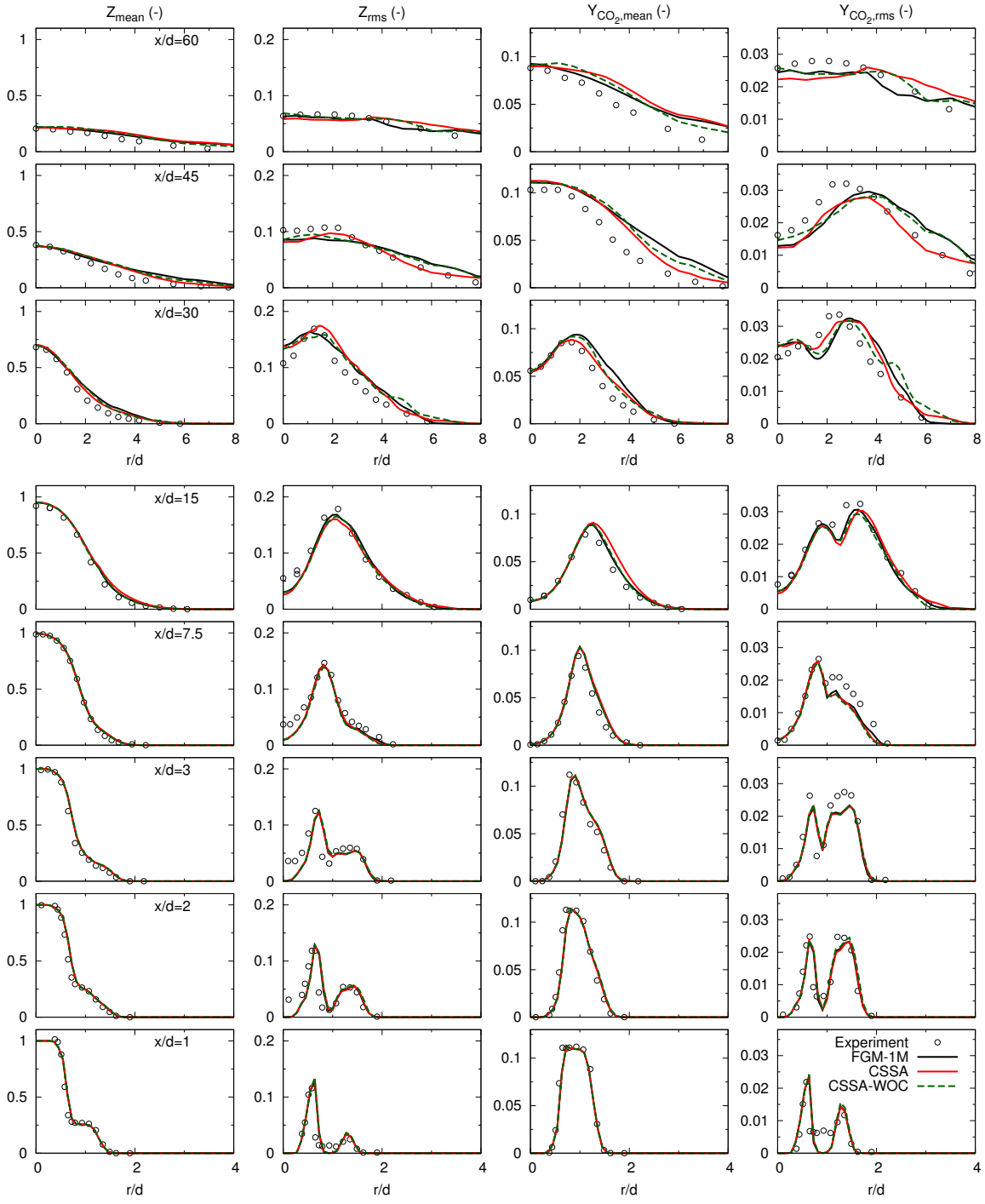

Figure 8.6: Profiles of the mixture fraction ($\mathcal{Z}$) and the CO_2 mass fraction (Y_{CO_2}) at different axial positions. Results are calculated with three different methods: FGM-1M (black solid line), CSSA (red solid line), CSSA without the correlations (green dashed line); and they are compared to experimental data denoted with symbols.

The simulation results are in good agreement with the experimental data except for the radial velocity at lower axial positions. This can be explained with that the $13d$-long main nozzle is not long enough for the turbulent velocity profile to fully develop. This is in

accordance with what we have seen in Figure 8.4. At higher axial positions the difference between the measured and the calculated radial velocities gradually diminishes which also shows that the discrepancy originates from the inlet profile. However, Vreman et al. [187] and Pitsch and Steiner [145] showed that the turbulent fluctuations imposed on the inlet velocities do not have a major effect on the results as we can see above $x/d = 30$. The vortices generated in the shear layer between the main jet and the pilot are much more important regarding the development of the flow field.

At lower axial positions the results obtained with the three different methods are essentially identical. Differences emerge at $x/d = 15$ and above. We can confirm what we experienced in the case of the planar jet: neglecting the correlations (solutions are denoted with CSSA-WOC in the figures) leads to slightly different profiles compared to the full CSSA model. This is especially obvious when we look at the profiles at higher axial positions.

It would be premature to conclude that one model is clearly more accurate than the others based on these results, however, it is worth pointing out that especially at $x/d = 45$ and $x/d = 30$ the CSSA results are closer to that of the experiments than the standard FGM-1M model. This is rather promising and shows the potential of the new approach.

As the profiles have already indicated, the calculated mean flow fields are almost identical regardless of which model has been used therefore contour plots are not informative. The only exception is the mean CO_2 source term ($\overline{\dot{\omega}}_{CO_2}$) depicted in Figure 8.7.

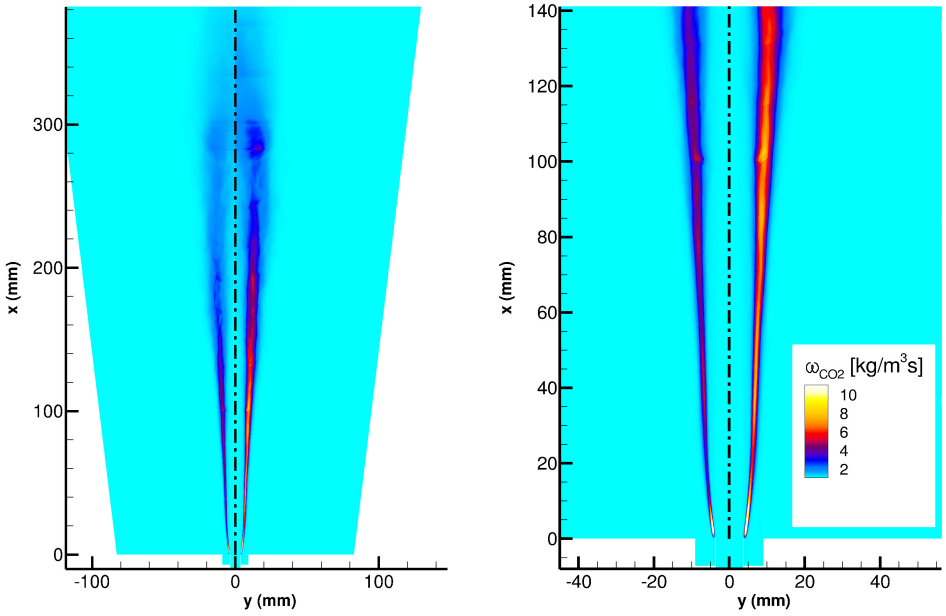

Figure 8.7: Two-dimensional cross-section of the distribution of the mean CO_2 source term. Results of the CSSA (right half of both images) and the FGM-1M (left halves) methods are compared.

When calculated with CSSA, the distribution of $\overline{\dot{\omega}}_{CO_2}$ becomes wider and its peak values are increased at higher axial positions compared to when we use the FGM-1M method. Since the source term is a strongly non-linear function of the control variables and it

is non-zero only in a very narrow zone, when it is not sufficiently resolved the FGM-1M method becomes rather inaccurate: it can underestimate a source term peak that is situated at the boundary of two adjacent control volumes but it can overestimate the source term if the narrow peak is located close to the center of the control volume. When the subgrid-scale variances are accounted for, this effect is dampened and consequently the $\bar{\dot{\omega}}_{CO_2}$ profile becomes wider with lower peak values. However, the CSSA method yields higher peak values for the mean source term at most axial positions. This is not contrary to the previous statement. Due to the wider profile, intermittency becomes less pronounced and fluctuations become lower (Figure 8.8) leading to a higher mean value than what can be obtained with FGM-1M.

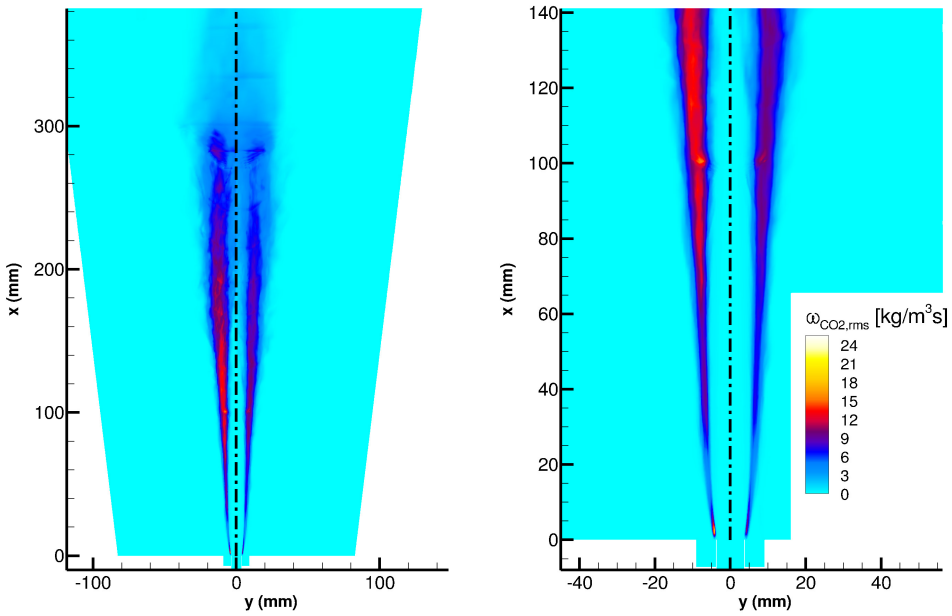

Figure 8.8: Two-dimensional cross-section of the distribution of the mean CO_2 source term. Results of the CSSA (right half of both images) and the FGM-1M (left halves) methods are compared.

8.1.5 Summary

The Sandia Flame D configuration has been calculated with three different methods - FGM-1M, CSSA, CSSA-WOC - and the results have been compared to experimental data. Based on the very good agreement we can conclude that the CSSA method provides valid results and at higher axial positions even slightly better ones than the FGM-1M method. Considering that Flame D is a simple case from the point of view of unresolved variances - no quenching, local extinction [20], or flame-wall interaction are present -, the subgrid-scale fluctuations are not expected to have a major effect. The FGM-1M and CSSA results are expected to be closely aligned, which is in agreement with the findings. It has also been observed that taking into consideration the correlations makes a difference as the CSSA and CSSA-WOC results slightly deviate from each other. The calculation of a single time step took on average 2.2 times longer with CSSA than with FGM-1M.

8.2 Bluff-Body Stabilized Non-Premixed Flame

We considered a jet burner in the previous section that is a rather simple configuration. It makes the investigation of flame-turbulence interaction possible, but with industrial applications in mind we should be able to handle more complex geometries and flow fields. In this section we move one step further and have a look at a more sophisticated setup with higher industrial relevance: a turbulent non-premixed flame stabilized on an axisymmetric bluff-body burner namely the HM1e configuration, which is part of the TNF workshop series. This setup was defined originally by Dally and Masri [46; 47] at Sydney University and has been thoroughly investigated by several research groups including EKT at TU Darmstadt [90; 93]. It is considered as one of the standard validation cases due to the existing and openly accessible detailed experimental results [13]. The initial and boundary conditions are simple and well-defined, furthermore the flame is nonsooting thereby facilitating laser diagnostics. These properties make the burner in question a favored model problem for industrial flows.

8.2.1 Description of Configuration

The geometry of the experimentally investigated burner is schematically illustrated in Figure 8.9. The cylindrical bluff-body, the diameter of which is $d = 2R = 50\ mm$, is surrounded by a coaxial co-flow inside a square-shaped wind tunnel with an edge length of 150 mm. The co-flow is pure air at atmospheric pressure and a temperature of 300 K. The fuel is a mixture of methane and hydrogen ($50-50\%$ by volume) and is injected into the domain through a cylindrical hole with a diameter of $d_j = 3.6\ mm$. The bore leading

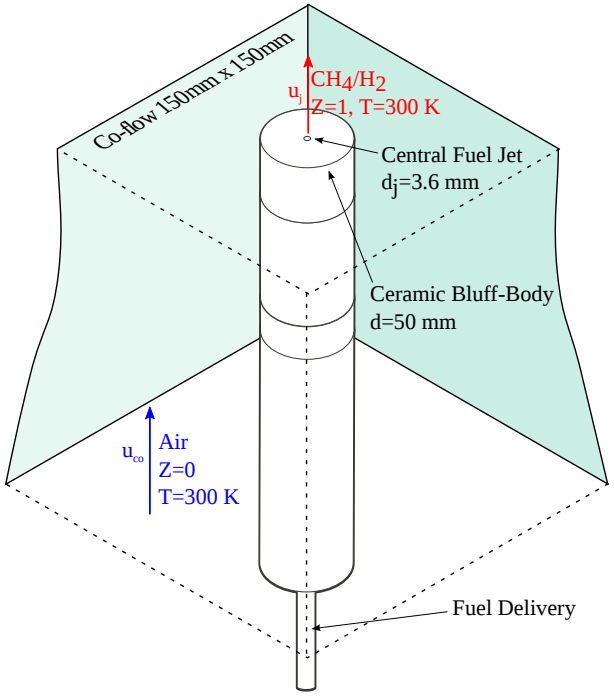

Figure 8.9: Configuration of the Sydney bluff-body burner [13]

to this inlet is coaxial with the outer surface of the bluff-body. The temperature and pressure of the fuel equals that of the co-flow. The co-flow enters the domain at a velocity of $u_{co} = 35\ m/s$ while the velocity of the fuel jet is $u_j = 108\ m/s$ yielding a Reynolds-number of $Re_j = 14600$. The case with these velocity settings is called HM1e. The developing flame is stabilized due to the recirculation, of hot burnt gases which preheat the incoming fuel. An instantaneous velocity field is illustrated in Figure 8.10 using uniformly sized vectors. The emerging recirculation zones can be clearly identified.

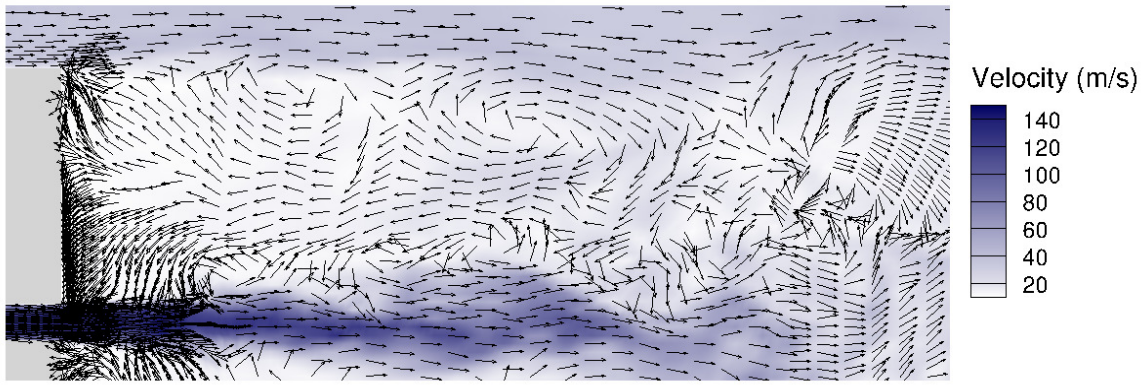

Figure 8.10: The recirculation zones can be identified behind the bluff-body in this vector-plot of an instantaneous velocity field. In the diagram the vectors have uniform lengths for illustration purposes and only every eighth of them is depicted.

8.2.2 Experimental Data

Dally et al. [13; 46; 47] measured the velocity, the species concentration, and the temperature profiles at different axial positions which are illustrated in Figure 8.11. For the velocity measurements Laser Doppler Anemometry (LDA) and Particle Image Velocimetry (PIV) were used and experiments were carried out using the HM1e settings. However,

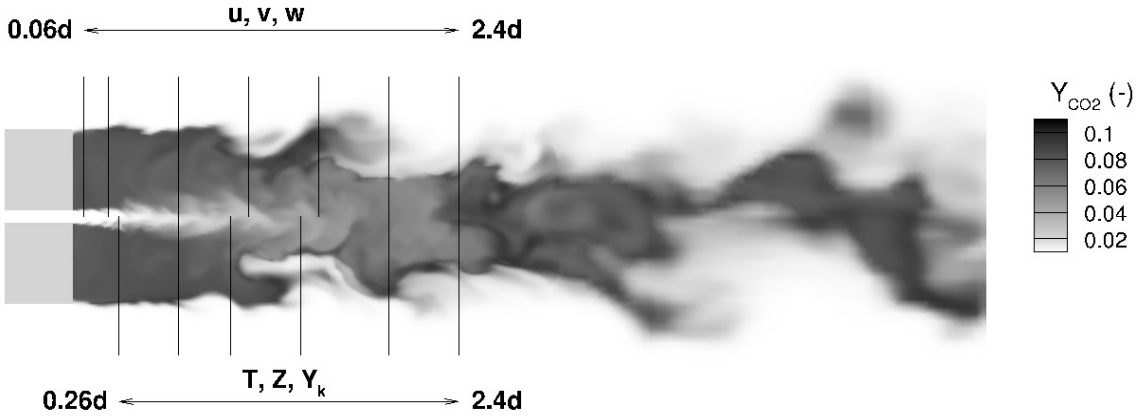

Figure 8.11: Axial locations of profile measurements.

for the scalar measurements - Raman/Rayleigh scattering combined with Laser Induced Fluorescence (LIF) - the velocities were slightly higher: $u_{co} = 40\ m/s$ and $u_j = 118\ m/s$. These settings are referred to as HM1. The reason for this difference is that the measurements were taken on two different test rigs. The Sydney wind tunnel, where the velocity data was taken, could not achieve a constant velocity at 40 m/s. It has been shown that both flames are at 50% of the blowoff velocity and therefore exhibit similar flow and scalar characteristics [91; 105].

8.2.3 Numerical Setup

The cross-section of the computational domain and the applied block structure is illustrated in Figure 8.12. The domain is $3d$ wide and has a length of $6.2d$, which is sufficient for capturing the flame length. The height of the bluff-body part included in the domain is d. This equals 13.9 times the diameter of the channel of the central fuel jet which is long enough for a turbulent flow field to develop within. On the bulk velocity of the co-flow we

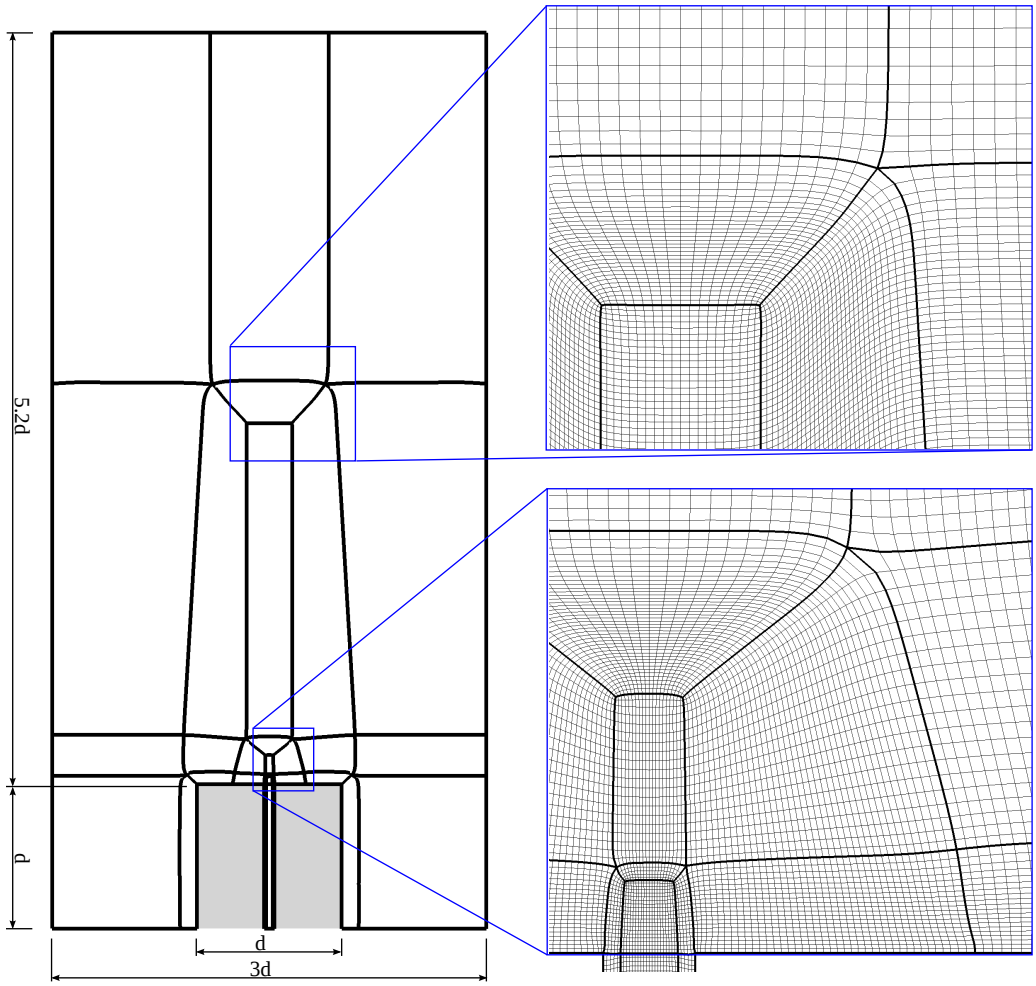

Figure 8.12: The grid consists of 56 blocks and 1.66 million cells. The resolution is refined with the application of O-grid structures.

impose artificially generated turbulent fluctuations with a turbulence intensity of 2.81% [93] using Klein's method as in the previous chapters [100]. This is necessary because the flow around the edge of the bluff-body is determined by the boundary layer on the bluff-body surface according to Kempf's results [90], therefore the effect of turbulence should be accounted for. Otherwise the boundary conditions corresponding to HM1e are applied at the inlets. On the surface of the bluff-body a simple no-slip condition is applied and convective outflow boundary condition is set at the outflow.

The entire grid consists of 1.66 million control volumes the sizes of which gradually increase from 0.1 mm in the fuel jet to almost 2 mm near the outflow. The fine resolution has been achieved by the application of O-grids certain parts of which are also depicted in Figure 8.12. The applied time step is $1 \cdot 10^{-7}$ s which keeps the CFL number under 0.9.

The fuel is not pure methane but a mixture of methane and hydrogen, therefore a different table is required than in the previous cases. This table features 1001 data points in the mixture fraction, 101 in the progress variable, and 186 in the enthalpy directions, respectively.

8.2.4 Results

The configuration has been calculated with the CSSA method both with and without setting the correlations as well as with the FGM-1M method. The results have been compared to each other and to the measurement data. The purpose of our investigation is to validate and evaluate the performance of the CSSA method which focuses on the treatment of flame-turbulence interaction. Consequently calculating the non-reactive flow field is not important from our point of view. Readers are referred to the work of Kempf [90; 91] who elaborated on both this topic and the observed differences between the FGM-1M results and the experimental data in the reacting case. Investigating the capabilities and limitations of the simple FGM-1M method is not in the focus of this work either. The applicability of FGM to combustion LES and to the Sydney bluff-body burner have been addressed by Olbricht [131] and Ketelheun [93] among others. We use the FGM-1M results as reference solutions to investigate how different the CSSA results are and where the new approach could bring some improvements.

In Section 6.2 we have already shown that the mixture fraction and the reaction progress variable are far from being uncorrelated (Figure 6.6). We concluded that the observed correlation coefficient values are in accordance with our expectations considering the structure of the non-premixed flame.

Figure 8.13 shows instantaneous snapshots and mean fields of the mixture fraction and the progress variable to illustrate the flame structure. As we saw in Figure 8.10 a recirculation zone develops downstream the bluff-body. Owing to this recirculation the fuel is preheated and the temperature distribution as well as the CO_2 concentration are nearly uniform above the bluff-body. Since the stoichiometric mixture fraction is very low, $\mathcal{Z}_{st} = 0.05$, the chemical reaction mainly takes place at the outer edge of the bluff-body as we can see in Figure 8.14.

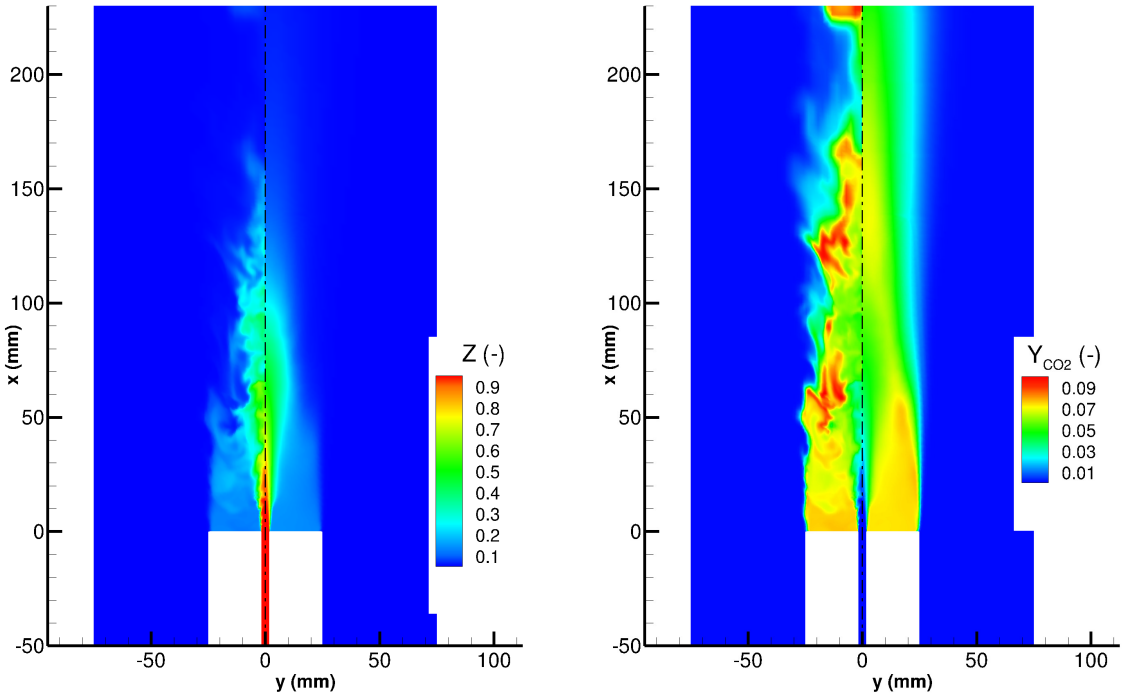

Figure 8.13: Instantaneous snapshot (left half of each plot) and time-averaged (right half of each plot) mixture fraction (left) and reaction progress variable (right) fields calculated with the CSSA method.

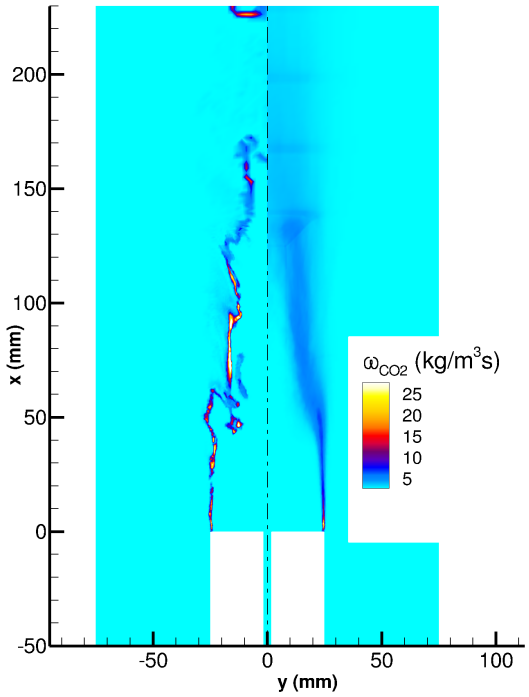

Figure 8.14: Instantaneous snapshot (left) and time-averaged (right) field of the CO_2 source term calculated with the CSSA method.

In general the FGM-1M and the CSSA results are closely aligned and they are in good agreement with the experimental data. However, while FASTEST has become more capable during the ages leading to significant improvements, the results still exhibit some of the discrepancies identified by Kempf [90]. The velocity fluctuations are no longer overpredicted in the shear layer of the central jet owing to the implementation of more sophisticated differencing schemes instead of the simple CDS. Having imposed artificial

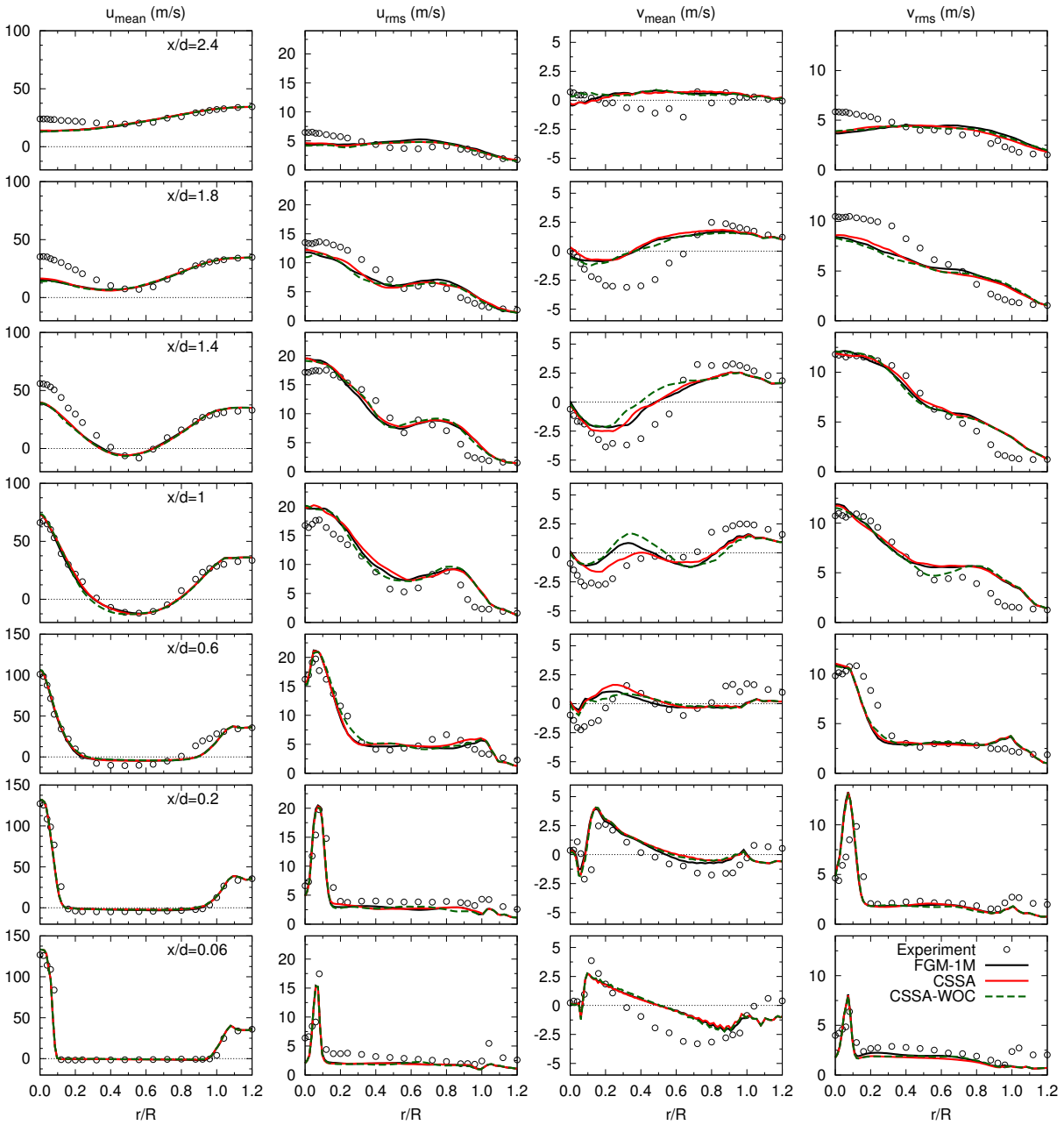

Figure 8.15: Axial u and radial v velocity profiles at different axial positions calculated with three different methods and compared to experimental results (symbols): FGM-1M (black solid line), CSSA (red solid line), CSSA without the correlations (green dashed line).

fluctuations on the co-flow velocity according to Kempf's suggestion we managed to obtain better results regarding the turbulent fluctuations in the co-flow shear layer, which were previously significantly underpredicted. The mean axial velocity near the centerline is underpredicted at higher axial positions by all the methods indicating that the central jet is predicted too short (Figure 8.15). This is confirmed by both the mixture fraction results depicted in Figure 8.16 and the radial velocity profiles at higher axial positions. The absolute radial velocity is underestimated suggesting that the recirculation zone is weaker than the experiments suggest and it does not reach the axial positions above $x/d = 1.8$. It should be noted that in the $1 \leq x/d < 1.8$ region the CSSA results are slightly better than the ones provided by FGM-1M.

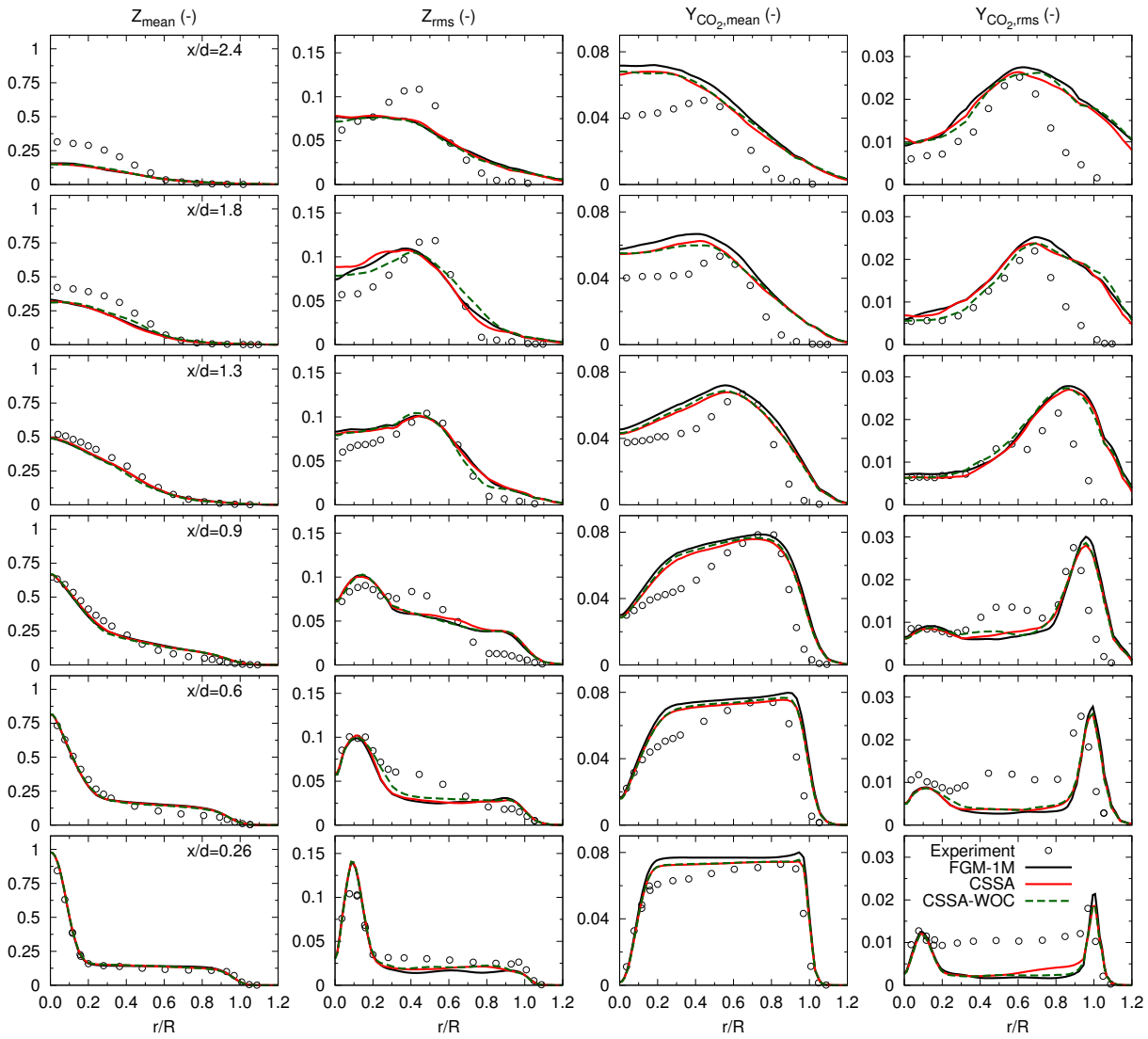

Figure 8.16: Profiles of the mixture fraction ($\mathcal{Z}$) and the CO_2 mass fraction (Y_{CO_2}) at different axial positions. Results are calculated with three different methods: FGM-1M (black solid line), CSSA (red solid line), CSSA without the correlations (green dashed line); and they are compared to experimental data denoted with symbols.

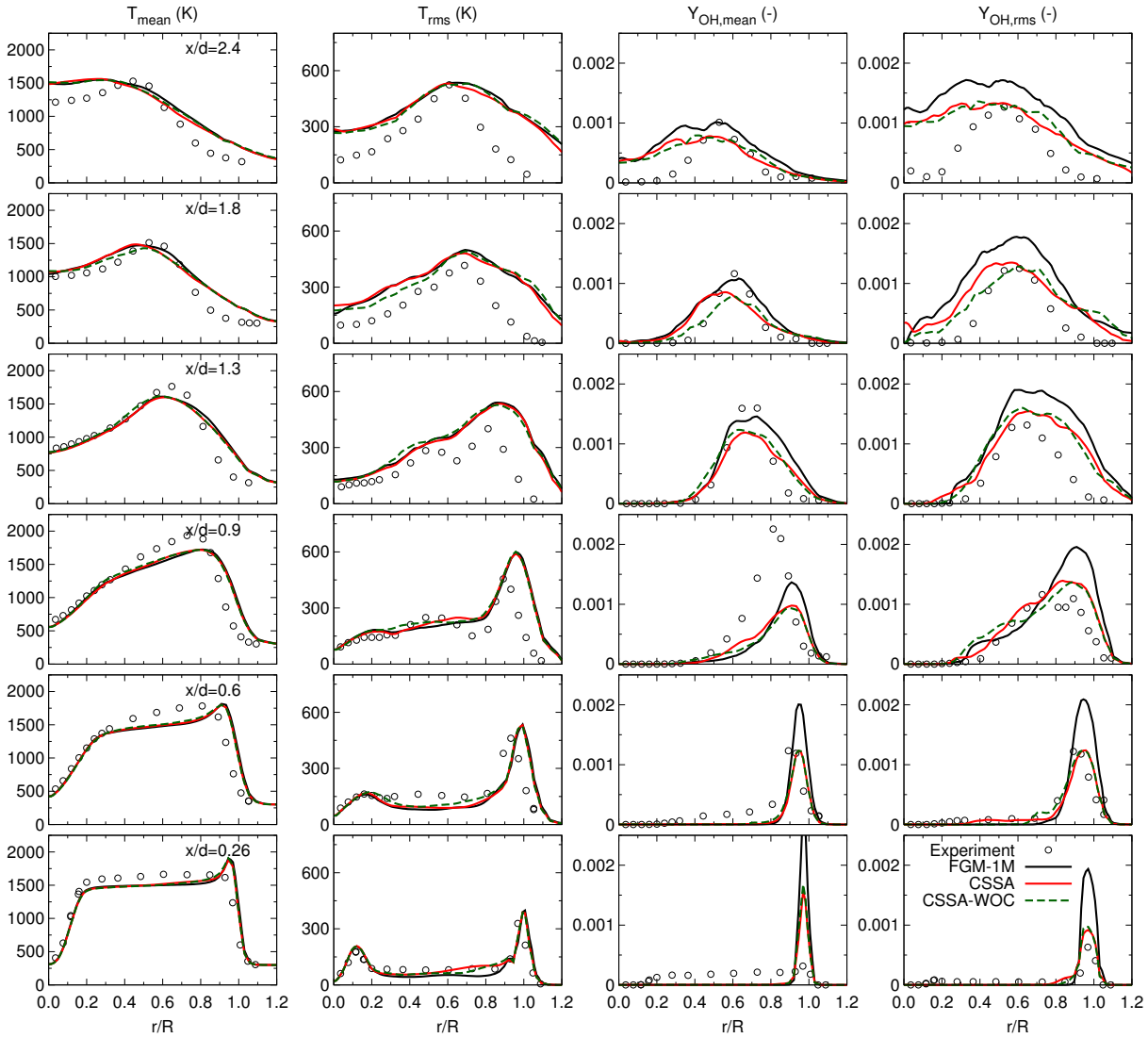

Figure 8.17: Profiles of the temperature (T) and the OH mass fraction (Y_{OH}) at different axial positions. Results are calculated with three different methods: FGM-1M (black solid line), CSSA (red solid line), CSSA without the correlations (green dashed line); and they are compared to experimental data denoted with symbols.

As we can see in Figure 8.17, the mean temperature is well-captured except for the highest axial position where it is overpredicted near the centerline which confirms, once again, that the main jet is predicted too short. The CO_2 mass fraction is significantly overpredicted in the same region but this partly comes from the limitations of the applied reduced chemical scheme and the tabulation [93]. CSSA yields slightly lower CO_2 mass fractions which are somewhat closer to the experimental results. The fluctuations of both the mixture fraction and the progress variable, and consequently of the temperature, are overpredicted at outer radial positions which can be due to the shear layer of the co-flow and the artificially set turbulent fluctuations.

The results corresponding to the OH mass fraction are the most interesting ones (Figure 8.17). In this case the CSSA method clearly outperforms FGM-1M with respect to both the mean and the fluctuating values especially at lower axial positions. OH is only present in a thin layer and, as Ketelheun [93] showed, its prediction is very sensitive to the table resolution since Y_{OH} is non-negligible only in a small parameter range in the FGM table and it is not easy to resolve. As a consequence the prediction is also extremely sensitive to the control variables. At the edge of the bluff-body both the mixture fraction and the progress variable experience sharp gradients which are not resolved sufficiently leading to further inaccuracies. Taking into consideration the subgrid-scale fluctuations with CSSA let us access the table at a wider range of parameters instead of only at the mean values. This leads to the virtual smoothing of the Y_{OH} distribution in the parameter space, consequently yielding lower peak values in the simulation at the sharp control variable gradients. This smoothing leads to lower values at higher axial positions as well.

So far we have only looked at the results of complete simulations which were carried out using the three methods: FGM-1M, CSSA, CSSA-WOC. These results are not suitable for evaluating the differences between the various methods at the level of accessing the look-up table at an individual time step as they show the cumulative effects of these step-level differences. In order to be able to directly compare the three methods, the same set of control variables has to be used to access the look-up table and the obtained thermochemical properties need to be compared. This is achieved by selecting a given time step from the simulation carried out with CSSA and extracting the control variables at different axial positions as it is illustrated in Figure 8.18.

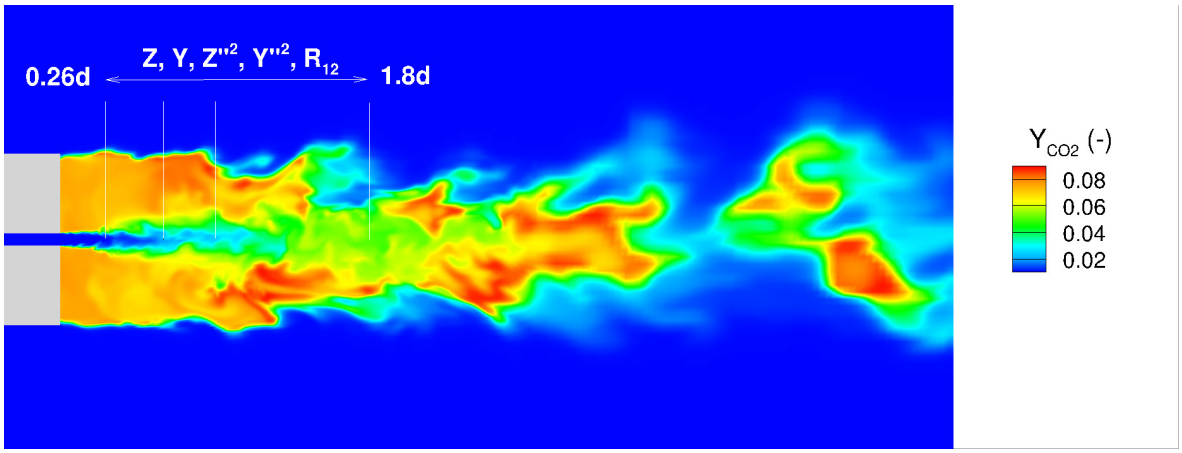

Figure 8.18: Axial locations of extracted instantaneous control variable profiles.

Using these statistical moments, the profiles of which are depicted in Figure 8.19, we look the various corresponding Φ properties up in the chemistry table following the three different methods: Φ_X denotes the value of Φ obtained with the X method. The absolute differences are small, therefore two relative differences are defined and plotted in Figure 8.20-8.25:

- the difference between the results calculated with the CSSA (or the CSSA-WOC)

and the FGM-1M procedure:

$$\Delta\Phi^1 = \frac{\Phi_{CSSA/CSSA-WOC} - \Phi_{FGM-1M}}{\Phi_{CSSA/CSSA-WOC}}. \tag{8.1}$$

$\Phi_{CSSA/CSSA-WOC}$ is used as a denominator as the methods that take into consideration the fluctuations often yield non-zero results even where Φ_{FGM-1M} equals 0, consequently this $\Delta\Phi^1$ definition leads to results that are easier to interpret than as if Φ_{FGM-1M} was the denominator.

- the relative difference between the CSSA and CSSA-WOC results to evaluate the effect of accounting for the correlation:

$$\Delta\Phi^2 = \frac{\Phi_{CSSA-WOC} - \Phi_{CSSA}}{\Phi_{CSSA}}. \tag{8.2}$$

Based on earlier results $\Delta\Phi^2$ is expected to be small compared to $\Delta\Phi^1$, therefore it is important to have a closer look at this quantity separately.

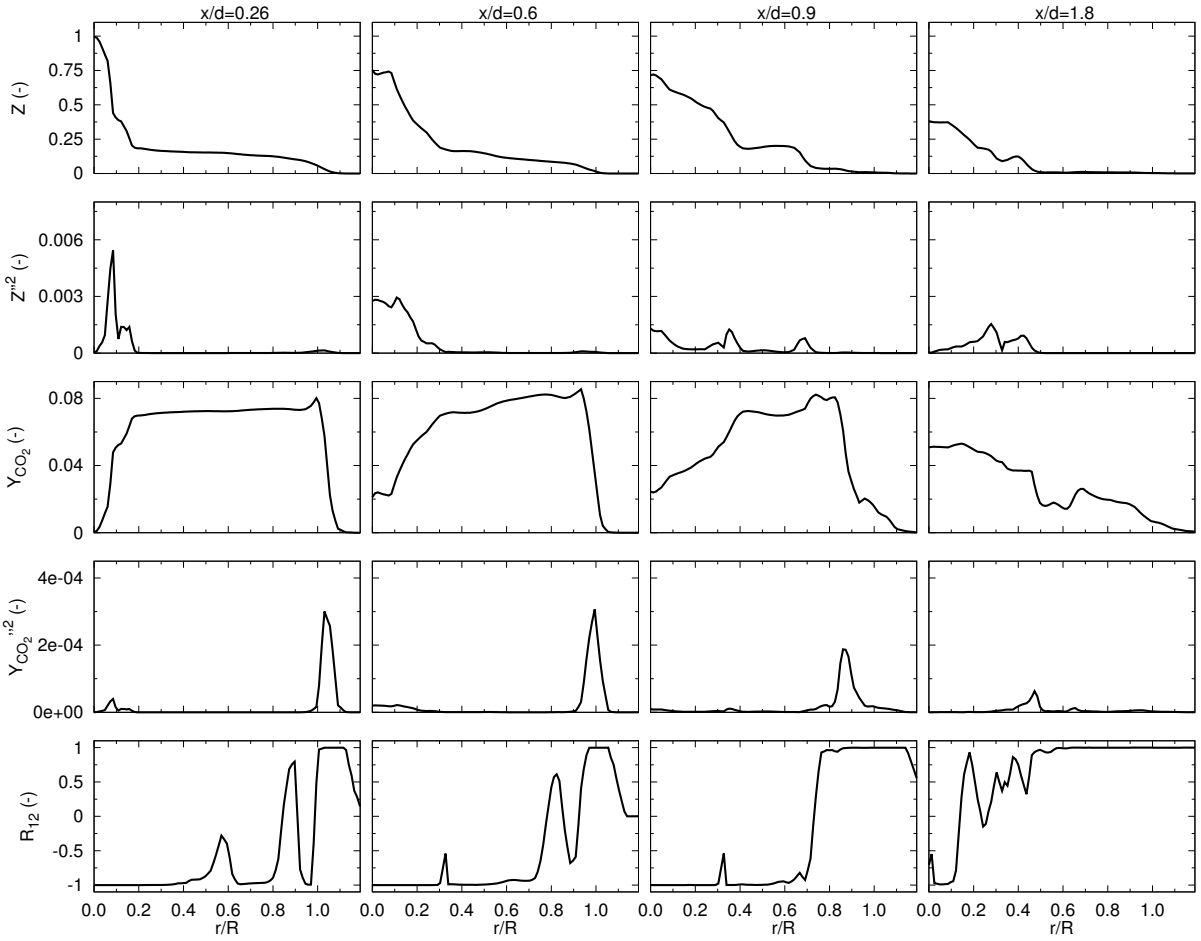

Figure 8.19: Profiles of the instantaneous mixture fraction and CO_2 mass fraction and their variances as well as the correlation coefficient at different axial positions. Results correspond to the flow field depicted in Figure 8.18.

Six properties are calculated: the temperature, the density (here contrary to the previous cases the second moments are considered when the look-up table is accessed using the CSSA method), the O_2 and the OH mass fractions, the chemical source term of CO_2, and that of NO. The NO source term is approximated using the following formula previously applied by Peters et al. [139] under the assumptions that the first reaction of the Zeldovich mechanism is rate determining and that O is in equilibrium with O_2:

$$\dot{\omega}_{\mathrm{NO}} = \rho B_{\mathrm{NO}} M_{\mathrm{NO}} \frac{Y_{\mathrm{N_2}}}{M_{\mathrm{N_2}}} \left(\frac{\rho Y_{\mathrm{O_2}}}{M_{\mathrm{O_2}}} \right)^{1/2} \exp\left(-\frac{E_{\mathrm{NO}}}{T} \right), \tag{8.3}$$

where $B_{\mathrm{NO}} = 5.74 \cdot 10^{14}$ $(\mathrm{cm}^3/\mathrm{mol})^{1/2}/s$, and $E_{\mathrm{NO}} = 66900$ K.

As we can see in Figure 8.20 and 8.21, there are only small differences between the different methods regarding the temperature and the density. The effect of the correlation is almost negligible, it is in the order of 0.1%. ΔT^1 and $\Delta \rho^1$ only become larger ($\sim 10 - 40\%$) where the temperature (or the density, respectively) gradient is large indicating that the positions of these high-gradient slopes are slightly different in the different cases. This is not surprising since the temperature and density gradients are aligned with the control variable gradients which are used for approximating the variances. If the variances are negligible then CSSA essentially reduces to the applied simple FGM-1M approach and the differences between the results obtained with the different methods diminish.

$\Delta Y^1_{\mathrm{O_2}}$ can reach values close to a 100% since the methods using the variances can yield results that are orders of magnitude higher than those obtained with the simple FGM-1M approach (Figure 8.22) for certain values of the control variables. However, these differences are of minor importance since at these locations $Y_{\mathrm{O_2}}$ is almost negligible anyway. The differences are most pronounced where the gradient of the considered thermochemical property increases abruptly. This was expected as taking into consideration the subgrid-scale distribution smooths these abrupt changes. At these locations the effect of the correlation can reach even $9 - 10\%$.

The same observations apply to the results corresponding to Y_{OH} (Figure 8.23) and the chemical source terms of CO_2 (Figure 8.24) and NO (Figure 8.25). Furthermore, in these latter cases the peak values calculated with the different methods are significantly different. This is in agreement with the previous conclusions and explanations regarding the complete simulations.

These quantitative results suggest that the second statistical moments play a more important role in the case of the mass fractions of minor species and the chemical source terms. Taking into consideration the correlation acts as a minor correction of the order of a few percentages on these rather fine grids. The effects are expected to be larger on coarser grids and this needs further investigations.

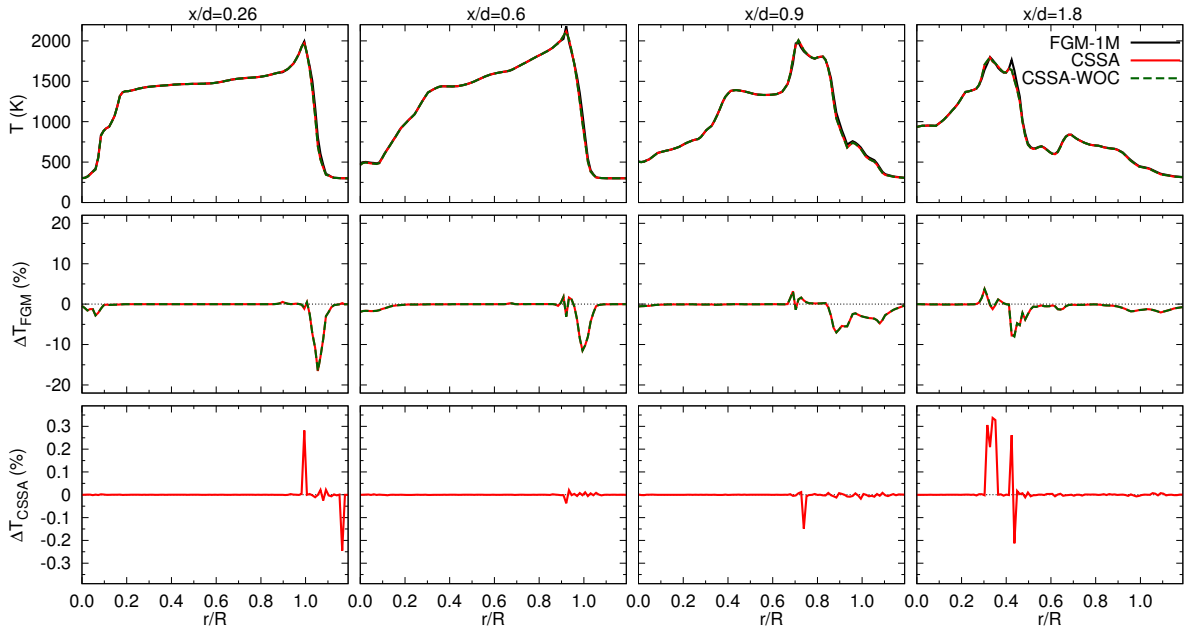

Figure 8.20: In the first row the temperature profiles obtained from the chemistry table using the three different methods and the control variables illustrated in Figure 8.18 are depicted. In the second and third rows the relative differences between these temperature profiles are shown following the (8.1) and (8.2) definitions.

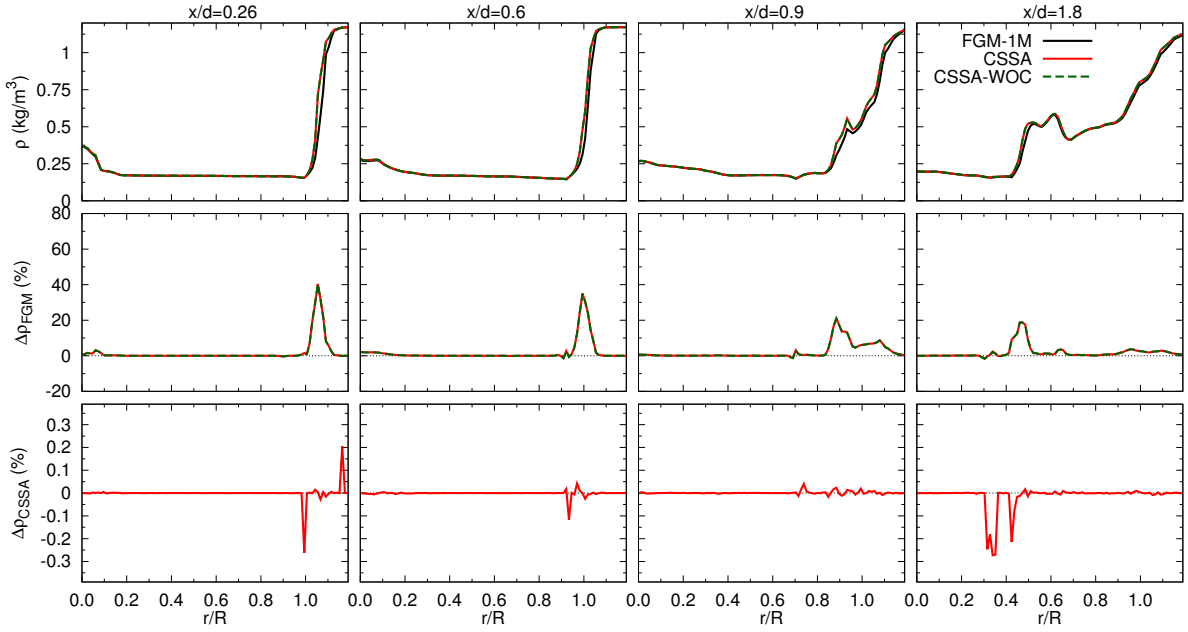

Figure 8.21: In the first row the density profiles obtained from the chemistry table using the three different methods and the control variables illustrated in Figure 8.18 are depicted. In the second and third rows the relative differences between these density profiles are shown following the (8.1) and (8.2) definitions.

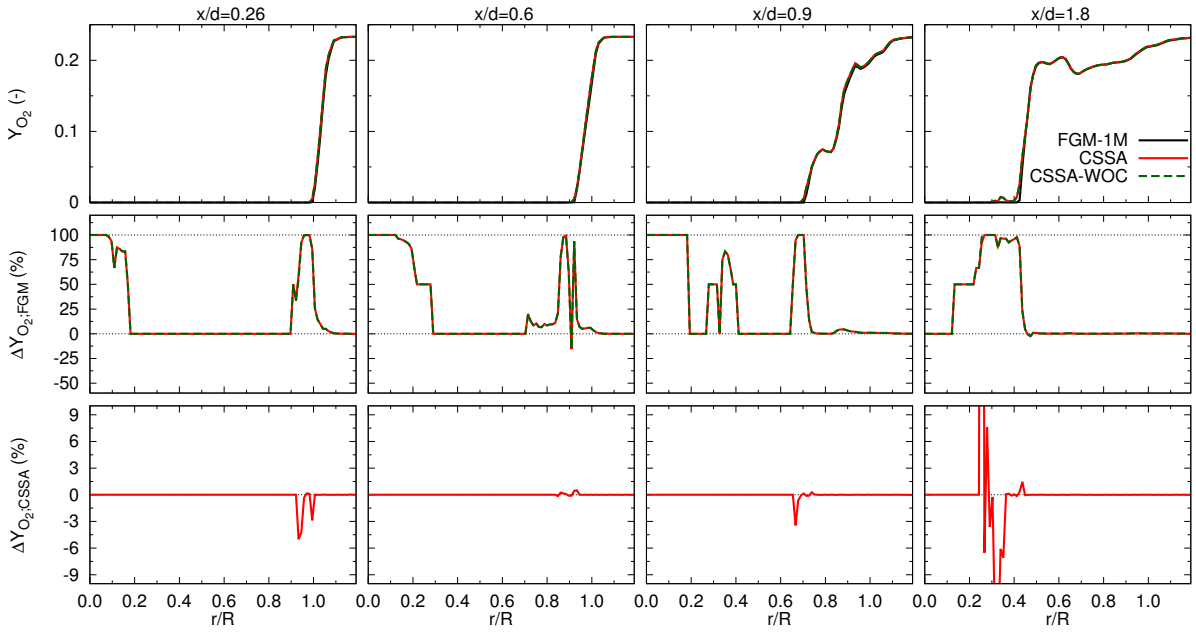

Figure 8.22: In the first row the O_2 mass fraction profiles obtained from the chemistry table using the three different methods and the control variables illustrated in Figure 8.18 are depicted. In the second and third rows the relative differences between these mass fractions are shown following the (8.1) and (8.2) definitions.

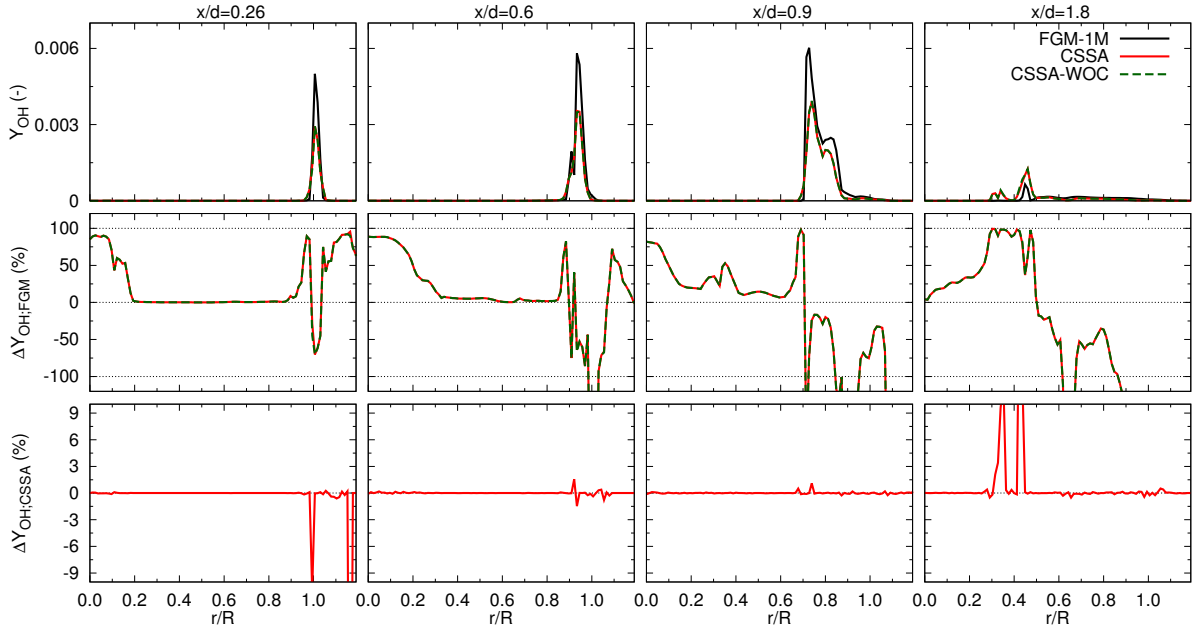

Figure 8.23: In the first row the OH mass fraction profiles obtained from the chemistry table using the three different methods and the control variables illustrated in Figure 8.18 are depicted. In the second and third rows the relative differences between these mass fractions are shown following the (8.1) and (8.2) definitions.

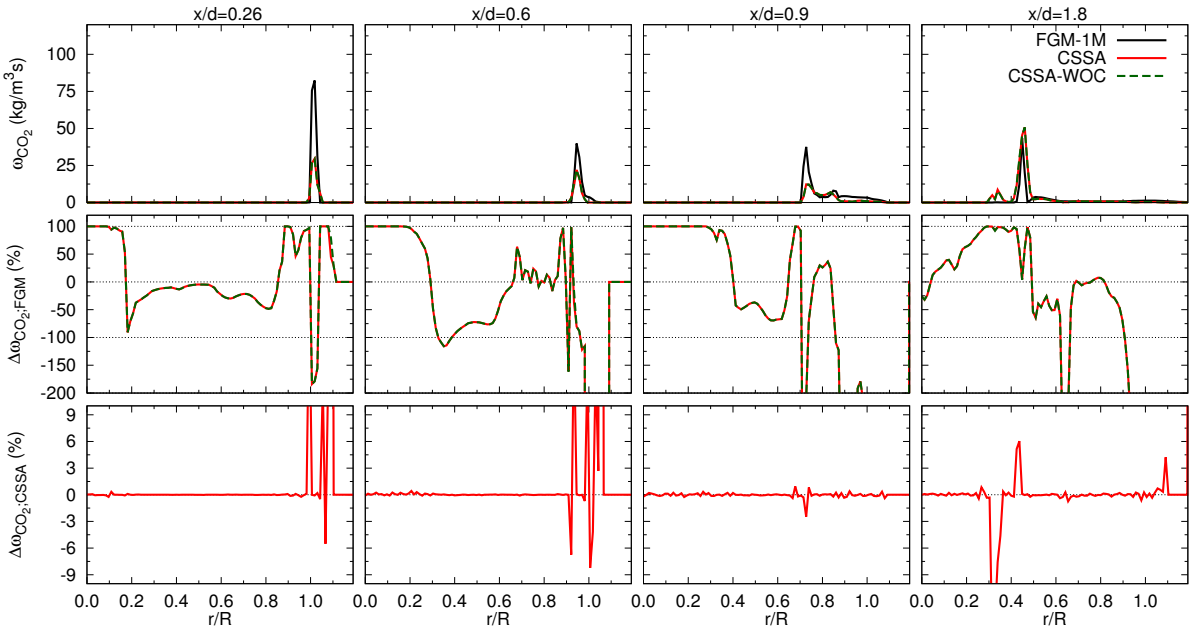

Figure 8.24: In the first row the profiles of the CO_2 source term obtained from the chemistry table using the three different methods and the control variables illustrated in Figure 8.18 are depicted. In the second and third rows the relative differences between the source terms extracted in different ways are shown following the (8.1) and (8.2) definitions.

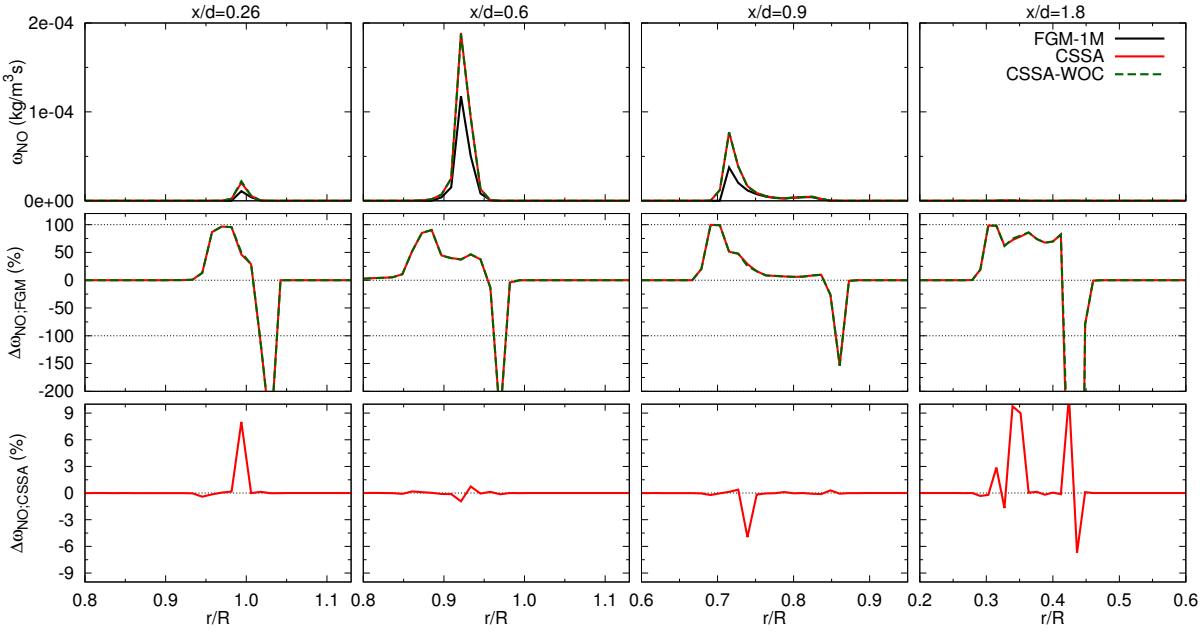

Figure 8.25: In the first row the profiles of the NO source term calculated according to equation 8.3 using the mass fractions obtained with the three different methods and the control variables illustrated in Figure 8.18 are depicted. In the second and third rows the relative differences between the source terms calculated in different ways are shown following the (8.1) and (8.2) definitions.

8.2.5 Summary

We have used our three methods - FGM-1M, CSSA, CSSA-WOC - to calculate the Sydney bluff-body burner which features a non-premixed flame stabilized with a recirculation zone emerging behind a bluff-body. This is a more complex configuration than Sandia Flame D discussed in the previous section but once again the CSSA results have been found to be in very good agreement with the experimental data thereby validating the new approach.

Only minor differences could be observed between the FGM-1M and the CSSA results due to the lack of significant quenching or flame-wall interaction, however, when differences did exist the CSSA results were mostly closer to those of the experiments than the FGM-1M results. This was especially pronounced with respect to the OH mass fraction. Calculating one time step with CSSA took 2.9 times more time than with FGM which can be considered as a moderate increase compared to a transported PDF method. The correlations play a minor role as the CSSA and CSSA-WOC results are closely aligned but differences can be observed especially regarding the minor species and the chemical source terms.

Chapter 9

Summary and outlook

In this work a new method has been proposed, and validated, to approximate multivariate scalar probability density functions (PDFs) within the framework of large eddy simulation (LES) of turbulent combustion.

One of the most powerful modeling concepts is the so-called flamelet generated manifolds (FGM) approach in which the one-dimensional laminar flamelet solutions are embedded in a statistical description of turbulent combustion. This made extraordinary progress possible in the last twenty years, however, properly describing and predicting such processes with sufficient accuracy in a computationally efficient manner still remains a formidable challenge. To make a simulation feasible, the number of degrees of freedom characterizing turbulent reacting flows must be reduced by a statistical averaging or filtering technique.

In LES structures smaller than the grid spacing are removed by means of a low-pass filter. As both the reaction kinetics and the turbulence-chemistry interaction are highly nonlinear, the filtering leads to the occurrence of unclosed terms that describe the effects of unresolved fluctuations and need to be modeled. One way of accounting for these effects is to describe the unresolved fluctuations in a statistical fashion by means of a PDF. A PDF transport equation can be derived but its solution is rather expensive. A more common approach is to assume the shape of the PDF and to parametrize it with the statistical moments of the distribution. Usually only the first and second moments are considered while higher moments and covariances are neglected.

Most processes can only be characterized with more than one control variable, however, it is a daunting task to come up with a viable assumption regarding the shape of such a joint PDF. The common assumption is that the control variables appearing in the FGM tables are statistically independent, consequently the sought joint PDF can be expressed as the product of univariate PDFs. However, experimental observations indicate that this assumption is a rather poor one. Furthermore, in this case when coupling with the FGM method, the second moments of the control variables have to be introduced as additional parameters and the table of laminar flamelet solutions has to be pre-integrated. It increases the table's dimensionality often causing storage and memory problems.

In this work a new multivariate discrete joint scalar PDF approach has been proposed (denoted with the acronym CSSA) to overcome these challenges. The algorithm has been implemented in the academic code FASTEST building on its already present FGM and

LES capabilities. The novelty of this method is that the covariances among the univariate samples drawn from the marginal distributions are set with Kirkpatrick's simulated annealing algorithm (SA), which ensures that all the first and second statistical moments match the specified values including the correlations of the fluctuating control variables. This is done in such an efficient manner that makes it possible to generate the samples on the fly during the simulations. Considerable amount of time and attention have been devoted to optimizing the algorithm by identifying and tuning its key parameters, especially the so-called artificial temperature and the annealing schedule. We have seen that for correlations of higher absolute value it is beneficial to sort the samples in an ascending or descending order in advance, thereby providing a better initial configuration than a purely random one.

Once the sample set in the parameter space with the desired statistical moments have been generated, the look-up table can be accessed by each sample individually. Then the mean values of the thermochemical properties of interest can be calculated by simple ensemble averaging. This eliminates the need of pre-integrating the look-up table and consequently the increase in its dimensionality. It is sufficient to store the variables as functions of only the first moments of the control variables since higher moments are accounted for through the distribution of the discrete samples. Furthermore, this method can be generalized and adjusted to many different conditions as it does not pose any constraints on either how the marginal PDFs can be chosen or the number of control variables. Decoupling the look-up table from the actual shape of the PDFs offers the necessary flexibility for evaluating different PDFs or multiple look-up tables.

CSSA has been tested on various one-dimensional cases at first, namely on a density wave, a premixed flame, and a stratified premixed flame. These tests revealed that the treatment of the density field requires special attention. As separate sample sets are generated for each individual cell, errors in neighboring cells are independent of each other and this could lead to spurious density gradients. Known smoothing techniques commonly applicable to the stochastic field method cannot work in this case because fluctuations occur with respect not only to time but also to space, therefore storing and filtering all the necessary values would be computationally unfeasible. As a consequence only one density value corresponding to the means of the control variables is extracted from the look-up table. The test cases have confirmed that the treatment of the control variables and the table access have been correctly implemented. The CSSA method has been able to match the flame speeds and flame positions calculated as a reference with the FGM-1M method.

For the purpose of verification four two-dimensional cases have been simulated and the results have been compared to reference solutions calculated with the well-established FGM-1M method. Each case focused on either a different control variable or on a specific phenomenon such as flame-turbulence interaction or heat loss. The results are in very good agreement thereby verifying the CSSA model.

Finally, the CSSA method has been applied to the Sandia Flame D and the Sydney Bluff-Body configurations for which detailed experimental data exist. The simulation results are in very good agreement with the measurements thereby validating the new method.

Only minor differences can be observed between the CSSA and the FGM-1M results. This can be explained with the fact that the investigated cases are simple ones regarding the unresolved variances. Since quenching, flame-wall interaction or local extinction are not present, the subgrid-scale fluctuations have only minor effects. This is why the correlations have been found to be of minor importance as well. When the SA algorithm was turned off, the results did not change significantly, however, the fact that they changed at all in certain cases shows that the effect of taking into consideration or neglecting the correlations needs to be further investigated. These results suggest that in LES assuming statistical independence is a reasonable approximation. The correlations are expected to have a more pronounced effect in a RANS context because of the coarser grids. Nevertheless, for both three-dimensional setups CSSA gave slightly better results than the FGM-1M method thereby revealing the great potential of this approach. It is important to highlight that the computational cost of the CSSA method is not prohibitive, especially when it is compared with that of the transported PDF methods. For the cases presented here the average CSSA time step took only 2.2-2.9 times longer than that of the standard FGM-1M method. This is due to the optimization of the procedure and the fact that SA only plays a role where the variances are not vanishing, which generally permits to exclude a large part of the computational domain.

The objective of this work has been to prove the viability of the CSSA approach. Therefore at this stage of development at several points the simplest solutions have been applied, consequently there is room for improvement and further investigations in the future. One area to have a closer look at is how the subgrid-scale variances and covariances are calculated. As we have seen a simple gradient approach has been implemented, however, it would be more accurate to solve transport equations for the second moments. This could give further insights into how big of a mistake we make when we assume the statistical independence of the control variables. To this end more complex configurations should be investigated as well in which processes at subgrid-scales are expected to play a more pronounced role. It would be interesting to implement CSSA in a RANS context and test it on coarser grids. Also, the method's great flexibility should be utilized to evaluate PDFs of different assumed shapes besides the beta functions applied in this work. The fact that the look-up tables do not have to be pre-integrated every time the PDFs are changed makes this kind of investigation easier than ever. A third, natural way of continuing this work would be to extend the method for more control variables.

Appendix A

Rhie and Chow momentum interpolation scheme

In this Appendix the Rhie and Chow momentum interpolation scheme is explained in more details following the derivation of [199]. The objective of this technique is to avoid an unphysical pressure field with a checkerboard pattern by adding a correction term to the interpolation of the cell-face velocity using pressure values from adjacent cells thereby smoothing the pressure field.

Let us consider the (2.27) momentum conservation equation. After discretization all the terms can be grouped together in Ω on the right hand side except for the pressure term and the new value of u_i after the considered Δt time step:

$$u_i^{N+1} + \frac{\Delta t}{\rho \delta V} \delta p \, \delta S_i = \Omega, \tag{A.1}$$

where $\delta S_i = n_i \delta S$. This equation can be written for both the P and E nodes following the notation of Fig. 6.1b and using P and E as indices to denote in which point the given variable is evaluated :

$$u_{i,P}^{N+1} + \frac{\Delta t}{\rho_P \delta V_P} \delta p_P \, \delta S_{i,P} = \Omega_P, \tag{A.2}$$

$$u_{i,E}^{N+1} + \frac{\Delta t}{\rho_E \delta V_E} \delta p_E \, \delta S_{i,E} = \Omega_E. \tag{A.3}$$

Mimicking this formulation, we can obtain a similar equation for the velocity at the cell face center e:

$$u_{i,e}^{N+1} + \frac{\Delta t}{\rho_e \delta V_e} \delta p_e \, \delta S_{i,e} = \Omega_e, . \tag{A.4}$$

where the terms with subscript e should be interpolated in an appropriate manner. For the surface and volume elements linear interpolation is carried out:

$$\delta V_e = w_P \, \delta V_P + w_E \, \delta V_E \tag{A.5}$$

$$\delta S_{i,e} = w_P \, \delta S_{i,P} + w_E \, \delta S_{i,E} \tag{A.6}$$

using the interpolation factors defined in equation (6.12). Then Ω_e is interpolated from its counterparts in the (A.2) and (A.3) formulas:

$$\Omega_e = w_P \, \Omega_P + w_E \, \Omega_E. \tag{A.7}$$

Using equations (A.2), (A.3) and (A.7), the (A.4) expression can be rewritten in the following form:

$$u_{i,e}^{N+1} = \left(w_P\, u_{i,P}^{N+1} + w_E\, u_{i,E}^{N+1}\right) + w_P \frac{\Delta t}{\rho_P \delta V_P}\delta p_P + w_E \frac{\Delta t}{\rho_E \delta V_E}\delta p_E - \frac{\Delta t}{\rho_e \delta V_e}\delta p_e \qquad \text{(A.8)}$$

The first term on the right hand side can be thought of as an uncorrected velocity on the cell face. The simple linear interpolation is then substituted with the MULI method (see Section 6.1.3). The pressure differences can be easily calculated leading to the final form of the interpolation which is implemented in FASTEST:

$$u_{i,e}^{N+1} = \left(u_{i,e}^{N+1}\right)_{MULI} + w_P \frac{\Delta t}{\rho_P \delta V_P}\delta p_P + w_E \frac{\Delta t}{\rho_E \delta V_E}\delta p_E - \frac{\Delta t}{\rho_e \delta V_e}(p_P - p_E) \qquad \text{(A.9)}$$

Bibliography

[1] IPCC Carbon Dioxide Capture and Storage, Cambridge University Press, 2005.

[2] ANSYS Inc., ANSYS ICEM CFD 13.0 (2010).

[3] Flightpath 2050, Europe's vision for aviation, Report of the High Level Group on Aviation Research, Advisory Council for Aviation Research and Innovation in Europe (2011).

[4] Can future coal power plants meet CO2 emission standards without carbon capture and storage?, Electric Power Research Institute, 2014.

[5] EU CO2 emission standards for passenger cars and light-commercial vehicles, International Council on Clean Transportation (2014).

[6] Technology Innovation Program: Carbon Capture, Electric Power Research Institute, 2014.

[7] BP Statistical Review of World Energy 2015, Technical report, BP, p.l.c, 2015.

[8] International Energy Agency, CO2 Emissions from Fuel Combustion (2015).

[9] International Energy Agency, Key World Energy Statistics, 2015.

[10] International Energy Agency, World Energy Outlook, 2015.

[11] International Energy Agency, World Energy Outlook Special Report: Energy and Climate Change, 2015.

[12] CHEM1D: A one-dimensional laminar flame code, developed at Eindhoven University, `https://www.tue.nl/en/university/departments/mechanical-engineering/research/research-groups/combustion-technology/research-activities/chem1d/`, Accessed: 2016-01-16.

[13] Bluff-body flows and flames, `http://web.aeromech.usyd.edu.au/thermofluids/bluff.php`, Accesses: 2016-01-06.

[14] E. Aarts, J. Korst, Simulated annealing and Boltzmann machines, John Wiley & Sons, UK, 1988.

[15] J.D. Anderson, Fundamentals of Aerodynamics, McGraw-Hill, New York, USA, 2007.

[16] K. Aschmoneit, Numerische Beschreibung technischer Verbrennungssysteme, Ph.D. thesis, TU-Darmstadt, Darmstadt, 2003.

[17] A. Avdić, Development and Application of Numerical Methods for the Simulation of Advanced Combustion Processes within Complex Devices, Ph.D. thesis, TU-Darmstadt, Darmstadt, 2014.

[18] G. Balarac, H. Pitsch, V. Raman, Development of a dynamic model for the subfilter scalar variance using the concept of optimal estimators, Physics of Fluids 20 (2008).

[19] R. Barlow, International Workshop on Measurement and Computation of Turbulent Nonpremixed Flames, `http://www.sandia.gov/TNF/abstract.html`, Accessed: 2015-12-11.

[20] R. Barlow, J.H. Frank, Effects of turbulence on species mass fractions in methane/air jet flames, Symposium (International) on Combustion 27 (1998) 1087–1095.

[21] R. Barlow, J.H. Frank, Piloted CH4/Air flames C, D, E, and F - Release 2.1, `http://www.sandia.gov/TNF/DataArch/FlameD/SandiaPilotDoc21.pdf`, 2007.

[22] R.S. Barlow, J.H. Frank, A.N. Karpetis, J.Y. Chen, Piloted methane/air jet flames: transport effects and aspects of scalar structure, Combustion and Flame 143 (2005) 443–449.

[23] G.K. Batchelor, An introduction to fluid dynamics, Cambridge University Press, 1967.

[24] R.A. Baurle, S.S. Girimaji, Assumed PDF turbulence-chemistry closure with temperature-composition correlations, Combustion and Flame 134 (2003) 131–148.

[25] R.W. Bilger, The structure of turbulent nonpremixed flames, Proceedings of the Combustion Institute 22 (1988) 475–488.

[26] M. Boger, D. Veynante, H. Boughanem, A. Trouvé, Direct numerical simulation analysis of flame surface density concept for large eddy simulation of turbulent premixed combustion, Symposium (International) on Combustion 27 (1998) 917–927.

[27] R. Borghi, Recent advances in aeronautical science, Pergamont, London, UK, 1984.

[28] D. Bradley, How fast can we burn?, 24th Symposium on Combustion 24 (1992) 247–262.

[29] A.R. Brandt, G.A. Heath, E.A. Kort, F. O'Sullivan, G. Petron, S.M. Jordaan, P. Tans, J. Wilcox, A.M. Gopstein, D. Arent, S. Wofsy, N.J. Brown, R. Bradley, G.D. Stucky, D. Eardley, R. Harriss, Methane leaks from North American natural gas systems, Science 343 (2014) 733–735.

[30] M. Brandt, W. Polifke, P. Flohr, Approximation of joint PDFs by discrete distributions generated with Monte Carlo methods, Combustion Theory and Modelling 10 (2006) 535–558.

[31] N. Branley, W.P. Jones, Large eddy simulation of a turbulent non-premixed flame, Combustion and Flame 127 (2001) 1914–1934.

[32] K.N.C. Bray, M. Champion, P.A. Libby, N. Swaminathan, Finite rate chemistry and presumed PDF models for premixed turbulent combustion, Combustion and Flame 146 (2006) 665–673.

[33] J. Burkardt, Source codes in fortran 90, Florida State University, `http://people.sc.fsu.edu/~jburkardt/f_src/f_src.html`, Accessed: 2015-07-24.

[34] T. Butler, P. O'Rourke, A numerical method for two-dimensional unsteady reacting flows, Symposium (International) on Combustion 16 (1977) 1503–1515.

[35] F. Charlette, C. Meneveau, D. Veynante, A power-law flame wrinkling model for LES of premixed turbulent combustion Part I: non-dynamic formulation and initial tests, Combustion and Flame 131 (2002) 159–180.

[36] D.C. Charmpis, P.L. Panteli, A heuristic approach for the generation of multivariate random samples with specified marginal distributions and correlation matrix, Computational Statistics 19 (2004) 283–300.

[37] J.Y. Chen, A Eulerian PDF scheme for LES of nonpremixed turbulent combustion with second-order accurate mixture fraction, Combustion Theory and Modelling 11 (2007) 675–695.

[38] R.C.H. Cheng, Generation of multivariate normal samples with given mean and covariance matrix, Journal of Statistical Computation and Simulation 21 (1985) 39–49.

[39] A.J. Chorin, Numerical solution of the Navier-Stokes equations, Mathematics of Computation 22 (1968) 745–762.

[40] W.G. Cochran, Sampling techniques, Third edition, John Wiley & Sons, 1977.

[41] G.H.A. Cole, An introduction to the statistical theory of classical simple dense fluids, Pergamon Press Ltd., Headington Hill Hall, Oxford, 1967.

[42] O. Colin, F. Ducros, D. Veynante, T. Poinsot, A thickened flame model for large eddy simulations of turbulent premixed combustion, Physics of Fluids 12 (2000) 1843–1863.

[43] A.W. Cook, J.J. Riley, A subgrid model for equilibrium chemistry in turbulent flows, Physics of Fluids 6 (1994) 2868–2870.

[44] R. Courant, K. Friedrichs, H. Lewy, Über die partiellen differenzengleichungen der mathematischen physik, Mathematische Annalen 100 (1928) 32–74.

[45] C.F. Curtiss, J.O. Hirschfelder, Transport properties of multicomponent gas mixtures, The Journal of Chemical Physics 17 (1949).

[46] B. Dally, D. Fletcher, A. Masri, Flow and mixing fields of turbulent bluff-body jets and flames, Combustion Theory and Modeling 2 (1998) 193–219.

[47] B. Dally, A. Masri, R. Barlow, G. Fiechtner, Instantaneous and mean compositional structure of bluff-body stabilized nonpremixed flames, Combustion and Flame 114 (1998) 119–148.

[48] G.Z. Damköhler, Turbulente flammenstruckturen 46 (1940).

[49] J.E. Dec, Advanced compression ignition engines: Understanding the in-cylinder processes, Proceedings of the Combustion Institute 32 (2009) 2727–2742.

[50] P. Domingo, L. Vervisch, S. Payet, R. Hauguel, DNS of a premixed turbulent V flame and LES of a ducted flame using a FSD-PDF subgrid scale closure with FPI-tabulated chemistry, Combustion and Flame 143 (2005) 566–586.

[51] C. Dopazo, Probability density function approach for a turbulent axisymmetric heated jet. Centerline evolution, Physics of Fluids 18 (1975) 397–404.

[52] F. Durst, M. Schäfer, A parallel block-structured multigrid method for the prediction of incompressible flows, International Journal for Numerical Methods in Fluids 22 (1996) 549–565.

[53] C. Duwig, C. Fureby, Large eddy simulation of unsteady lean stratified premixed combustion, Combustion and Flame 151 (2007) 85–103.

[54] A. Favre, Statistical equations of turbulent gases, Problems of hydrodynamics and continuum mechanics (1969) 231–266.

[55] J.H. Ferziger, M. Perić, Computational Methods for Fluid Dynamics, Springer, 2007.

[56] B. Fiorina, R. Baron, O. Gicquel, D. Thevenin, S. Carpentier, N. Darabiha, Modelling non-adiabatic partially premixed flames using flame-prolongation of ILDM, Combustion Theory and Modelling 7 (2003) 449.

[57] B. Fiorina, O. Gicquel, L. Vervisch, S. Carpentier, N. Darabiha, Approximating the chemical structure of partially premixed and diffusion counterflow flames using FPI flamelet tabulation, Combustion and Flame 140 (2005) 147–160.

[58] B. Fiorina, R. Mercier, G. Künne, A. Ketelheun, A. Avdić, J. Janicka, D. Geyer, A. Dreizler, E. Alenius, C. Duwig, P. Trisjono, K. Kleinheinz, S. Kang, H. Pitsch, F. Proch, F. Cavallo Marincola, A. Kempf, Challenging modeling strategies for LES of non-adiabatic turbulent stratified combustion, Combustion and Flame 162 (2015) 4264–4282.

[59] B. Fiorina, D. Veynante, S. Candel, Modeling combustion chemistry in large eddy simulation of turbulent flames, Flow, Turbulence and Combustion 94 (2015) 3–42.

[60] B. Fiorina, R. Vicquelin, P. Auzillon, N. Darabiha, O. Gicquel, D. Veynante, A filtered tabulated chemistry model for LES of premixed combustion, Combustion and Flame 157 (2010) 465–475.

[61] H. Forkel, Über die Grobstruktursimulation turbulenter Wasserstoff-Diffusionsflammen, Ph.D. thesis, TU-Darmstadt, Darmstadt, 2000.

[62] J.A. Francis, S.J. Vavrus, Evidence linking Arctic amplification to extreme weather in mid-latitudes, Geophysical Research Letters 39 (2012).

[63] J.H. Frank, R.S. Barlow, C. Lundquist, Radiation and nitric oxide formation in turbulent non-premixed jet flames, Proceedings of the combustion Institute (2000) 447–454.

[64] S.H. Fuller, L.I. Millett, Computing performance: Game over or next level?, Computer 44 (2011) 31–38.

[65] F. Gao, E.E. O'Brien, A large-eddy simulation scheme for turbulent reacting flows, Physics of Fluids A: Fluid Dynamics 5 (1993) 1282–1284.

[66] J.E. Gentle, Random number generation and Monte Carlo methods, Springer-Verlag, New York, USA, 1998.

[67] P. Germano, U. Piomelli, P. Moin, W. Cabot, A dynamic subgrid-scale eddy viscosity model, Physics of Fluids 3 (1991) 1760–1765.

[68] S. Ghosal, P. Moin, The basic equations for the large eddy simulation of turbulent flows in complex geometry, Journal of Computational Physics 118 (1995) 24–37.

[69] D. Ghosh, A. Vogt, Drawing a sample from a given distribution, Proceedings of the Survey Research Methods Section, American Statistical Association (2008).

[70] O. Gicquel, N. Darabiha, D. Thevenin, Laminar premixed hydrogen/air counterflow flame simulations using flame prolongation of ILDM with differential diffusion, Proceedings of the Combustion Institute 28 (2000) 1901–1908.

[71] S.S. Girimaji, Assumed β-PDF model for turbulent mixing: Validation and extension to multiple scalar mixing, Combustion Science and Technology 78 (1991) 177–196.

[72] R.M. Gorman, Cooking up bigger brains, Scientific American 298 (2008) 102–105.

[73] G. Graham, S. Menon, A comparison of scalar PDF turbulent combustion models, Combustion and Flame 113 (1998) 442–453.

[74] E. Gutheil, Multivariate PDF closure applied to oxidation of CO in a turbulent flow, In A. L. Kuhl, K.-C. Leyer, A. A. Borisov and W. A. Sirignamo - Dynamics of Deflagrations and Reactive Systems, Volume 131 of Progress in Astronautic and Aeronautics, AIAA, Washington DC, USA (1991) 288–302.

[75] E. Gutheil, H. Bockhorn, The effect of multi dimensional PDF's on the turbulent reaction rate in turbulent reactive flows at moderate Damköhler numbers, Physicochemical Hydrodynamics 9 (1987) 525–535.

[76] S. Hada, K. Takata, Y. Iwasaki, M. Yuri, J. Masada, High-efficiency gas turbine development applying 1600°C class J technology, Mitsubishi Heavy Industries Technical Review 52 (2015).

[77] F. Hahn, Zur Vorhersage technischer Verbrennungssysteme im Hinblick auf fluessige Brennstoffe, Ph.D. thesis, TU-Darmstadt, Darmstadt, 2008.

[78] F. Hahn, C. Olbricht, J. Janicka, Study of various configurations under variable density mixing conditions aiming on gas turbine combustion using LES, ASME Turbo Expo Conference Proceedings (2008) 155–165.

[79] C. Hasse, N. Peters, A two mixture fraction flamelet model applied to split injections in a DI diesel engine, Proceedings of the Combustion Institute 30 (2005) 2755–2762.

[80] G. Hauke, L. Valiño, Computing reactive flows with a field Monte Carlo formulation and multi-scale methods, Computer methods in applied mechanics and engineering 193 (2004) 1455–1470.

[81] E.R. Hawkes, R.S. Cant, A flame surface density approach to large eddy simulation of premixed turbulent combustion, Proceedings of the Combustion Institute 28 (2000) 51–58.

[82] D.C. Haworth, Progress in probability density function methods for turbulent reacting flows, Progress in Energy and Combustion Science 36 (2010) 168–259.

[83] C. Hirsch, Numerical Computation of Internal and External Flows, Elsevier, 2007.

[84] R.J. Hodrick, E.C. Prescott, Post-war U.S. business cycles: An empirical investigation, Journal of Money, Credit and Banking 29 (1997) 1–16.

[85] M. Ihme, L. Shunn, J. Zhang, Regularization of reaction progress variable for application to flamelet-based combustion models, Journal of Computational Physics 231 (2012) 7715–7721.

[86] R.L. Iman, W.J. Conover, A distribution-free approach to inducing rank correlation among input variables, Communications in Statistics - Simulation and Computation 11 (1982) 311–334.

[87] R.B. Jackson, J.G. Canadell, C. Le Quere, R.M. Andrew, J.I. Korsbakken, G.P. Peters, N. Nakicenovic, Reaching peak emissions, Nature Climate Change 6 (2016) 7–10.

[88] J. Janicka, W. Kolbe, W. Kollmann, Closure of the transport equation for the probability density function of turbulent scalar fields, Journal of Non-Equilibrium Thermodynamics 4 (1979).

[89] J. Janicka, W. Kollmann, A two-variables formalism for the treatment of chemical reactions in turbulent H2-air diffusion flames, Symposium (International) on Combustion 17 (1979) 421–430.

[90] A. Kempf, Large-Eddy Simulation of Non-Premixed Turbulent Flames, Ph.D. thesis, TU-Darmstadt, Darmstadt, 2003.

[91] A.M. Kempf, R.P. Lindstedt, J. Janicka, Large-eddy simulation of a bluff-body stabilized non-premixed flame, Combustion and Flame 144 (2006) 170–189.

[92] A.R. Kerstein, W. Ashurst, F.A. Williams, Field equation for interface propagation in an unsteady homogenous flow field, Physical Review A 37 (1988) 2728–2731.

[93] A. Ketelheun, Development of Tabulated Chemistry Methods for the Accurate Simulation of Turbulent Combustion Systems, Ph.D. thesis, TU-Darmstadt, Darmstadt, 2014.

[94] A. Ketelheun, G. Künne, J. Janicka, Heat transfer modeling in the context of large eddy simulation of premixed combustion with tabulated chemistry, Flow, Turbulence and Combustion 91 (2013) 867–893.

[95] A. Ketelheun, C. Olbricht, F. Hahn, J. Janicka, Premixed generated manifolds for the computation of technical combustion systems, Proceedings of ASME Turbo Expo 2009: Power for Land, Sea and Air, GT2009, Orlando, FL (2009).

[96] S. Kirkpatrick, Optimization by simulated annealing: Quantitative studies, Journal of Statistical Physics 34 (1984) 975–986.

[97] S. Kirkpatrick, C.D. Gelatt, M.P. Vecchi, Optimization by simulated annealing, Science 220 (1983) 671–680.

[98] E.V. Klapdor, Simulation of Combustor-Turbine Interaction in a Jet Engine, Ph.D. thesis, TU-Darmstadt, Darmstadt, 2011.

[99] E.V. Klapdor, F. di Mare, W. Kollmann, J. Janicka, A compressible pressure-based solution algorithm for gas turbine combustion chambers using the PDF/FGM model, Flow, Turbulence and Combustion 91 (2013) 209–247.

[100] M. Klein, A. Sadiki, J. Janicka, A digital filter based generation of inflow data for spatially developing direct numerical or large eddy simulations, Journal of Computational Physics 186 (2003) 652–665.

[101] R. Knikker, D. Veynante, C. Meneveau, A dynamic flame surface density model for large eddy simulation of turbulent premixed combustion, Proceedings of the Combustion Institute 29 (2002) 2105–2111.

[102] G.D. Knott, Interpolating Cubic Splines, Springer, 2000.

[103] D.E. Knuth, The Art of Computer Programming - Volume 2: Seminumerical Algorithms, 3rd edition, Addison-Wesley, Reading, Massachusetts, USA, 1998.

[104] A.N. Kolmogorov, The local structure of turbulence in incompressible viscous fluid for very large Reynolds numbers, Doklady Akademiia Nauk SSSR 30 (1941) 301–305.

[105] T.S. Kuan, R.P. Lindstedt, Transported probability density function modeling of a bluff-body stabilized turbulent flame, Proceedings of the Combustion Institute 30 (2005) 767–774.

[106] J. Kühne, A. Ketelheun, J. Janicka, Analysis of sub-grid PDF of a progress variable approach using a hybrid LES/TPDF method, Proceedings of the Combustion Institute 33 (2011) 1411–1418.

[107] G. Künne, Large Eddy Simulation of Premixed Combustion Using Artificial Flame Thickening Coupled with Tabulated Chemistry, Ph.D. thesis, TU-Darmstadt, Darmstadt, 2012.

[108] G. Künne, A. Ketelheun, J. Janicka, LES modeling of premixed combustion using a thickened flame approach coupled with FGM tabulated chemistry, Combustion and Flame 158 (2011) 1750–1767.

[109] C.D. Lai, Morgenstern's bivariate distribution and its application to point processes, Journal of Mathematical Analysis and Applications 65 (1978) 247–256.

[110] L.D. Landau, E.M. Lifschitz, Statistical Physincs, Vol. 5., Butterworth-Heinemann, 1980.

[111] W. Lazik, T. Doerr, S. Bake, Low NOx combustor development for the Engine3E core engine demonstrator, ISABE paper 2007-1190 (2007).

[112] T. Lehnhäuser, Eine effiziente numerische Methode zur Gestaltsoptimierung von Stroemungsgebieten, Ph.D. thesis, TU-Darmstadt, Darmstadt, 2004.

[113] T. Lehnhäuser, M. Schäfer, Improved linear interpolation practice for finite-volume schemes on complex grids, International Journal for Numerical Methods in Fluids 38 (2002) 625–645.

[114] S.T. Li, J.L. Hammond, Generation of pseudorandom numbers with specified univariate distributions and correlation coefficients, IEEE Transaction on Systems, Man, and Cybernetics 5 (1975) 557–561.

[115] D.L. Libby, M.R. Novick, Multivariate generalized beta distributions with applications to utility assessment, Journal of Educational Statistics 7 (1982) 271–294.

[116] D.K. Lilly, A proposed modification of the Germano subgrid-scale closure method, Physics of Fluids A: Fluid Dynamics 4 (1992) 633–635.

[117] Y. Liu, K.S. Lau, C.K. Chan, Y.C. Guo, W.Y. Lin, Structures of scalar transport in 2D transitional jet diffusion flames by LES, International Journal of Heat and Mass Transfer 46 (2003) 3841–3851.

[118] P.M. Lurie, M.S. Goldberg, An approximate method for sampling correlated random variables from partially-specified distributions, Management Science 44 (1998) 203–218.

[119] U. Maas, S.B. Pope, Simplifying chemical kinetics: Intrinsic low-dimensional manifolds in composition space, Combustion and Flame 88 (1992) 239–264.

[120] A. Majda, J. Sethian, The derivation and numerical solution of the equations for zero Mach number combustion, Combustion Science and Technology 42 (1985) 185–205.

[121] A. Maltsev, Towards the Development and Assessment of Complete CFD Models for the Simulation of Stationary Gas Turbine Combustion Process, Ph.D. thesis, TU-Darmstadt, Darmstadt, 2003.

[122] A.R. Masri, R.W. Dibble, R.S. Barlow, The structure of turbulent nonpremixed flames revealed by Raman-Rayleigh-LIF measurements, Progress in Energy and Combustion Science 22 (1996) 307–362.

[123] C. Meneveau, T. Poinsot, Stretching and quenching of flamelets in premixed turbulent combustion, Combustion and Flame 86 (1991) 311–332.

[124] S. Menon, W.H. Jou, Large eddy simulations of combustion instability in an axisymmetric ramjet combustor, Combustion Science and Technology 75 (1991) 53–72.

[125] N. Metropolis, A.W. Rosenbluth, M.N. Rosenbluth, A.H. Teller, E. Teller, Equation of state calculations by fast computing machines, The Journal of Chemical Physics 21 (1953) 1087–1092.

[126] P. Moin, J. Kim, Numerical investigation of turbulent channel flow, Journal of Fluid Mechanics 118 (1982) 341–377.

[127] D. Morgenstern, Einfache beispiele zweidimensionaler verteilungen, Mitt. Math. Statist. 8 (1956) 234–235.

[128] P.D. Nguyen, L. Vervisch, V. Subramanian, P. Domingo, Multidimensional flamelet-generated manifolds for partially premixed combustion, Combustion and Flame 157 (2010) 43–61.

[129] J.A. van Oijen, L.P.H. de Goey, Modelling of premixed laminar flames using FGM, Combustion Science and Technology 161 (2000) 113–137.

[130] J.A. van Oijen, F.A. Lammers, L.P.H. de Goey, Modeling of complex premixed burner systems by using flamelet-generated manifolds, Combustion and Flame 127 (2001) 2124–2134.

[131] C. Olbricht, Numerische Berechnung technischer Verbrennungssysteme, Ph.D. thesis, TU-Darmstadt, Darmstadt, 2008.

[132] C. Olbricht, F. Hahn, A. Ketelheun, J. Janicka, Strategies for presumed PDF modeling for LES with premixed flamelet generated manifolds, Journal of Turbulence 11 (2010) 1–18.

[133] R.S. Parrish, Generating random deviates from multivariate Pearson distributions, Computational Statistics and Data Analysis 9 (1990) 283–295.

[134] S.V. Patankar, D.B. Spalding, Calculation procedure for heat, mass and momentum-transfer in 3-dimensional parabolic flows, International Journal of Heat and Mass Transfer 15 (1972) 1787–1806.

[135] N. Peters, Turbulent Combustion, Cambridge University Press, 1980.

[136] N. Peters, Laminar diffusion flamelets in non-premixed turbulent combustion, Progress in Energy and Combustion Science 3 (1984) 319–339.

[137] N. Peters, Laminar flamelet concepts in turbulent combustion, Symposium (International) on Combustion 21 (1988) 1231–1250.

[138] N. Peters, The turbulent burning velocity for large-scale and small-scale turbulence, Journal of Fluid Mechanics 384 (1999) 107–132.

[139] N. Peters, S. Donnerhack, Structure and similarity of nitric oxide production in turbulent diffusion flames, Symposium (International) on Combustion 18 (1981) 33–42.

[140] C.D. Pierce, P. Moin, A dynamic model for subgrid-scale variance and dissipation rate of a conserved scalar, Physics of Fluids 10 (1998) 3041–3044.

[141] D. Pinner, M. Rogers, Solar power comes of age, Foreign Affairs 94 (2015) 111–118.

[142] A. Pires Da Cruz, A. Dean, J. Grenda, A numerical study of the laminar flame speed of stratified methane/air flames, Proceedings of the Combustion Institute 28 (2000) 1925–1932.

[143] H. Pitsch, Large-eddy simulation of turbulent combustion, Annual Review of Fluid Mechanics 38 (2006) 453–482.

[144] H. Pitsch, M. Chen, N. Peters, Unsteady flamelet modeling of turbulent hydrogen-air diffusion flames, Symposium (International) on Combustion 27 (1998) 1057–1064.

[145] H. Pitsch, H. Steiner, Large eddy simulation of a turbulent piloted methane/air diffusion flame (Sandia Flame D), Physics of Fluids 12 (2000) 2541–2554.

[146] T. Poinsot, Using direct numerical simulations to understand premixed turbulent combustion, 26th Symposium (International) on Combustion, Pittsburgh (1996) 219–232.

[147] T. Poinsot, D. Veynante, Theoretical and Numerical Combustion, Aquaprint, Bordeaux, France, 2012.

[148] S.B. Pope, A Monte Carlo method for the PDF equations of turbulent reacting flow, Combustion Science and Technology 25 (1981) 159–174.

[149] S.B. Pope, PDF methods for turbulent reacting flows, Progress in Energy and Combustion Science 11 (1985) 119–192.

[150] S.B. Pope, Computations of turbulent combustion: progress and challenges, Proceedings of the Combustion Institute 23 (1990) 591–612.

[151] S.B. Pope, Turbulent Flows, Cambridge University Press, Cambridge, UK, 2000.

[152] L. Prandtl, Über die ausgebildete turbulenz, ZAMM 5 (1925) 136–139.

[153] V.N. Prasad, Large Eddy Simulation of Partially Premixed Turbulent Combustion, Ph.D. thesis, Imperial College London, London, 2011.

[154] W.H. Press, S.A. Teukolsky, W.T. Vetterling, B.P. Flannery, Numerical Recipes in C, Cambridge University Press, 1992.

[155] S.J. Pyne, Fire: a Brief History, University of Washington Press, 2011.

[156] S.J. Pyne, The fire age, AEON magazine, `https://aeon.co/essays/how-humans-made-fire-and-fire-made-us-human`, Accessed: 2016-01-21.

[157] C.R. Reeves, Modern Heuristic Techniques for Combinatorial Problems, McGraw-Hill, UK, 1995.

[158] O. Reynolds, An experimental investigation of the circumstances which determine whether the motion of water shall be direct or sinuous, and of the law of resistance in parallel channels, Proceedings of the Royal Society of London 35 (1883) 84–99.

[159] C.M. Rhie, W.L. Chow, Numerical study of the turbulent flow past an airfoil with trailing edge separation, AIAA Journal 21 (1983) 1525–1532.

[160] R.P. Rhodes, A probability distribution function for turbulent flows, In S. N. B. Murphy (ed.), Turbulent Mixing in Nonreactive and Reactive Flows (1975) 235–241.

[161] L.F. Richardson, Weather Prediction by Numerical Process, Cambridge University Press, Cambridge, UK, 1922.

[162] K. Richter, R. Friedrich, L. Schmitt, Large eddy simulation of turbulent wall boundary layers with pressure gradient, Symposium on Turbulent Shear Flows, 6th, Toulouse (1987).

[163] P. Sagaut, Large Eddy Simulation for Incompressible Flows, An introduction, Springer, Heidelberg, Germany, 2001.

[164] M.M. Salehi, B.W. K., Presumed PDF modeling for RANS simulation of turbulent premixed flames, Combustion Theory and Modelling 14 (2010) 381–403.

[165] M. Schäfer, Computational Engineering, Springer, 2006.

[166] C. Schneider, A. Dreizler, J. Janicka, E.P. Hassel, Flow field measurements of stable and locally extinguishing hydrocarbon-fuelled jet flames, Combustion and Flame 135 (2003) 185–190.

[167] E. Schneider, Numerische Simulation Turbulenter Vorgemischter Verbrennungssysteme: Entwicklung und Anwendung eines RANS-basierten Gesamtmodells, Ph.D. thesis, TU-Darmstadt, Darmstadt, 2005.

[168] V.A. Shvab, Relation between the temperature and velocity fields of the flame of a gas burner, Gos. Energ. Izd., Moscow-Leningrad, 1948.

[169] J. Slotnick, A. Khodadoust, J. Alonso, D. Darmofal, W. Gropp, E. Lurie, D. Mavriplis, CFD vision 2030 study: A path to revolutionary computational aerosciences, NASA/CR-2014-218178 (2014).

[170] J. Smagorinsky, General circulation experiments with the primitive equations, 1. the basic experiment, Monthly Weather Review 91 (1963) 99–164.

[171] G.P. Smith, D.M. Golden, M. Frenklach, N.W. Moriarty, B. Eiteneer, M. Goldenberg, C.T. Bowman, R.K. Hanson, S. Song, W.C. Gardiner Jr., V.V. Lissianski, Z. Oin, GRI-Mech 3.0 , `http://www.me.berkeley.edu/gri_mech`, Accesses: 2015-12-09.

[172] M. Smooke, Reduced Kinetic Mechanisms and Asymptotic Approximations for Methane-Air Flames, Springer, Berlin, Germany, 1991.

[173] B. Somers, The Simulation of Flat Flames with Detailed and Reduced Chemical Models, Ph.D. thesis, TU-Eindhoven, Eindhoven, 1994.

[174] D.B. Spalding, Development of the eddy-break-up model of turbulent combustion, Symposium (International) on Combustion 16 (1976) 1657–1663.

[175] M. Staufer, Large Eddy Simulation of Premixed and Partially Premixed Flames, Ph.D. thesis, TU-Darmstadt, Darmstadt, 2009.

[176] T. Stocker, D. Qin, G.K. Plattner, M. Tignor, S.K. Allen, J. Boschung, A. Nauels, Y. Xia, V. Bex, P.M. Midgley, IPCC, 2013: Climate Change 2013: The Physical Science Basis. Contribution of Working Group I to the Fifth Assessment Report of the Intergovernmental Panel on Climate Change, Cambridge University Press, Cambridge, United Kingdom and New York, NY, USA, 2013.

[177] H.L. Stone, Iterative solution of implicit approximations of multidimensional partial differential equations, SIAM Journal of Numerical Analysis 5 (1968) 530–558.

[178] S. Subramaniam, S.B. Pope, A mixing model for turbulent reactive flows based on Euclidean minimum spanning trees, Combustion and Flame 115 (1998) 487–514.

[179] J. de Swart, G. Groot, J.A. van Oijen, J.H.M. ten Thije Boonkkamp, L.P.H. de Goey, Detailed analysis of the mass burning rate of stretched flames including preferential diffusion effects, Combustion and Flame 145 (2006) 245–258.

[180] Q. Tang, J. Xu, S.B. Pope, Probability density function calculations of local extinction and NO production in piloted-jet turbulent methane/air flames, Proceedings of the Combustion Institute 28 (2000) 133–139.

[181] H. Tennekes, J. Lumley, A First Course in Turbulence, MIT Press, 1972.

[182] C.D. Vale, V.A. Maurelli, Simulating multivariate non-normal distributions, Psychometrika 48 (1983) 465–471.

[183] L. Valiño, A field Monte Carlo formulation for calculating the PDF of a single scalar in a turbulent flow, Flow, Turbulence and Combustion 60 (1998) 157–172.

[184] L. Vervisch, T. Poinsot, Direct numerical simulation of non-premixed turbulent flame, Annual Review of Fluid Mechanics 30 (1998) 655–691.

[185] D. Veynante, L. Vervisch, Turbulent combustion modeling, Progress in Energy and Combustion Sciences 28 (2002) 193–266.

[186] J. Villermaux, J. Devillon, Représentation de la coalescence et dela redispersion des domaines de ségrégation dans un fluide per modéle d'interaction phénoménologique, Proceedings of the Second International Symposium on Chemical Reaction Engineering (1972).

[187] A.W. Vreman, B.A. Albrecht, J.A. van Oijen, L.P.H. de Goey, R.J.M. Bastiaans, Premixed and nonpremixed generated manifolds in large-eddy simulation of Sandia Flame D and F, Combustion and Flame 153 (2008) 394–416.

[188] C. Wall, B.J. Boersma, P. Moin, An evaluation of the assumed beta probability density function subgrid-scale model for large eddy simulation of nonpremixed, turbulent combustion with heat release, Physics of Fluids 12 (2000).

[189] J. Warnatz, U. Maas, R.W. Dibble, Combustion: Physical and Chemical Fundamentals, Modeling and Simulation, Experiments, Pollutant Formation, Springer, Berlin, Germany, 2009.

[190] G. Warwick, Must try harder, Aviation Week and Space Technology, September 14-27 (2015) 19.

[191] G. Warwick, On track, Aviation Week and Space Technology, November 23 - December 6 (2015) 63.

[192] G. Warwick, Test tales, Aviation Week and Space Technology, November 23 - December 6 (2015) 60–62.

[193] B. Wegner, A Large Eddy Simulation Technique for the Prediction of Flow, Mixing and Combustion in Gas Turbine Combustors, Ph.D. thesis, TU-Darmstadt, Darmstadt, 2006.

[194] D.C. Wilcox, Turbulence Modeling for CFD, DCW Industries, Inc., La Cafiada, CA, 2006.

[195] F.A. Williams, Recent Advances in Theoretical Descriptions of Turbulent Diffusion Flames, Turbulent Mixing in Nonreactive and Reactive Flows, Plentum Press, 1975.

[196] F.A. Williams, A review of some theoretical combustions of turbulent flame structure, AGARD Conference Proceedings II.1 (1975) 1–25.

[197] F.A. Williams, Combustion Theory, Benjamin Cummings, Menlo Park, CA, 1985.

[198] J.H. Williamson, Low-storage Runge-Kutta schemes, Journal of Computational Physics 35 (1980) 48–56.

[199] B. Yu, W.Q. Tao, J.J. Wei, Y. Kawaguchi, T. Tagawa, H. Ozoe, Discussion on momentum interpolation method for collocated grids of incompressible flow, Numerical Heat Transfer, Part B 42 (2002) 141–166.

[200] Y.B. Zeldovich, The oxidation of nitrogen on combustion and explosion, Acta Physicochim URSS 21 (1946).

[201] Y.B. Zeldovich, On the theory of combustion of initially unmixed gases, Zhur. Tekhn. Fiz. 19 (1949) 1199.

[202] G. Zhou, L. Davidson, E. Olsson, Transonic inviscid/turbulent airfoil flow simulations using a pressure based method with high order schemes, Fourteenth International Conference on Numerical Methods in Fluid Dynamics, Lecture Notes in Physics 453 (1995) 372–378.

Curriculum Vitae

Personal data

Name:	Dávid Jesch
Date of Birth:	11.04.1984
Place of Birth:	Nagykanizsa, Hungary

Education

Elementary school	09/1990 - 06/1994	Zrínyi Miklós Elementary School, Nagykanizsa
Secondary school	09/1994 - 06/2002	Batthyány Lajos Grammar School, Nagykanizsa
University studies	09/2002 - 06/2007	Master of Science in Physics Eötvös Loránd University, Budapest
	09/2006 - 06/2010	Bachelor of Science in Mechatronics Engineering Budapest University of Technology and Economics
	09/2010 - 08/2011	PhD Student Budapest University of Technology and Economics Department of Fluid Mechanics
	09/2012 - 05/2016	PhD Student Technische Universität Darmstadt Department of Energy and Power Plant Technology

Internships, Scholarships, Research Projects

Exchange Student	08/2009 - 01/2010	University of Arizona
Research Engineer	01/2010 - 09/2010	Department of Fluid Mechanics Budapest University of Technology and Economics
Research Assistant	08/2011 - 08/2012	Engine Research Center University of Wisconsin-Madison